Vol. 44 No. 1 *Journal of the Communications Research Laboratory* *March 1997*
Printed in Tokyo, Japan *pp. 11 - 186*

A STUDY ON THE ION COMPOSITION OF THE TOPSIDE IONOSPHERE BY SATELLITE-BORNE MASS SPECTROMETERS

By
Iwao IWAMOTO

ABSTRACT

The ionospheric ion composition of the earth and other planets is reviewed. The basic characteristics of the composition, relevant chemical reactions and ion transport processes ionospheres are summarized. The operation principle and basic characteristics of the Bennett mass spectrometer, which was flown on the ISS-b and EXOS-D satellites, are described in detail. The global ion distributions at an altitude of 1100 km, as observed by the ISS-b satellite, are presented. A prominent feature in these distributions is that dependence on the longitude is much larger compared to previous studies. From LT maps, global structures that persist for a few months are found. Variations in ion densities are statistically analyzed with respect to a selected parameter, such as latitude, local time, season, solar activity, or geomagnetic activity. Several interesting features are found in the He^+ distributions. One is that the winter bulge structure in the ionic helium can be seen only in the day - it disappears at night. Another is that the equatorial trough in the He^+ distribution becomes dominant at night. The density of H^+ at 1100 km has negative correlation with F10.7. He^+ density has weak positive correlation with F10.7 in the global average sense, either positive or negative correlation is statistically significant in the sub-divided domains. A new energy and mass analyzer, in which the retarding potential analyzer and the Bennett mass spectrometer are combined, is described. This SMS analyzer is flown on the EXOS-D in collaboration with a Canadian scientist group. It has been observing the magnetospheric and the ionospheric ion composition since its launch in 1989.

Keywords: mass spectrometer, ion composition, ionosphere, satellite observation

1. Introduction

Research on the ionosphere has a rather long history, starting with the pioneering experiments by Appleton and by Barret in the U.K., and Breit and Tuve in the U.S., both of which took place in 1924. Ionospheric research was especially important when short waves were used as the primary means of international telecommunications. The International Geophysical Year (IGY) of 1957 brought profound changes in our knowledge of the ionosphere, and the space around the Earth and planets became better understood with the exploration by space vehicles and spacecrafts. At the same time, development of satellite communication reduced the role of the ionosphere and short wave communication; in turn, the ionosphere and the magnetosphere took on a new role as a space environment.

It is important to learn as much as we can about the Earth's ionosphere and magnetosphere in their own right because they are the only fields in the plasma universe that can be touched directly by man. As 99.9% of the universe is said to be composed of plasma, plasma science plays a crucial role in space research. Plasmas are also important in many practical applications, such as nuclear fusion

and material processing. It is surprising that plasma seems to be ruled by the same law, from the microscopic scale in solid-state devices, to the vast macroscopic scale of the universe[1].

The pollution and destruction of earth's environment by human activities are becoming a great international concern. Global warming due to the green-house effect gases and the depletion of the stratospheric ozone layer due to halocarbons have frequently been the subject of mass media attention. Although the ionosphere and magnetosphere are usually not discussed, these regions are not exempt from contamination due to human activities. For example, debris from rockets and satellites are accumulating in earth orbit. It is estimated that if space activities continue at their current rate, the growth of space debris will be accelerated suddenly sometime in the near future and form a "debris belt" around the earth[2]. The construction of a big space station or solar power system would also seriously impact the ionosphere and/or the magnetosphere. Space scientists and engineers must consider these problems, along with impact on earth's environment.

Owing to the global nature of ionospheric and magnetospheric physics, such international campaign, as the IGY, the IMS, and the MAP, played a great role in these studies. The Ionosphere Sounding Satellite-b (ISS-b), which is the main data source for this paper, was originally intended to dedicate to such a campaign, namely the IMS. In the IMS and MAP programs, a particular region was studied in great detail, but in the STEP program, interactions between various regions and the energy flows between regions are more important. For this program, several satellites have been launched. The EXOS-D satellite, or the AKEBONO as it was named after launch in 1989, is one of these satellites. I and my colleagues have developed ion-mass spectrometers for these satellites. This paper describes the ion mass spectrometers and the results obtained from them.

Many observations have been made of the ion composition of the ionosphere and magnetosphere mainly by U.S. satellites. Compared to these, the ISS-b satellite observations provided a much longer time period data at a fixed altitude, so it has been possible to obtain global distributions of the ion densities with respect to many reference frames, including latitude, longitude, local time, season, and solar activity. This was not by chance. From the very beginning of the ISS project, global mapping of the ionospheric parameters was the main objective. Following this initial plan, many global maps have been obtained and published. The global maps of the ion densities obtained from ISS-b are presented in this paper.

While the ISS-b mass spectrometer did not have the capability to analyze energy, the ion-mass spectrometer aboard the EXOS-D satellite does. It combines the functions of the Bennett mass spectrometer with a retarding potential analyzer (RPA) into a new type analyzer. Various instrument parameters, such as resolution and sensitivity, can be adjusted, allowing various observation modes to be easily selected by issuing software commands to the on-board processor. The operation principles of this instrument and the initial observational results are presented in this paper. Since the observations were in progress when this paper was prepared, the results presented here are preliminary.

2. Review of ionospheric ion composition

The main objective of this paper is to study the ion composition in the upper part of the ionospheric F region, or the topside ionosphere. The later sections discuss the ion density distributions in the topside ionosphere as observed by satellite ion-mass spectrometer. To lay a basis for this discussion, this section reviews the ion composition of the ionosphere in general. Although the history of ionospheric research is long and it is very rich in physics and chemistry, this review is restricted mainly to materials related to this paper.

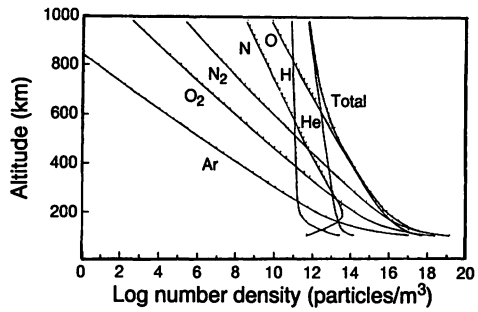

Fig. 1 Neutral air composition calculated by MSIS-86 model. [Conditions: Date = Jan. 1, Local time = 12:00, Lat. = 35, Long. = 135, f10.7 = 120, Mean f10.7 = 120, Ap = 4.0].

2.1 Models of the neutral atmosphere and the ionosphere

Since an ionosphere is produced when a neutral atmosphere absorbs solar UV radiation, ionospheric research needs knowledge of the neutral composition and the intensity of the solar radiation. Below about 80 km, the atmosphere is well mixed, so the composition is about the same everywhere. Above about 120 km, however, differences in composition increase with altitude due to gravitational separation. Since in this region the atmosphere absorbs EUV radiation, causing higher temperatures at higher altitudes, this region is called the thermosphere. Because the thermosphere includes most of the ionosphere, its composition is especially important for understanding the ionosphere.

The CIRA (Cospar International Reference Atmosphere) model has been a reliable model of the thermosphere. MSIS-86 was recently developed by Hedin[3]. This model better models the region above 120 km than the CIRA. While the CIRA model was based on early satellite drag data, the MSIS model relies mainly on the mass spectrometer data from the AE-series satellites and from incoherent scatter (IS) radar. For the convenience of researchers, the MSIS model is available as a computer program.

In contrast to the lower atmosphere, the composition of the thermosphere depends on solar activity, the latitude, local time, and so on. Figure 1 shows an example of calculation by this program. Molecular nitrogen and oxygen are dominant below about 200 km, similar to the lower atmosphere. Above this altitude, the density of the atomic oxygen, which is produced by the photo dissociation of O_2, becomes dominant. Helium prevails above about 600 km and atomic hydrogen eventually becomes dominant above about 2000–3000 km. Thus in the region of the topside ionosphere, O, He, and H are the major constituents of the thermosphere. This is strongly reflected in the ion composition of the ionosphere. Atomic and ionic He prevails in this region, while it is a very minor constituent in the lower atmosphere. This is one of the peculiarities of the topside ionosphere. We will look at various aspects of the ionic helium distribution in later sections.

Temperature is an important parameter in determining the thermospheric composition. It determines the altitude profile of the composition. However, since the temperature itself depends on the absorption of EUV radiation, which varies according to composition, temperature and composition must be solved self-consistently. This is the "ultimate problem" of the ionospheric physics[4]; it has not yet been fully solved. In most of studies, the temperature is given empirically based on measurement.

Table 1 Modeled solar EUV irradiance [after Torr and Torr, 1985[6]].

Uv Spectrum from 50–1050A			Intensity Incident on Earth (10^9 Photons cm^{-2} s^{-1})				
SOLAR FLUX PERIOD			74113	76200	78348	79022	79050
Interval		Ion					
1	50–100		.3984	.4382	1.0337	1.2904	1.3710
2	100–150		.1497	.1687	.3623	.4419	.4675
3	150–200		2.3683	1.8692	4.1772	5.3708	5.7024
4	200–250		1.5632	1.3951	4.7953	6.6473	7.1448
5	256.3	HeII, SiX	.4600	.5064	.8805	1.0331	1.0832
6	284.51	FeXV	.2100	.0773	3.2613	5.2352	5.7229
7	250–300		1.6974	1.3556	7.5081	11.2278	12.1600
8	303.31	SiXI	.8000	.6000	2.9100	4.3380	4.6908
9	303.78	HeII	6.9000	7.7625	12.3424	13.8172	14.3956
10	300–350		.9650	.8671	4.3119	6.3164	6.8315
11	368.07	MgIX	.6500	.7394	1.2891	1.4661	1.5355
12	350–400		.3140	.2121	1.5298	2.3413	2.5423
13	400–450		.3832	.4073	1.0922	1.4330	1.5310
14	465.22	NeVII	.2900	.3299	.6102	.7004	.7358
15	450–500		3.25851	.3081	1.2120	1.6912	1.8229
16	500–550		.4520	.5085	1.2303	1.5496	1.6486
17	554.37	OIV	.7200	.7992	1.2943	1.4537	1.5163
18	584.33	HeI	1.2700	1.5875	3.4608	4.0646	4.3005
19	550–600		.3568	.4843	.8732	.9985	1.0477
20	609.76	MgX	.5300	.6333	1.6782	2.3242	2.4836
21	629.73	OV	1.5900	1.8484	3.2443	3.6938	3.8701
22	600–650		.3421	.4002	.9609	1.2842	1.3672
23	650–700		.2302	.2623	.4521	.5149	.5388
24	703.31	OIII	.3600	.3915	.6363	.5152	.7461
25	700–750		.1409	.1667	.3439	.4046	.4287
26	765.15	NIV	.1700	.1997	.3647	.4178	.4386
27	770.41	OIV	.2600	.2425	.7760	1.1058	1.1873
28	789.36		.7024	.7831	1.2870	1.4501	1.5140
29	750–800		.7581	.8728	1.8909	2.3132	2.4541
30	800–850		1.6250	1.9211	3.9211	4.5911	4.8538
31	850–900		3.5370	4.4325	9.7798	11.5292	12.2187
32	900–950		3.0003	3.6994	7.9445	9.3134	9.8513
33	977.02	CIII	4.4000	4.8400	8.5523	9.7478	10.2165
34	950–1000		1.4746	1.7155	3.3468	3.8723	.4.0779
35	1025.72	HI	3.5000	4.3750	9.5375	11.2000	11.8519
36	1031.91	OVI	2.1000	1.9424	4.2929	5.7459	6.1049
37	1000–1050		2.4665	2.4775	4.7145	5.7798	6.0928
F10.7	($10^{-22}Wm^{-2}Hz^{-1}$)		71.0	68.0	206.0	234.0	243.0

Another important parameter in determining the composition of the thermosphere and ionosphere is, of course, EUV radiation from the sun. The ion composition of the ionosphere depends on EUV in a two-fold manner: ions are produced by EUV from the thermospheric constituents, which are themselves affected by EUV. Information on the spectral irradiance of solar EUV has been provided mainly by the AE-series satellites[5]. Typical modeled values of the EUV spectra are shown in Table 1[6]. Table 2 shows photo ionization cross sections and Table 3 shows integrated ionization frequencies relevant to Earth's ionosphere[6].

Using the neutral atmosphere and EUV radiation models described above, it is in principle possible to calculate an ionospheric model. While numerical simulations have been successful for several limited regions and problems, their use for global-scale calculations has recently been challenged[7]-[9]. Since the ionosphere is strongly affected by such dynamic features as neutral winds, atmospheric tides, drift motion due to electric fields, and the bombardment of auroral particles at higher latitudes, the situation is complicated and it is difficult to calculate a completely theoretical model.

In contrast to the theoretical approach, several empirical modeles based on observation have been developed. The International Reference Ionosphere (IRI) model developed by Rawer[10] is the most representative of these empirical models. Since it includes the ion composition, whereas most of others do not, it is very important to this study. We will thus describe the IRI model in some detail.

2.1.1 IRI model

The International Reference Ionosphere is a purely empirical computer model of the ionosphere; it is based on observations by ionosondes, rockets, satellites, and IS radar. It calculates the electron density, the relative ion composition, and the electron and ion temperature when the location (latitude, longitude, and altitude), time (month, local time or universal time) and solar activity (sunspot number, or F10.7) are given as inputs.

Figure 2 shows the regions where the ionospheric parameters are calculated[10]. First, the NmF2 (the maximum electron density in F2 region) is obtained either from the CCIR model, or given by other method, such as from actual observation. Since the CCIR model is based on a huge data base obtained from a worldwide ionosonde network, it is considered to be very reliable. However, since there are no observation stations over the ocean areas, the model extrapolates the data for these areas. The data from the topside sounder on ISS-b remedied this shortcoming[11]. The IRI model estimates the peak height of the F2 region, or HmF2, by using M(3000) data. Starting from NmF2 and HmF2, the electron densities of the lower and higher altitudes are calculated using a specific functional form. For the topside region, this functional form is $Ne(h) = NmF2 \cdot Exp(-\gamma)$, where h is altitude and γ depends on the location, time, and solar activity. The value of γ is determined by the data from Alouette-1 and -2 satellites.

Table 2 Cross sections of photoionization and photoabsorption for the main constituents in the thermosphere [after Torr and Torr, 1985[6]].

		Photoionizion				Photoabsorption		
	Wavelength (A)	O	He	N_2	O_2	0	N_2	O_2
1	50–100	1.06	0.21	0.60	1.18	1.06	0.60	1.18
2	100–150	3.53	0.53	2.32	3.61	3.53	2.32	3.61
3	150–200	5.96	1.02	5.40	7.27	5.96	5.40	7.27
4	200–250	7.55	1.71	8.15	10.50	7.55	8.15	10.50
5	256.3	8.43	2.16	9.65	12.80	8.43	9.65	12.80
6	284.15	9.26	2.67	10.60	14.80	9.26	10.60	14.80
7	250–300	8.78	2.38	10.08	13.65	8.78	10.08	13.65
8	303.81	9.70	3.05	11.58	15.98	9.70	11.58	15.98
9	303.78	9.78	3.05	11.60	16.00	9.72	11.60	16.00
10	300–350	10.03	3.65	14.60	17.19	10.03	14.60	17.19
11	368.07	10.84	4.35	18.00	18.40	10.84	18.00	18.40
12	350–400	10.70	4.25	17.51	18.17	10.70	17.51	18.17
13	400–450	11.21	5.51	21.07	19.39	11.21	21.07	19.39
14	465.12	11.25	6.53	21.80	20.40	11.25	11.25	20.40
15	450–500	11.64	7.09	21.85	21.59	11.64	21.85	21.59
16	500–550	11.91	0.72	24.53	24.06	11.91	24.53	24.06
17	554.37	12.13	0.00	24.69	25.59	12.13	24.69	25.59
18	584.33	12.17	0.00	23.20	22.00	12.17	23.20	22.00
19	550–600	11.90	0.00	22.38	25.04	11.90	22.38	25.04
20	609.76	12.23	0.00	23.10	26.10	12.23	23.10	26.10
21	629.73	12.22	0.00	23.20	25.80	12.22	23.20	25.80
22	600–650	12.21	0.00	23.22	25.94	12.21	23.22	26.02
23	650–700	10.04	0.00	25.06	22.05	13.04	29.75	26.27
24	703.31	11.35	0.00	23.00	23.00	11.35	26.30	25.00
25	700–750	8.00	0.00	23.20	23.81	8.00	30.94	29.05
26	765.12	4.18	0.00	23.77	8.59	4.18	35.36	21.98
27	770.41	4.18	0.00	18.39	8.69	4.18	26.88	25.18
28	789.36	4.28	0.00	10.18	11.05	4.28	19.26	26.66
29	750–800	4.23	0.00	16.75	9.39	4.23	30.71	27.09
30	800–850	4.38	0.00	0.00	6.12	4.38	15.05	20.87
31	850–900	4.18	0.00	0.00	4.69	4.18	46.63	9.85
32	900–950	2.12	0.00	0.00	9.34	2.12	16.99	15.54
33	977.62	0.00	0.00	0.00	2.50	0.00	0.70	4.00
34	950–1000	0.00	0.00	0.00	12.22	0.00	36.16	16.53
35	1025.72	0.00	0.00	0.00	1.00	0.00	0.00	1.60
36	1031.91	0.00	0.00	0.00	0.00	0.00	0.00	1.00
37	1000–1050	0.00	0.00	0.00	0.27	0.00	0.00	1.10

Table 3 Photo ionization frequencies for the main constituents in the thermosphere[after Torr and Torr, 1985[6]].

Species	Banks and Kockarts (1973)	AE 1974 Epoch Chemistry	(F)74113	76200	78348	79022	79050
	(sec^{-1})	(sec^{-1})	(sec^{-1})	(sec^{-1})	(sec^{-1})	(sec^{-1})	(sec^{-1})
$O^+(4S)$		1.4(–7)	9.903(–8)	1.092(–7)	2.544 (–7)	3.189(–7)	3.389(–7)
$O^+(2D)$	1.2(–7)		9.023(–8)	9.591(–8)	2.358(–7)	3.048(–7)	3.246(–7)
$O^+(2P)$			5.275(–8)	5.563 (8)	1.400(–7)	1.322(–7)	1.9242(–7)
$O^+(4P)^{\#}$			1.363(–8)	1.337(–8)	3.723(–8)	4.995(–8)	5.342(–8)
$O^+(2P^*)^{\#}$			6.446(–9)	6.171(–9)	1.708(–8)	2.292(–8)	2.450(–8)
TOTAL O^+	3.2±1.3(–7)	2.92(–7)	2.610(–7)	2.801(–7)	6.842(–7)	8.781(–7)	9.349(–7)
$O2^+$	7.0±3.0(–7)	4.29(–7)	4.967(–7)	5.429(–7)	1.280(–6)	1.622(–6)	1.725(–6)
$N2^+$	4.9±2.3(–7)	3.1(–7)	3.604(–7)	3.888(–7)	9.356(–7)	1.201(–6)	278(–6)
He^+	8.0±4.0(–8)		4.820(–8)	4.887(–8)	1.350(–7)	1.802(–7)	1.927(–7)
CO^+			4.026(–7)	4.420(-7)	1.050(–6)	1.330(–6)	1.415(–6)
$CO2^+$			6.421(–7)	6.972(–7)	1.686(–6)	2.151(–6)	2.290(–6)

$^{\#}$ inner shell

1.4(–7) means 1.4×10^{-7}

Relative ion composition is also provided by the IRI model. For the topside ionosphere, the data from the AEROS satellite[12] and the OGO satellite[13] are used. Since these two satellites did not sufficiently cover all space and time regions, the composition model calculated from the IRI is not necessarily complete and must be improved. Data from the ISS-b provided the data needed for improvement. For the ion composition in the bottomside ionosphere, the main data sources are from rocket experiments.

IRI also calculates the electron and ion temperatures. This calculation is based mainly on IS radar and partly on AEROS observations. Furthermore, the IRI model gives the neutral temperature, which is based on the CIRA model. If we assume diffusive equilibrium, for example, the densities and temperatures of the plasma constituents should be related in a self-consistent manner. It should be borne in mind that the IRI model is purely empirical and does not produce a self-consistent model. Figure 3 shows an example of an IRI model calculation. The IRI program is written in FORTRAN, and can easily be implemented on a small PC.

2.2 Ion composition of E and F1 regions

Figure 4 shows the results of ion composition measurement which we made using an ion mass spectrometer on the S-10-8 rocket. The time and date were, 17:45 JST (solar zenith angle: 95 deg.) on Feb. 2, 1980. The geomagnetic index, ΣKp, on that day was 16, so these results represent a

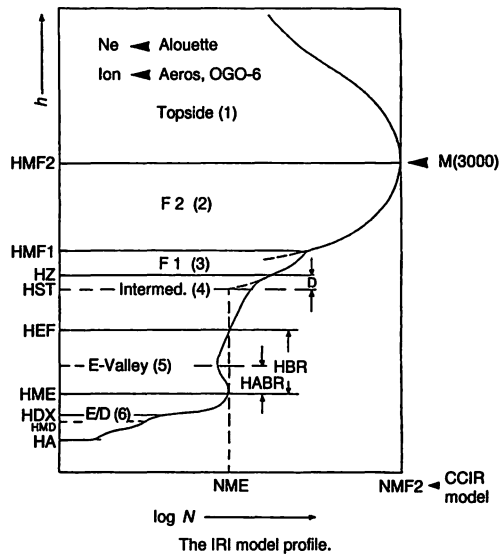

Fig. 2 Configuration of IRI model[10].

typical quiet day at mid-latitude in winter. Molecular ion, NO^+, dominated throughout the E region, but above 160 km the dominant species changed rapidly to O^+. The wave-like variations in the NO^+ profile suggests the existence of dynamical process in the E region. The chemical processes, which are described below, cannot explain such variations. To our knowledge, the dynamical processes in the E region have not been well documented, so investigating these processes is important in future research.

For the region below F1, the ion composition is mainly determined by ion chemistry. As shown in Fig. 1, dominant neutral components are N_2 and O, and the main ionization source is given by following reactions:

$$N_2 + h\nu \rightarrow N_2^+ + e \quad (1)$$

$$O + h\nu \rightarrow O^+ + e \quad (2)$$

The ionization of O_2;

$$O_2 + h\nu \rightarrow O_2^+ + e \quad (3)$$

is not important in this altitude region.

The N_2^+ produced by (1) undergoes the following reactions;

$$N_2^+ + O_2 \rightarrow O_2^+ + N_2 \quad (4)$$

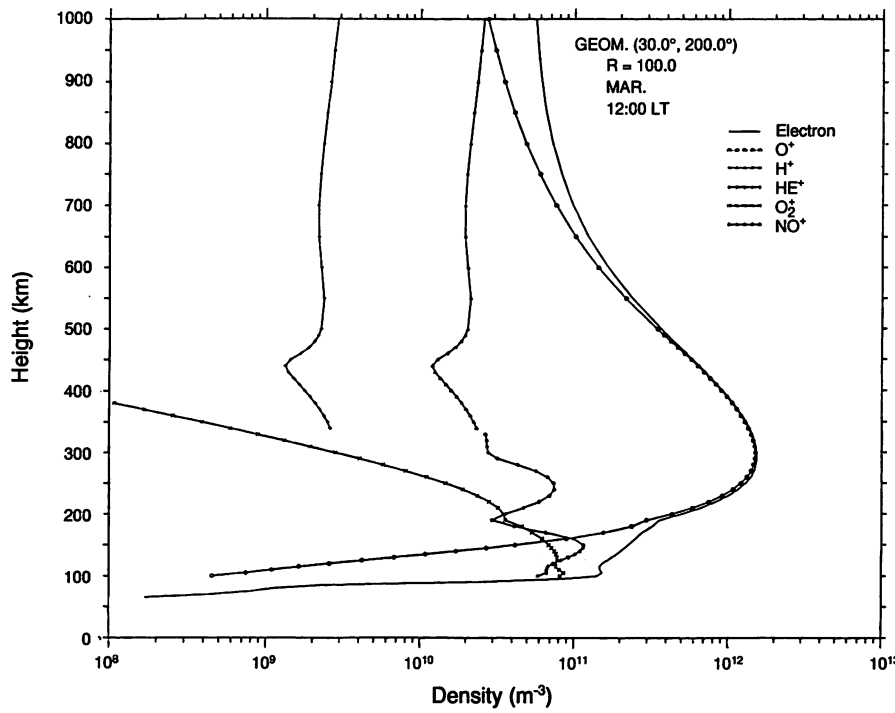

Fig. 3 Electron and ion densities calculate by IRI-86 model [conditions: Geomag. lat. = 30, Geomag. lon. = 200, month = March, LT = 12, Rz = 100].

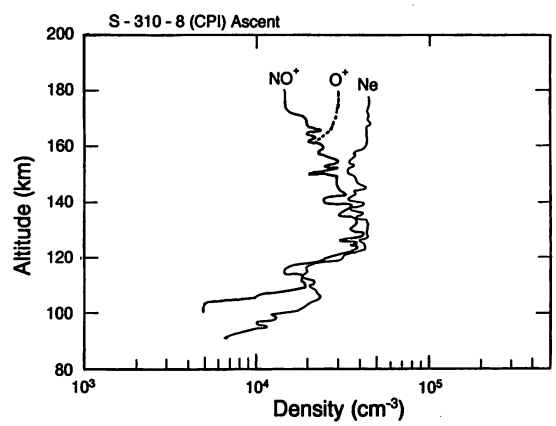

Fig. 4 Ion composition observed by S-310-8 rocket.

$$N_2^+ + O \rightarrow NO^+ + N \quad (5)$$

$$N_2^+ + O \rightarrow O^+ + N_2 \quad (6)$$

rapidly changing N_2^+ to NO^+ and O_2^+, so that it no longer remains the dominant species. On the other hand O^+ undergoes:

$$O^+ + O_2 \rightarrow O_2^+ + O \quad (7)$$

$$O^+ + N_2 \rightarrow NO^+ + N \quad (8)$$

so O^+ also does not remain dominant below the F1 region. The dominant ion species are therefore NO^+ and $O2^+$ in this region. These molecular ions are lost through the following dissociative recombination reactions:

$$NO^+ + e \rightarrow N + O \quad (9)$$

$$O_2^+ + e \rightarrow O + O \quad (10)$$

As shown in Table 4[14], the rates of these reactions are very fast, so the dissociative recombinations remove the molecular ions very efficiently. The fact that N_2^+ is not a main constituent while it is the most abundant ionization product, and that NO^+ is a major constituent while neutral NO is very minor, is a very interesting consequence of the ion chemistry in the ionosphere.

Let q be the rate of ionization, as given by (1), (2), or (3), and H be the scale height of the neutral atmosphere. If we assume the atmosphere is composed of a single constituent, q is given by the Chapman function[4]:

$$q = q_m \exp[1 - Z/H - \exp(-Z/H)\sec\chi] \quad (11)$$

where the height Z is measured from the point where optical depth becomes unity, and χ is the solar zenith angle. If the ion loss reactions are given by the dissociative recombination of (9) and (10), then the electron density, Ne, of the chemical equilibrium state is given by:

$$q = \alpha N e^2 \quad (12)$$

where α is the effective recombination coefficient introduced by Yonezawa[15]. From (11) and (12),

Table 4 Reaction rates for main ions in the ionosphere [after Roble et al., 1978[14]]. The references in the table are due to the original paper.

Reaction	Reaction rate (cm^3s^{-1})	Reference
$O_2^+ + N_2 \rightarrow NO^+ + NO$	5×10^{-16}	Ferguson(1974)
$O_2^+ + NO \rightarrow NO^+ + O_2$	4.4×10^{-10}	Lindinger et al., (1975)
$O_2^+ + N(^2D) \rightarrow N^+ + O_2$	2.5×10^{-10}	Dalgarno (1970)
$O_2^+ + e \rightarrow O + O(^3P,^1D,^1S)$[B1]	$1.1 \times 10^{-5}Te^{-0.7}$ for Te≤1000K	Torr et al. (1976)
	$1.6 \times 10^{-7}(Te/300)^{-0.55}$; Te>1000	
$0_2^+ + N(^4S) \rightarrow NO^+ + O$	1.8×10^{-10}	Goldan et al. (1966)
$NO^+ + e \rightarrow O^+ + N(^2D,^4S)$[B3]	$5 \times 10^{-7}(Te/300)^{-1.0}$; Te>1000	Torr et al. (1976)
	$4.2 \times 10^{-7}(Te/300)^{-0.85}$ for Te≤1000K	Ferguson (1974)
$O^+(^4S) + H \rightarrow H^+ + O$	6.0×10^{-10}	Lindinger et al. (1974)
$O^+(^4S) + N_2$ $NO^+ + N(^4S)$	5.0×10^{-13}; T_R<1000K	
	$4.5 \times 10^{-14}(T_R/300)^2$;$T_R$>1000K	McFarland et al. (1973)
$O^+(^4S) + O_2 \rightarrow O_2^+ + O$	$2.0 \times 10^{-11}(T_R/300)^{-0.4}$; T_R<1800K	
	$1.3 \times 10^{-12}(T_R/300)^{-1.2}$; T_R>1800K	Ferguson (1974)
$O^+(^4S) + NO \rightarrow NO^+ + O$	8×10^{-13}	Lindinger (1974)
$O^+(^2D) + N_2$ $NO^+ + N(^4S)$	5.6×10^{-13} for T_R<1000K	Henry et al. (1969)
$O^+(^2D) + e \rightarrow O^+(^4S)$+ e	$7.8 \times 10^{-8}(300/Te)^{1/2}$	Rutherford and Vroom (1971)
$O^+(^2D) + N_2 \rightarrow N_2^+ + O$	1.0×10^{-9}	Lindinger et al. (1974)
$N_2^+ + O_2$ $NO^+ + N_2$	$5.0 \times 10^{-11}(T_R/300)^{-0.8}$; T_R<3560K	McFarland et al. (1973)
$N_2^+ + O \rightarrow NO^+ + N(^2D,^4S)$[B2]	$1.4 \times 10^{-10}(T_R/300)^{-0.44}[1-0.07(T_R/300)^{0.21}]$: T_R<1500K	Orsini et al. (1976)
	$5.2 \times 10^{-11}(T_R/300)^{-0.2}[1-0.07(T_R/300)^{0.21}]$: T_R>1500K	
$N_2^+ + e \rightarrow N + N(^4S,^2D)$[B4]	$1.8 \times 10^{-7}(Tv/Te)^{-0.4}$	McFarland et al. (1973)
$N_2^+ + O \rightarrow O^+ + N^2$	$1.4 \times 10^{-10}(T_R/300)^{-0.44}.0.07(T_R/300)^{0.21}]$: T_R<1500K	Fehsenfeld et al. (1970)
	$5.2 \times 10^{-11}(T_R/300)^{0.20}.0.07(T_R/300)^{0.21}]$: T_R≥1500K	
$N_2^+ + NO \rightarrow NO^+ + N_2$	3.3×10^{-10}	Banks (1967)
$H^+ + O \rightarrow O^+ + H$	$6.0 \times 10^{-10} \frac{8}{9}\left(\frac{T_i + T_n/16}{T_n + T_i/16}\right)^{1/2}$	Lin and Kaufman (1971)
	5.0×10^{-12}	Oran et al. (1975)
$N(^2D) + O_2 \rightarrow NO + O$	4.5×10^{-13}	Frederick and Rusch (1977)

Te = electron temperature
Ti = ion temperature
Tn = neutral temperature
Tv = vibrated temperature
TR = relative reactant kinetic temperature

Table 4 Reaction rates for main ions in the ionosphere [after Roble et al., 1978[14]]. The references in the table are due to the original paper.—continued

Reaction	Reaction rate (cm^3s^{-1})	Reference
$N(^2D) + O \rightarrow N(^4S) + O$		Rusch et al. (1975)
	$1.0 \times 10^{-9}(Te/300)^{1/2}$	Black et al. (1969)
$N(^2D) + e \rightarrow N(^4S) + e$	7×10^{-11}	Wilson (1967)
$N(^2D) + NO \rightarrow N_2 + O$	$2.4 \times 10^{-11}\exp(-3975/Tn)$	Phillips and schff (1962)
$N(^4S) + O_2 \rightarrow NO+ O$	$1.5 \times 10^{-12}Tn^{1/2}$	Strobel (1971)
$N(^4S) + NO \rightarrow N_2 + O$	8.3×10^{-6}	Strobel (1971)
$NO + hv \rightarrow N(^4S) + O$	6.0×10^{-7}	Winters (1966)
$NO + hv \rightarrow NO^+ + e$		Gastrang (1956)
$N_2 + e(fast) \rightarrow N(^4S) + N(^2D)$[B5]	1.06×10^{-5}	
$N(^2D) \rightarrow N(^4S) + hv$		

Te = electron temperature
Ti = ion temperature
Tn = neutral temperature
Tv = vibrated temperature
TR = relative reactant kinetic temperature

$$Ne = (q_m / \alpha)^{1/2} \exp(1/2)[1 - Z/H - \exp(-Z/H)\sec\chi] \quad \text{..... (13)}$$

This formula is well known α-Chapman layer. Because the time scale to reach this equilibrium in the E region is on the order of several seconds, the real distribution in this region is considered to be near this chemical equilibrium. This kind of distribution has been taken to be the "normal" state. Any deviation from this distribution has been called an anomaly. Many kinds of anomalies have been identified[15], such as the equatorial-, winter-, and sunrise-anomalies. We will discuss some of the anomalies observed by ISS-b in later sections.

2.3 Composition of F2 and topside regions

As shown in the experimental data in Fig. 4, O^+ prevails above the F1 region. The main loss processes of O^+ are given by reactions (9) and (10). Radiative recombination between O^+ and electrons is negligible because the reaction rate is very small. The electron density, *Ne*, is given by:

$$Ne = q / \beta[O]/[N_2] \exp[0.75Z/H(12)] \quad \text{..... (14)}$$

where β is the effective attachment coefficient, [O] and [N_2] are the densities of *O* and N_2, and H(12) is the scale height for an atom of 12 AMU. Equation (14) represents distribution in which the density increases indefinitely with an increasing altitude. While we assumed a chemical equilibrium to obtain (14), this assumption breaks at the altitude where the collision frequency becomes small. This altitude roughly corresponds to the maximum electron density in the F2 region (HmF2). Above around HmF2, the effect of diffusion becomes important and (14) no longer applies. Consequently, the distribution given by (14) represents that between the F1 and F2 region. It is also interesting to note

that Ne depends on the $[O]/[N_2]$ ratio. In severe ionospheric storms, the electron density has been known to decrease drastically. This phenomenon is considered to be due to the decrease in this ratio caused by uplift of the lower atmosphere.

The most important reaction in the topside region is

$$O^+ + H \leftrightarrow H^+ + O \quad \text{..... (15)}$$

Almost all the H^+ in the topside ionosphere are produced by this charge transfer reaction. Direct photoionization of neutral H by solar radiation is negligible. The density of H^+ due to the chemical equilibrium of (15) is given by

$$[H^+] = 9/8[H][O^+]/[O] \quad \text{..... (16)}$$

$[H^+]$ increases with the scale height of H(7)[16].

Next to O^+ and H^+, He^+ is the most important species in the topside ionosphere. Because the He atom has the highest ionization potential, He^+ cannot be produced by charge transfer. The major source of He^+ is photoionization:

$$He + h\nu \rightarrow He^+ + e \quad \text{..... (17)}$$

The production rate of this reaction is $\sim 10^{-7}$/sec[6]. Since the optical depth in the topside region is small, production of He^+ is proportional to the neutral He density. The main loss process for He^+ is

$$He^+ + N_2 \rightarrow He + N_2^+ \quad \text{..... (18)}$$

When the chemical equilibrium of (17) and (18) holds, $[He^+]$ increases with the altitude at a scale height of H(24), which holds below about 600 km. According to the OGO and ISIS satellite observations during solar minimum, He^+ is a minor constituent around 1000 km. However, we will see later from ISS-b observations that during solar maximum periods $[He^+]$ becomes comparable to $[O^+]$ or $[H^+]$, or He^+ even becomes the dominant species. The dominance of He^+ during solar maximum was also observed by the DE-2 satellite[17]. The He^+ observation data from ISS-b was very good in quality and gave an important data base.

In contrast to these observations, we will take a look at the vertical distribution observed by rocket experiment. Figure 5 shows a schematic diagram of the ion-mass spectrometer launched on the L-3H-9 rocket[18] on August 16, 1977 at 20:15 JST. A typical mass spectrum obtained during this flight is shown in Fig. 6. This quadrupole mass spectrometer has a higher mass resolution than the Bennett type on the ISS-b, so the mass peaks at $1^+(H^+)$, $4^+(He^+)$, $14^+(N^+)$, $16^+(O^+)$, and $18^+(H_2O^+)$ are clearly identified. The mass 18^+ is identified as H_2O^+ rather than $^{18}O^+$ based on the isotopic ratio. H_2O^+ is not a natural ion in the ionosphere, rather is an artifact of the rocket observation. The same kind of situation was reported by Brinton et al.[19]. In the case of satellite observation, Hoffman[20] pointed out that the $[18^+]$ decreases gradually following launch, which is evidence of outgassing from the instruments.

The height profiles of four ion species observed by the above rocket experiment are shown in Fig. 7. It is seen that O^+ is dominant at lower altitudes and that H^+ becomes dominant at higher

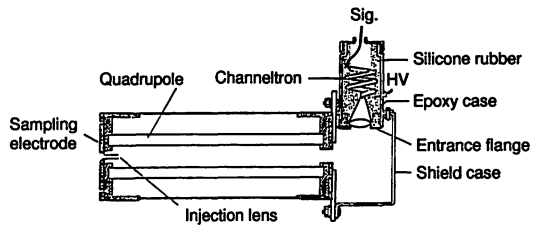

Fig. 5 Schematic drawing of the mass spectrometer for L-3H-9 rocket experiment [after Sagawa et al., 1980[18]].

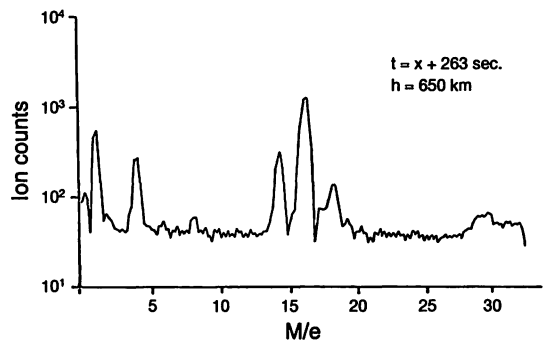

Fig. 6 Mass spectra obtained from L-3H-9 [after Sagawa et al., 1980[18]].

altitudes. The transition height between them is about 700 km. The density of N^+ is about 10% that of O^+ and this ratio does not change much as the height changes. It is apparent from this observation that N^+ is also an important constituent in the topside ionosphere. There have been few reports about the N^+ distribution because it is difficult for most of the mass spectrometers launched so far to resolve N^+ from O^+. Since the situation was the same for the ISS-b observations, it also was not able to analyze N^+. However, N^+ should be studied more thoroughly in future missions.

From the dynamical point of view, N^+ is expected to behave like O^+, because their masses are similar, but from the chemical point of view, N^+ should behave differently than O^+ because N^+ does not have a strong coupling to H^+, like O^+ does. The EXOS-D satellite observations have provided good N^+ data[21] since its mass spectrometer is able to distinguish N^+ from O^+.

Figure 8 shows the height distribution of the $[H^+]/[O^+]$ ratio from the L-3H-9 experiment. This ratio has different slopes below about 500 km and above about 700 km. In the lower region, it is believed that the chemical equilibrium of (15) holds and that the $[H^+]/[O^+]$ ratio is proportional to [H]/[O] because of (16). We can obtain the temperature of the neutral atmosphere from this portion of the plot. The dotted line in the figure shows the linear regression of the observed data points, from which the neutral temperature is estimated to be 800°k.

The higher altitude corresponds to the region of diffusive equilibrium, which is discussed in the next section. The slope in this region gives the ion temperature, T_i. Linear regression analysis gives a T_i of 2800k, which is a bit higher than that measured directly by the Explorer 32 satellite[22]. This discrepancy may be attributed to assumption of the diffusive equilibrium. Since the L-3H-9 observation was done in the evening, rapid recombination had already occurred in the lower

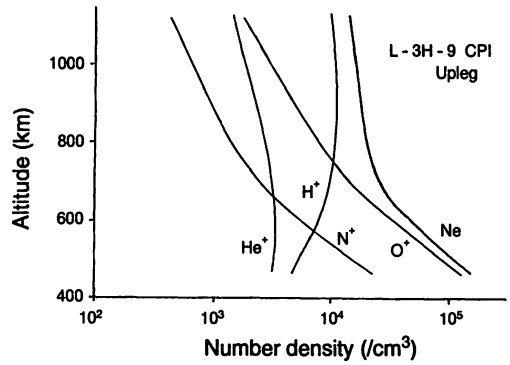

Fig. 7 Distribution of ion densities in the topside ionosphere obtained from L-3H-9 [after Sagawa et al., 1980[18]].

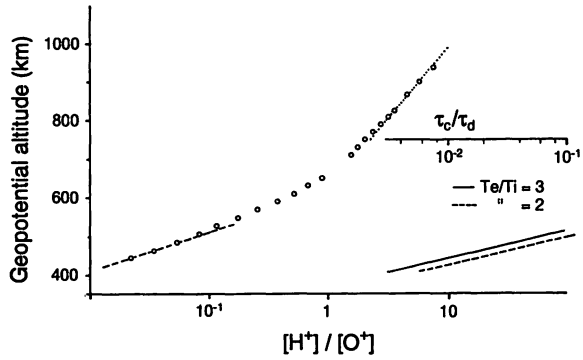

Fig. 8 Vertical distribution of $[H^+]/[O^+]$ ratio obtained from L-3H-9 [after Sagawa et al., 1980[18]].

ionosphere and the plasma in the topside ionosphere had started to move downward, breaking the diffusive equilibrium condition.

The time constants of chemical- and diffusive-equilibrium, τ_c and τ_d are shown in Fig. 8. These time constants were introduced by Marubashi et al.[23] and they are very useful for characterizing the topside ionosphere. Marubashi indicated that chemical equilibrium does not hold when the value of τ_c/τ_d exceeds 0.01–0.05, which is consistent with the figure. We have seen in this section that chemical reaction and dynamical transport through diffusion play a major role in the topside ionosphere.

2.4 Composition and chemistry in the D region

Collisions are very important in the D region, causing various chemical processes to take place. Since satellites do not traverse the D region, almost the only method for measuring the ion composition in the D region is through rocket observation. We developed rocket ion mass spectrome-

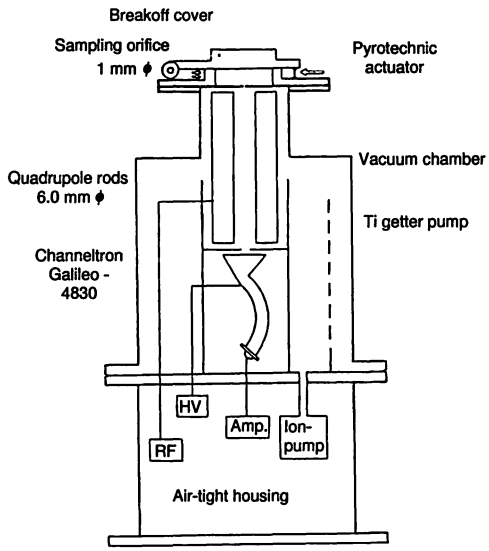

Fig. 9 Schematic drawing of the mass spectrometer on board S-310-8 Rocket.

ters to study the D region. A schematic diagram of the mass spectrometer which was launched on the S-310-8 rocket is shown in Fig. 9.

It was a quadrupole mass spectrometer, or mass filter. Since a pressure below about 10^{-5} Torr is necessary for the spectrometer to operate normally, and the ambient pressure in the D region is over about 10^{-2} Torr, differential pumping is needed. A titanium getter-pump is therefore used.

The analyzer section is evacuated and sealed before the flight and the top cover is broken off with a pyrotechnic actuator when the rocket reaches the D region. A reliable mechanism is needed to ensure both a tight vacuum seal and easy break-off. Both the differential pumping inlet orifice and the ion flux are small, so a channel electron multiplier (CEM) is used to detect the selected ions. Since the CEM needs a high voltage source, the electronics housing is pressurized to avoid electrical breakdown. Since ion mass spectrometers to measure the D region need a complex configuration, very few experiments have been done so far in the world.

Figure 10 shows a typical mass spectrum obtained from the S-210JA-12 rocket, which was launched from the Antarctica Syowa base[24][25]. Masses of 37^+, 48^+, and 66^+ were detected, along with two major ions species: $30^+(NO^+)$ and $32^+(O_2^+)$. The former masses are identified as, $H_3O^+H_2O$, $NO^+(H_2O)$, and $NO^+(H_2O)_2$, respectively. The ions with $(H_2O)_n$ molecules are called water cluster ions. The existence of these water cluster ions is the most prominent feature of the D region. Let us look at these water cluster ions in more detail.

The main ionization source in the D region is x-ray radiation, because the solar EUV radiation is absorbed almost completely in the F and E regions. The main x-ray ionization products are N_2^+ and O_2^+. However, N_2^+ is rapidly converted to NO^+ and O_2^+, as in the E and F1 regions. Another important source peculiar to the D region is the ionization of NO molecules by Lyman α radiation (λ= 121.6 nm), because the Lyman α radiation is not absorbed in the E region and its intensity is very strong. NO^+ is a very important ions in the D region. It is particularly important in the high latitude region, where the concentration of NO is enhanced due to auroral electron precipitation. Thus, the primary ion species in the D region are NO^+ and O_2^+. These ions undergo a variety of chemical reactions shown in Fig. 11[26]. First, O_2^+ reacts with O_2 and then with H_2O:

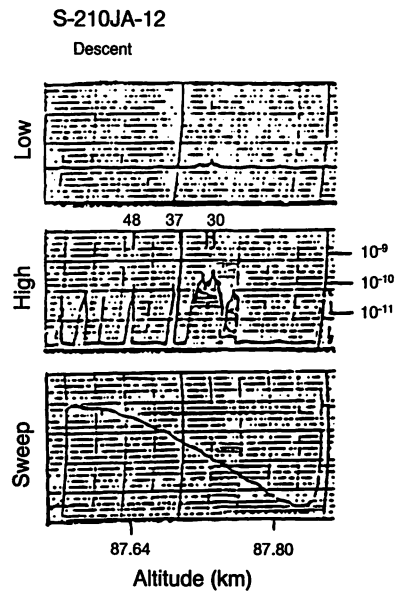

Fig. 10 An example of mass spectrum in the D region observed from the Antarctica rocket S-310JA-12 [after Fugono et al., 1975[25]].

$$O_2^+ + O_2 + M \rightarrow O_4^+ + M \quad (19)$$

$$O_4^+ + H_2O \rightarrow O_2^+(H_2O) + O_2 \quad (20)$$

to form O_2^+ water cluster ions. Next this ion react further with H_2O:

$$O_2^+ + (H_2O) + H_2O \rightarrow H_3O^+ + OH + O_2 \quad (21)$$

$$\rightarrow H_3O^+(OH) + O_2 \quad (22)$$

$$H_3O^+(OH) + H_2O \rightarrow H_3O^+(H_2O) + OH \quad (23)$$

$$H_3O^+(H_2O) + H_2O + M \rightarrow H_3O^+(H_2O)_2 + M \quad (24)$$

$$H_3O^+(H_2O)_n + H_2O + M \rightarrow H_3O^+(H_2O)_{n+1} + M \quad (25)$$

Eventually the ionization starting from O_2^+ is converted into $H_3O^+(H_2O)_n$, where n is an arbitrary

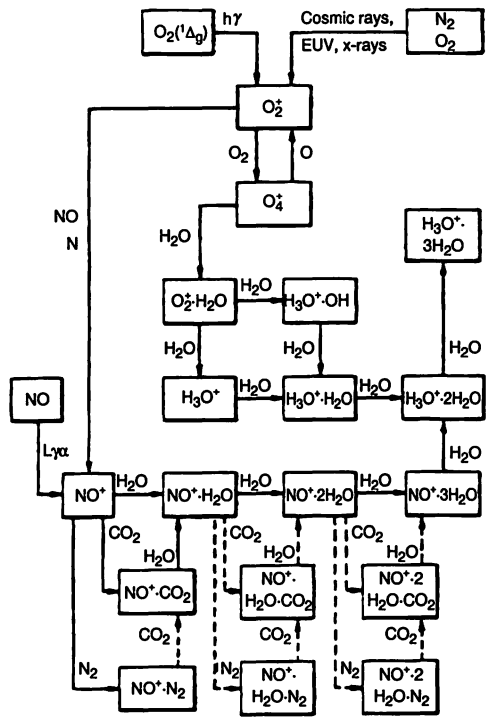

Fig. 11 Chemical reactions of the positive ions in the D-region [after Ferguson et al, 1979[26]].

integer. NO^+ proceeds differently. It first reacts with CO_2 to form cluster ions and the CO_2 is replaced by H_2O to produce water cluster ions. However, this clustering does not go on indefinitely. The reaction:

$$NO^+(H_2O)_3 + H_2O \rightarrow H_3O^+(H_2O)_2 + HNO_2 \quad \text{(26)}$$

converts NO^+ clusters to $H_3O^+(H_2O)_n$ clusters. It might be thought that n grows indefinitely to produce water droplets. However, depending upon the ambient temperature, the reverse reaction:

$$H_3O^+(H_2O)_n + M \rightarrow H_3O^+(H_2O)_{n-1} + H_2O + M \quad \text{(27)}$$

can take place and a chemical balance can be reached at some specific n value. Noctilucent clouds are occasionally observed over high latitude regions. Although it has been speculated that (25) and (27) are related to their formation, rigorous proof has yet to be done.

2.4.1 Negative ions in the D region

The existence of negative ions is another important characteristic of the D region[27]. It is well known that the electron density profile has a "ledge" structure in the D region. This ledge is due to

the formation of negative ions below about 80 km. Negative ions are produced by two following reactions:

$$e + O_2 + M \rightarrow O_2^- + M \quad \text{(28)}$$

$$e + O_2 \rightarrow O^- + O \quad \text{(29)}$$

N_2 and N do not form negative ions. It was once thought that the dominant negative ions were O_2^- or O^-. When there is solar radiation O_2^- is detached by the reaction, when hν is greater than 0.44 eV (λ = 2.0 μm). O^- has similar electron affinity (EA) value. On the other hand, detailed observations of VLF absorption at sunrise revealed that the radiation passing through the ozone layer causes photodetachment of the negative ions, so only direct UV radiation causes the detachment. That is, negative ions with electron affinities greater than O_2^- or O^- do exist in the D region. Direct measurement by rocket revealed the negative ions in question to be NO_2^- and NO_3^-.

$$O_2^- + h\nu \rightarrow O_2 + e \quad \text{(30)}$$

Table 5 shows the negative ions identified by rocket experiment by Arnold and Viggiano[28]. The reaction chain that produces NO_2^- or NO_3^- is shown in Fig. 12[26]. The time needed to produce $O_2^- \rightarrow O_4^- \rightarrow CO_4^- \rightarrow CO_3^-$ is considered to be very short. However, CO_3^- undergoes two reactions:

$$CO_3^- + O \rightarrow O_2^- + CO_2 \quad \text{(31)}$$

$$CO_3^- + h\nu \rightarrow O^- + CO_2 \quad \text{(32)}$$

so the composition return to original one. Only a small fraction of the CO_3^- reacts as

$$CO_3^- + NO \rightarrow NO_2^- + CO_2 \quad \text{(33)}$$

to produce NO_2^-. Since NO is minor constituent, the rate of NO_2^- production is very small. But because NO_2^- has a large electron affinity of 3.9 eV, its concentration eventually increases.

It is interesting to note that Cl^- could be seen in Fig. 12. The EA of Cl^- is 3.82 eV, which is comparable to that of NO_2^-. It is thought that Cl^- also accumulates below the D region. The main natural source of Cl is considered to be meteors, but recently an anthropogenic source has been identified, particularly for the stratosphere. This source is the chlorofluoro carbons (CFCs) used for cooling and washing agents. About one million tons of CFCs are produced each year in the world and most of them are eventually released into the atmosphere. When they rise above the stratosphere, they are photo-dissociated and produce Cl. It is well known that this Cl destroys ozone by

Table 5 The mass numbers of ions observed in D–region and their chemical identification [after Arnold and Viggiano, 1982[28]].

Mass	Tentative ion identity
16	O^-, OH^-
32	O_2^-
35	Cl^-
46	NO_2^-, SiO^-(44)
52	ClO^-, $Cl^-(H_2O)$(51)
60	NO_3^-, $CO_3^-HCO_3$, SiO_2^-(60)
66	
68	
76	SiO_3^-, CO_4^-
78	60(H_2O)
82	66(16)
94	76(H_2O)
96	78(H_2O)
105	76 (28) = $Si_2O_3^-$
107	76 (32) = SiO_5^-

$$O_3 + Cl \rightarrow ClO + O_2, \text{ and} \quad (34)$$

and

$$ClO + O \rightarrow Cl + O_2 \quad (35)$$

That is, Cl destroys O_3 catalytically. If there are electrons, however, ClO is rapidly converted into Cl^- through the reaction:

$$ClO + e \rightarrow Cl^- + O \quad (36)$$

Cl^- is very stable as stated above, and does not react to destroy O_3. Wong et al.[29] proposed conservation of the atmospheric ozone through this mechanism by enhancing the electron density with high-power radio waves. Although this proposal is not immediately applicable, it does suggest the importance of ion chemistry for the ozone problem.

2.4.2 Ion composition in the lower atmosphere

In the stratosphere and below, cosmic rays are the primary ionization source; their normal concentration is considered to be on the order of 10^3/cc down to ground level[30]. Several rocket and balloon experiments in the stratosphere have measured the positive and negative ion composition[31]. It was found that for the positive ions, the dominant ions are type $H_3O^+(H_2O)_n$, and for the negative ions, clusters including NO_2^- and HSO_4^- have been identified.

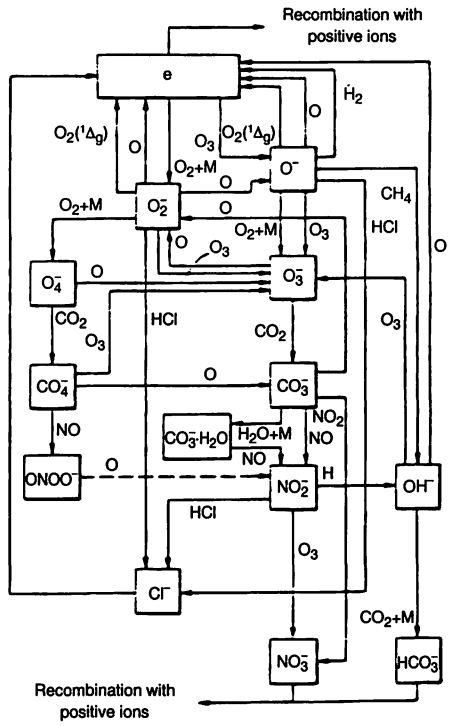

Fig. 12 Chemical reactions of the negative ions in the D-region [after Ferguson et al., 1979[26]].

Mass spectrometric observations at ground level have also been attempted[32]–[34]. Although high pressure hinders precise measurements at ground level, similar cluster ions were identified in these experiments. We used a mass spectrometer developed to measure the ionospheric D region to detect atmospheric pollution[35]. UV ionization from a microwave discharge lamp was used to selectively ionize trace pollutants which have lower ionization potentials than the dominant species, N_2 and O_2.

2.5 Ion composition of the planetary ionospheres

2.5.1 The earth-like planets

The innermost planet, Mercury has no appreciable atmosphere and hence has no ionosphere. Since many spacecrafts have approached Venus, the ionosphere of Venus has been investigated more thoroughly than other planets, except the Earth. The Pioneer Venus Orbiter (PVO) for example, observed Venus for more than ten years. For Mars, the Viking-1 and Viking-2 investigated the Martian ionosphere for a short time before landing.

Figure 13 shows the ion composition of the Venus ionosphere as measured by the Pioneer Venus/BIMS experiment by Taylor et al.[36]. Figure 14 shows that of Mars as measured by the RPA on the Viking Spacecraft[37]. It is well known that the major constituent at the surfaces of Venus and Mars is CO_2.

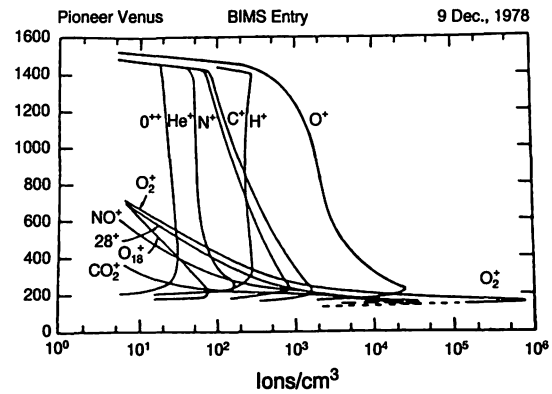

Fig. 13 Vertical distribution of ions in the Venus ionosphere observed by the Pioneer Venus/BIMS experiment [after Taylor et al., 1979[36]].

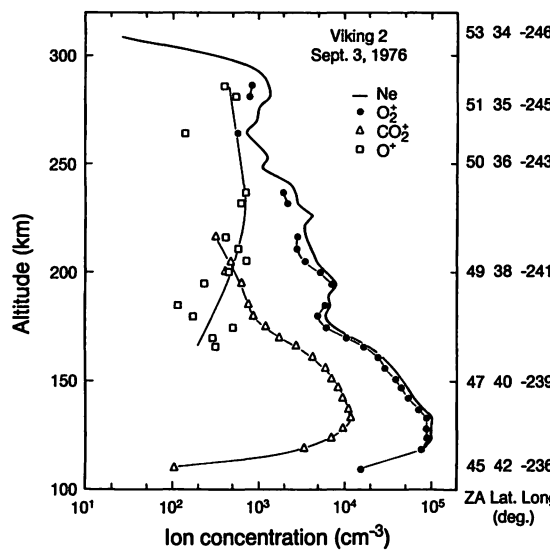

Fig. 14 Vertical distribution of ions in the Mars ionosphere from the Viking [after Hanson et al., 1977[37]].

Although the ground-level pressure on Venus and Mars is about 90 and 0.01 times that on Earth, respectively, at about 120 km, the distribution of the neutral atmosphere of both planets is not much different from that of the Earth. The transition heights from CO_2 to O are 160 km for Venus and 200 km for Mars. The primary photoionization product is therefore CO_2^+ and O^+ for lower and higher altitudes, respectively. At lower altitudes, CO_2^+ is rapidly converted to O_2^+ through the reaction

$$CO_2^+ + O \rightarrow O_2^+ + CO \quad \text{..... (37)}$$

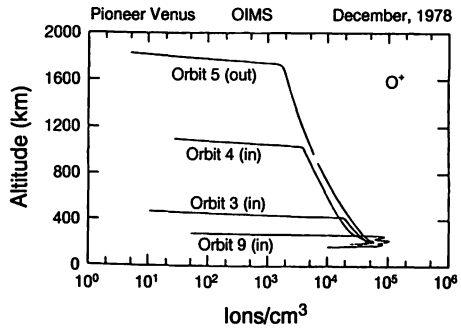

Fig. 15 Variations of the position of the Venus ionopause observed by the Pioneer Venus/OIMS [after Taylor et al., 1979[38]].

O_2^+ dominates the ionospheres of both planets. The CO_2^+ in both planets' atmosphere plays a role similar to N_2 in the Earth's. A part of O_2^+ is converted to NO^+ by

$$O_2^+ + N \rightarrow NO^+ + O \quad \text{..... (38)}$$

The concentration of NO^+ is comparable to that of CO_2^+. Ionization reaches maximum at the region of O_2^+ dominance, which corresponds to Earth's E region, and the height profile is like a pure α-Chapman layer.

On the other hand, at higher altitudes, O^+ is lost through the

$$O^+ + CO_2 \rightarrow O_2^+ + CO \quad \text{..... (39)}$$

reaction, and the density of O^+ is determined by

$$[O^+] \propto [O]/[CO_2] \quad \text{..... (40)}$$

For the chemical equilibrium condition, the scale height of the $[O^+]$ is H(28). But unlike on Earth, the diffusion effect becomes important above about 200 km.

Another important difference between Venus or Mars and the Earth arises due to the absence of an intrinsic magnetic field for both planets. Mars may possibly have a weak magnetic field, which is a target of research for future Mars missions. While the Earth and most of the outer planets have intrinsic magnetic fields and thus form magnetosphere, the ionospheres of Venus and Mars interact directly with the solar wind. A typical example, as observed by PVO/OIMS[38], is shown in Fig. 15.

The position of the ionopause varies significantly depending on the dynamic pressure of the solar wind. It is interesting that there seems to exist some mechanism in which the ionospheric ions are accelerated in this interaction.

The hatched area in Fig. 16, also obtained from PVO/OIMS[39], indicates the existence of suprathermal ions. OIMS was unable to identify the species of these suprathermal ions. It is an

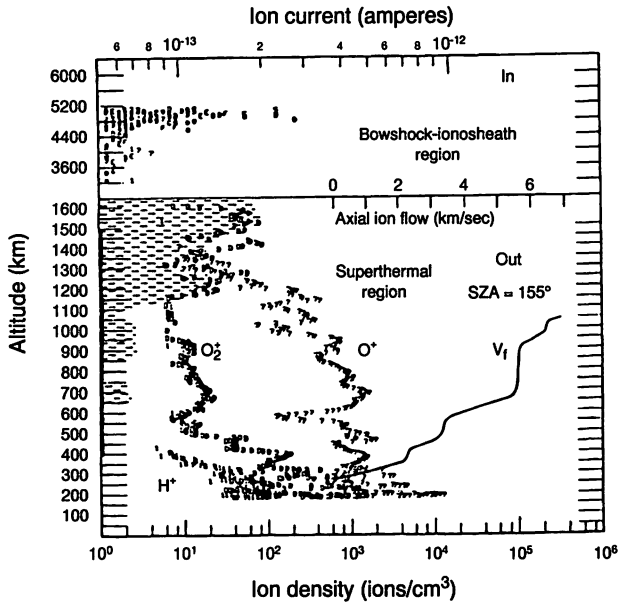

Fig. 16 Suprathermal ions in the Venus ionosphere observed by the Pioneer Venus/OIMS [after Taylor et al., 1980[39]].

interesting question whether the acceleration in the Venus ionosphere is similar to that of the Earth's. We proposed an advanced mass and energy analyzer for a planned Japanese Venus exploration[40]. This type of analyzer has become popular and indispensable for studying Earth's magnetosphere. So far, the suprathermal ions in the ionospheres and magnetospheres of other planets have not been sufficiently analyzed. Simultaneous mass and energy analyses will provide valuable information about the processes taking place on other planets.

It has been suggested that the ionosphere of Mars is very similar to that of Venus, however, data on the Mars ionosphere are very scarce. The Phobos mission had a good opportunity to explore the Mars ionosphere. Unfortunately a communication failure limited the amount of data received[41]. New U.S. spacecraft to Mars is also missing recently. Japanese scientists have a plan to send a Mars orbiter, PLANET-B, in 1998. We hope that this mission will solve many unanswered questions about the Mars ionosphere.

The comets are more like the inner planets. The Giotto spacecraft approached to within 600 km of the nucleus of Halley's comet and provided important information about its ionosphere. Balsiger et al.[42] found that H_2O^+, H_3O^+, OH^+, and O^+ were the major ion species. Data from the Giotto is reproduced in Fig. 17. Other ions, such as C^+, CO^+, CO_2^+, $C_2H_n^+$, which included a C atom, and S^+, H_2S^+, CS^+, and SO_2^+, which include an S atom were identified.

Direct interaction between the ionosphere and the solar wind is also significant for comets. However, for small comets, the effect of gravity is less significant and the interaction between free expanding neutral gas and the solar wind is more important. Therefore, an ionopause is not formed for Halley's comet as it is for the Venus ionosphere, instead, a "contact surface" (CS) is formed at the boundary. At this CS, a dynamic balance between the magnetic pressure gradient and the drag force of ion-neutral gas is established. The interplanetary magnetic field prevails outside of this boundary,

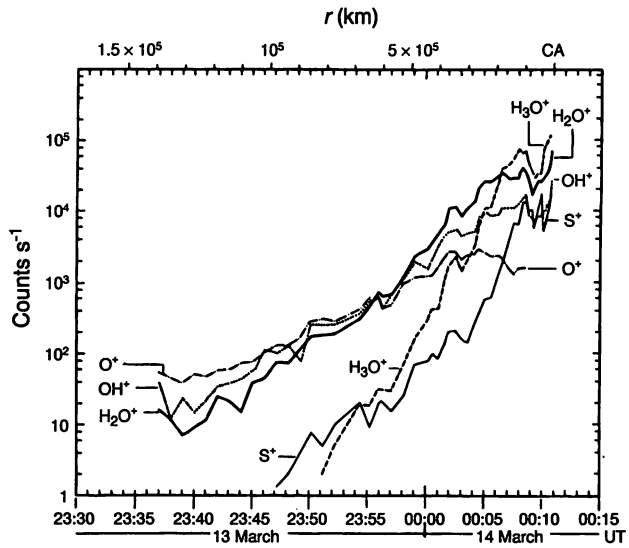

Fig. 17 Ion composition of the ionosphere of comet Halley observed by the Giotto/IMS [after Balsiger et al., 1986[42]].

and there is almost no magnetic field inside. Figure 18 shows the CS as observed by the Giotto [Balsiger et al., 1986]. The CS is located 4600 km from the surface of Halley's comet. It is clearly seen that there are discontinuities in the velocity and temperature at the boundary and the ion density varies as r^{-1} inside and as r^{-2} outside. The dependence of r^{-1} suggests photochemical equilibrium [ibid.].

2.5.2 Outer planets

Since outer planets, such as Jupiter, Saturn, and Uranus, do not have a rigid surface, the altitude of the ionosphere usually refers to that where the pressure is 1 mbar (hecto-Pascal). The neutral constituents of the upper atmosphere of these planets have been identified by photometric observations from the earth as mainly H_2, with some He, CH_3, and NH_3. These planets have rather strong intrinsic magnetic fields, so they have magnetospheres. Auroral activities have also been identified for Jupiter and Saturn. The magnetic axis of Uranus lies almost in the ecliptic plane. So far, no direct measurement has been done for these outer planets. The composition of these planets has been studied theoretically by using the electron density profiles obtained by radio occultation. Since the major neutral constituent is H_2, primary ionization is

$$H_2 + h\nu \rightarrow H_2^+ + e \quad (\sim 95\%) \qquad (41)$$

$$\rightarrow H^+ + H + e \quad (\sim 5\%) \qquad (42)$$

H_2^+ undergoes the following reactions:

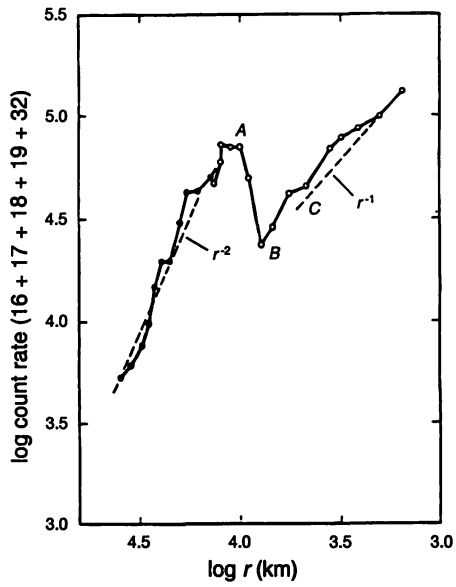

Fig. 18 "Contact surface" (C, r = 4,600 km) of the ionosphere of comet Halley observed by the Giotto/IMS [after Balsiger et al., 1986[42]]. Note that the distance from the comet, r, is shown in logarithmic scale.

$$H_2^+ + H \rightarrow H_3^+ + H \quad \text{(43)}$$

$$H_3^+ + e \rightarrow H_2 + H \quad \text{(44)}$$

The H^+ loss process is

$$H^+ + e \rightarrow H + h\nu \ (\alpha = 10^{-11} cm^3/sec) \quad \text{(45)}$$

Because reaction (45) is slow, the lifetime of H^+ is very long and hence H^+ is considered to be a major ion component at higher altitudes. If only the chemical balance between (42), (43), and (45) is assumed, the ionization distribution should be Chapman-like and the maximum altitudes of the ionosphere should be about 650 km for Jupiter and 1200 km for Saturn. Comparison with observational profiles obtained from the Voyager show that for Jupiter, agreement between theory and observation is good, with some small uncertainty, but for Saturn, the degree of agreement is rather weak[43]. Theoretical and observational profiles of the Jupiter ionosphere are compared in Fig. 19[44]. It should be pointed out that agreement becomes better if the reaction between H^+ and vibrationally excited H_2*,

$$H^+ + H_2^* \rightarrow H_2^+ + H \quad \text{(46)}$$

is taken into account[44].

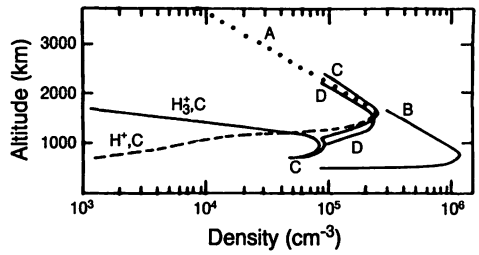

Fig. 19 Comparison of the observed (curve A) by Voyager 1 and calculated (Curve B, C, and D) ion distributions in the Jupiter ionosphere [after McCornell and Majeed[44]].

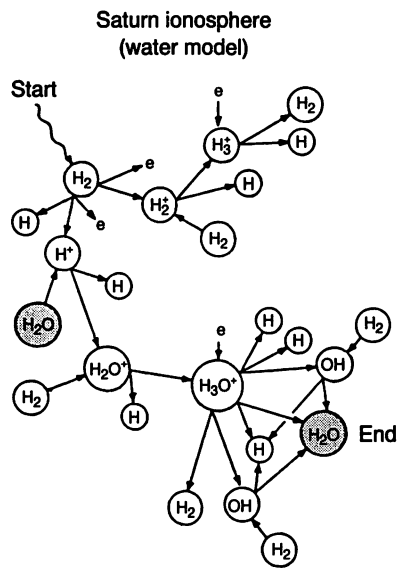

Fig. 20 A model of the chemical reactions in the Saturn ionosphere taking the "rain fall" from the ring [after Waite and Cravens, 1987[43]].

For Saturn, a "Saturn Electrostatic Discharge" (SED) has been found. Local time distributions of the total electron content (TEC) have been obtained by monitoring the cutoff frequency of the SED in the equatorial region. The results suggest that the density is too low in this region compared to theory, so the lifetime of H^+ should be shorter than the theoretical model. It was also found that the density was correlated with the rings of Saturn. From these observations, better agreement is obtained if water precipitation, or "rain", from the rings is assumed. Figure 20 shows the reaction scheme when H_2O is assumed. Through the reaction chain $H^+ \rightarrow H_2O^+ \rightarrow H_3O^+$, H_2O catalytically destroys H^+. The resulting profile is shown in Fig. 21[43]. An "equatorial anomaly" exists also in the Saturnian ionosphere[45].

The Voyager measured the ionosphere of Uranus. It found multiple layers that extends above 10,000 km, although the reliability of this measurement is low because of high background noise.

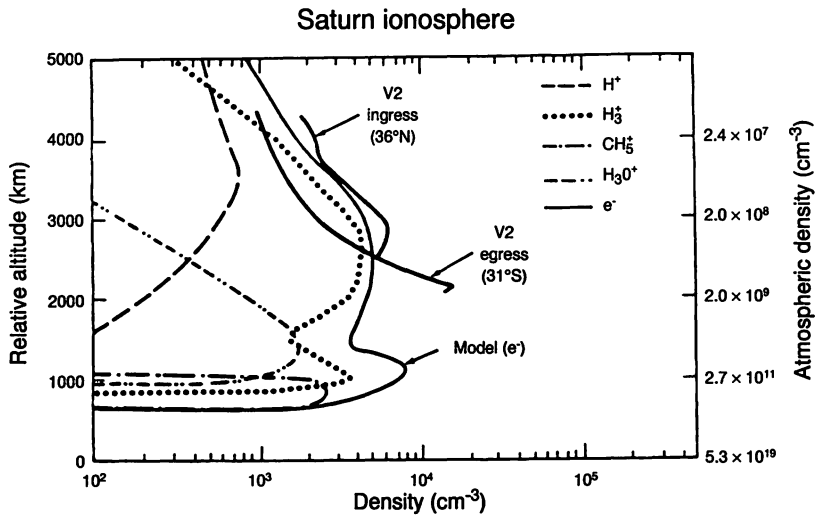

Fig. 21 Modeled distribution of ion density in the Saturn ionosphere assuming rain fall from the ring [after Waite and Cravens, 1987[43]].

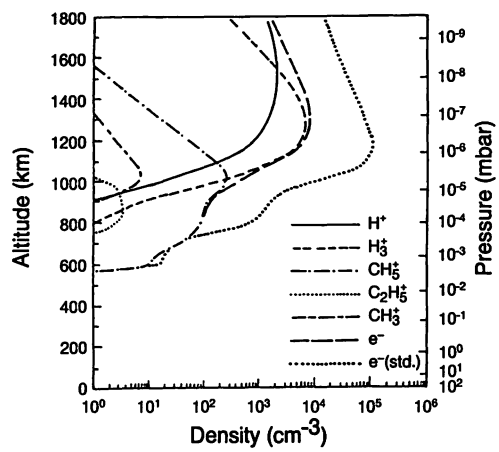

Fig. 22 Modeled ion composition of the Uranus ionosphere assuming CH_4 fall [after Chandler and Waite, 1986[47]].

The existence of multiple layers suggests that Uranus also has precipitation of H_2O or CH_4 from its rings[46]. Because the rings of Uranus look darker than those of Saturn, CH_4 is more likely than H_2O to be the major ring constituent.

Figure 22[47] shows a theoretical profile of the Uranus ionosphere assuming CH_4 precipitation. H^+ and H_3^+ are the dominant species, as they are for Saturn, but CH_5^+ and CH_3^+ extend to a higher altitude.

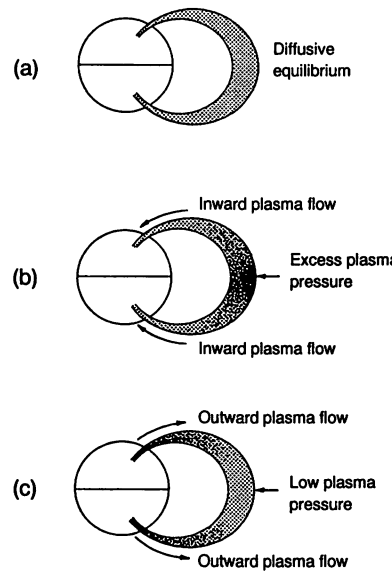

Fig. 23 Schematic illustration of diffusion of the ionospheric plasma.

The ionospheres of the outer planets satellites are also very interesting in terms of their ionic composition. Jupiter's Io satellite has an SO_2 atmosphere, so its major ionic component is SO_2^+. Saturn's Titan has an N_2/CH_4 atmosphere, so its main ionic species is believed to be H_2CN^+. The ionospheres of both satellites strongly affect the ionospheres and magnetospheres of their mother planets.

3. Ion transport processes in the ionosphere

3.1 Ion diffusion in the topside ionosphere

The ion composition in the topside ionosphere is strongly influenced by the transport processes. When there is no electric field, diffusion occurs along the geomagnetic field. As shown schematically in Fig. 23, the ionospheric plasma usually flows downward (case b) or upward (case c). A special case is diffusive equilibrium (case a) that occurs when there is no flow. The ionospheric plasma is usually in a flow state and very seldom in diffusive equilibrium, particularly at high latitudes. However, diffusive equilibrium is a very convenient concept as an ideal state. Cases (b) and (c) correspond to the night and day ionosphere, respectively, while case (a) might be regarded as an average state after geomagnetic activity has subsided for several days.

Geomagnetic disturbances occur frequently during solar maximum periods. Enhancement of convection due to these storm prevents diffusive equilibrium. According to numerical simulations[48], relative calm for one or two weeks is necessary for equilibrium to be established. Satellite observation near geostationary orbit also suggests that it takes about 3–7 days for the geomagnetic flux tubes to refill[49], making diffusive equilibrium a real occurrence.

Now let us discuss fundamental equations governing this diffusion process. The continuity equation for the density of the i-th particle, N_i, is given by

$$\frac{\partial N_i}{\partial t} + \nabla \cdot (N_i u_i) = P_i - L_i \quad (47)$$

where u_i, P_i, and L_i are the velocity, production rate, and loss rate, respectively, of the i-th particle. The equation for momentum conservation is

$$\frac{\partial u_i}{\partial t} + u_i \frac{\partial u_i}{\partial s} + g + \frac{1}{N_i m_i} \frac{\partial p_i}{\partial s} - \frac{Z_i e}{m_i} E = \sum_k \nu_{ik} (u_i - u_k) \quad (48)$$

where

- g parallel component of gravity along the magnetic field
- s length along magnetic field
- E electric field strength along magnetic field
- ν_{ik} collision frequency between i-th and k-th particles
- Zi charge of i-th particle
- mi mass of i-th particle
- e electronic charge
- p_i pressure due to i-th particle, and

Pi is expressed by the temperature of the i-th ion, T_i as

$$p_i = N_i k T_i \quad (49)$$

When the diffusion term can be neglected, and if

$$P_i - L_i = 0 \quad (50)$$

chemical equilibrium is established. This condition corresponds to the region below F1. The time constant to reach this equilibrium, τ_c, is given by

$$\tau_c = N_i / L_i \quad (51)$$

If the local production and loss are negligible, and if

$$\nabla (N_i u_i) = 0 \quad (52)$$

diffusive equilibrium is established. The time constant for this equilibrium, τ_d, is given by Bauer[16]:

$$\tau_d = H_i^2 / D_i \quad (53)$$

where H_i is the scale height, D_i is the diffusion constant.

The chemical time constant increases and the diffusive constant decreases with increasing height. The height at which

$$\tau_c = \tau_d \quad (54)$$

corresponds to the boundary between chemical and diffusive equilibrium. For the earth's ionosphere, this height is roughly 300 km, 600–800 km, and 500–600 km for O^+, H^+, and He^+, respectively. The diffusion process dominates at the 1100 km altitude of the ISS-b satellite.

The electric field E in equation (48) plays an important role in diffusive equilibrium. It is generated by the charge separation between the light electrons and the heavy ions. This electric field partly cancels gravity and buoys the ions.

Since $u_i = 0$ for diffusive equilibrium, from (48) we have

$$\frac{1}{N_i} \cdot \frac{\partial p_i}{\partial s} + m_i g - Z_i e E = 0 \quad (55)$$

$$\frac{1}{N_e} \cdot \frac{\partial p_e}{\partial s} + eE = 0 \quad (56)$$

From (49), (55), and (56) and using

$$N_e = \sum_i Z_i N_i \quad (57)$$

electric field is given by[50]

$$eE = \frac{g \sum Z_j m_j / N_e + kT_j [\partial(\ln T_i / T_e) / \partial s]}{(T_i / T_e) + \sum (Z_j^2 N_j / N_j)} \quad (58)$$

For the simple case where i = O^+ only and $T_i = T_e$,

$$eE = m(O^+) g / 2 \quad (59)$$

This relation shows that one half of the gravity force is canceled by the electric field. In this case, N_e is given by

$$\frac{1}{N_e}\frac{\partial(N_e kT_e)}{\partial s} = -\frac{m(O^+)g}{2} \quad \text{(60)}$$

If we assume that T_e is constant, then the scale height of N_e, H, is given by $H = 2kT_e/m(O^+)g$.

This indicates that the scale height of plasma is twice that of the corresponding neutral gas under the same conditions.

When the plasma is composed of multiple ion species, and if the temperature does not change with height, the distribution of the i-th ion is given by an exponential function of the scale height:

$$H_i = \frac{kT_i}{m_i g}\left[1 - \frac{T_i}{T_i + T_e}\frac{m(+)}{m_i}\right]^{-1} \quad \text{(61)}$$

where m(+) expresses the average ion mass. A general solution can be obtained by substituting (58) into (55) and (56). However, the resulting equations are non-linear, so it is difficult to obtain the an analytical solution even for the diffusive equilibrium condition.

Next let us consider the case where $u_i \neq 0$. The equations are non-linear because of the term $u_i(\partial_i u_i/\partial s)$. If we assume that u_i is slow, we can neglect this non-linear term. We get the following equation from (48):

$$\frac{\partial u_i}{\partial t} + \frac{1}{N_i}\frac{\partial p_i}{\partial s} + g + \frac{Z_i e}{N_e m_i}\frac{\partial p_e}{\partial s} = -\sum_k \nu_{ik}(u_i - u_k) \quad \text{(62)}$$

Let us assume that the major ions (O^+) are stationary and that the j-th minor ions (H^+ and He^+) move with $u_j \neq 0$, as is the case in the Earth's topside ionosphere. Since $N_j << N_i$, and $N_i \approx N_e$, and neglecting time dependence, equation (62) for electrons, and the i-th and j-th ions becomes

$$\frac{1}{N_e}\frac{\partial p_e}{\partial s} + eE = 0 \quad \text{(63)}$$

$$\frac{1}{m_i N_i}\frac{\partial p_i}{\partial s} + g - \frac{eE}{m_i} = \nu_{ij} u_j \quad \text{(64)}$$

$$\frac{1}{m_j N_j}\frac{\partial p_j}{\partial s} + g - \frac{eE}{m_j} = -\nu_{ji} u_j \quad \text{(65)}$$

Eliminating E from these equations gives

$$u_j = -D_{ji}\left[\frac{1}{N_j}\frac{\partial N_j}{\partial s} + \frac{m_i g}{kT_i} + \frac{T_e/T_i}{N_e}\frac{\partial N_e}{\partial s} + \frac{1}{T_i}\frac{\partial (T_e+T_i)}{\partial s}\right] \quad (66)$$

where

$$D_{ji} = (kT_i/m_j)\nu_{ji} \quad (67)$$

Furthermore, if we assume that the distribution of the major ions is not affected by the minor ions, we get

$$\frac{1}{m_i N_e}\frac{\partial (p_i + p_e)}{\partial s} = -g \quad (68)$$

From this we obtain

$$\frac{1}{N_e}\frac{\partial N_e}{\partial s} = -\frac{m_i g}{k(T_e+T_i)} - \frac{1}{(T_e+T_i)}\frac{\partial (T_e+T_i)}{\partial s} \quad (69)$$

We define the scale heights of the minor ions, H_j, and the plasma, H_p, as

$$H_j = kT_i/m_j g, \text{ and} \quad (70)$$

and

$$H_p = k(T_e+T_i)/m_i g \quad (71)$$

Substituting (69) into (67) gives

$$u_j = D_{ji}\left[\frac{1}{N_j}\frac{\partial N_j}{\partial s} + \frac{1}{H_j} - \frac{T_e/T_i}{H_p} - \frac{1}{T_e+T_i}\frac{\partial (T_e+T_i)}{\partial s}\right] \quad (72)$$

Using this expression and the continuity equation (48) of the j-th ion, we get 2nd order linear simultaneous equations for N_j. For the simple case where the temperatures are independent of altitude, an analytical solution can be obtained[50] as

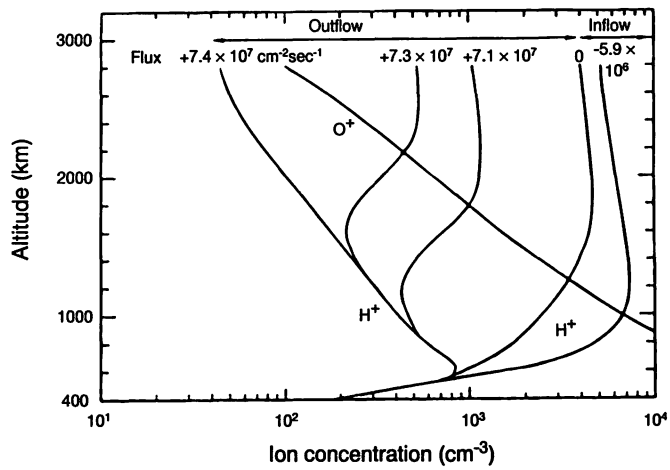

Fig. 24 Calculated distribution of ion density assuming the limiting flux [after Banks and Kockarts[50]].

$$N_j = N_j^a \exp[(\frac{T_e/T_i}{H_p} - \frac{1}{H_j})(s-a)] \quad (73)$$

$$N_j = N_j^a \exp[-(s-a)/H_p] \quad (74)$$

where a is some reference height.

The first solution (73) corresponds to the diffusive distribution of $u_j = 0$. The second solution (74) gives the solution for $u_j \neq 0$. A general solution is given by a linear combination of the two.

Substituting (74) into (72) we obtain the velocity of the minor constituent as

$$u_j = D_{ji}[\frac{1+T_e/T_i}{H_p} - \frac{1}{H_j}] \quad (75)$$

From this, the limiting flux of the j-th minor component in the major i-th ion is given by

$$F_j \equiv N_j u_j = N_j^a D_{ji}^a (\frac{1+T_e/T_i}{H_p} - \frac{1}{H_j}) \quad (76)$$

This flux represents the maximum flux rate of the j-th component in the i-th dominant ion and gives a convenient measure of the flow in the ionosphere.

Figure 24[50] shows a calculated example using this flux as a parameter. This example shows that a small variation in the limiting flux can cause large difference in the ion distribution.

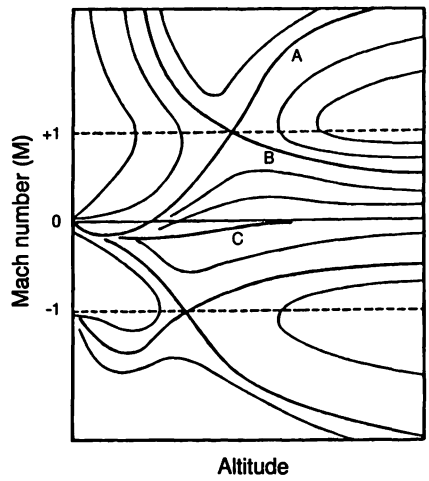

Fig. 25 Diagram of the polar wind solution [after Banks and Holtzer, 1969[51]].

Now let us consider the case when the diffusion velocity is large, so the convective derivative cannot be neglected. We define sound velocity c as

$$c^2 = k(T_e + T_i)/m_i \quad \text{..... (77)}$$

The Mach number M is defined by

$$M \equiv u_i / c \quad \text{..... (78)}$$

The Mach number as calculated by nonlinear equation (48) has a supersonic solution (A) in Fig. 25 [51]. This solution is called "polar wind", which is an analogy of the solar wind. The polar wind is one of the most important processes in transporting ionospheric ions to the magnetosphere. Flows due to the polar wind were confirmed at 1400 km by the ISIS-2 satellite[52][53] and at higher altitudes by the DE-1 satellite[8][54]. This process is also very important for the analysis and interpretation of the data from the ISS-b and EXOS-D satellites, which will be discussed later.

3.2 Ion transport by neutral wind and electric field

The neutral atmosphere in the ionosphere, or thermosphere, is quite dense, so the neutral wind significantly affects the ionosphere. Heating of the thermosphere by solar EUV radiation causes thermospheric wind. Figure 26 shows the thermospheric wind velocities at 300 km (upper panel) and at 120 km (lower panel) as calculated by the TGCM (Thermosphere General Circulation Model)[55]. The direction of the wind is mainly horizontal, and is generally pole-ward during day and equator-ward at night. Because this wind drags the ions (air drag), it can change the distribution of the ionospheric plasma.

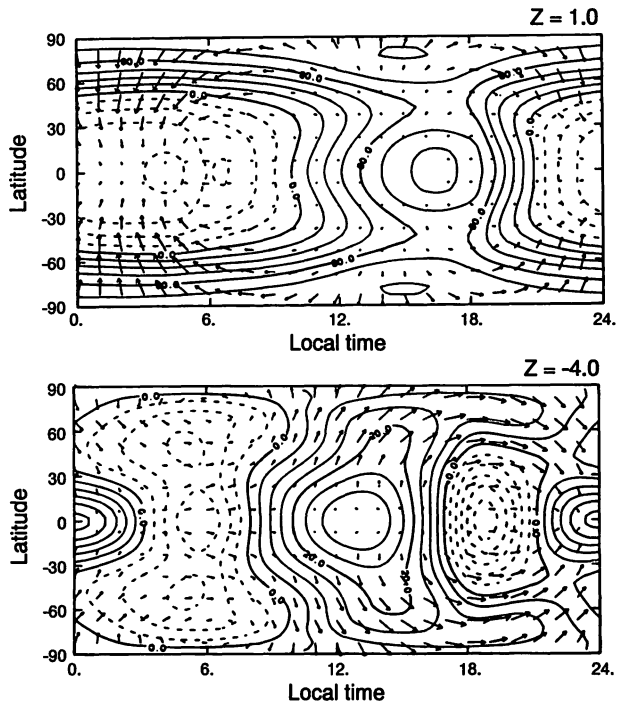

Fig. 26 An example of calculated global wind distribution by TGCM [after Dickinson et al., 1981[55]].

Since movement of charged particles across magnetic field lines is not possible, the north-south neutral wind exerts vertical component of plasma movement along the field lines. Let U be the horizontal velocity of wind and I be the dip angle of the geomagnetic field. Since the velocity component along the field line is $U \cos I$ and the vertical component exerted is $U \cos I \sin I = (U/2)\sin 2I$, it is apparent that this effect is large around the region where I ~ 45 degrees. The transport direction due to this wind is downward during day and upward at night. In the F2 region, this effect has roughly the same magnitude as that of diffusion discussed in the previous section. The "midday bite-out" of NmF2[56] is an example of this effect.

Besides the global-scale thermospheric wind, neutral air motion due to tidal waves is also important. The atmospheric tides are caused by the heating of ozone and water vapor in the stratosphere and they propagate upwards. It has been thought that one-day or half-day tidal-mode periods prevail. Shorter-period waves of several hours also exist and are called internal gravity waves. The amplitude of these waves at the stratospheric altitudes is very small, so that their density variation is on the order of 0.1% and their velocity, v, is on the order of 0.05 m/sec[57].

However, since the wave energy, $\rho v^2/2$, is conserved during the propagation from the stratosphere to higher altitudes, the velocity should increase while ρ decreases. The ultimate velocity in the F region becomes on the order of several hundred m/sec[57] and eventually has a large effect on the F region. Since the atmospheric tides also create a dynamo electric field in the E region, and this field causes drift motion in the ionospheric plasma, the importance of tides is two-hold meaning.

The drift motion due to the electric field is another important mechanism affecting the ionosphere. It is well known that electric field E, in the presence of magnetic field B, creates plasma

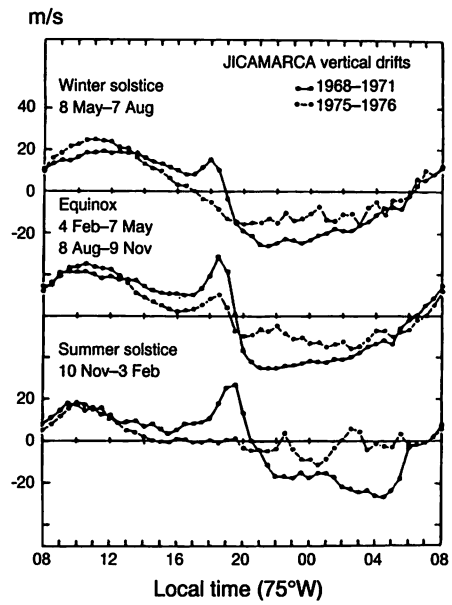

Fig. 27 Vertical plasma drift velocity observed by IS radar at Jicamarca [after Fejer et al., 1979[61]].

drift with a velocity of $E \times B/B^2$. The origins of the ionospheric electric field are the E region dynamo and the solar wind-magnetosphere interaction. Electric fields caused by thunder storms may have a large magnitude, but their effect on the ionosphere is small[58].

The F region dynamo field is due to a slightly different mechanism than that of the E region as pointed out by Matuura[59] or Kelley[60].

The drift motions due to electric fields can be measured by ground-based IS radar. The vertical drifts observed by the Jicamarca radar are shown in Fig. 27[61]. The enhancement of the drift around 18–20 LT is due to the F region dynamo. The drift velocity is generally larger during solar maximum than during solar minimum.

The magnetospheric convection electric field is created by the interaction between the solar wind and the earth's magnetosphere, as in an MHD generator. The direction of the field is dawn to dusk and its magnitude is about 30 kV across 10–20 earth radii[62]. Besides causing the large-scale convection in the magnetosphere, this field is projected along the geomagnetic field line into the polar ionosphere, driving the plasma there. As shown in Fig. 28[63], it typically creates a drift motion of the two-cell pattern in the polar ionosphere. Expansion of the polar atmosphere due to heating by this motion also drives the ionospheric plasma. Joule heating due to auroral particle precipitation also causes similar effects. The plasma drifts and the neutral winds have been extensively investigated by using the DE-1 and DE-2 data[64][65].

The neutral air motion not only affects the plasma distribution, but the neutral air is also influenced by plasma motion (ion drag). Ion drag becomes important at the F2 maximum altitude. Since the collision frequency is already smaller at this altitude, the effect of ion drag occurs over a long times scale[4].

We have seen above that the interaction between the thermosphere, the ionosphere, and the magnetosphere is important in view of ion transport. More generally, this interaction is also important

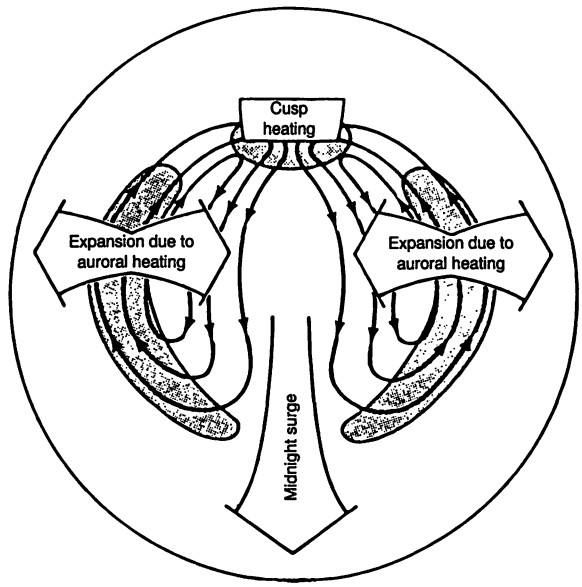

Fig. 28 Schematic illustration of the plasma convection at the high latitude [after Babcock and Evans, 1979[63]].

in energy coupling. This is the central problem for the STEP program. The ionospheric and magnetospheric plasma studies so far have produced little observational data on the neutral air motion. This information is urgently needed.

3.3 Ion transport to the magnetosphere

The ion mass spectrometers used for ionospheric and magnetospheric studies before the mid-1970's were unable to analyze energy of ions, so the observations were limited to cold ions. A typical example of such an observation by Chappell et al.[66] is shown in Fig. 29.

Mass spectrometers are now able to analyze energy of ions; they have been flown on the S3-3[67], the SCATHA[68], the ISEE[69], the GEOS[70], and the DE-1 satellites[71]. Observations by these satellites have revealed that there are ionospheric ions, which have been accelerated from low to high energy, everywhere in the magnetosphere in the plasma sheet, plasma mantle, tail regions and so on.

Figure 30 shows two-year average spectra in the 2.8–4.3 keV range, as observed near geosynchronous orbit by the GEOS-2 satellite[72]. O^+ and He^+ are clearly of ionospheric origin. Possible candidates for 2^+ ions are He^{++} and D^+, but they were identified as He^{++} of solar wind origin for higher energy range.

While it is not possible to discriminate them based only on mass number information, Young and Farrugia[73] analyzed the temperature distribution against the spin phase and found that they can be discriminated when one of them dominates. They also showed that D^+ sometimes dominates at very low energy[74].

The ratio between $[O^{++}]$ and $[O^+]$ is rather large; the mean ratio $[O^{++}]/[O^+]$ is about 0.057 in 0.9–13.9 keV range, but for particular passes the ratio increased to about 1.0[73]. For the topside ionosphere, this ratio was reported to be about 3×10^{-3}[20][75].

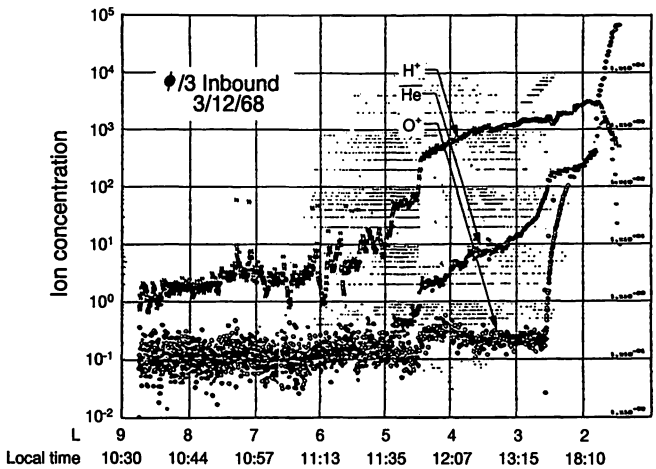

Fig. 29 Ion composition near the plasmapause observed by OGO-5 [after Chappell et al., 1970[66]].

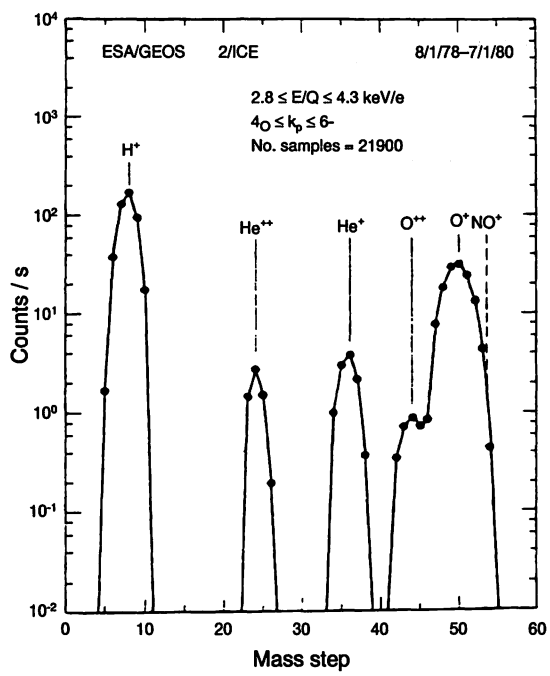

Fig. 30 Averaged mass spectrum in the magnetosphere observed by GEOS [after Young et al., 1982[72]].

Production of O^{++} is given by

$$O^+ + (h\nu, e) \rightarrow O^{++} + e \quad (79)$$

$$O + (h\nu, e) \rightarrow O^{++} + 2e \quad (80)$$

It is shown from model calculation that the ratio $[O^{++}]/[O^+]$ will become about 1.0 when geomagnetic activity remains quiet for about five days[76]. Experimental data shows that this ratio has a negative correlation with the kp index and that $[O^{++}]$ tends to accumulate during quiet periods. The amount of O^{++} in the magnetosphere is thus a good indicator of how long it has been since the magnetospheric plasma was transported from the ionosphere.

The existence of molecular ions at high altitudes is another peculiar feature of the magnetospheric ion composition. Using the DE -1 data, it was found that a flux of 10^6 ions/cm^2/sec for N_2^+, NO^+, and O_2^+ at about 3 Re position in the energy range of 200 eV[77]. High energy NO^+ and O_2^+ of 160 keV at 7 Re and in the ring current region were detected by the AMPTE satellite[78]. In this case, the ratio of molecular species to O^+ was 0.031 ± 0.004. These observations were done on very geomagnetically disturbed days. These molecular ions usually exist below 200 km and decay very rapidly at higher altitudes. When the charge exchange reaction with O is taken into account, molecular ions cannot exist at high altitudes unless they are produced above 400 km. That is to say, detection of molecular ions at high altitudes implies that the neutral molecular gases rise up during highly active periods.

There is no doubt that the ion transport from the ionosphere to the magnetosphere described above occurs preferentially in the polar ionosphere. Figure 31 schematically shows how the ions are transported into the magnetosphere[79]. Most of the H^+ flow can be explained by "classical" polar wind theory[80][81]. However, the O^+ flows that have been found in many recent observations cannot be explained by this theory. The polar wind theory can be modified, however, to include O^+ acceleration if the high electron temperature is taken into account[82][83]. One more important point in Fig. 31 is "cleft ion fountain". The DE-1 observations revealed that the flow-out of the ionospheric ions is concentrated in the cleft region. The flow of H^+, He^+, and O^+ from this narrow cleft region is dispersed as if the Earth's magnetic field acts as a mass spectrometer[79]. It should also be noted that the ion flows take the form of conics, ion beams, or TAI (transversely accelerated ions) and that ions not only flow up (UFI), but they also flow down (DFI). The DFI is very rare compared to UFI[84]. This suggests that there is some scattering process at the apex of the geomagnetic field, or at the geomagnetic equator.

As for the ion acceleration mechanism, many processes, such as the electric field due to the double layer, anomalous registivity, wave-particle interaction and polar wind have been proposed[85]. So far, it seems that no single mechanism has been found to be decisively responsible for various observations. EXOS-D is expected to dedicate for such studies as stated by Sagawa et al.[86].

4. Ion mass spectrometer on ISS-b satellite

4.1 Ionosphere Sounding Satellite-b (ISS-b)

The Ionosphere Sounding Satellite program began in 1967 at Radio Research Laboratory (RRL) inspired by the success of the Alouette and ISIS programs. The main objective of the program was to

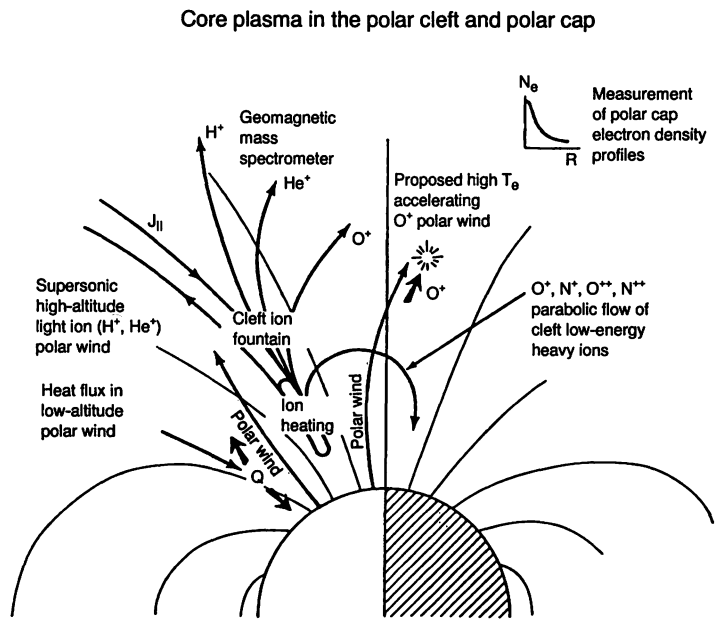

Fig. 31 Schematic illustration of ion outflow from the polar ionosphere [after Horwitz, 1987[79]].

acquire worldwide distributions of ionospheric parameters, namely, foF2, radio noise, and electron and ions densities and temperatures. The program was formally approved by the Space Activity Commission in 1969.

The system designs and fabrication of the satellite were transferred to NASDA, the National Space Development Agency, which was established in 1969. The first model of the ISS was launched successfully on February 29, 1976 by N-rocket, but it stopped sending telemetry signals after about one month because of troubles in the power supply system.

An improved (back-up) model, ISS-b was launched on February 16, 1978. After two-months of initial checking, RRL took over the operation of ISS-b. Regular observations at RRL began on April 24, 1978[87]. At first, data were acquired from four passes per day except during periods of the total sun-lit condition. However, after about one and a half years, the power from the solar cells reduced considerably so that the number of passes had to be reduced gradually. Finally the operation was ceased in July, 1982 because the available power was so low. Throughout its mission, the ISS-b provided continuous streams of data covering comparatively long time periods thanks to its long-lived on-board tape recorder, while the recorder on the ISIS-2 satellite, for example, failed at very early phase after launch. The data were used to obtain many world maps of ionospheric parameters [see the special issue about the results of ISS-b in Rev. RRL, vol. 28, No. 146].

4.1.1 Satellite System

The ISS-b satellite carried the following four observational instruments;

1) **Topside Sounding (TOP)**

TOP-A: Automatic scaling of the critical frequencies and detection of the lowest interference frequencies

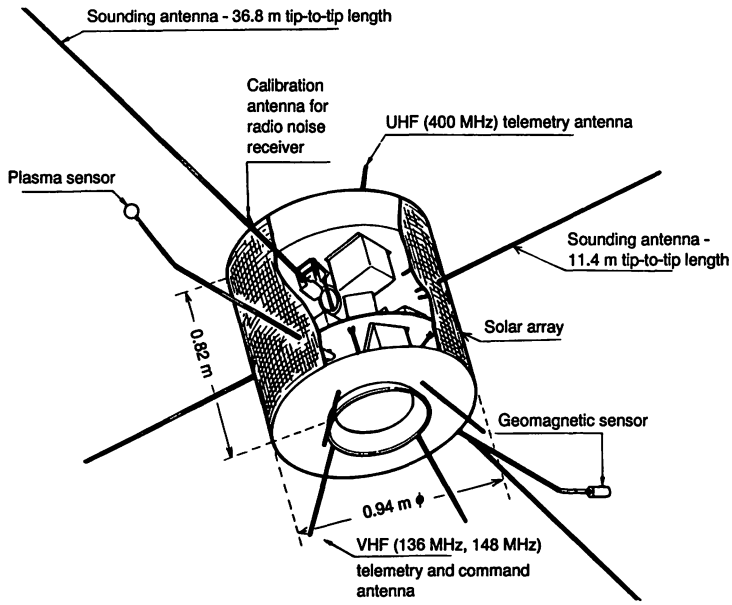

Fig. 32 Structure of the Ionosphere sounding Satellite (ISS-b).

TOP-B: Measurement of the topside ionogram and the spectrum of cosmic radio noise

2) **Radio Noise Measurement (RAN)**

Four narrow-band receivers to detect radio atmospherics and average intensity of radio noise

3) **Plasma Measurement (RPT)**

Measurement of the density and temperatures of electrons and ions by a spherical retarding potential analyzer.

4) **Positive Ion Composition Measurement (PIC)**

A pair of Bennett ion mass spectrometers to measure the composition of positive ions.

As shown in Fig. 32, the ISS-b spacecraft consisted of a circular cylinder measuring 0.94 m $\phi \times$ 0.82 m H with PIC sensor mounted at the center of its top and bottom covers of the spacecraft. The main characteristics of the ISS-b are shown in Table 6.

The orbit of ISS-b was approximately circular with an altitude of 1100 km and an inclination angle of 70 degrees. As shown in Fig. 33, observations were made by the four instruments sequentially every 64 seconds. The data rate was 1024 bits/sec. The on-board data recorder was a conventional tape recorder, which worked well with no problems throughout the mission.

4.1.2 Operation of ISS-b

The operating system for ISS-b at RRL is shown in Fig. 34. Observations were made by ISS-b from April, 1978 to July, 1981.

Because the ISS-b orbit was inclined at 70 degrees and the orbital plane rotates westwards at 3 degrees per day (2 degrees due to gravity anomaly and 1 degree due to the revolution of the earth), an observational period of four months is necessary for all the sub-satellite latitude to experience a

Table 6 Main characteristics of ISS-b.

1. Orbit			
	Perigee		972 km
	Apogee		1220 km
	Inclination		70 deg
	Period		107 km
	Apogee		1220 km
2. Attitude			
	Spin stabilized		1220 km
		Initial spin rate	100 rpm
		Spin rate after extension of antennas	13.7 rpm
3. Shape			
	Cylindrical		
	Diameter		94 cm
	Height		70 deg
4. Weight			141 kg
5. Mission Subsystems			
	a. Topside Sounder (TOP)		
	b. Radio Noise Receiver (RAN)		
	c. Retarding Potential Trap (RPT)		
	d. Ion-Mass Spectrometer (PIC)		
6. Attitude Sensors			
	a. Sun sensor		
	b. Earth sensor		
	c. Magnetic Sensor (3 axes)		
7. Housekeeping Subsystem			
	Temperatures, Voltages, Currents, Operation status, etc., 139 items on various parts of subsystems		
8. Telemetry subsystem			
	a. Transmitters		
		Frequency	136 MHz band
			400 MHz band
		Modulation	PCP/PM (BPL)
		Transmission Rate	1,024 bps (real time)
			26,624 bps (play back)
	Power		
		Play back, real	1 W (136 MHz)
		Time mode	0.7 W (400 MHz)
		Beacon mode	0.1 W (136 MHz)
			0.07 W (400 MHz)

Table 6 Main characteristics of ISS-b.—continued

b. Tape Recorder		
	I/O channel	1 channel
	Record time	115 min
	Play back time	270 sec
	I/O signal type	Bi-phase level
	Bit rate	1,024 bps (record)
		26,624 bps (play back)
9. Command subsystem		
a. Receivers		
	Frequency	148 MHz band
b. Decoders		
	Signal type	Tone burst (1 address tone burst, 3 execute tone bursts)
	Tone frequency	2 address frequencies, 4 excecute frequencies
	Command items	64 items + 8 items (duplicate use)
10. Antennas		
a. Radio observation antennas		2 pairs (tip-to-tip length 36.8 m, 11.4 m
b. Telemetry-command VHF antenna		Turnstile antenna
c. Telemetry UHF antenna		Whip antenna
d. RAN calibration antenna		
11. Power Subsystem		
a. Solar cells		2 cm × 2 cm, 4940 units
	Power	60 W
b. Battery		Nickel-cadmium 5 AH
12. Thermo-Control		Passive
13. Structure		Shell and honeycomb sandwich
14. Life		Survival probability 70% at 1.5 years after launch
15. Launch		
		a. N-vehicle
		b. Tanegashima Space Center, NASDA
		c. 04h00m UT, February 16, 1978

24-hour local time change, as shown in Fig. 35. That is, four month's consecutive data are necessary to produce world maps of ionospheric parameters, and the time resolution of the world maps obtained by ISS-b is thus about equal to one seasonal change.

Since the main objective of ISS-b was to obtain world maps of the ionosphere, the sub-satellite points were planned to be distributed uniformly in latitude, longitude, and local time. To improve the data distribution, data acquisition from a station in Ottawa, Canada, was added in April, 1979. The monthly numbers of data points actually obtained are shown in Fig. 36. Because the ISS-b did not have an active attitude control system other than spin-stabilization and so the angle between the spin

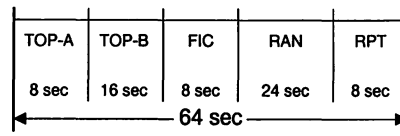

Fig. 33 Observation sequence of ISS-b.

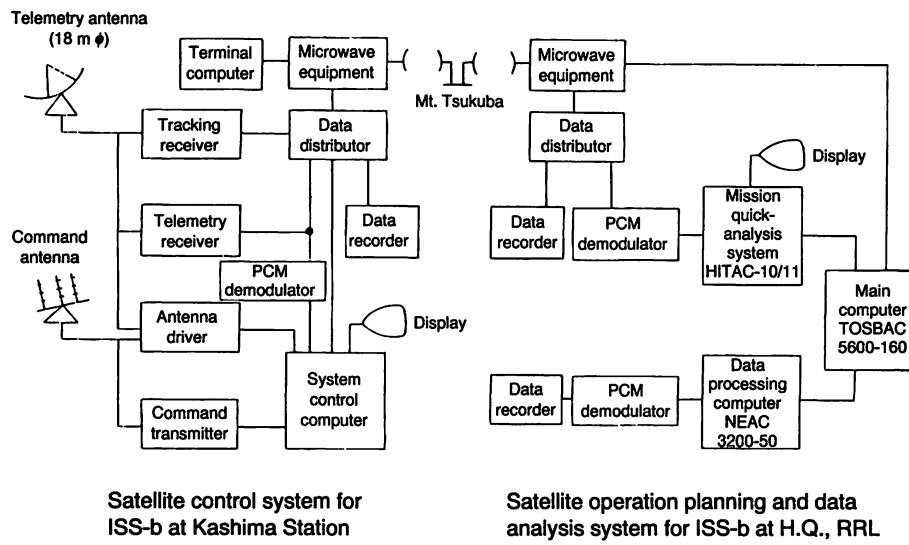

Fig. 34 The operating system for ISS-b.

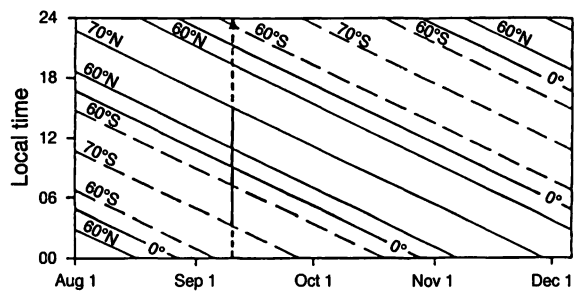

Fig. 35 Variation of local time for subsatellite latitude of ISS-b.

axis and the sun-earth line changed considerably, the power from the solar cells also changed accordingly. And further, during full solar illumination, the top or bottom cover became too hot for normal operation. Due to these restrictions, few observations were made during June and July every year. The generated power reduced at a rate of 20% per year, which is much greater than that expected from the earth's high energy radiation. The cause of this excessive reduction of power is

assumed to be cracks in the solar cells resulting from thermal stress. Because of this power reduction, the number of observational passes per day was reduced to two from January 1980. From January 1981 observations were made only in real time mode above the Kashima station, and in July, 1981 the observations ceased all together. Consequently, meaningful data for world mapping were obtained up to December, 1980.

4.2 Bennett Mass Spectrometer

The ion mass spectrometer on ISS-b was of the type invented by Bennett[88]. This analyzer discriminates a specific mass from others by selective acceleration with a radio frequency voltage[89]. It weighs relatively little because it has no permanent magnet, unlike conventional magnetic mass spectrometers, and is suited for space use. Ion mass spectrometers of this type were flown on early Soviet satellites[90][91], as well as American spacecraft, such as the OGO series[92][93], the Atmosphere series[94], and the Pioneer Venus[39]. Prototypes of the ISS-b analyzer were flown in rocket experiments[95] and on the TAIYO satellite[96]. Although the first ISS satellite which was launched in 1976 failed after one month, there was just enough time to make observations using its mass spectrometer[97]. These observations provided valuable in-flight test data, which were utilized to make improvements to the back up model, ISS-b.

Details of the Bennett ion mass spectrometer on ISS-b are presented below.

4.2.1 Operating Principle of Bennett mass spectrometer

1) **Single-stage analyzer**

Figure 37 illustrates the operating principle of the Bennett mass spectrometer with single-stage acceleration. Firstly, the incident ion is accelerated by a DC voltage, V, and then enters the spaces composed of three planar grids. A sinusoidal voltage, $V_{RF}\sin(\omega t + \theta)$, is applied to the center grid, where ω is angular frequency and θ is an arbitrary phase. The ion is accelerated or decelerated by this voltage, according to the time at which it entered relative to the RF phase. Let m and v be mass and velocity of the ion, respectively. The energy increment, ΔW, of the ion is given by

$$\Delta W = \Delta(mv^2/2) = v \cdot \Delta(mv) = v \cdot F dt \quad \text{..... (81)}$$

where F represents the force which is exerted by the RF field. Let F_1 and F_2 be the values of F in the left side and right side of the RF grid, respectively. Then,

$$F_1 = -F_2 = e(V_{RF}/s)\sin(\omega t + \theta) \quad \text{..... (82)}$$

where s is the distance between the grids. Because the origin of time t is arbitrary, we let t = 0 at the instant the ion traverses the center grid. Then,

$$\begin{aligned} \Delta W &= eV_{RF}\, v/s\left[\int_{-s/v}^{0} \sin(\omega t + \theta)dt - \int_{0}^{s/v} \sin(\omega t + \theta)dt\right] \\ &= 2e\,V_{RF}\ \ v/(\omega s)[\cos\theta - \cos(-s\omega + \theta) - \cos(s\omega/v + \theta)] \end{aligned} \quad \text{..... (83)}$$

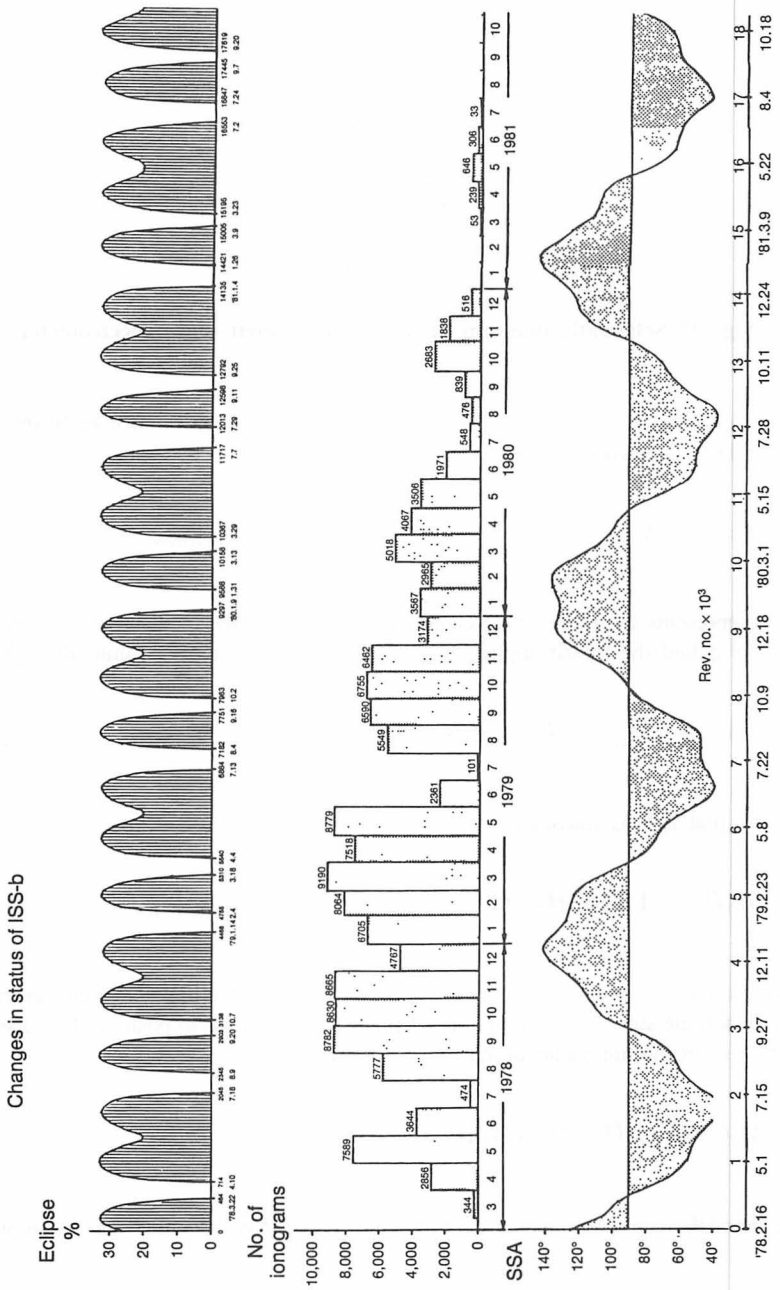

Fig. 36 History of the number of observation points, eclipse rate and sun-spin angle for ISS-b.

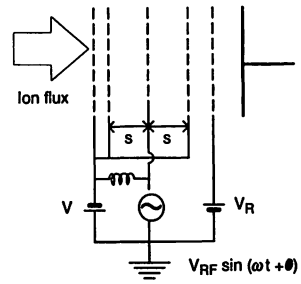

Fig. 37 Schematic diagram of one-stage Bennett mass spectrometer.

where we assume that the velocity change due to the acceleration is sufficiently small compared to the initial value. Now we let

$$\alpha = s\omega / \mathrm{v} \quad \text{..... (84)}$$

where α represents the phase angle change during the passage of distance s at velocity v, and hence it is called the transit angle. If we measure W in unit of eV unit, then (83) becomes

$$\Delta W = -2V_{RF}\cos\theta(1-\cos\alpha)/\alpha \quad \text{..... (85)}$$

It is clear that ΔW is maximum when

$$\cos\theta = -1 : \text{ ie. } \theta = \pi \quad \text{..... (86)}$$

This means that the maximum energy is gained by the ion if the ion passes the center grid at the moment when the sign of the RF voltage changes from negative to positive. It is also intuitively evident. The maximum value of ΔW is given by;

$$\Delta W = 2V_{RF}(1-\cos\alpha)/\alpha \quad \text{..... (87)}$$

In Fig. 38 ΔW is plotted against α. From this figure ΔW becomes maximum when

$$\alpha = \alpha_0 = 2.3311(\text{radians}) \quad \text{..... (88)}$$

The corresponding maximum value of ΔW is

$$\Delta W = 1.45V_{RF} \quad \text{..... (89)}$$

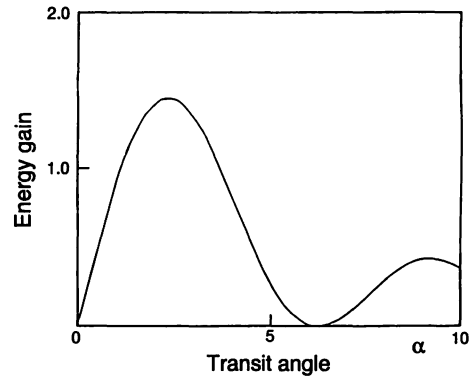

Fig. 38 Energy gain in one-stage Bennett mass spectrometer.

It may be expected at first glance that a maximum occurs if the transit time of the ion between the grid spacing is just equal to the period of the RF field, however, (88) shows that the actual transit time is about 74% (α_0/π)) of the RF period. This comes from the fact that the voltage varies sinusoidally.

Finally, if we apply a retarding voltage, V_R, which passes only those ions that have acquired the maximum energy gain, we can select the ions of a specific mass. That is, since

$$mv^2/2 = eV \quad \text{..... (90)}$$

from (84) and (90) the selected mass is given by

$$m = 2eV\alpha^2/s^2\omega^2 \quad \text{..... (91)}$$

If we let

$$m = M \cdot m_a \quad \text{..... (92)}$$

where m_a is the atomic mass unit and M is the mass number in AMU, then

$$\mathrm{M(AMU)} = 0.2636\mathrm{V(volt)}/\mathrm{s}^2(cm)\mathrm{f}^2(\mathrm{MHz}) \quad \text{..... (93)}$$

Because it is evident from equation (84) that the velocity of the resonant ion takes the constant value of $v = s\omega/\alpha_0$, this analyzer acts as a velocity filter. Compared to this, it is well known that the conventional magnetic mass analyzer is a momentum (mv) filter. The mass spectrum can be obtained by sweeping either DC acceleration voltage or the RF frequency, f. DC voltage scanning is preferred because it is linear with mass number.

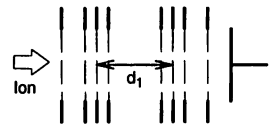

Fig. 39 Energy gain in one-stage Bennett mass spectrometer.

Next let us discuss the resolving power of this analyzer. The retarding voltage determines the ion energy pass band. If m_0 and Δm are the central mass and width of the mass band, respectively, the resolution R can be defined as

$$R = m_0 / \Delta m \quad \text{(94)}$$

Substituting from (91) we get

$$R = \alpha_0^2 / 2(\alpha^2 - \alpha_0^2) \quad \text{(95)}$$

Since the limiting value of α in (95) is determined by (87), putting $\Delta W = V_R$, the resolution can be controlled by changing the magnitude of the retarding voltage, V_R. This feature is the prominent advantage of this analyzer compared to the static magnetic sector type analyzer, for which the resolution is fixed mechanically and it is difficult to control electrically. If we let V_R be 99% of ΔW_0, the corresponding resolution is R = 2.8, which is rather a poor value. We cannot expect high resolution from this single stage analyzer. This fact is also seen in the very broad maximum in Fig. 38.

2) **Two-stage analyzer**

Let us consider the two stage acceleration Bennett analyzer. Another set of three grids are placed with a spacing d_1. If d_1 is arranged so that the time for resonant ions to pass this drift space is an integral multiple of the RF period, the resonant ions in the first stage are also resonant at the second stage. This condition is expressed as

$$d_1 / v_0 = N_1 / f \quad \text{(96)}$$

where N_1 is an arbitrary integer. Substitution from (82) yields

$$d_1 = (2\pi / \alpha_0) s N_1 = 2.695 N_1 s = \beta_1 s \quad \text{(97)}$$

The energy gain in this case is easily obtained as in the single-stage case. The result is

$$\Delta W = -2V_{RF}[(1 - \cos\alpha)/\alpha][\cos\theta + \cos(\beta_1\alpha + \theta)] \quad \text{(98)}$$

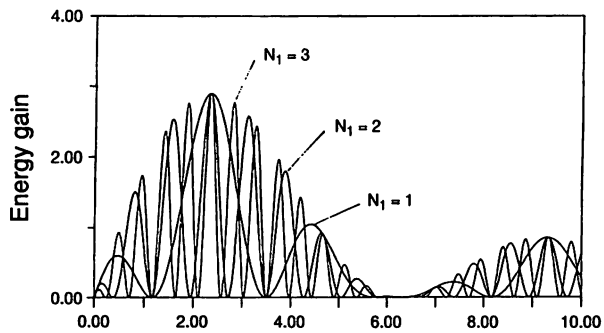

Fig. 40 Energy gain in two-stage Bennett mass spectrometer for N_1 = 1, 2, and 3.

The maximum of ΔW is also obtained when θ = π and α = α_0. Figure 40 shows ΔW at θ = π when N_1 = 1, 3, and 5. It can be seen from this figure that the gain curve becomes sharper for larger value of N_1. Instead, however, there are more peaks and the difference in the adjacent peaks becomes smaller for larger value of N_1. The peaks other than the first give spurious mass spectra. Generally speaking, these spurious spectra complicate the measurements and are not desirable.

3) **Three-stage analyzer**

Addition of one more acceleration stage can suppress the spurious mass spectra. The energy gain for the three-stage case is given by[98]

$$\Delta W = -2V_{RF}[(1-\cos\alpha)/\alpha][\cos\theta + \cos(\beta_1\alpha+\theta)+\cos(\beta_2\alpha+\theta)] \quad \text{(99)}$$

where

$$\beta_2 = 2\pi/\alpha_0(N_1+N_2) = 2.695(N_1+N_2) \quad \text{(100)}$$

The energy gain is plotted in Fig. 41 for the cases of N_1 = 5 and N_2 = 3 (5-3 cycle analyzer) and of N_1 = 7 and N_2 = 5 (7-5 cycle analyzer). Compared to Fig. 40, it is seen that the second harmonic peak is suppressed.

To see the improvement in resolution, let us define the gain factor for simplicity as

$$G(\alpha) = 2[(1-\cos\alpha)/\alpha][\cos\theta+\cos(\beta_1\alpha+\theta)+\cos(\beta_2\alpha+\theta)] \quad \text{(101)}$$

If we let $\theta = \pi$ and expand G(α) in the vicinity of α_0 in Taylor series, we get

$$G(\alpha) = G(\alpha_0)[1-\beta_1^2+\beta_2^2)(\alpha-\alpha_0)^2/6] \quad \text{(102)}$$

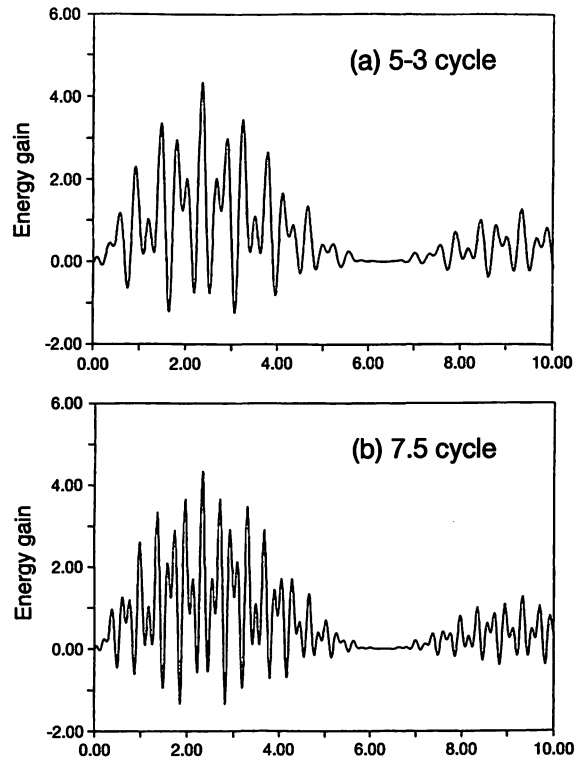

Fig. 41 Energy gain in three-stage Bennett mass spectrometer. (a)5-3 cycle (b)7-5 cycle

Substituting (102) into (95),

$$R = \alpha_0[(\beta_1 + \beta_2)/(1 - G(\alpha_0))]^{1/2} / (4\sqrt{6}) \quad \text{(103)}$$

Using (99) we get

$$R = \pi\sqrt{6/12}[\{N_1^2 + (N_1 + N_2)^2\}/(1 - g)]^{1/2} \quad \text{(104)}$$

where

$$g = V_R / [G(\alpha_0)V_{RF}] \equiv V_R / V_{R\,\text{max.}} \quad \text{(105)}$$

The expression (104) shows that the mass resolution depends only on the ratio between the retarding potential and the maximum gain voltage, and on the cycle numbers of drift spaces, and that it is independent of RF frequency, grid spacing and so on.

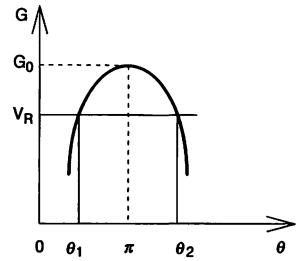

Fig. 42 Schematic illustration of pass band for Bennett mass spectrometer.

Next, we will derive the sensitivity of this spectrometer. This spectrometer transmits only those ions which arrive at the center grids when the phase angle θ is close to π. Since the incident ions can be assumed to be uniformly distributed against the phase angle, it can be seen by referring Fig. 42 that the transmission efficiency, T can be defined by

$$T = (\theta_2 - \theta_1) / 2\pi \quad \text{(106)}$$

Substituting θ given by (106) into (101) and putting $\theta = \pi$, we obtain

$$G = G(\alpha_0)\cos\theta = G(\alpha_0)(\pi - \pi T) \quad \text{(107)}$$

From this we get

$$T = (1/\pi)\cos^{-1} g \quad \text{(108)}$$

This is a very simple expression, but this transmission factor only takes the phase into account. Another factor which influences the efficiency is the transmission of the grids. If the transmission efficiency of one grid is η and if n identical grids are used, the total efficiency is η^n. Since 15 grids are used for the three-stage analyzer as described later, η should be greater than about 90%, otherwise the transmission efficiency becomes very small.
If the value of g is close to 1.0, (108) can be approximated as

$$T = (\sqrt{2}/\pi)\sqrt{(1-g)} \quad \text{(109)}$$

From (104) and (109) we find that the product of R and T is independent of g, that is, independent of the retarding voltage. The product of the resolution and sensitivity is usually called the "figure of merit", and in this case depends only on cycle numbers, N_1 and N_2. Inspection of (104) shows that the figure of merit is greater for greater values of N_1 and N_2. This means that the longer the analyzer, the better the quality, although a long tube is inconvenient for space use, of course. Figure 43 shows the resolutions and transmission coefficients for 5-3 and

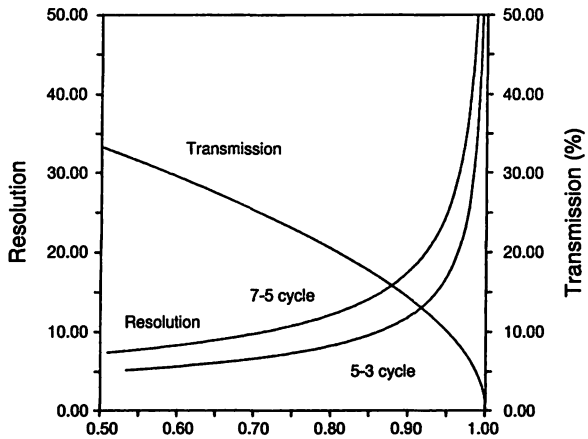

Fig. 43 Mass resolution and transmission coefficient for three-stage Bennett mass spectrometer.

7-5 cycle analyzers. As a numerical example, if we set g = 95%, we obtain R = 27. This value is sufficient for the mass analysis of the topside ionosphere.

4.3 Characteristics of the flight model

4.3.1 Mechanical

Figure 44 shows a schematical cross-sectional view of the positive ion composition (PIC) instrument on ISS-b. The essential part is a 5-3 cycle three-stage Bennett ion mass spectrometer. The dashed lines represent planar grids of the same shape. Each grid consists of a stainless steel ring with an inner diameter of 36 mm (area: 10 cm^2), an outer diameter of 56 mm and a thickness of 1.0 mm. Tungsten wires of 0.05 mm are welded to the ring with a 1.0 mm pitch distance. Each grid is insulated with a steatite ring whose inner diameter is greater than that of the planar grid so that the ions in the analyzer do not see the insulator directly. Thus, the spacing between the grids is

$$s = 0.3\ \text{cm} \quad \text{(110)}$$

and hence from equation (97),

$$d_1 = 4.04\,\text{cm} \quad \text{(111)}$$

$$d_2 = 2.43\ \text{cm} \quad \text{(112)}$$

and the overall length is about 10 cm. Consequently, the analyzer itself is very compact.

Ions selected by the analyzer are detected by a channel electron multiplier (Galileo Electro-optics, CEM 4013) in pulse count mode. The grid Gs in the figure is provided to suppress secondary

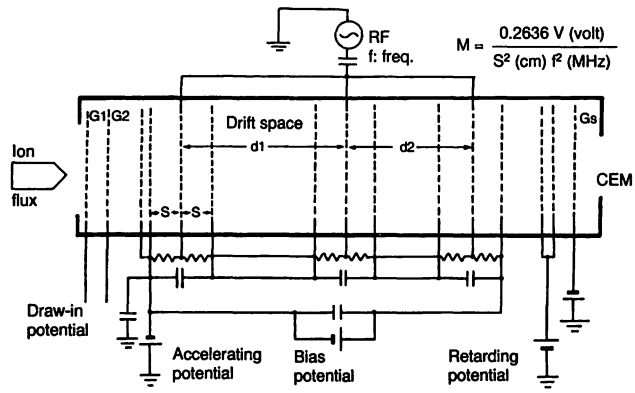

Fig. 44 Cross sectional view of the mass spectrometer on ISS-b (PIC).

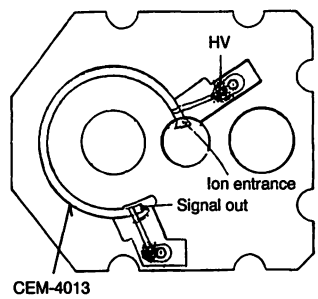

Fig. 45 Holder of channel electron multiplier for ISS-b/PIC.

electrons when the selected ions are detected in ion current mode. In order to prevent solar UV radiation from reaching the CEM, a small orifice is placed between the analyzer and the CEM.

The CEM is very fragile because it is made from very thin glass.

A rather thick and tough cable must be connected to the very fragile CEM to provide a high voltage (3 kV). Because of these facts, the CEM must be mounted with great care. As shown in Fig. 45, the CEM is sandwiched with a pair of insulator plates in which ring-shaped grooves are carved.

Figure 46 shows the construction of the sensor part of the PIC instrument which includes the Bennett analyzer tube, the CEM holder and a preamplifier for the CEM. It is cylindrical, measuring 110 mm × 173 mm, and weighs 1.3 kg. Because the satellite velocity is much greater than the thermal velocity of ions on the orbit, measurement of the ionospheric ions must be done in the ram condition. In order to always assure this condition, two sets of sensors are prepared, one mounted at the top and the other at the bottom cover of the spacecraft. These two sensors are controlled by an electronics box measuring 162 mm × 202 mm × 104 mm, and weighing 2.6 kg.

4.3.2 Electrical

A block diagram of PIC experiment is shown in Fig. 47 and its sequence of observation is shown in Fig. 48.

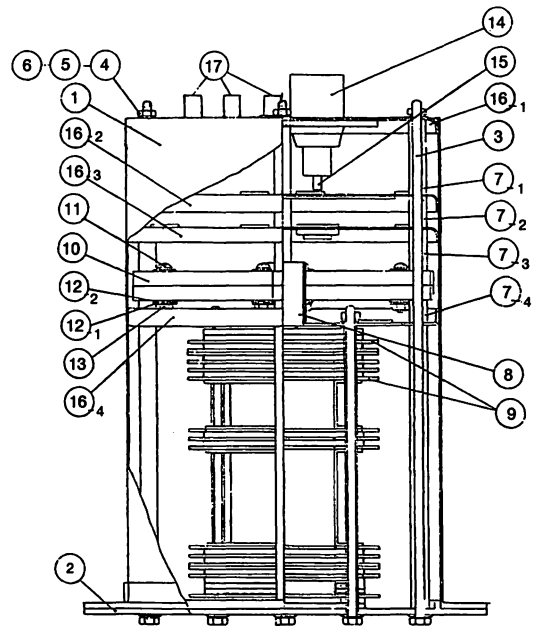

Fig. 46 Mechanical configuration of sensor part of ISS-b/PIC. 1: Cylindrical casing, 2: Flange, 3: Bolt, 4 5 6: Washer, 7: Spacer, 8: Collector, 9: Bennett tube, 10: Channeltron holder, 11 12 13: Screw and nut, 14: Connector for HV, 15: Wire for HV, 16: Flange, 17: Connectors for RF and signal output

One sequence of ISS-b observation is done in 64 seconds, of which eight seconds are assigned to PIC observation. In these eight seconds, the RF frequency is switched to 14 MHz and 6 MHz, and the retarding voltage is switched to two values. For these four kinds of condition, mass spectra are measured with both sensors, that is, eight mass spectra are obtained in one 8-second observation time.

Mass scanning is performed by stepping the acceleration voltage by 2.6 volts with 116 steps so that the voltage range is 0–299 volts and the mass range is 0–4.5 AMU (f = 14 MHz), or 0–24 AMU (f = 6 MHz). The combination of two values for the retarding voltage is selected by command from the ground. The draw-in potential can also be selected by command. The bias potential shown in Fig. 44 decelerates the resonant ions by just the same amount they gained from the RF field so that the resonant ions pass the analyzer tube with a constant velocity. The output from the CEM is detected in pulse count mode. The gate time of the counter is automatically selected from 0.0488, 0.488 or 4.88 msec.

As shown in Fig. 49, two bits of the telemetry word are assigned to the selection of the gate time and the other six bits represent ion counts. The ion counts which can be measured in this manner are in the range of 2.05×10^2–1.3×10^6 counts/sec. The counts from sensor1 and sensor2 are telemetered alternately, as shown in Fig. 48. The total power for this instrument is 6 Watts.

4.3.3 Performance

Fabrication of the spacecraft and on-board instruments and general tests were done by NASDA, but the performance tests for the PIC instrument with real ion input were conducted at RRL. The

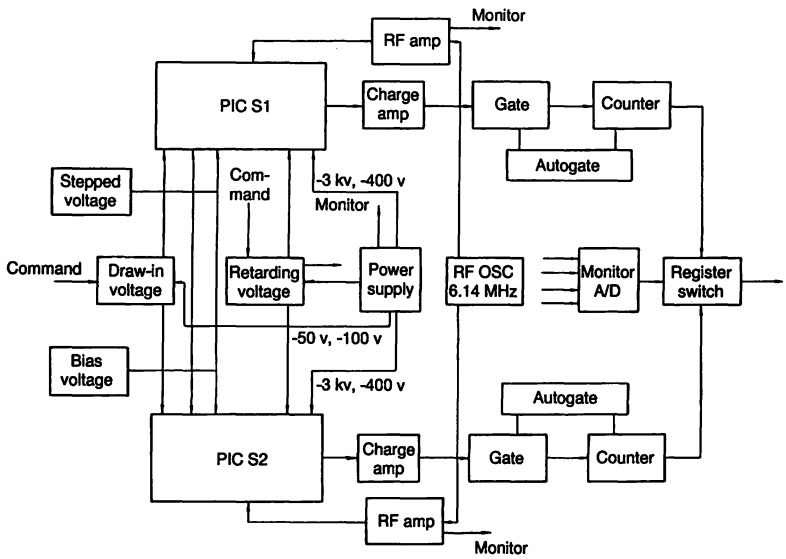

Fig. 47 Block diagram of the mass spectrometer system on ISS-b(PIC).

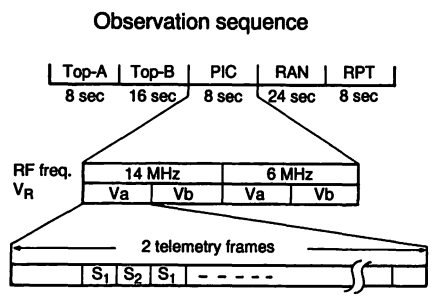

Fig. 48 Observation sequence of ISS-b/PIC experiment.

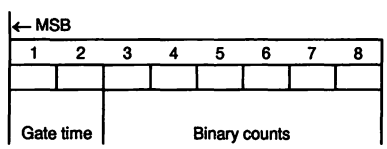

Fig. 49 Format of telemetry data for ISS-b/PIC experiment.

configuration of the vacuum test chamber and ion source are shown in Figs. 50 and 51, respectively. This ion source generates a pencil-beam mono-energetic ion flux.

Figure 52 shows the mass spectra obtained when the ion energy, V_I, is set to 1.0 volt and the retarding voltage V_R is stepped from 10 to 20 volts. In contrast to this, V_I is stepped with V_R kept to

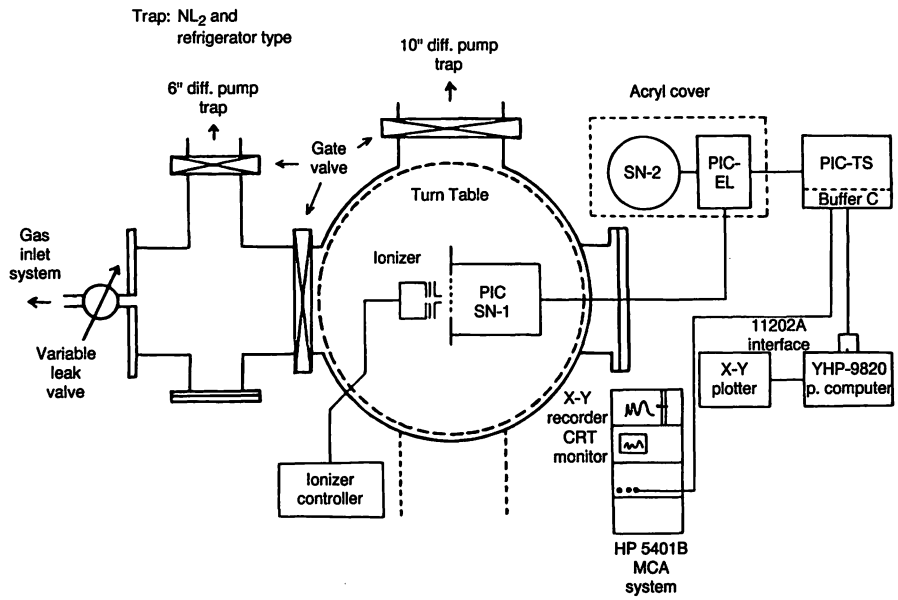

Fig. 50 Schematic illustration of calibration facility for ISS-b/PIC experiment.

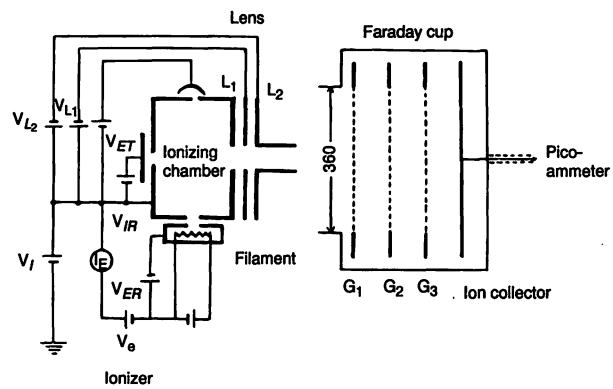

Fig. 51 Schematic drawing of the ion source and Farady cup for calibration of ISS-b/PIC.

a constant value in Fig. 53. These spectra show that decreasing the retarding voltage has almost the same effect as increasing the ion energy. When the retarding voltage is lower than the critical value, spurious mass spectra are obtained due to harmonic gain peaks described before.

Although these harmonic peaks complicate the interpretation of the mass peaks, they can be utilized if the mass spectra is simple enough and in such cases as when the primary peaks saturate or cannot be used for some other reason, because the higher order peaks have lower sensitivity. Table 7 shows the basic data concerning these harmonic peaks.

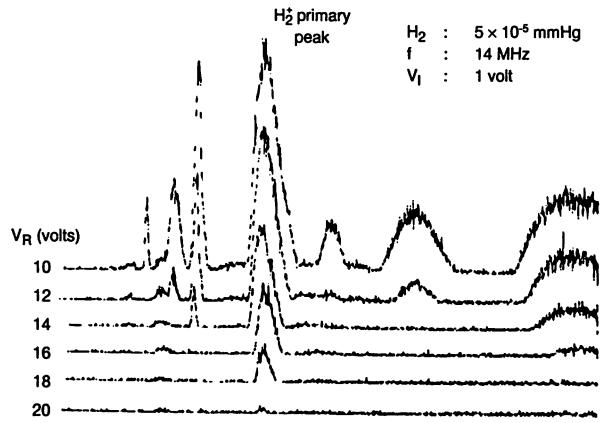

Fig. 52 Mass spectra from PIC when the retarding potential (VR) is varied with the ion energy fixed (VI = 1 volt).

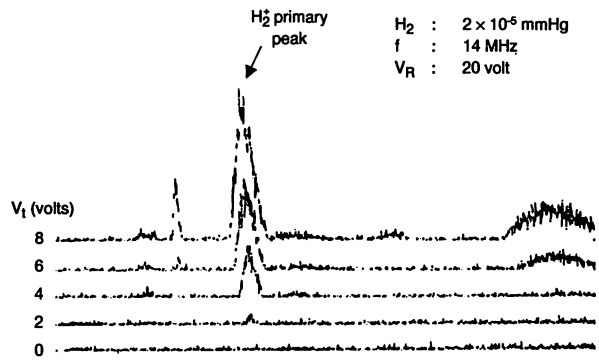

Fig. 53 Mass spectra from PIC when the ion energy is varied with the retarding potential fixed.

Since the velocity of the spacecraft in orbit is about 8 km/sec, ions at rest in the ionosphere have this velocity relative to the instrument, corresponding to energy of 0.3, 1.2 and 4.8 eV for H^+, He^+ and O^+, respectively. This energy is not negligible in the case of O^+. The satellite potential relative to the ambient space also has a similar effect. This potential is around 1–3 volts negative in the normal ionosphere. The combined effect of the satellite velocity and the satellite potential acts to lower the retarding voltage. The PIC measuring sequence stated above was the result of a trade-off between these effects as estimated at the time of design.

Angular response is another important factor to be taken into consideration. ISS-b is spin-stabilized with its axis perpendicular to the ecliptic plane and its orbital plane is inclined by 70 degrees relative to the equatorial plane.

Because the faces of the PIC sensors are directed parallel and anti-parallel to the spin axis, the angle of incident ions can change from 0 to 180 degrees so that angular correction for sensitivity is necessary. It was pretty hard to obtain the correction factors experimentally. Instead, a model calculation was adopted for this correction. The configuration of this model is shown in Fig. 54. It is

Table 7 Relation between the mass peaks due to harmonics effect and the energy gain.

h	α_M	G_M	f = f1 = 14 MHz				f = f2 = 6 MHz				
			M = 1		M = 2	M = 4	M = 1		M = 2	M = 4	M = 16
			V	N	N	N	V	N	N	N	N
0	2.33	21.75	66.8	25.7	51.4	102.8	12.3	4.7	9.4	18.9	75.6
1	3.22	17.25	35.0	13.5	27.0	53.9	6.42	2.5	5.0	9.9	39.5
2	1.44	16.80	175.1	67.3	-	-	32.1	12.3	24.6	49.4	-
3	2.88	14.91	43.8	16.8	33.6	67.3	8.03	3.0	6.2	12.4	49.4
4	1.78	14.86	114.6	44.0	88.1	-	21.0	8.0	16.1	32.3	-
5	3.77	13.34	25.5	9.8	19.6	39.3	4.69	1.8	3.6	7.2	28.8
6	0.89	11.56	458.3	-	-	-	84.1	32.3	64.6	-	-
7	2.65	19.13	51.7	19.9	19.8	79.5	9.48	3.7	7.3	14.6	58.4

h: Harmonics order, G_M: The maximum value of G, α_M: Value of α which gives G_M, M: Mass number of ion, V: Accelerating voltage, N: Number of acceleration stepping (N = V/2.6), -: Outside of sweep range (i.e., N > 115)

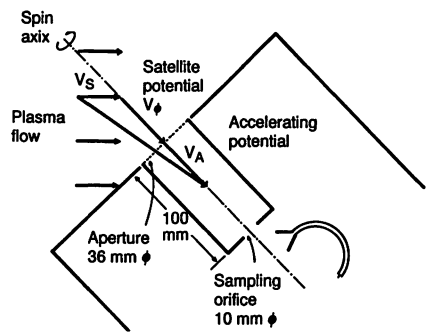

Fig. 54 A model of the angular response for ISS-b/PIC.

assumed in this model that the satellite is charged to a constant potential and moves with fixed velocity, and that initial velocity of ions and thickness of the sheath are neglected. The transmission coefficient is calculated geometrically as a function of the incident angle. Figure 55 shows some results of this model calculation. Angular correction of the ISS-b data was done using this model.

4.3.4 Evaluation of the data from the first ISS satellite

The first flight model of ISS, also known as UME-1, was successfully launched on February 29, 1976 but failed to transmit telemetry signals after about one month due to problems in its power system. Because a high voltage is used for the PIC experiment, its initial tests in orbit were only just completed before the trouble arose. Typical mass spectra obtained on this occasion are shown in Fig. 56 (a) low mass range, and (b) high mass range. Many higher harmonic peaks appear in the spectra. Although the primary peak of O^+ saturates in this case, we can utilize the higher harmonics. Figure 57 shows the distribution of ions Rev. No. 402 obtained by this method[97].

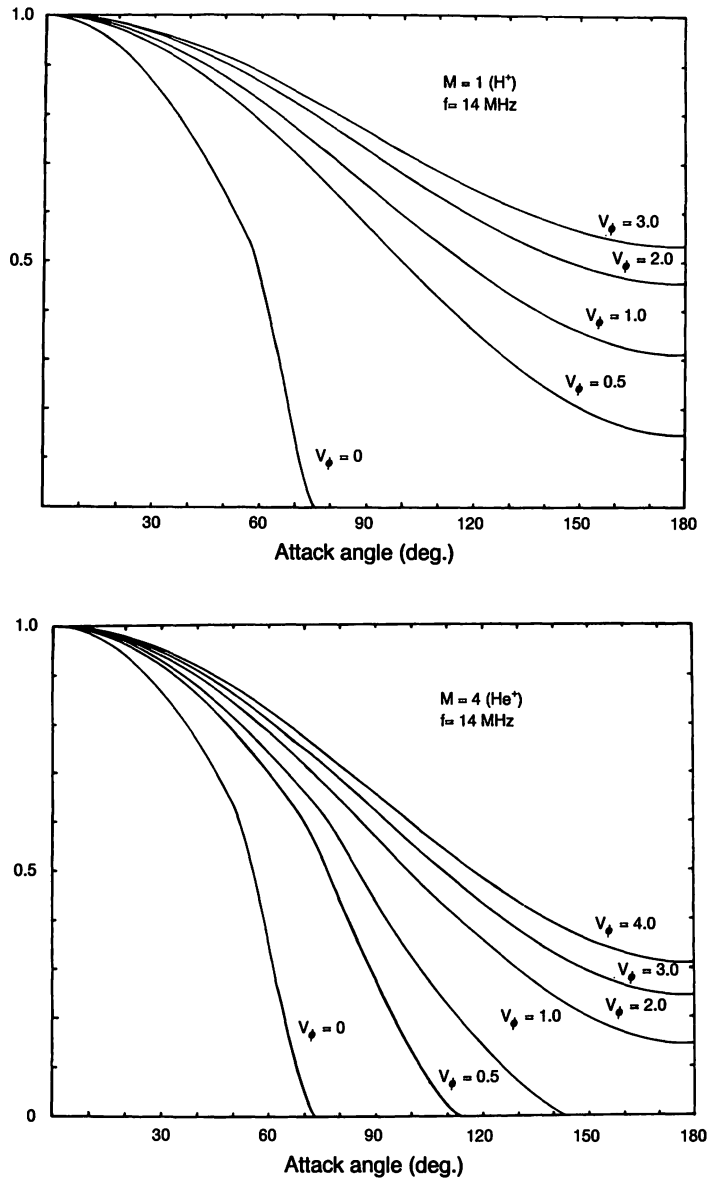

Fig. 55 Transmission coefficient with respect to the incidence angle.(a) for H^+.(b) for He^+.

4.3.5 Evaluation of the data from ISS-b

ISS-b, the back-up model of ISS, was launched February 16, 1978. Only minimal modifications were made to this back-up model mainly to the power supply system, because it was considered to be a crucial problem at that time to keep the predetermined schedules in the space development activity. As for the PIC experiment, it was found in laboratory experiments that the performance of the

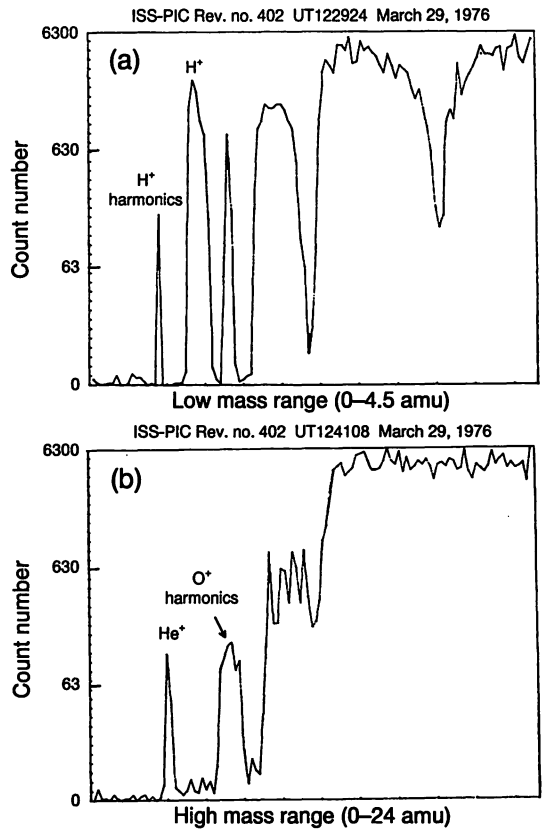

Fig. 56 Typical mass spectra from the ISS (UME-1). (a) low mass range. (b) high mass range.

instrument could be improved if the voltage applied to the suppresser grid was reduced without making any other modifications to the mechanical or electrical designs.

Figure 58 shows typical examples of the mass spectra obtained from ISS-b in orbit. The major ions, H^+, He^+ and O^+ are clearly identified, although there remain some harmonic peaks and the base line increases for higher acceleration voltages. For these reasons, it is somewhat difficult to identify minor constituents such as He^{++}, or O^{++}.

Figure 59 shows the responses of the spectrometer when the retarding voltage was changed, which were obtained during initial test period. These spectra show that the spectrometer works as theory predicts. From these tests, the combination of (24, 26) volts for the retarding voltage was selected for regular observations. This selection was never changed through the whole period of the observations after the initial performance tests. This simplified the data processing and was found to be very appropriate for global mapping analyses.

Figure 60 shows the data obtained in June, 1981, when more than three years had elapsed since the launch. Comparing with the initial data of Fig. 58, we can hardly recognize any degradation. By inspecting the mass spectra in this manner and comparing them with absolute electron densities obtained from the topside sounder, it was presumed in the data processing that the correction of sensitivity change during the observational period could be neglected.

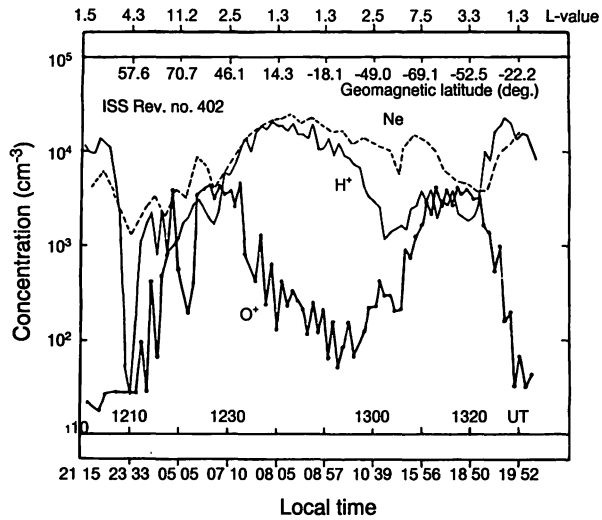

Fig. 57 Distribution of ion densities observed by ISS (UME-1) [after Iwamoto et al., 1977[97]].

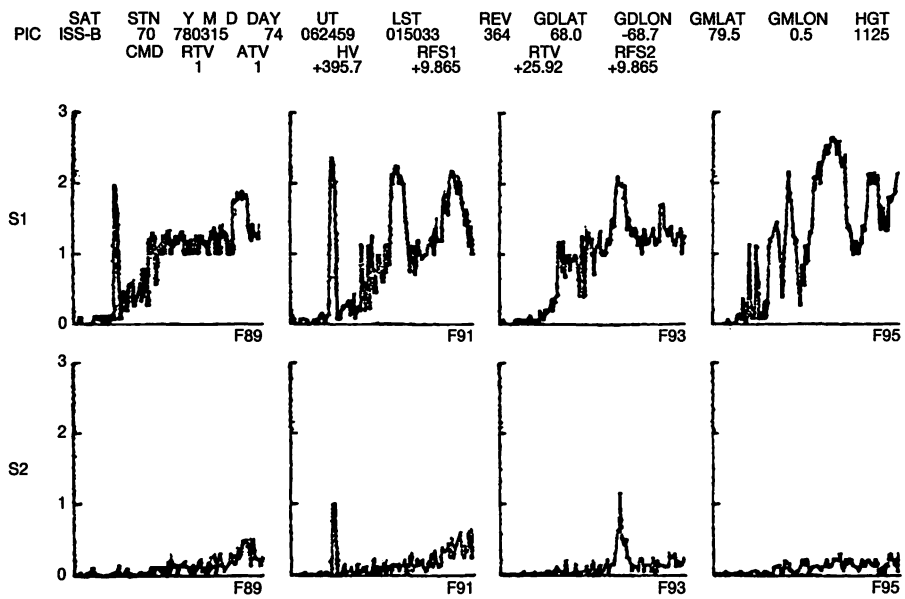

Fig. 58 Typical mass spectra from the quick-look system for ISS-b/PIC.

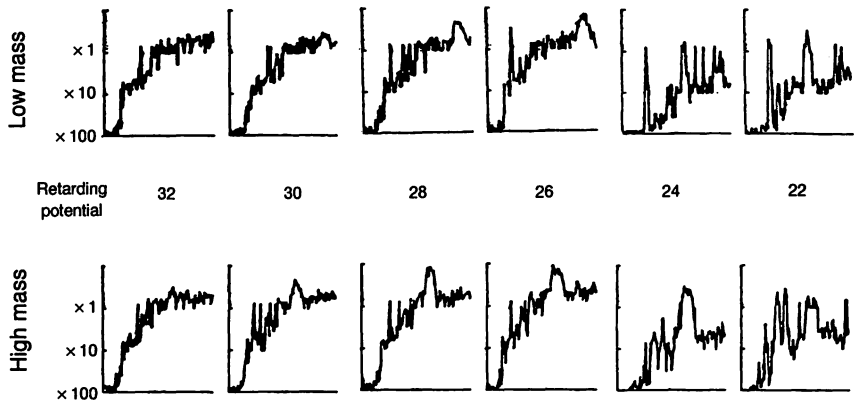

Fig. 59 Variation of mass spectra when the retarding potential is changed.

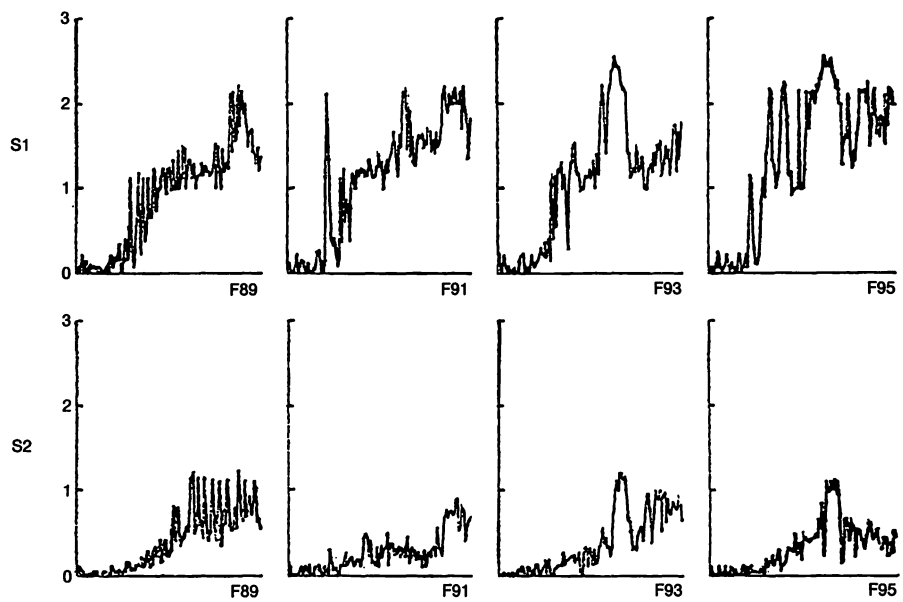

Fig. 60 An example of mass spectrum on June 9, 1981, near the end of ISS-b life time.

4.4 Processing of ISS-b data

4.4.1 Primary Processing

As shown in Fig. 61, ISS-b's observations were scheduled according to an "Operation Plan Program (OPP)" and controlled by radio commands transmitted from the Kashima station, which also carried out most of the data acquisition. Later on in this mission, data acquisition was also performed

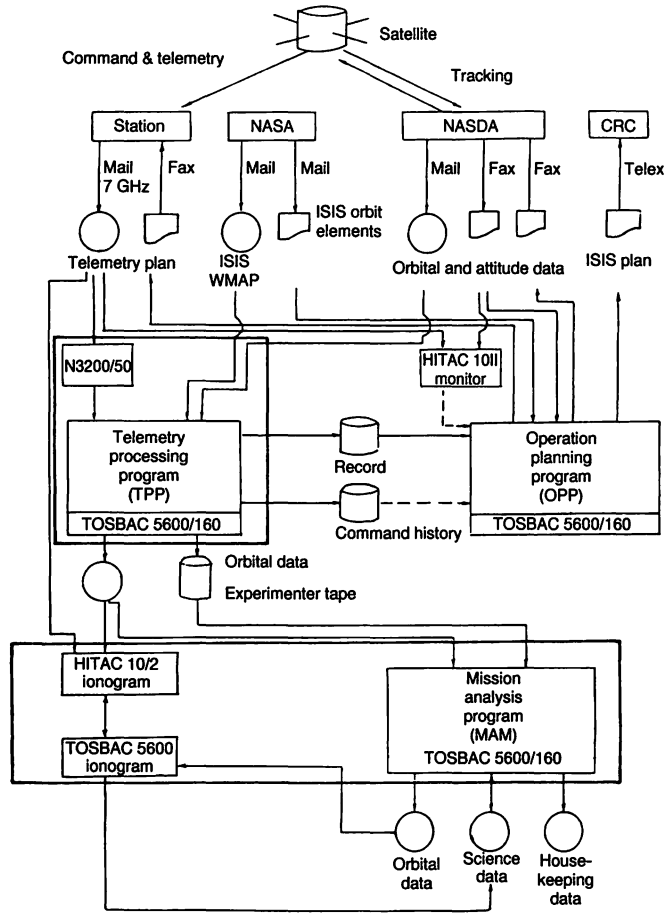

Fig. 61 Flow diagram of ISS-b observation, operation and data processing.

by a station in Ottawa, in Canada. The data was edited by a "Telemetry Processing Program (TPP)" to produce an "Experimenter Tape" for each experiment. Each experimenter tape includes the following records:

1) Header record:

   Satellite name, Mission ID, date of tape production.

2) Pass Title Record:

   Station name, Date of observation, etc. One pass title for each pass operation.

3) Mission Title Record:

   Orbital parameters and attitude data. One mission title for each 64-second observation.

4) Data Record:

   The data obtained in one 64-second observation.

The experimenter tapes were produced at a rate of one volume per week, and in total 151 volumes were accumulated for the PIC experiment in four operational years.

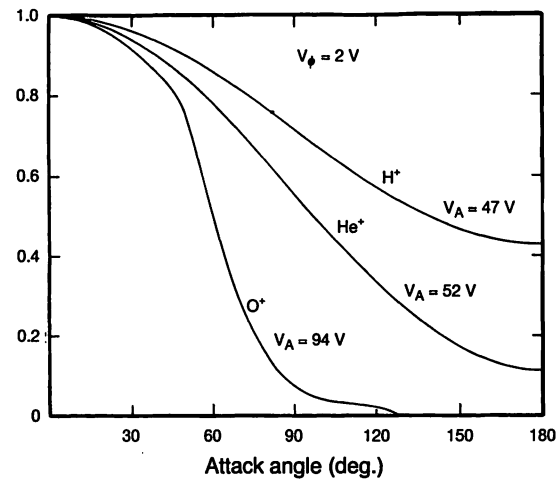

Fig. 62 The angular response used for processing of the ISS-b data.

4.4.2 Secondary Processing

To obtain ion densities from the experimenter tapes, the following processing was done:

1) Decoding
   The encoded data are decoded to real ion counts per second.
2) Removal of Random Noise
   Spiky random noise in the mass spectra is removed mainly by running average.
3) Subtraction of Bias Counts
   The spurious bias counts, which give rise to the increased baseline in the mass spectra shown in the previous section, are subtracted.
4) Detection of Mass Peaks
   Since the positions of mass peaks in the mass spectra tended to move a little due to variations of satellite potential and/or ion energy, the peak counts corresponding to individual masses are detected in prescribed ranges.
5) Conversion to Ion density
   To obtain an absolute density the peak counts for each mass are multiplied by a correction factor, as described below.
6) Summary File
   The ion density data are accumulated with the appropriate orbital data in the Summary File. This file is the basis of the mapping analyses.

4.4.3 Attack angle correction

The change of sensitivity with attack angle was corrected using coefficients calculated from the model described earlier. This model needs information regarding the potential besides that of the satellite attitude. According to the plasma measurement experiment (RPT), the satellite potential varied in the range from -1.0 to -3.0 volts for some particular passes.

If these values were available for all the observational points, they could have been used for correction. Unfortunately however, good RPT data were limited mainly to non sunlit conditions, thus

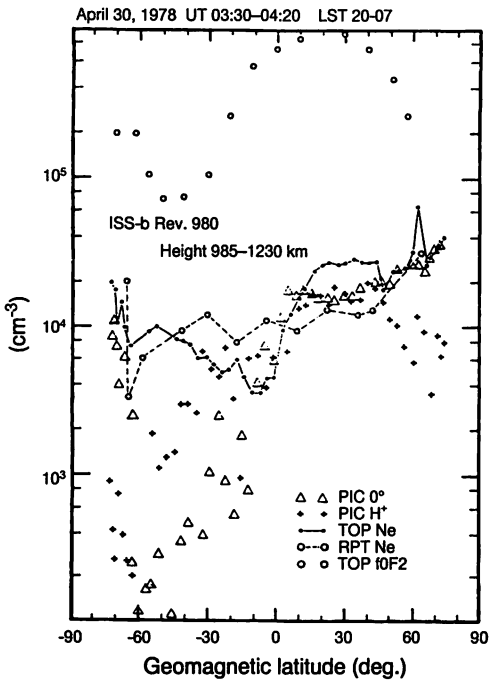

Fig. 63 Absolute calibration of ion density by TOP and RPT data.

we assumed a fixed value for the satellite potential, namely, -2.0 volts. The transmission coefficients for this case are shown in Fig. 62. If the variations of real potential are assumed to be in the range of -1.0–3.0 volts, the worst case error due to above assumption (when the attack angle equals 90 degrees) is estimated to be about 10, 25 and 50% for H^+, He^+ and O^+, respectively.

4.4.4 Absolute Calibration

For absolute calibration, we assume that the ion counts obtained after angular correction as described above are proportional to the ion densities in the ambient plasma. This assumption does not always hold true if effects such as the satellite potential or the sheath are considered.

Because laboratory calibration is rather difficult, we adopted an "in-flight calibration method"[20], in which the outputs from the spectrometer are compared with the measurements of other on-board instruments. For the plasma density, this was achieved using the data from the TOP and RPT. The resonance spikes in the topside ionogram give absolute values of plasma density. As it is well known that H^+ and O^+ are dominant species at about 1100 km altitude, we first assume the dominance of these ions.

Because measurements by the PIC, TOP and RPT are not made simultaneously, we also assume that the plasma density changed smoothly along the orbit. By comparing distributions of the electron density obtained from the TOP and RPT with those of the H^+ and O^+ counts, we can determine the absolute calibration factors for H^+ and O^+ in the mean sense. Figure 63 shows the result of such calibration. It is noted from this figure that the agreement between the PIC data and that of the TOP and RPT is generally satisfactory at lower latitudes, but there is marked discrepancy at higher

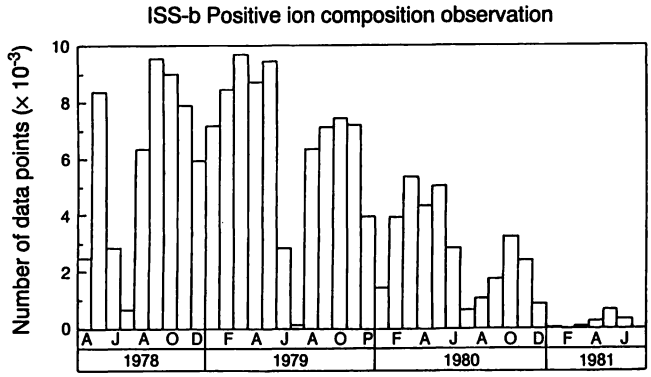

Fig. 64 Distribution of the number of observed points per month.

latitudes, where the density becomes very low. This discrepancy is attributable to the fact that the plasma density measurement by the TOP and RPT becomes less reliable when plasma density becomes lower than about 10^4/cc.

The calibration factors thus determined for H^+ and O^+ are almost the same and to be 1.7 (ions/cm^3)/(ion counts/sample time). From this we can assume that the difference of calibration factors for different ion species is small, so that the same factor is also applicable to He^+. It is also justified because the transmission coefficient of the spectrometer and quantum efficiency of the CEM may not change much due to the change of ion species. The results of this calibration are not inconsistent with the observations from the DE satellite[17] which were made over a similar period to that of ISS-b.

4.4.5 Data Base

All the data included in the 151 volumes of experimenter tapes were analyzed by above procedure and the results were accumulated in the summary file. One data record in the summary file consists of the ion densities of H^+, He^+ and O^+, the orbital and attitude data obtained in the 64-second observation time, and the NmF2 and electron densities at the satellite altitude as deduced from the topside sounder. The distance between adjacent observational points is about 500 km, or 3 degrees in latitude. As shown in Fig. 64, almost consecutive data were acquired for three years duration and the total number of observed points is about 150,000. Although the spatial resolution is not so high, the observational points are distributed fairly uniformly in latitude, longitude and local time. These data are suited for mapping analyses. It is noted here that the summary data of PIC begins from August 1978 while the regular observations started in April 1978. This was because the attitude data had some problems before August 1978. Summary plots prepared from this data base have been published by RRL[99].

Figure 65[100] shows the solar activity corresponding to the period of ISS-b observations. ISS-b was operated just at the solar maximum period, so that the geomagnetic activity was also high. Since ion composition data for solar maximum conditions was rather scarce before the ISS-b experiment, it provided a valuable data source for the solar maximum periods. Figure 66 shows the observations made by many satellites, including ISS-b, during solar cycle 21[101].

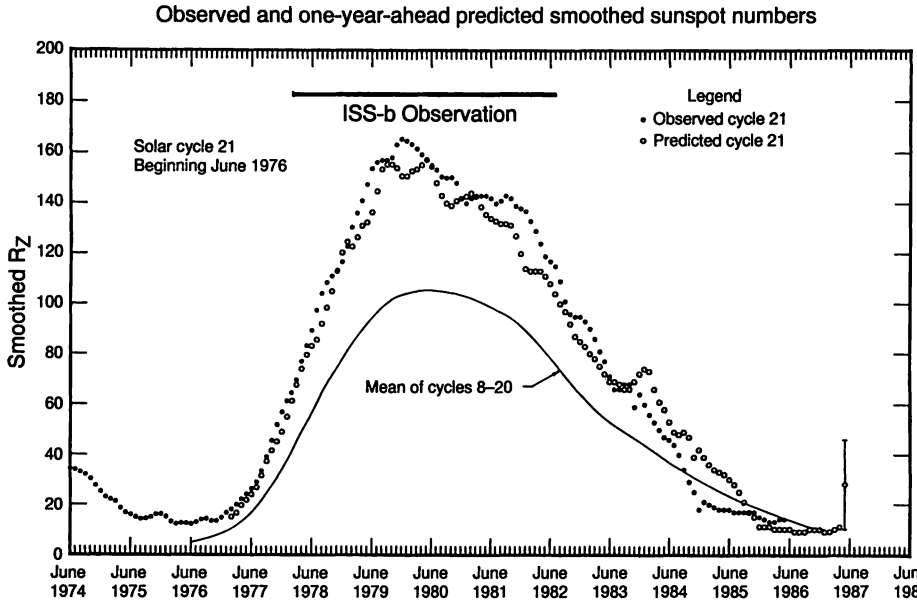

Fig. 65 Variation of sun spot number during ISS-b observations [after Solar-Geophysical Data, 1986[100]].

5. Analyses of global distribution of ions

5.1 Prominent features observed from individual passes

Although the main objective of this paper is directed to statistical analysis of ISS-b data, this section presents the basic characteristics of the ion plots for individual passes.

During the earlier stages of the ISS-b mission, four passes per day were scheduled so as to distribute the observations uniformly throughout the world. Figure 67 shows pass plots of ion densities along the geodetic latitude observed on August 24 and 25, 1978. The graphs aligned in the vertical direction show plots for different longitudes of equatorial crossing. Those on the left show the data of August 24, and those on the right show the data of August 25, for which the respective longitudes of equatorial crossing are almost the same. In ascending passes the satellite goes from south to north, and in descending passes from north to south. The local times when the satellite crossed the equator were about noon and midnight in these periods, and the ascending pass was in the dayside and the descending pass in the nightside.

According to the kp indices shown in Fig. 68, the geomagnetic activity was quiet during the week or so up to and including August 25. The values of solar flux, F10.7, for August 24 and 25 were within 105.0 ±1.0 and hence the variation of these values was small. That is to say that there was no particular geomagnetic or solar event on these two days, and Fig. 67 compares the data obtained on a pair of typical quiet days. The values of longitude and the local time (LT) are roughly shown in the upper and lower parts of each graph. It should be noted that at higher latitudes the local time changes faster for small changes in latitude. Since the difference in local time at particular latitudes on the two days is very small, the variations between the graphs in the vertical column show

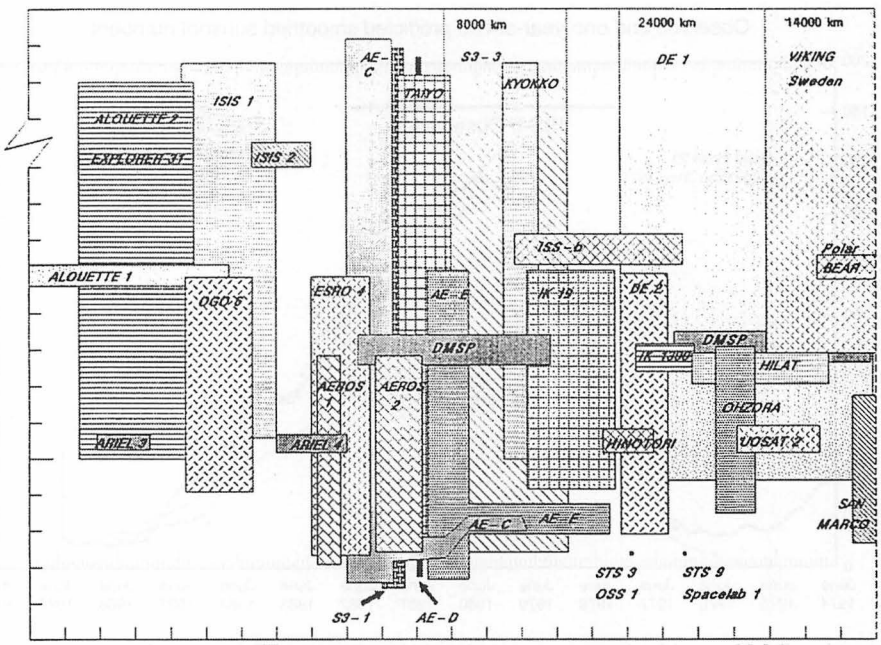

Fig. 66 Data base archived at NSSDC near the period of ISS-b observation [after Bilitza, 1989[101]].

the longitudinal dependence of the ion densities. The difference between the pairs of left and right graphs shows some day-to-day effect because the longitudes are almost the same. Now let us examine the basic characteristics at day and night separately;

5.1.1 Characteristics in the dayside

The first clear feature in the dayside is that O^+ and H^+ are major ion species in the lower latitudes and the density of He^+ is smaller than those of O^+ and H^+ by an order of magnitude. This feature is consistent with the observations by OGO series satellites at the similar altitude rages[102][103].

The second feature is that $[H^+]$ and $[He^+]$ decrease more sharply than $[O^+]$ at middle to high latitudes. This feature is consistent with the earlier observations by OGO series satellites[102][104]. This reflects the fact that the light ion diffuse upwards more easily than heavy ones in the plasmasphere and their densities at high latitude becomes lower since the volume of magnetic flux becomes greater there

The third feature is that we can see a very large longitudinal dependence for different passes made on the same day. The longitudinal dependence seems to be greater for H^+ and He^+ than for O^+. For example, we can see density enhancement of H^+ around -60 degrees of geodetic latitude for the pass starting on 0350 UT (the uppermost graph of Fig. 67), while we cannot observe such a structure at the corresponding position in the other pass on the same day (the pass starting on 0904 UT).

We notice that wavy structures are present mainly in H^+ and He^+ profiles. These are also longitude dependent. We will discuss the average features of the longitudinal dependence in a later section, but here let us examine a little more closely this wavy structure observable in the individual passes because this structure does not appear in the averaged profiles;

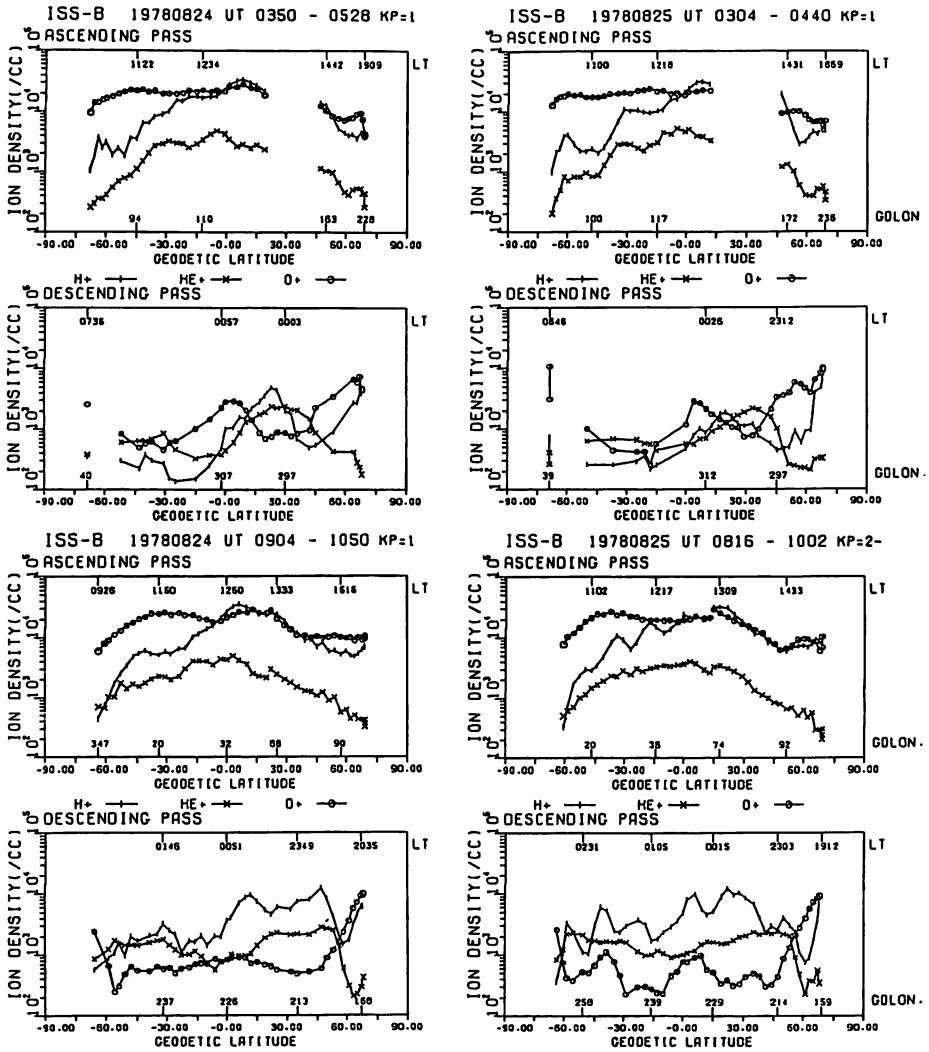

Fig. 67 Pass plot of ion densities on August 24 and 25, 1978. Data of similar longitudes at the equator crossing on the two days are displayed in the left and right panels.

For the pass beginning on 0816 UT, August 25 (the third graph from the top in the right column of Fig. 67), we can see a wavy structure in the H^+ profile, while such a structure is not discernible for the pass of similar longitude on August 24 (the third graph in the left column).

Figure 69 compares the profiles observed on August 26 and 27 in the same way as Fig. 67. We can discern similar wavy structures in the corresponding passes of both days. But these structures are deformed considerably day by day. Thus we can say from these data that the wavy structure continuously existed for about three days at a particular longitude region (around the northern part of South Africa, in this case). We can see similar wavy structures for He^+ profiles, but these are generally of smaller amplitude and do not seem to correlate well with those of the H^+ profiles. As for

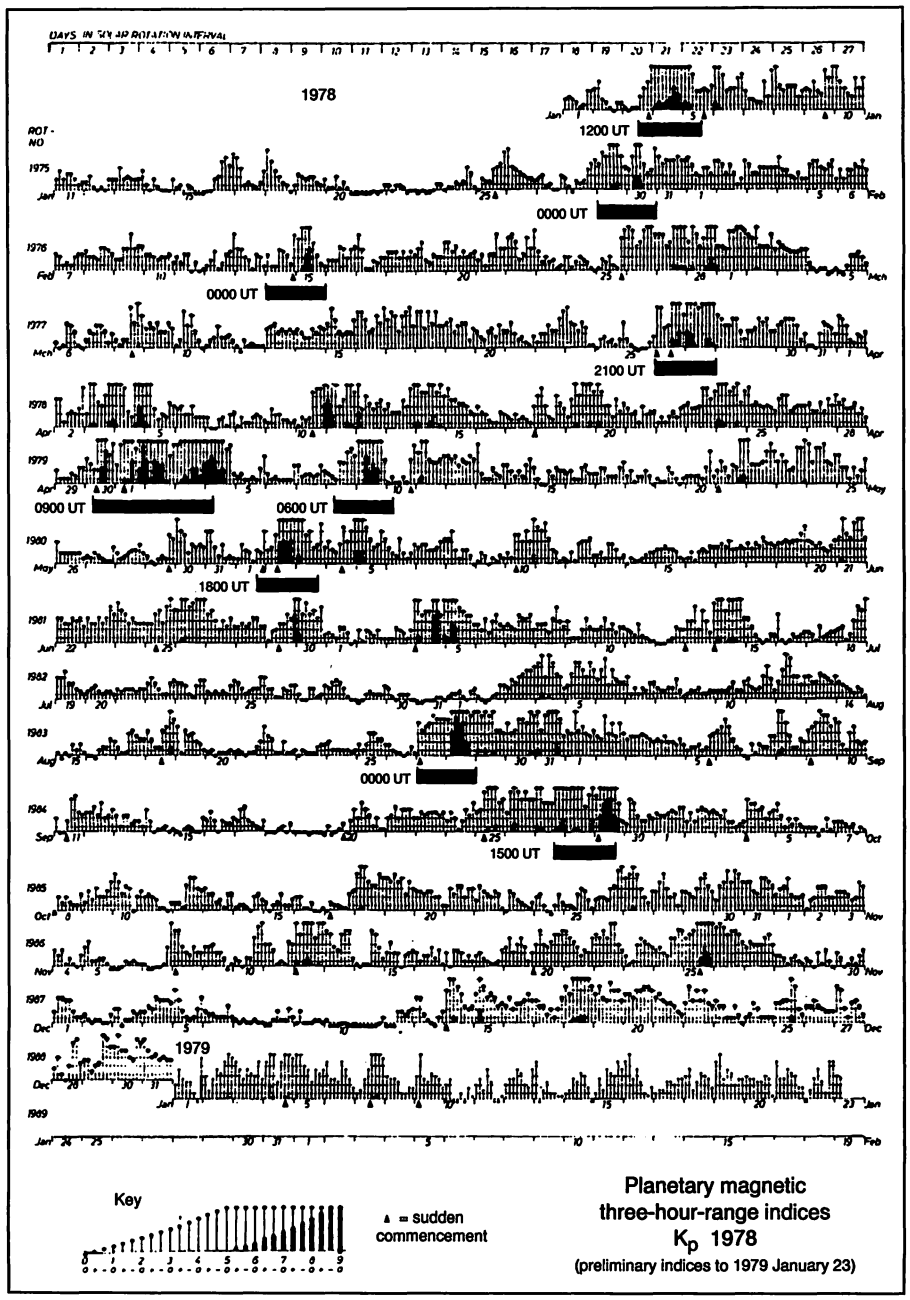

Fig. 68 The geomagnetic activity in 1978.

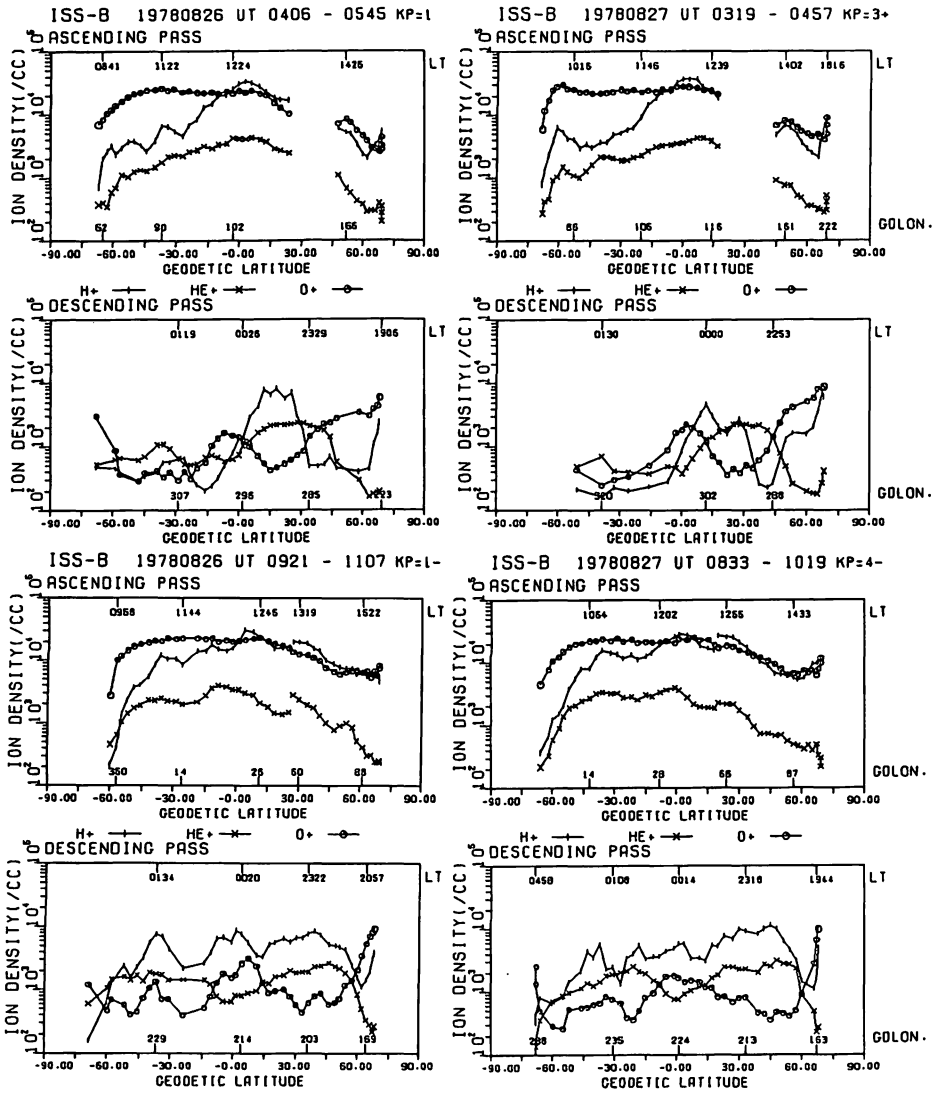

Fig. 69 Comparison of the pass plots on August 26 and 27, 1978.

O^+, we can hardly recognize any wavy structure at all, or the amplitude is very small if any. That is, the wavy structure seems to be mass dependent.

Figure 70 shows examples of quite a regular wavy structure observed on February 2 and February 4, 1979. We can recognize wave structures for both H^+ and He^+ and for both the ascending and descending passes.

It is interesting to note that the amplitudes for He^+ are greater than those for H^+ in this case, and that the phases of oscillation are almost opposite for H^+ and He^+. Inspection of other passes on these two days indicated that the wave structures were present for most of the passes observed. That is, the oscillation seems to have extended all over the world during this period.

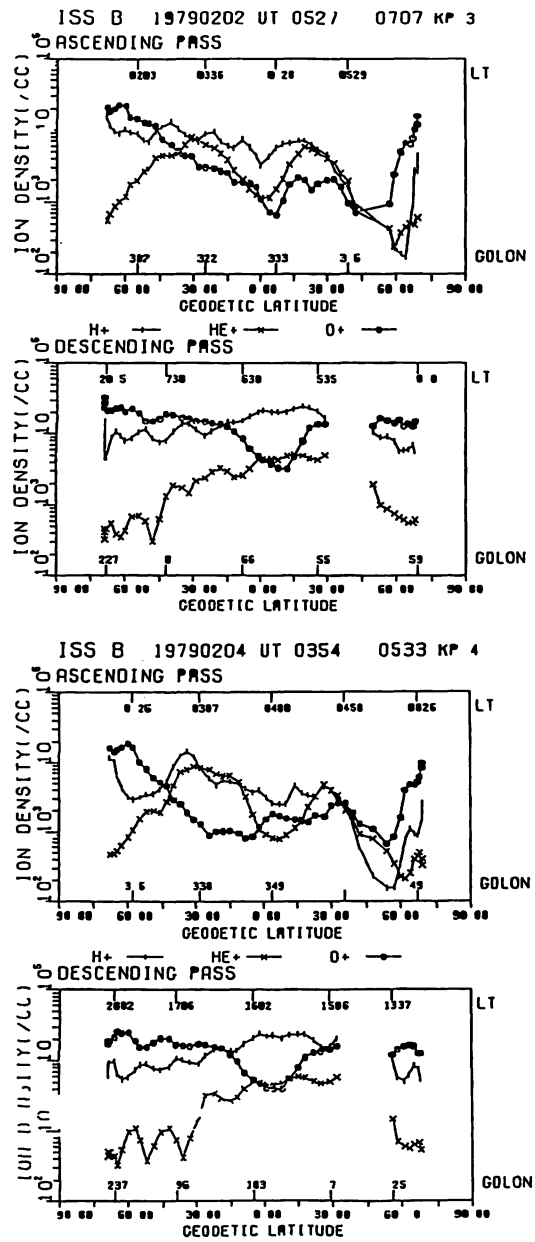

Fig. 70 Wavy structures in the ion density distribution observed on February 2 and 4, 1979 by ISS-b.

More examples of regular oscillation in the H^+ profile are shown in Fig. 71. We can observe sinusoidal oscillation in H^+ profiles for the descending passes which cross the equator at about 170 degrees longitude on both January 24 and 25 (left column). But in the passes which cross the equator

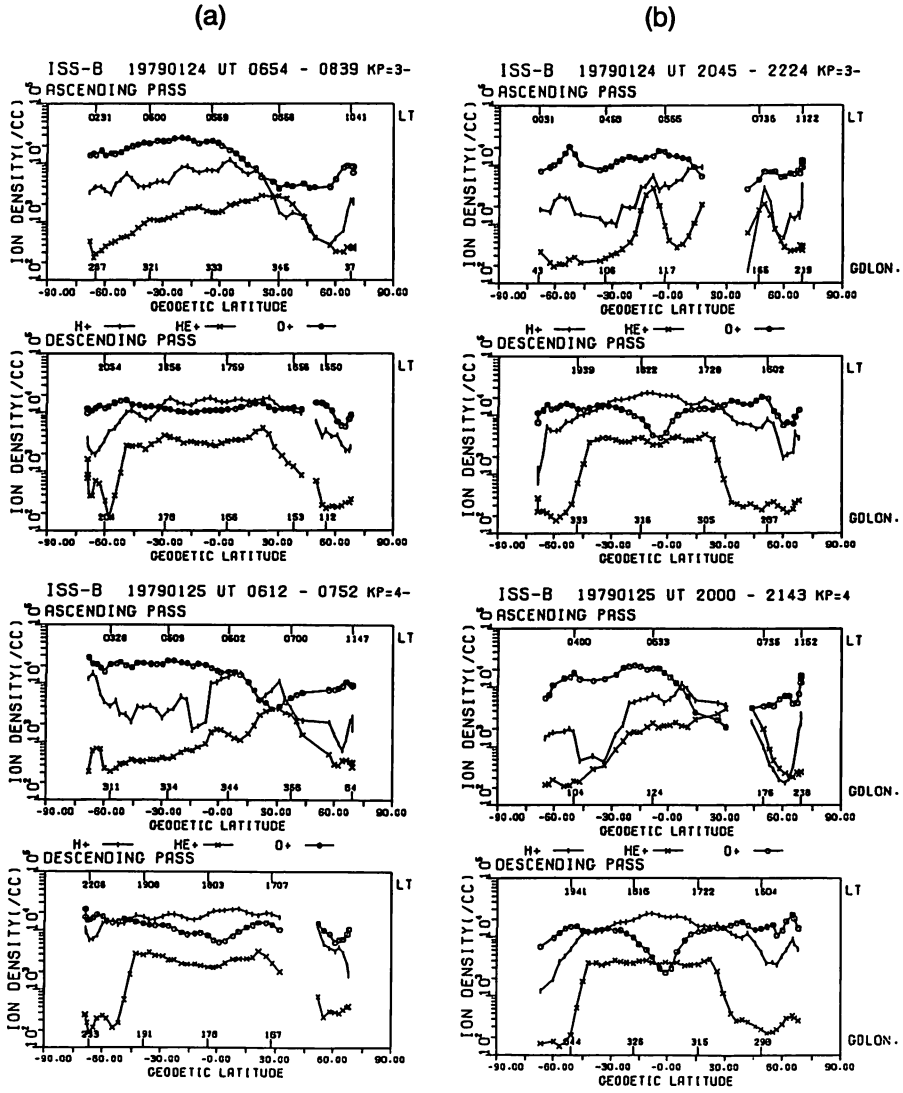

Fig. 71 Comparison of pass plots on January 24 and 25, 1979. (a) Passes of like longitudes for which the wavy structure is seen on the consecutive days. (b) Passes of like longitudes for which the wavy structure is not seen for both days.

at about 320 degrees longitude (right column), we can hardly observe any regular oscillation. In this case the regular oscillation is confined to a limited longitudinal region.

So far, we have not found reports on such wavy structures in ion density profiles. In order to search for the cause of these structures, all the profiles of ion densities from August 1978 to May 1979 were checked visually. The wavy structure exhibited the following characteristics:

1) Its occurrence rate is large for H^+, small for He^+, and very small for O^+. Variations of H^+ and He^+ are generally not in-phase.

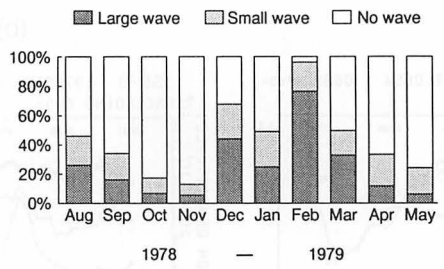

Fig. 72 Occurrence rate of the wavy structure in H^+ distribution during about one year period (August 1978–May 1979).

2) The occurrence rate for H^+ is very large in February as shown in Fig. 72. It seems that the rate depends on season.
3) The maximum amplitude of oscillation is about 30%. It tends to be larger in higher latitude
4) Apparent wave length along the orbit is about 10°–20° in latitude, or 1000–2000 km in distance.
5) It occurs over limited ranges of longitude and continues to exist there for a few days.
6) It is not correlated with the geomagnetic activity

The above characteristics suggest that the cause of the wavy structure is probably due to the oscillation of the neutral atmosphere. Wave-like fluctuations in the neutral constituents were observed by AE-C[105][106] and DE-2[107]. Hedin and Mayr[107] reported that the wave length was 400–4000 km and the amplitudes and phase of the oscillation were different for different species. The relative amplitudes typically change by 6–20%. The variation in helium soon fell out of phase with that of N_2, suggesting most likely source is gravity waves generated by auroral activities. In the case of ISS-b, the altitude is 1100 km so that the gravity waves would not propagate to this altitude directly. However, if the waves modulate the plasmas in the lower ionosphere, say around F2 region, the effect would be transferred along the magnetic field, allowing the wavy structure be detected there. We currently have no further evidence to support this speculation, and it is beyond the scope of the present study. Generally speaking, the effects of the neutral atmosphere have not been well documented[108]. This is an important and interesting area for future investigation, particularly in the STEP program.

5.1.2 Characteristics in the nightside

The descending pass observations shown in Fig. 67 and 69 were made in the nightside, where is seen that H^+ generally dominates over O^+ in lower latitudes. That is, the transition height between O^+ and H^+ goes up and down beyond the 1100 km altitude of ISS-b during this period. The transition height has been reported to be lower during periods of lower solar activity[109]. Another prominent feature here is that the density of He^+ is comparable to those of H^+ or O^+. According to previous studies, He^+ has always been considered a minor constituent in the topside ionosphere[10]. The present study shows that this is not the case, at least during the solar maximum period. We will see later that dependence of averaged [He^+] on solar activity is small, suggesting that it should have relatively high value even during periods of lower solar activity at about 1000 km altitude.

The another prominent feature is that the latitudinal distribution is very irregular and its dependence on longitude seems to be greater than in daytime. However, when we compare the distributions of similar longitudes on consecutive days, we can confirm that similar structures continue to exist, while the profiles measured on the same day but at different longitudes do not

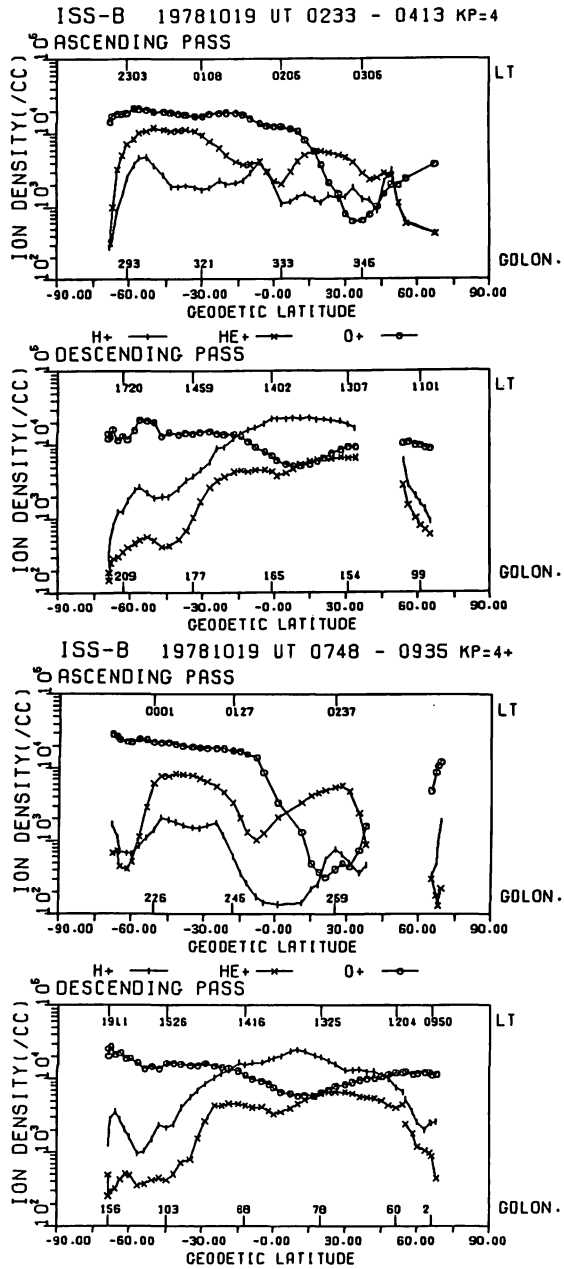

Fig. 73 Comparison of pass plots observed on October 19, 1978.

resemble each other. Inspection of many plots shows that the life time of these structures seems to be a few days. This feature is similar to dayside cases and hence it is very probable that these structures continue to exist through day and night. Unfortunately, however, we cannot confirm this because of the limitation of satellite orbits.

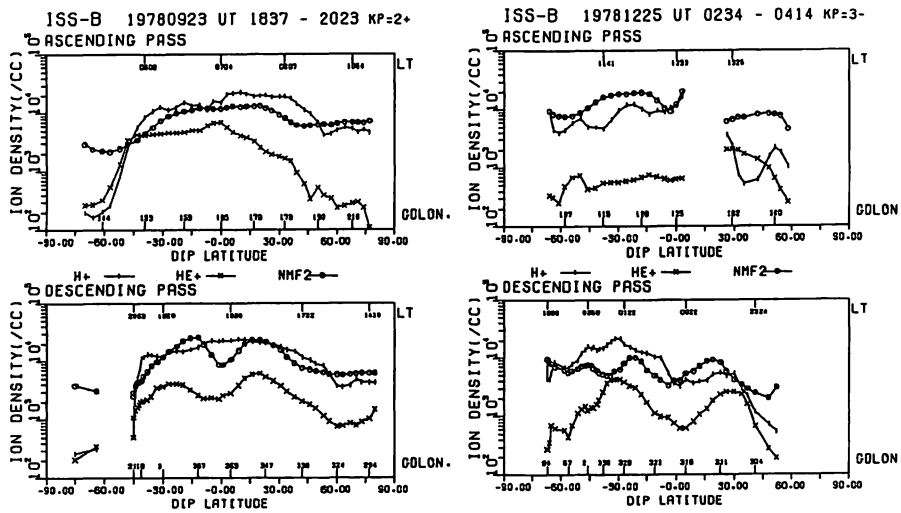

Fig. 74 Comparison of latitudinal profiles of H^+, He^+ and NmF2. Note that NmF2 is multiplied by 0.01 for the convenience of display.

Figure 73 shows two pass plots observed on October 19, 1978, when the ascending passes corresponded to the nightside. The basic characteristics stated above are also confirmed in this figure. For the nightside, we can see that the light ion profiles have a deep equatorial minima, or trough (ET) structure. From inspection of all the plots, it was found that generally the trough is deeper for He^+ than for H^+. Sometimes we can also observe weak ET structures in the dayside, but they are much shallower than those at night. We also notice that the depths of the ETs are different at different longitudes.

The equatorial trough structure in [He^+] was first pointed out from the OGO series satellite observations[103]. To the author's knowledge, nobody has yet been able to fully explain why these structures are formed. As a representative nighttime structure, let us take a closer look at ETs in the following:

5.1.3 Equatorial troughs of He^+

Examination of many pass plots of ISS-b shows that ETs in He^+ density are persistently observed at night, and that they are very similar to the equatorial anomaly in NmF2. Typical examples are shown in Fig. 74. The NmF2 data were obtained from the TOP experiment on ISS-b and are multiplied by 0.01 for convenience of display. Dip latitude is used in this figure and it is clearly seen that both [He^+] and NmF2 reach minima at the dip equator. However, the distance between the crests is wider for He^+ than for NmF2. The same features are generally observed for other passes. Examination of all the passes between September and December, 1978 revealed that for 93% of the passes in which the equatorial anomaly in NmF2 can be identified, we can also identify ET in [He^+]. It has been well known that "the fountain effect" due to E × B produces the equatorial anomaly in NmF2 and results in a single peak in electron density at the topside ionosphere[110]. It is very peculiar that ETs exist in [He^+] distributions but not in the major constituents, H^+ and O^+, unlike the equatorial anomaly

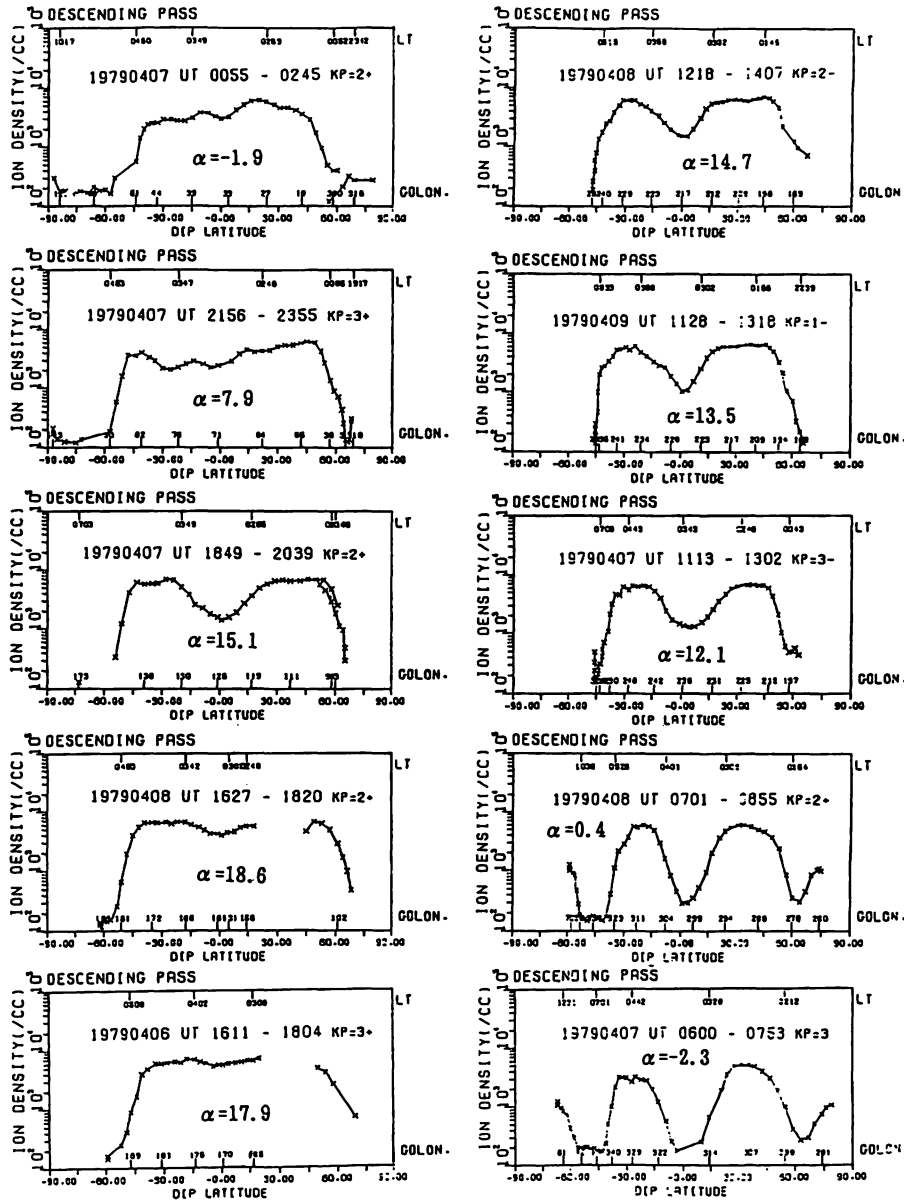

Fig. 75 Longitudinal dependence of the equatorial He^+ trough. The profiles observed between April 4 and 6, 1979 are sorted according to respective longitudes of equator crossing. The angle between sun-earth line and the geomagnetic equatorial plane is denoted by α.

As shown in Figs. 75 to 79, ETs in [He^+] has very large longitudinal dependence. In Fig. 75, the pass plots observed from April 3 to 6, 1979 are reordered with respect to the longitude of equator crossing. The local times at the equator crossing are within 03–04 hours. In the panels on the left side

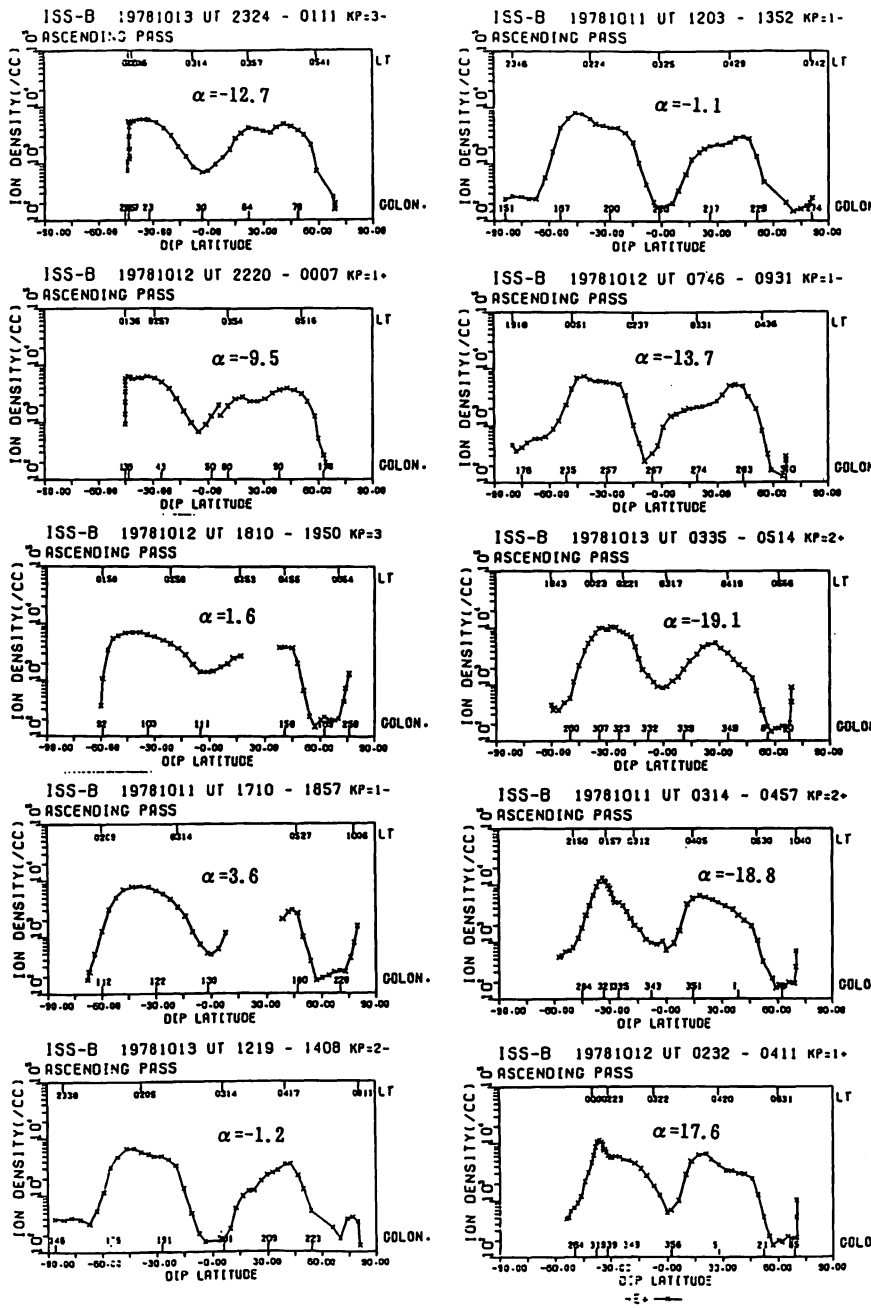

Fig. 76 The same as the previous figure but profiles are observed between October 11 and 13, 1978.

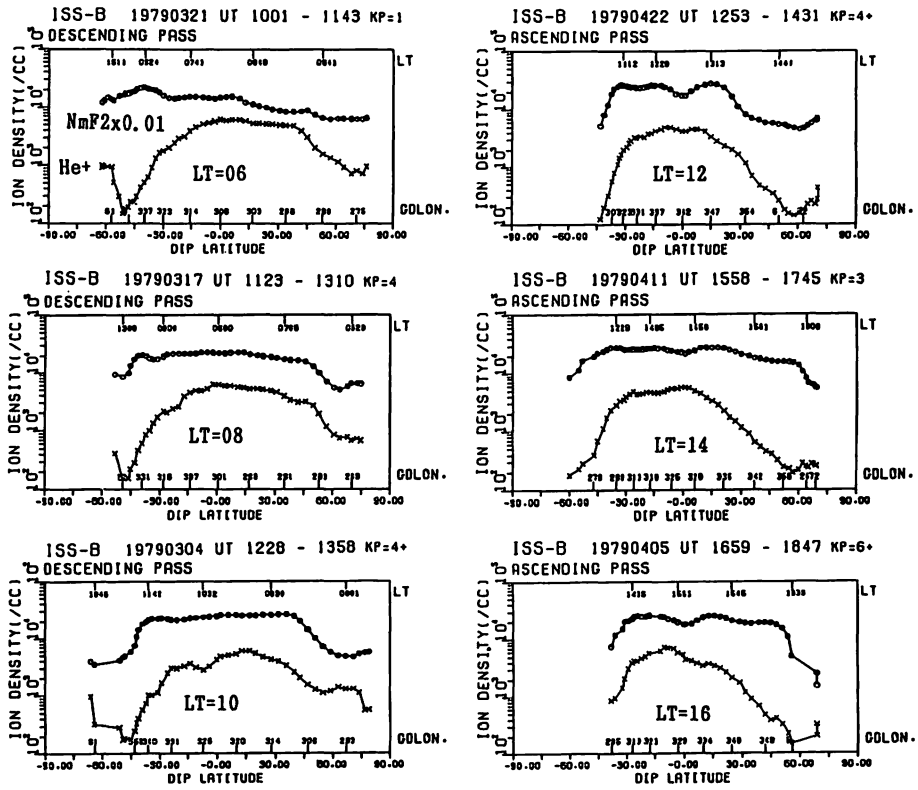

Fig. 77 LT dependence of the equatorial He^+ trough around 300 degrees in longitude at the equatorial crossing, for daytime case. The local time at the equator changes about two hours for each panel. See text for details.

where the longitude is 30–170 degrees, the ETs are very shallow, while in the right side panels where the longitude is 217–320 degrees, the ETs are deep and reach a minimum depth at about 320° longitude. The density at the deepest trough is an order of magnitude less than that of the crests.

These examples were selected somewhat arbitrarily, but such features are commonly observed in particular periods. In Figs. 75 and 76 the angle between the sun-earth line and the plane of geomagnetic equator is shown by α. Significance of this angle is discussed later in this section.

Figure 76 shows the pass plots with similar LTs at the equatorial crossing observed during October 11–13, 1978. In this example, the longitudinal dependence is smaller than before and the maximum trough appears at 200–210° longitude. Figures 77 and 78 show pass plots of He^+ and Nmf2 which illustrate the dependence of ET on LT for the passes which cross the dip equator at about 300 longitude, where the troughs seem to maximize during the period around April 1979.

Similarly Fig. 79 shows dependence of ET on LT for the passes which cross the equator at 100–180 longitude, where the trough seem to minimize during the same period. It should be noted that a period of about two months is necessary for the LT at a fixed latitude to change by 24 hours. In this figure, the ET in [He^+] begins to appear at 18 LT, it maximizes at 00–03 LT and it disappears at about 06 LT. On the other hand, for NmF2 the anomaly begins around 12 LT, maximizes at 22 LT and disappears at 06 LT. There is apparent delay of several hours between ET in [He^+] and the equatorial anomaly in NmF2. Thus according to the comparison of individual pass plots, we can see a very

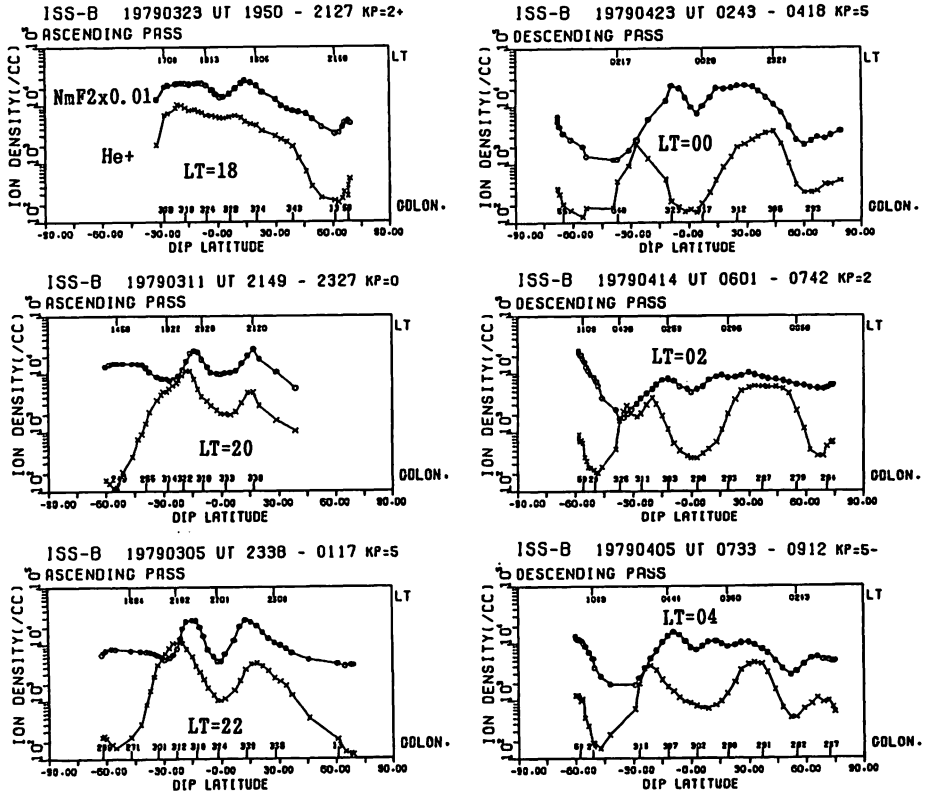

Fig. 78 The same as Fig. 77, but for nighttime case.

close resemblance and slight differences between ET in [He^+] and the equatorial anomaly in NmF2. We will investigate these features more closely by statistical analysis in the next section.

5.1.4 Correlation with geomagnetic activity

The observation period between August 24 and 26, 1978, shown in Figs. 67 and 69, corresponded to a geomagnetically quiet period lasting for about one week, and ending with a SC at 04 UT on August 27. As shown in Fig. 69, *Kp* began to increase at about 08 UT and reached a maximum value of 8- at 11 UT on August 28. Figure 80 shows the data on August 28 and 30 (observation not done on August 29). Let us examine the data in time sequence after 0833 UT, August 27. Little appreciable variation can be seen for the pass beginning at 0422 UT on 28 compared to the previous pass, but for the pass beginning at 1157 UT on 28 when *Kp* was maximum of 8-, [H^+] is depleted much at higher latitudes and latitudinal cutoff is very sharp. For the passes on 30, [H^+] looks almost recovered the quiet time values while the geomagnetic activity was still higher (*Kp* = 4+). Compared to H^+, O^+ and He^+ show not much variations.

Figure 81 compares scatter plots of the densities of three ion species during a quiet period (August 20–27) and disturbed period (August 28–September 3). In the disturbed period, [H^+] decreases very notably in the southern hemisphere. It is noted, however, that the scatter of data points is larger in the quiet period than in the disturbed period. This scatter may be due to longitudinal

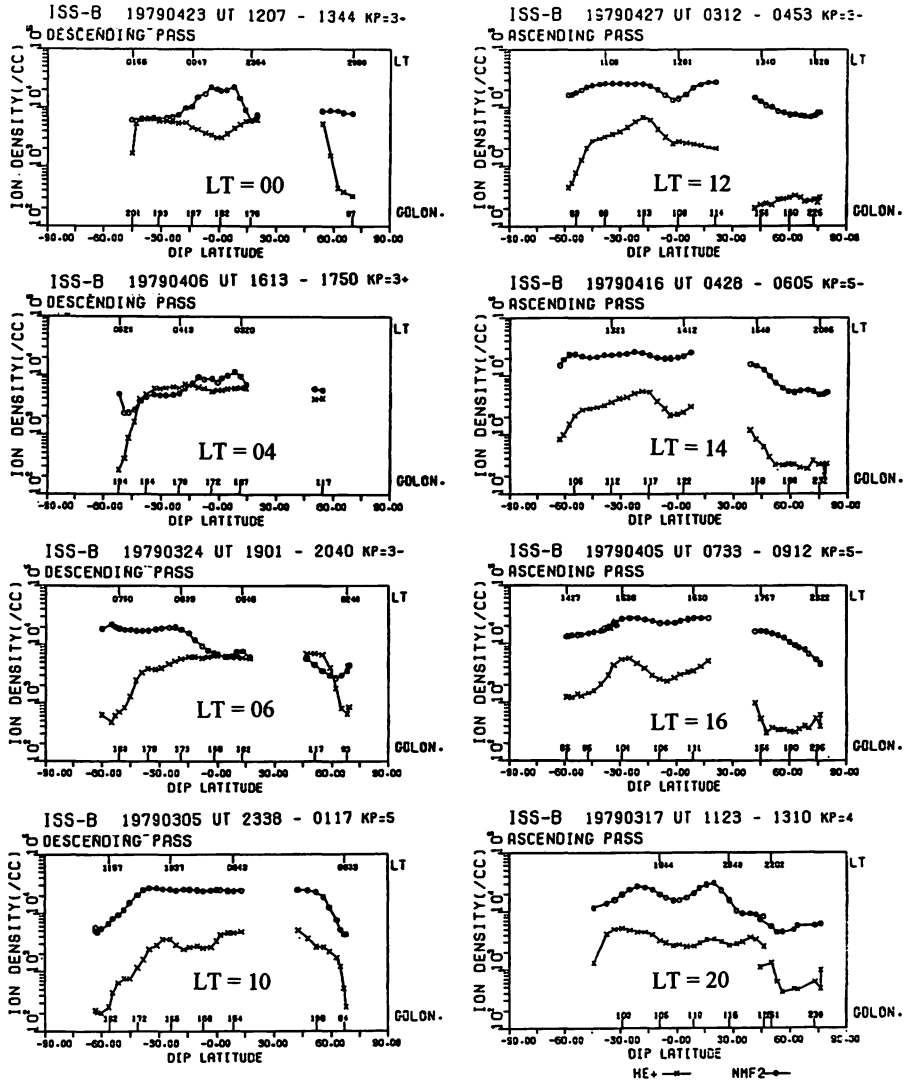

Fig. 79 The same as the previous figure but the longitude at the equator is between 100 and 180 degrees for each panel.

variations as seen before. Fukao et al.[111] pointed out by IS radar observations that the nighttime H^+ concentration at 500 km over Arecibo had strong anti-correlation with *Kp*-index. Present observation seems to be consistent with that study, but more careful treatment may be needed to confirm it. For He^+, the scatter of data is larger for the disturbed period than for the quiet period contrary to H^+ case. As for O^+, we notice there are slight density increases at night in the lower latitudes (descending pass) during the disturbed period.

Thus, when we look at individual passes carefully, variations in ion densities are noticeable. However, as described later, multi-parameter regression analysis of ISS-b data did not give consistent dependence on *Kp*-index except for higher latitudes. Dependence of the light ion trough on *Kp* is discussed in the next section.

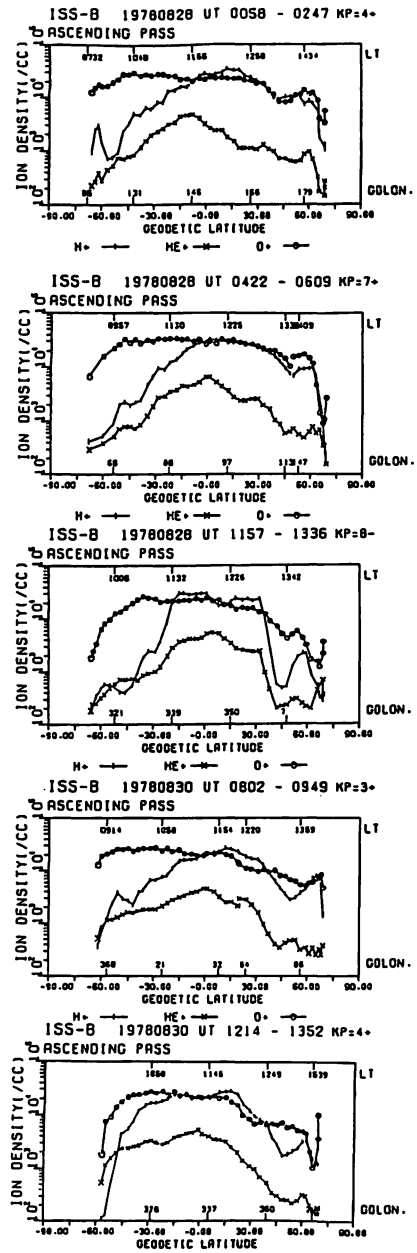

Fig. 80 Comparison of pass plots on August 28 and 30, 1978 when *Kp* index became very large.

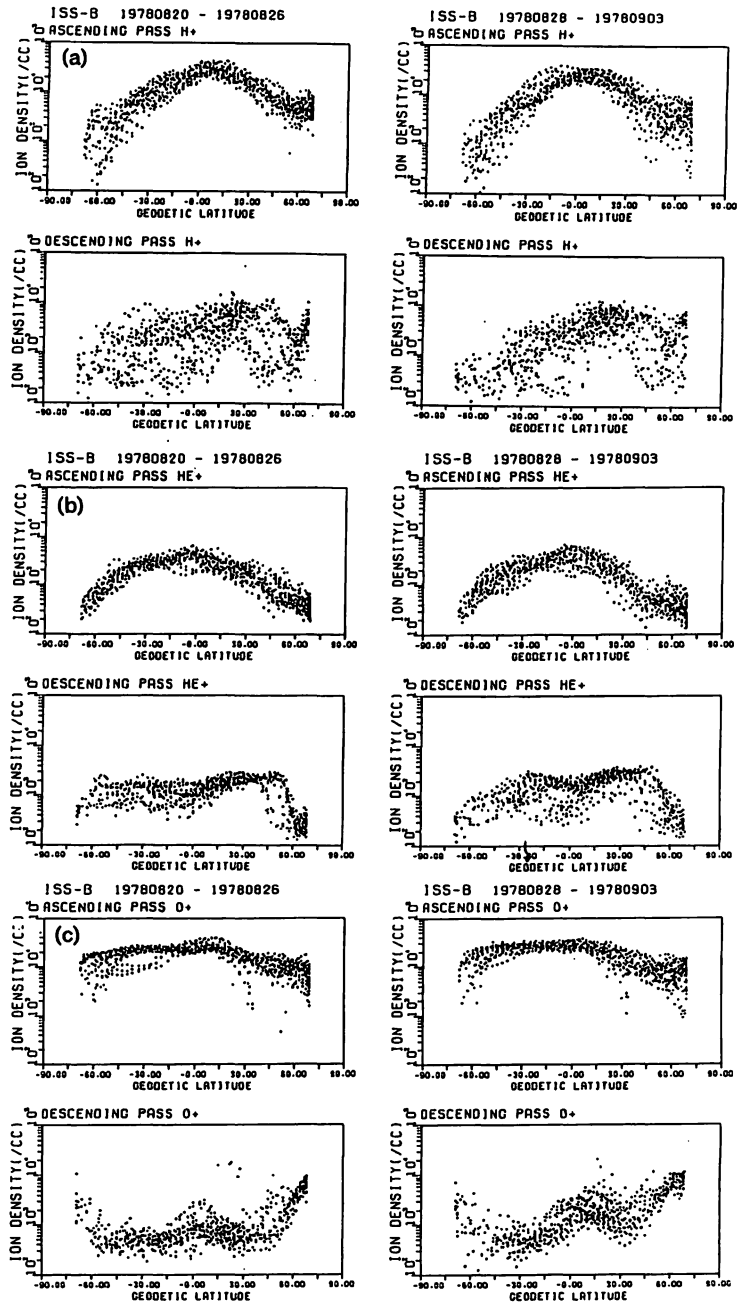

Fig. 81 Comparison of the scatter pass plots between geomagnetically quiet (August 20–26, 1978) and disturbed (August 28–September 3, 1978) periods. (a) H^+ (b)He^+ (c)O^+

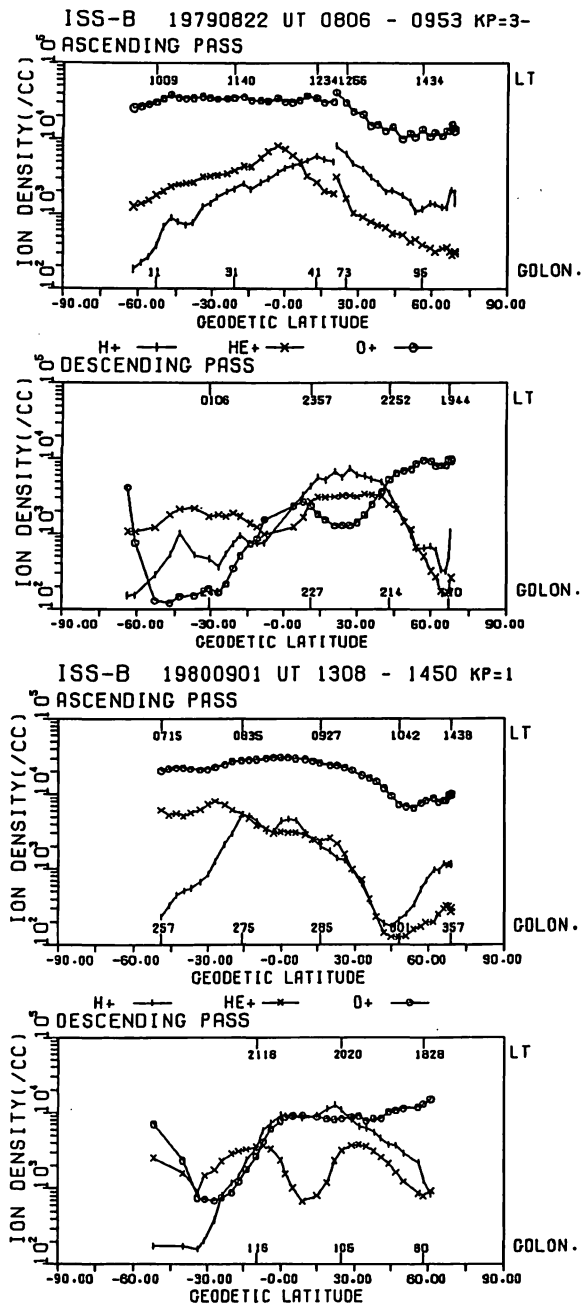

Fig. 82 Examples of pass plot on the date about one year and two years after that of Fig. 67.

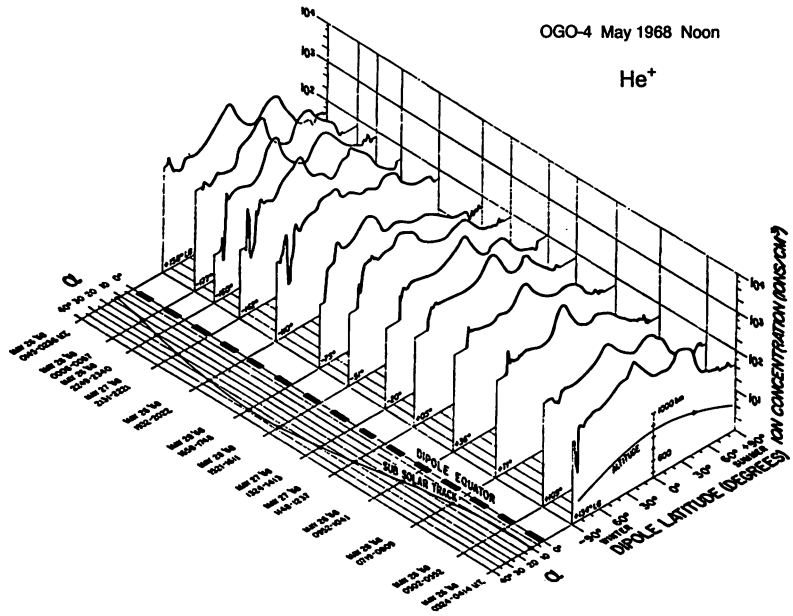

Fig. 83 Distribution of the He^+ observed by OGO-6 showing the pronounced latitudinal variation [after Taylor et al., 1971[13]]. The angle α is defined as the angle between the sun-earth line and the plane of geomagnetic equator when the satellite cross the geomagnetic equator.

5.1.5 Year-to-year changes

Figure 82 shows the data observed in August 1979 and August 1980, one year and two years, respectively, after the period shown in Fig. 67. Since the period of the full diurnal cycle was almost exactly four months and the relationship between the subsatellite latitude and local time is almost the same for every year, very similar profiles are reproduced every year for the three ion species. It is noted that in 1979 and 1980, $[O^+]$ increased and $[H^+]$ decreased while $[He^+]$ did not change appreciably compared to 1978. These differences can be attributed to the solar activity, which is verified statistically in the later section. Statistically meaningful data were obtained for a period of three years. From these data, the dependence of ion densities on solar activity has been obtained. The durations of ion observations by previous satellites, such as OGO or ISIS series, are not so long compared to ISS-b. This is a unique feature of the ISS-b observations.

5.1.6 Comparison with other satellite observations

Before the ISS-b mission, the OGO series satellites (-2, -4 and -6) and ISIS-2 observed the ion composition in the topside ionosphere. In particular, the OGO series carried Bennett ion mass spectrometers of the same type as that on ISS-b, and observations by these satellites revealed basic characteristics of the topside ion composition which had not been known before.

Unlike ISS-b, however, the OGO orbits were not circular; for example, the altitude of the OGO-6 satellite changed between 400 and 1100 km. Consequently, statistical analysis of its data might be rather difficult, and no such analysis has been reported so far.

A typical example of He^+ distribution obtained from OGO-6 is reproduced in Fig. 83 from Taylor et al.[13]. Although it should be noted that the change of LT along the satellite pass is smaller for OGO-6 than for ISS-b because the inclination is 80 degrees, we can confirm that the basic characteristics of the distribution are essentially similar to the results of ISS-b observations. The angle between the sun-earth line and the plane of the geomagnetic equator, is shown in the figure. This angle was named as the "solar geomagnetic season" [103][112] and they emphasized that this angle characterizes the longitudinal variations of ion distribution.

That is, they claim that the latitudinal distributions are similar for similar values of α and vice versa for unlike values of α, thus α should correspond to the seasonal angle. For example, as for the equatorial trough (ET) of He^+, they report that when α is negative, which means the solar geomagnetic season is winter, the trough is shallow and wide, but when α is positive (geomagnetic summer), the trough is deep and narrow. They also emphasize that this feature is maintained as long as α takes similar values even if the real (geographic) season changes.

5.2 Analyses by LT-MAP

As discussed in the previous section, the ion densities in the topside ionosphere depend upon the latitude, longitude, local time, season, solar activity, geomagnetic activity and possibly other factors.

Since the ISS-b mission lasted for three years, it provided a useful data base that makes it possible to analyze the variations due to various factors. One of the most basic distributions is in the latitude-longitude plane, or world maps. A world map produced from the data of constant UT is called as UT-MAP. It represents the instantaneous world distribution of ion density.

On the other hand, a map which is produced from the data of constant local time is called an LT-MAP. An LT-MAP represents the pattern which can be observed when the ionosphere is viewed from a fixed LT angle for one earth rotation.

LT-MAPs of the ion densities for the periods between October 1978 and August 1979 were published by RRL[113]. The procedure to produce an LT-MAP is as follows;

The observed data selected by a prescribed condition are fitted to the following spherical expansion by the least squares method[11].

$$F(\lambda,\phi)=\sum_{m=0}^{M}\sum_{n=m}^{N}[A_{nm}P_n^m(\cos\theta)\cos m\phi+B_{nm}P_n^m(\cos\theta)\sin m\phi] \quad \text{..... (113)}$$

where

λ geodetic latitude

ϕ geodetic longitude

P_n^m associated Legendre function

θ corrected co-latitude,

$$\theta=\cot^{-1}[I(\lambda,\phi)/\sqrt{\cos\lambda}] \quad \text{..... (114)}$$

I dip angle of the geomagnetic field.

The corrected co-latitude, which was introduced by Jones et al.[114], is parallel to the constant dip angle in the low latitude and its poles coincide with those of the geodetic one. The coefficients A_{nm}

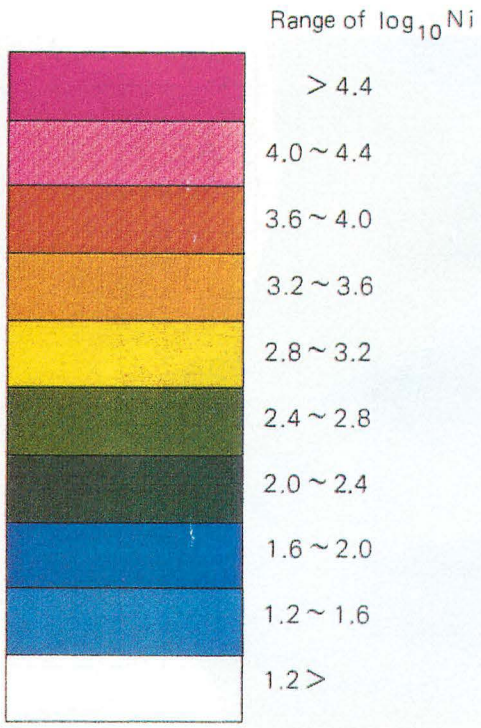

Fig. 84 Color charts for global maps.

and B_{nm} are to be determined by the least squares method. In this analysis, n = 9 and m = 2 are used. As for the geomagnetic activity, the data obtained during the period when *Kp* is less than or equal to 4+ are used.

5.2.1 LT-MAP of H^+

Figures 84, 85, 86, 87 and 88 show LT-MAPs of H^+ from LT = 00 to 18 hours for the period between October 22, 1978 and February 22, 1979. This period corresponds to the winter season for the northern hemisphere.

Figure 85 shows the distribution for LT = 00 hours. If the ion distributions were determined solely by geographic factors, such as latitude, season and solar zenith angle, there would be no longitudinal dependence and the contours would be horizontal. Of course this is not the case as evident from the figure. It is natural to consider that the outstanding longitudinal dependence is primarily due to the geomagnetic effect. It is noted that there is a very strong asymmetry between the northern (winter) and southern (summer) hemispheres. In the northern hemisphere there are two low density regions over Europe and the Pacific Ocean and two high density regions over east Asia and the Atlantic Ocean. On the other hand in the southern hemisphere there is one low density region over the South Indian Ocean and one high density region over South America. Let us pursue this distinct longitudinal dependence. The above noted characteristics are maintained in the maps for LT = 02 and LT = 04 hour, although these are not quoted here (see Hakura, 1982).

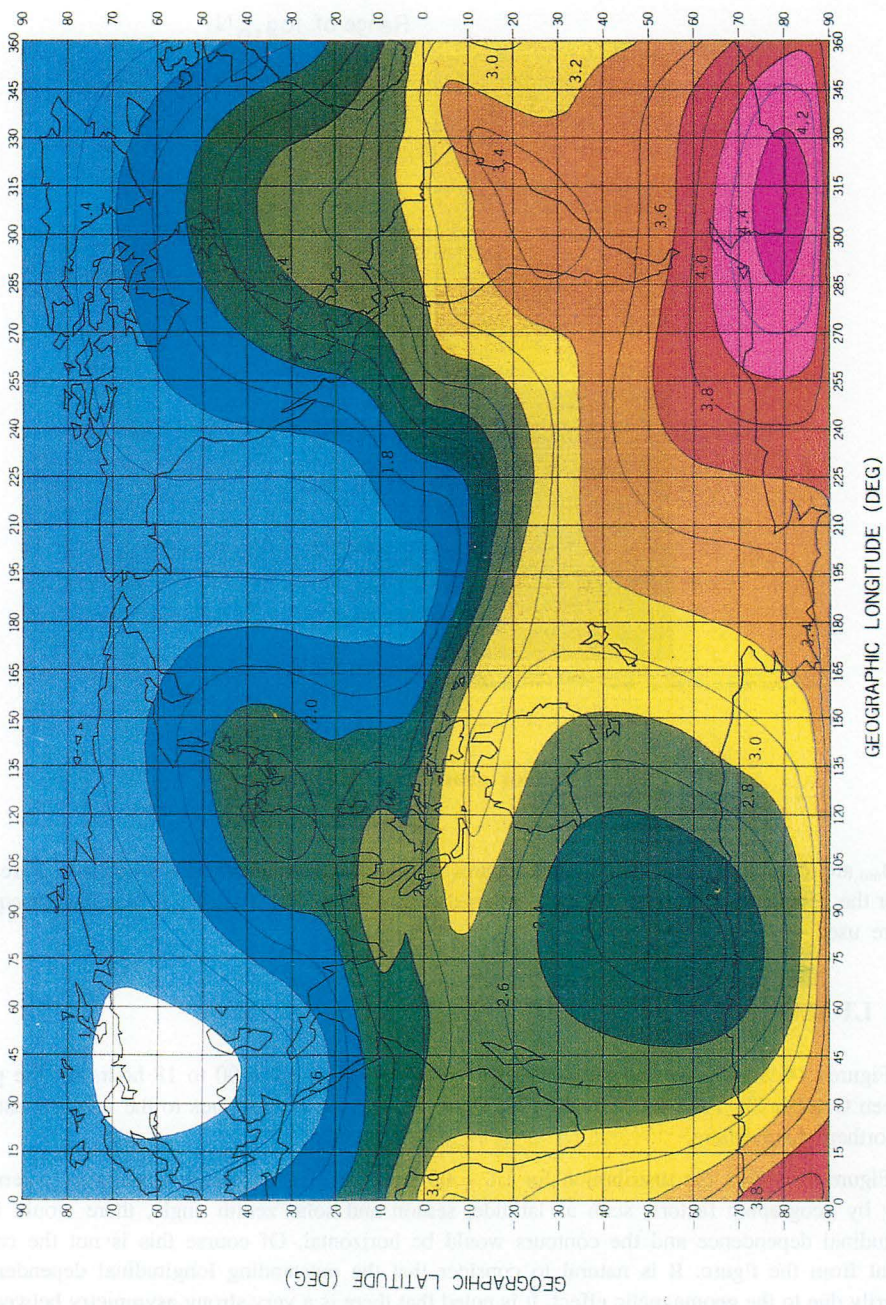

Fig. 85 LT map of H^+ density for LT = 00 hr. during northern winter.

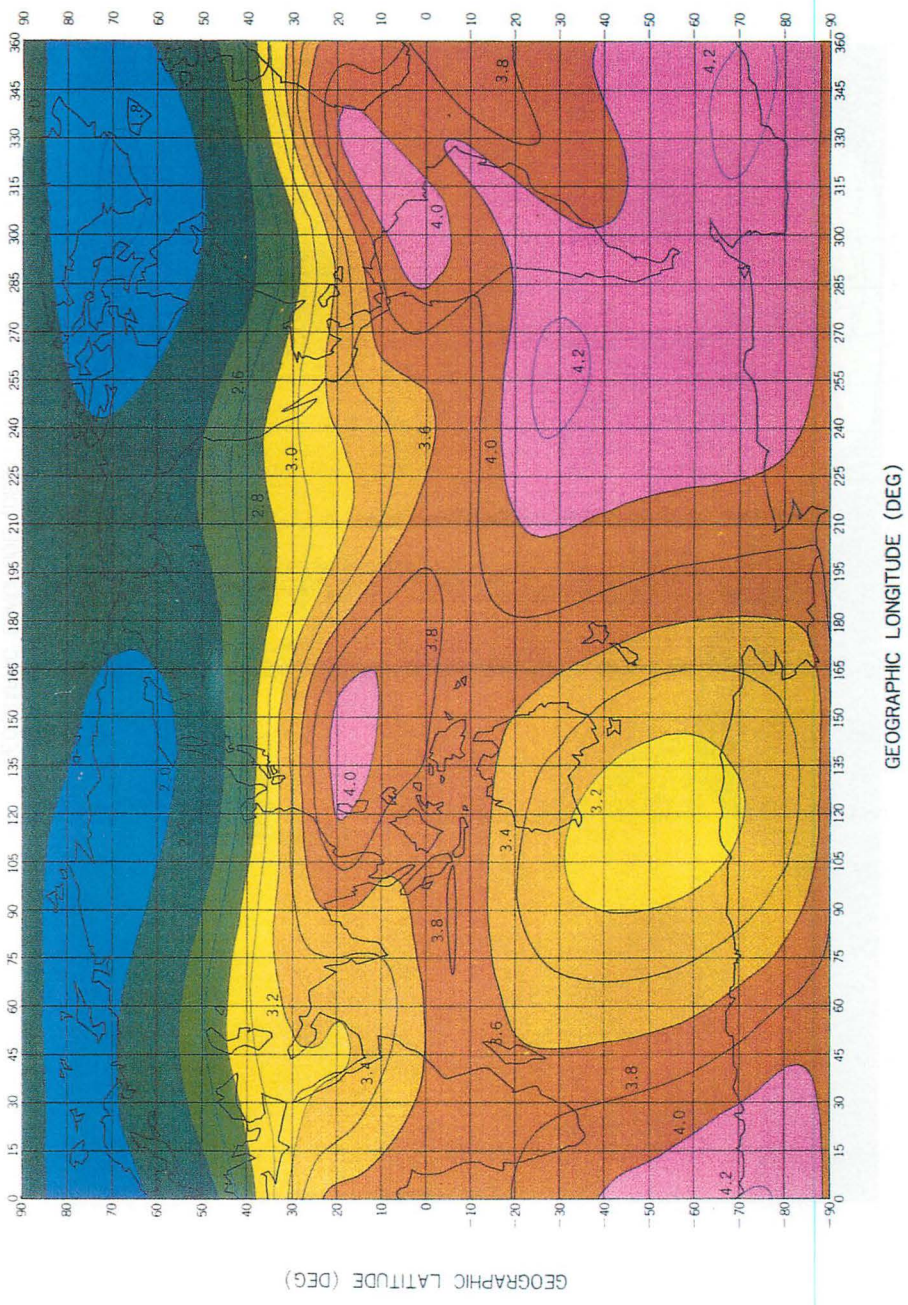

Fig. 86 LT map of H^+ density for LT = 06 hr. during northern winter.

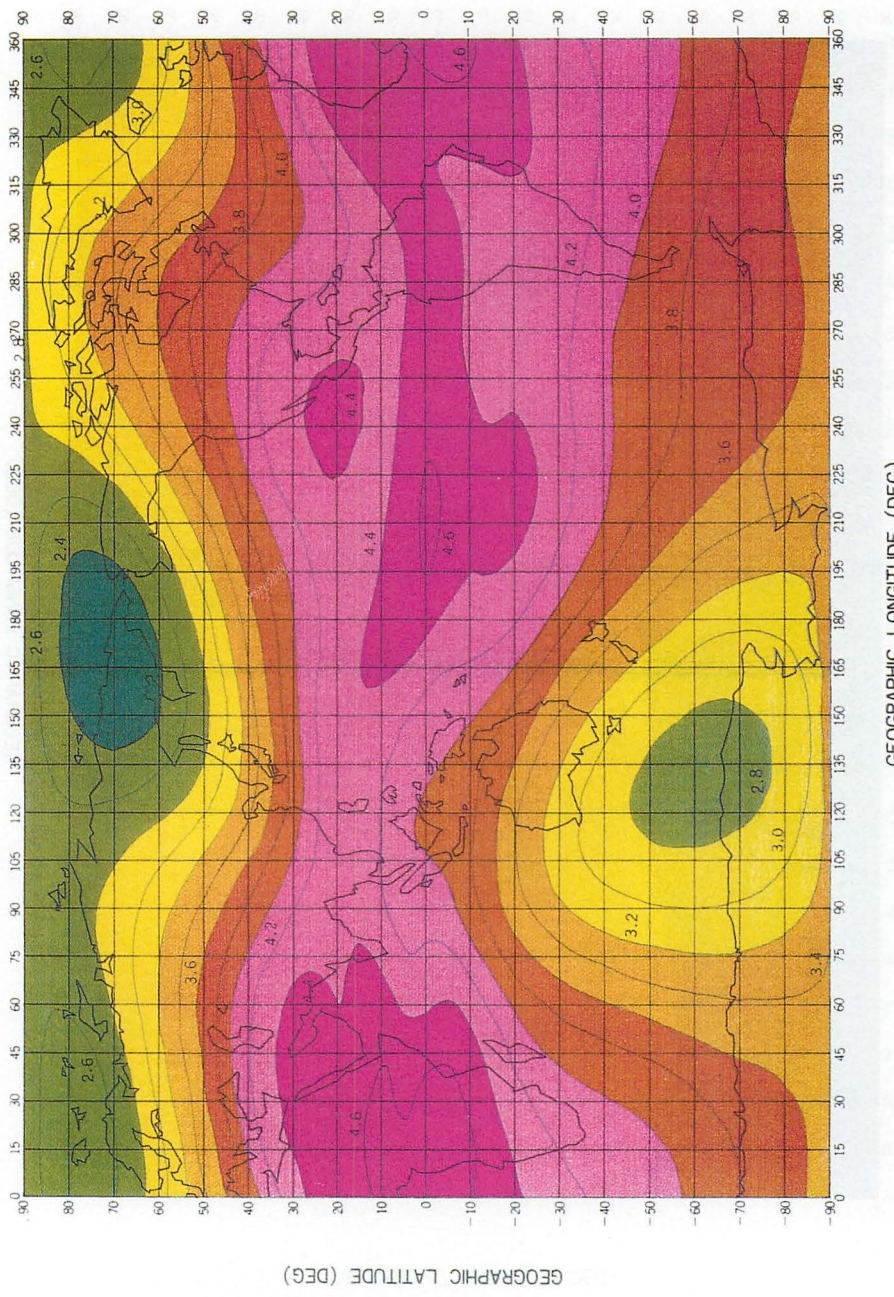

Fig. 87 LT map of H^+ density for LT = 12 hr. during northern winter.

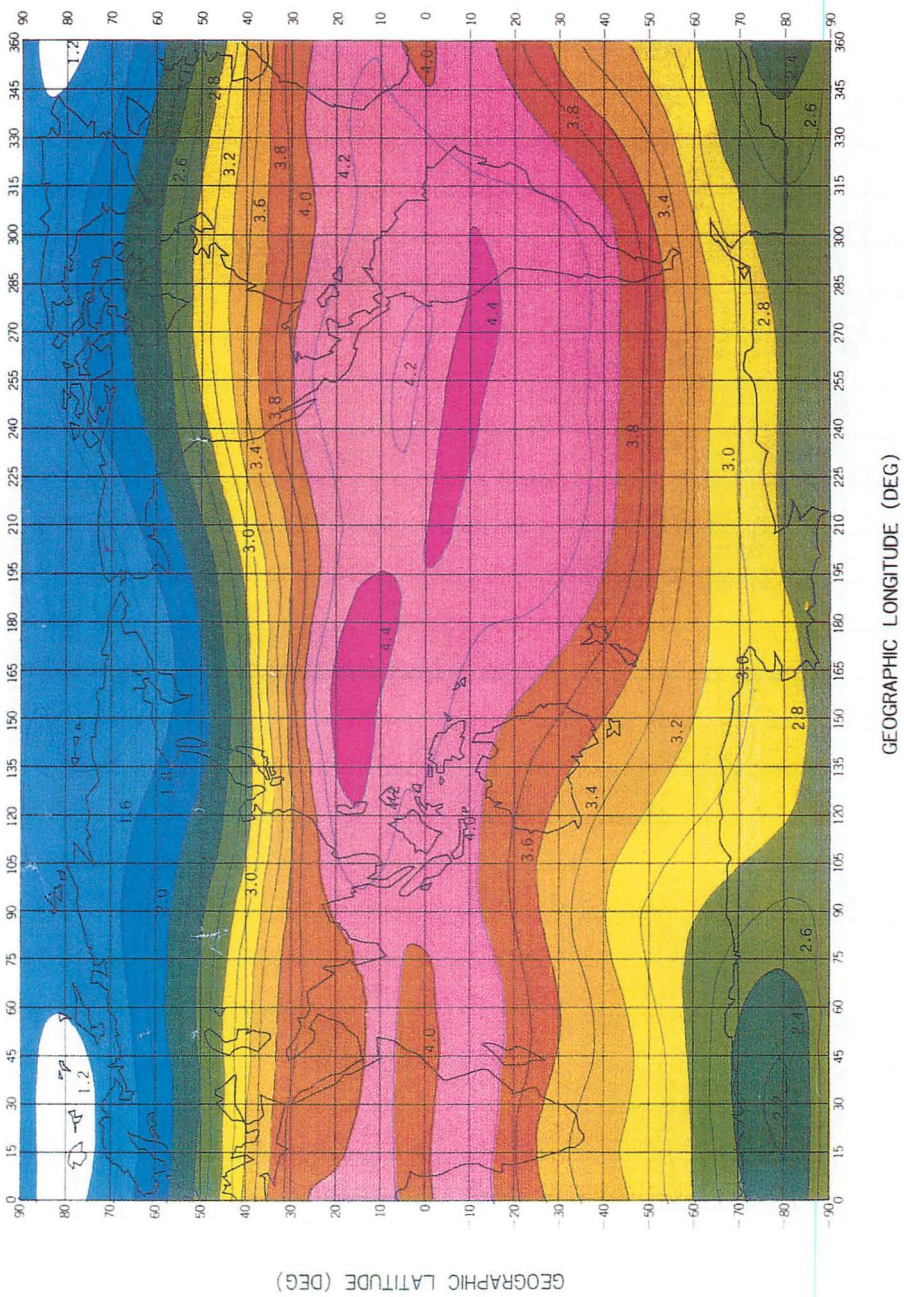

Fig. 88 LT map of H^+ density for LT = 18 hr. during northern winter.

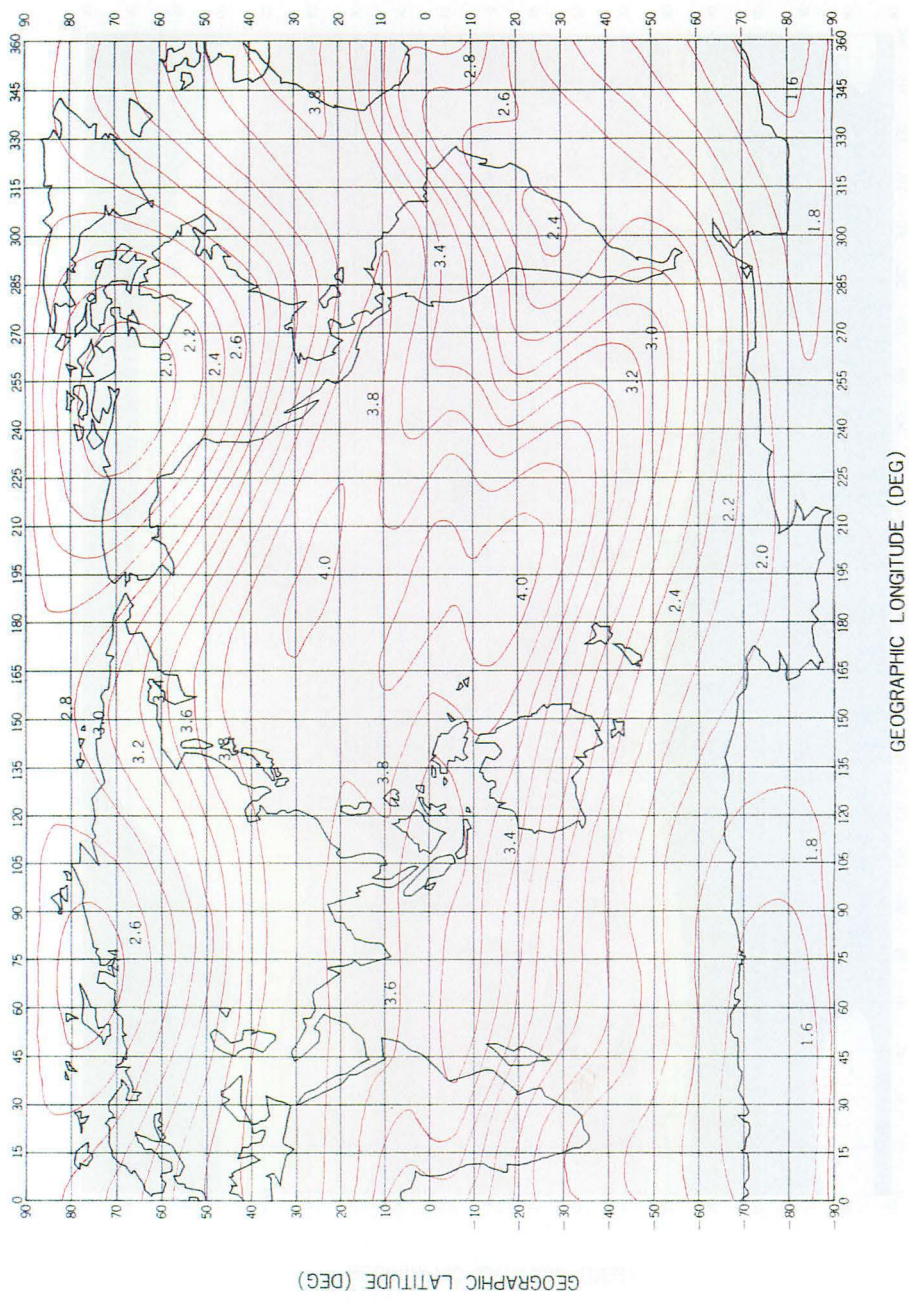

Fig. 89 LT map of H^+ density for LT = 00 hr. during northern summer.

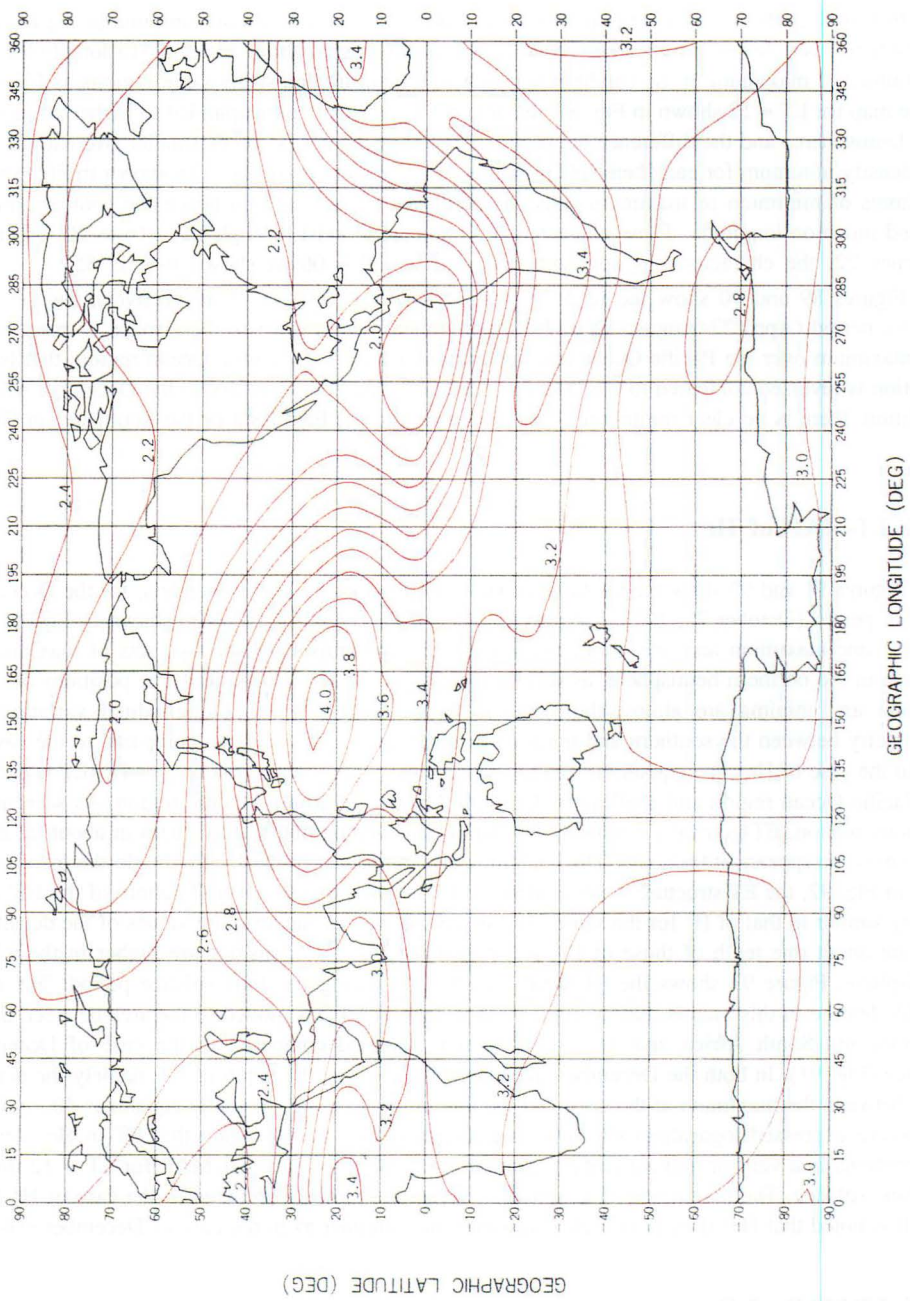

Fig. 90 LT map of H^+ density for LT = 12 hr. during northern summer.

In Fig. 86, which displays the map for LT = 06 hours, the two density minima in the northern hemisphere have almost disappeared and the maxima still exist at about 135 and 315 longitudes. The minimum and maximum in the southern hemisphere remain in almost the same regions as LT = 00. In the map for LT = 12 shown in Fig. 87, the areas of high density are expanded to higher latitudes in both hemispheres and the difference between the two hemispheres becomes smaller. We can also see one density minimum for each hemisphere in this case. In the map for LT = 18 shown in Fig. 88, the structures of minimum or maximum cells can hardly be recognized and hence the contours do not depend much on longitude. These characteristics continue to exist through LT = 16 to 20. When LT becomes 22, the characteristics approach that seen at LT = 06 as shown in Fig. 85.

Figures 89 and 90 show the LT-MAPs of H^+ for LT = 00 and 12, respectively, for the June solstice period (April 22–August 22, 1979). A prominent feature seen in these maps is that there is one maximum over the Pacific Ocean and one minimum over the Atlantic Ocean region, that is, the situation is reversed compared to the December solstice condition. Contrary to the December solstice condition, there is no clear minimum or maximum in Europe, East Asia or the South Indian Ocean area.

5.2.2 LT-MAP of He^+

Figures 91 and 92 show the LT-MAP of He^+ for LT = 00 and 12, respectively, for the December solstice period (October 22, 1978–February 22, 1979). Firstly as for LT = 00 shown in Fig. 91, we can see one maximum and one minimum in the southern hemisphere and two sets of maxima and minima in the northern hemisphere, as seen in the case of the H^+ distribution. The positions of these maxima and minima are almost the same as those for H^+, but the longitudinal variations or asymmetry between the southern and northern hemispheres are not so large compared to the case of H^+. In the case of He^+, the equatorial trough (ET) is clearly seen while it is not for H^+. ET is deep in the Pacific Ocean region and shallow in the south America to South Atlantic region. As seen in the previous section, ET generally begins to develop in the evening hours, maximizes at about 02 hours and almost disappears at 06 hours. This feature is also confirmed in the LT-MAPs. In the map for LT = 12 in Fig. 92, the ET structure is not evident, and it is noted that the overall pattern of the He^+ map is very similar to that of H^+ for the same LT (Fig. 88). However, the absolute values of the density of He^+ are about one tenth of those of H^+, and it is noted that He^+ densities are higher in the winter hemisphere. Figure 93 shows the LT-MAP for LT = 00 during the June solstice period. The most notable feature in this map is that the region of the deepest ET has moved to the area between South America and South Africa, that is, the situation is reversed compared to the case of December solstice (Fig. 91). In both the December and June solstice cases, the depth of ET, namely the density ratio between the maximum at the crest and the minimum at the geomagnetic equator is 40, or about 1.6 where expressed logarithmically. This is rather large, and shows again that ET in He^+ density distributions is a very prominent feature. Similarly, Fig. 94 shows the LT-MAP for LT = 12 during the June solstice. The magnitude of longitudinal variation is lower compared to the case of H^+ (Fig. 90). It is noted that He^+ density is higher in winter than summer as in the case of December solstice.

5.2.3 LT-MAP of O^+

Figures 95 and 96 show the LT-MAPs of O^+ for LT = 00 during the December and June solstice, respectively. As in the case of H^+, we can see a large asymmetry between the winter and summer hemispheres. The O^+ density in the summer hemisphere is high and it has a relatively flat distribution. On the other hand in the winter hemisphere, the latitudinal gradient is very steep. We can also see a distinct longitudinal structure in both maps.

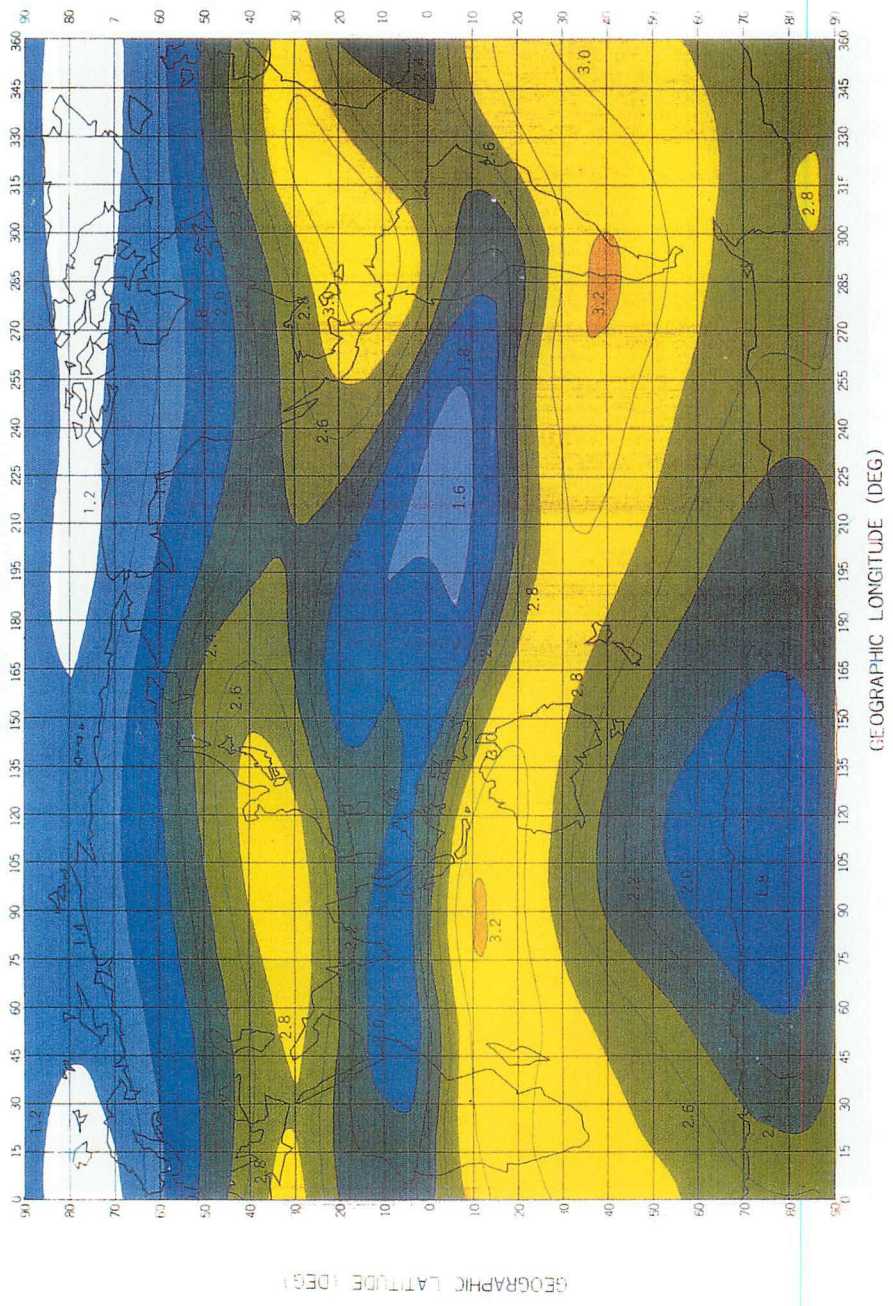

Fig. 91 LT map of He^+ density for LT = 00 hr. during northern winter.

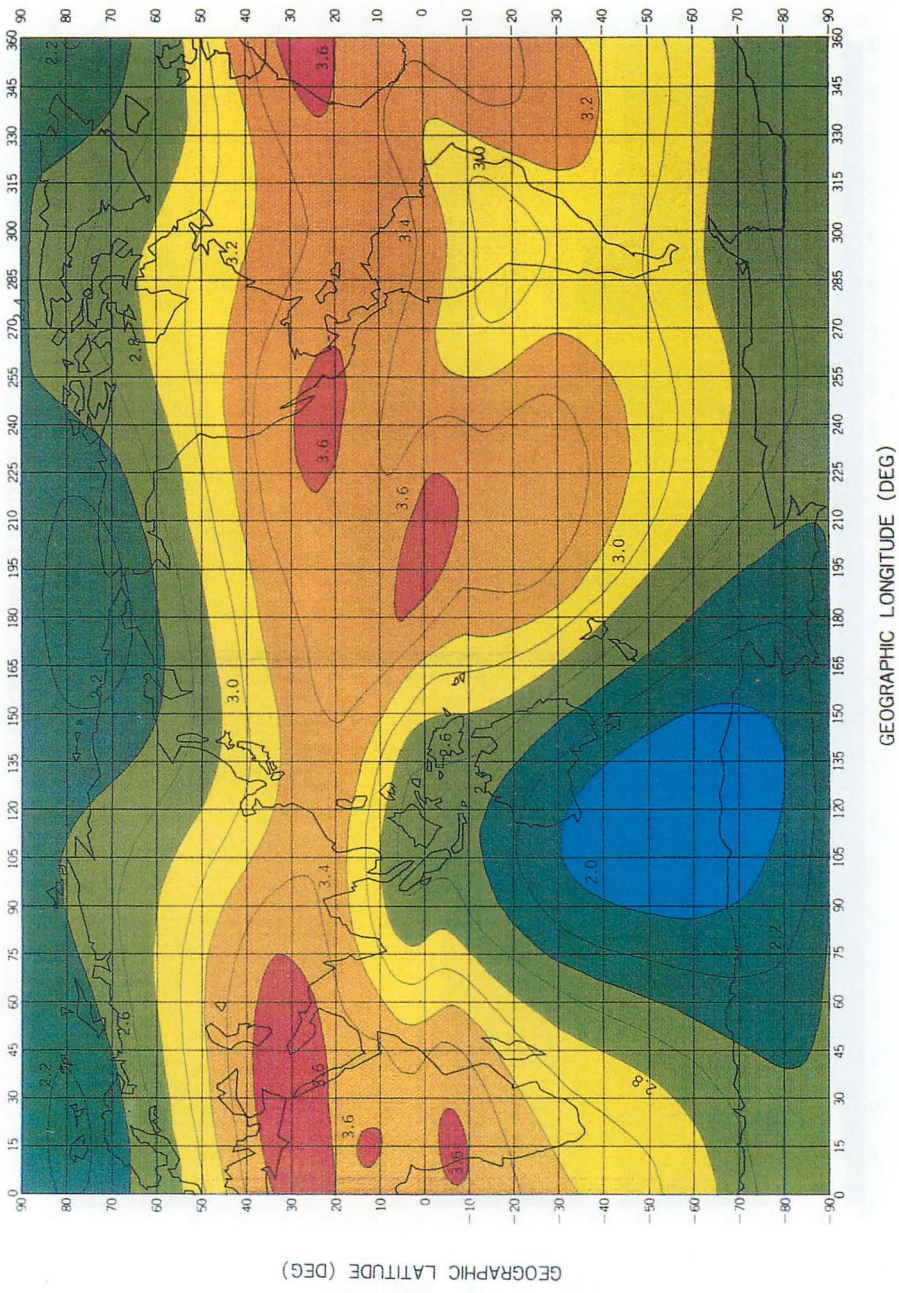

Fig. 92 LT map of He^+ density for LT = 12 hr. during northern winter.

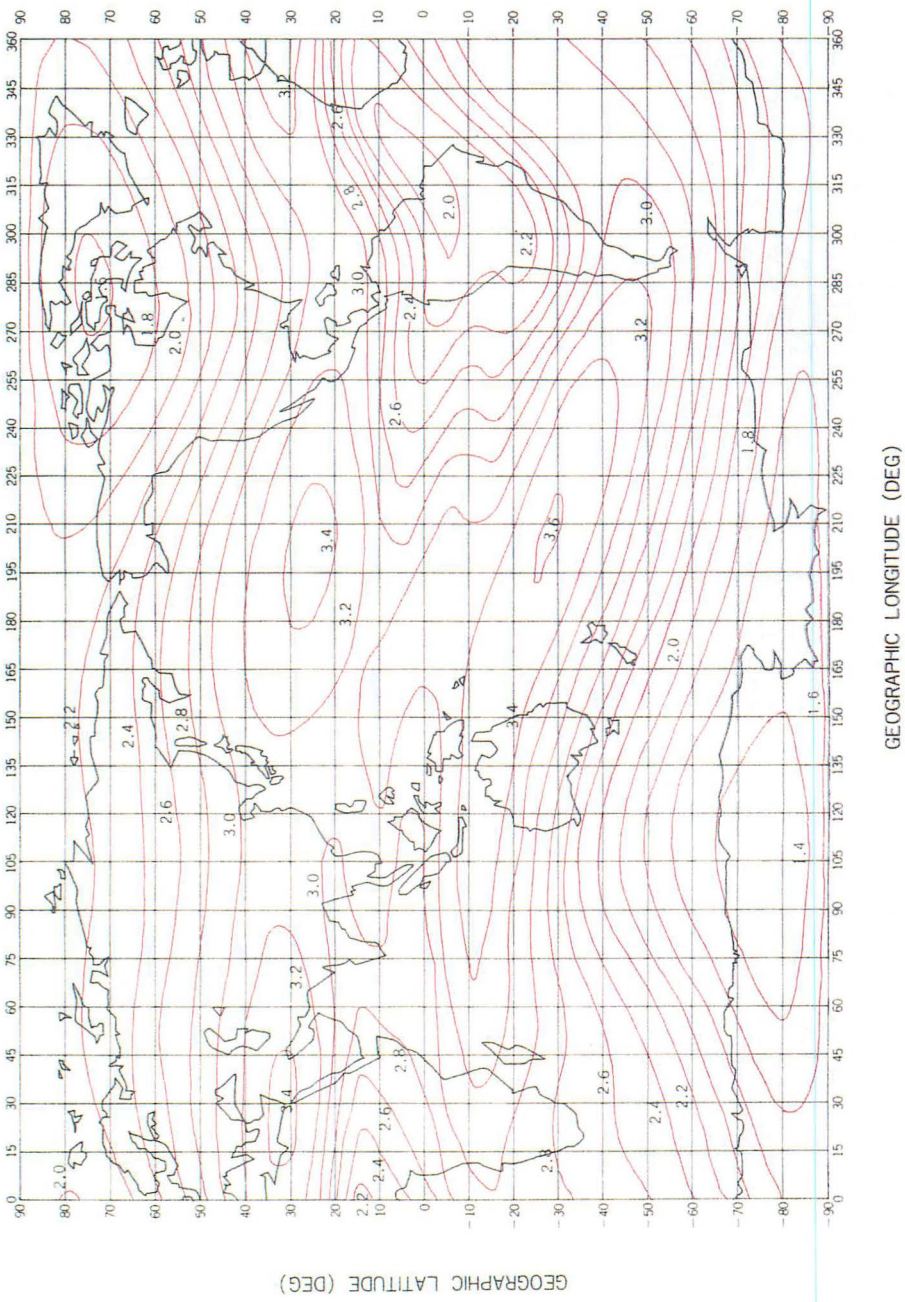

Fig. 93 LT map of He^+ density for LT = 00 hr. during northern summer.

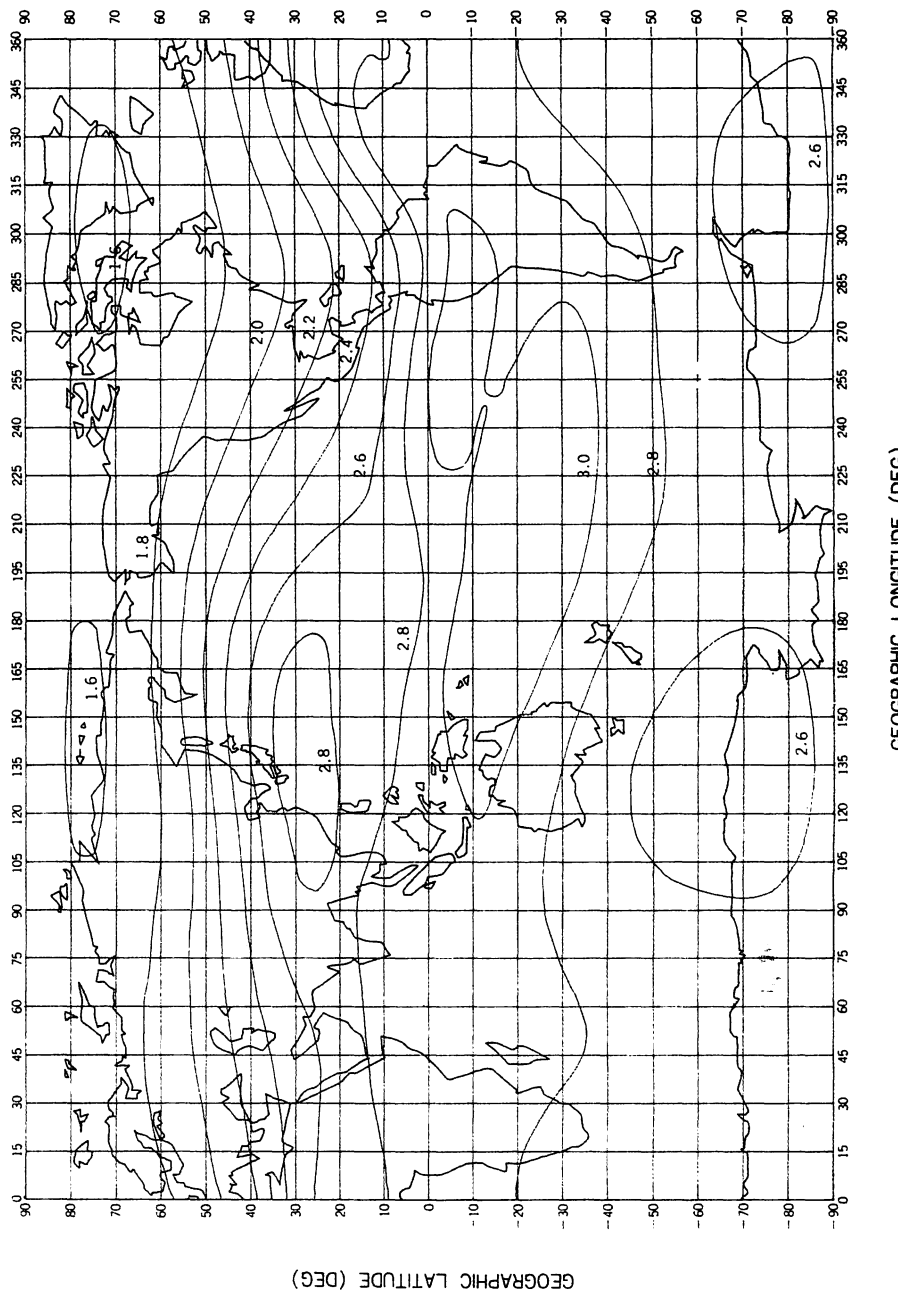

Fig. 94 LT map of He^+ density for LT = 12 hr. during northern summer.

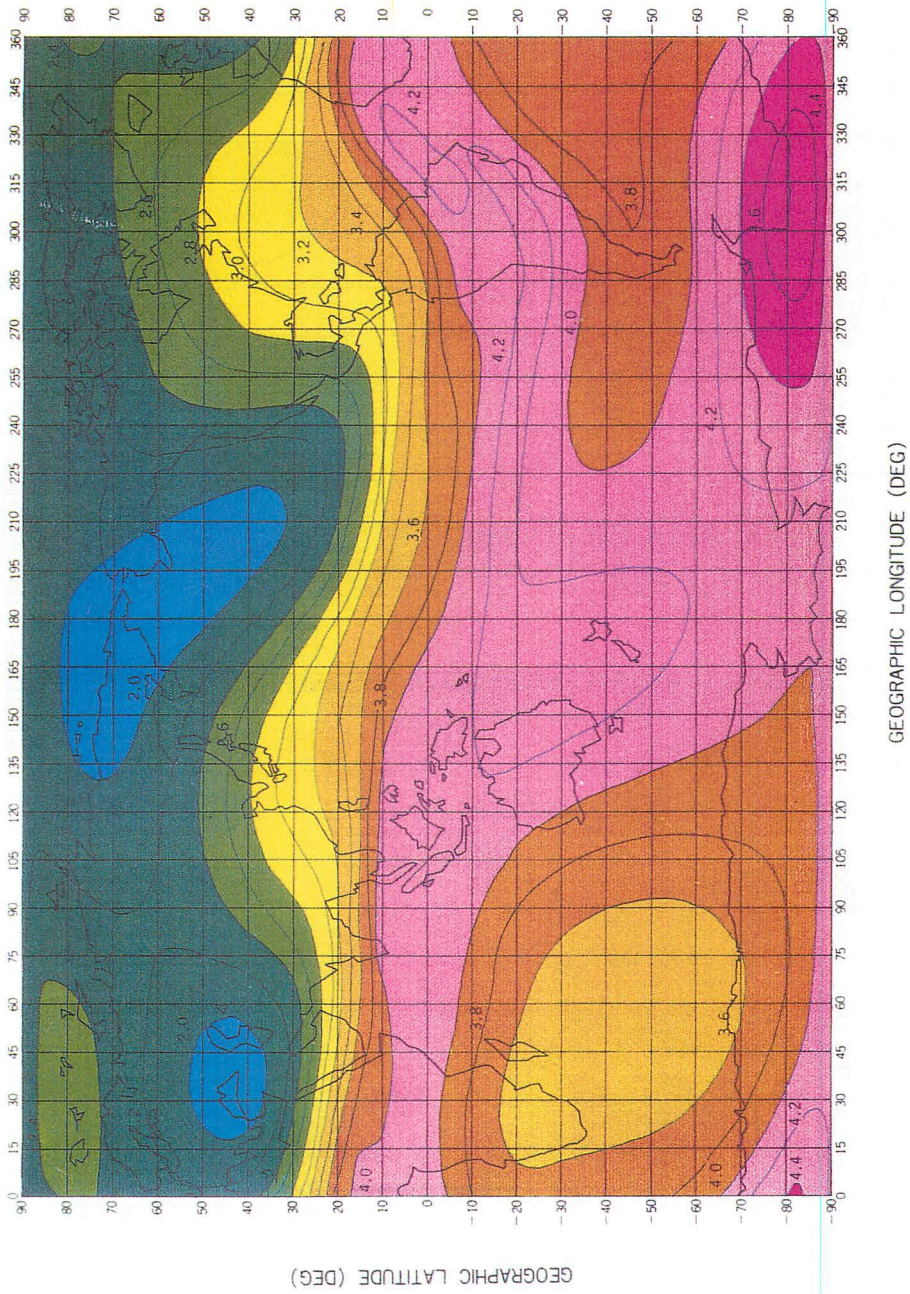

Fig. 95 LT map of O^+ density for LT = 00 hr. during northern winter.

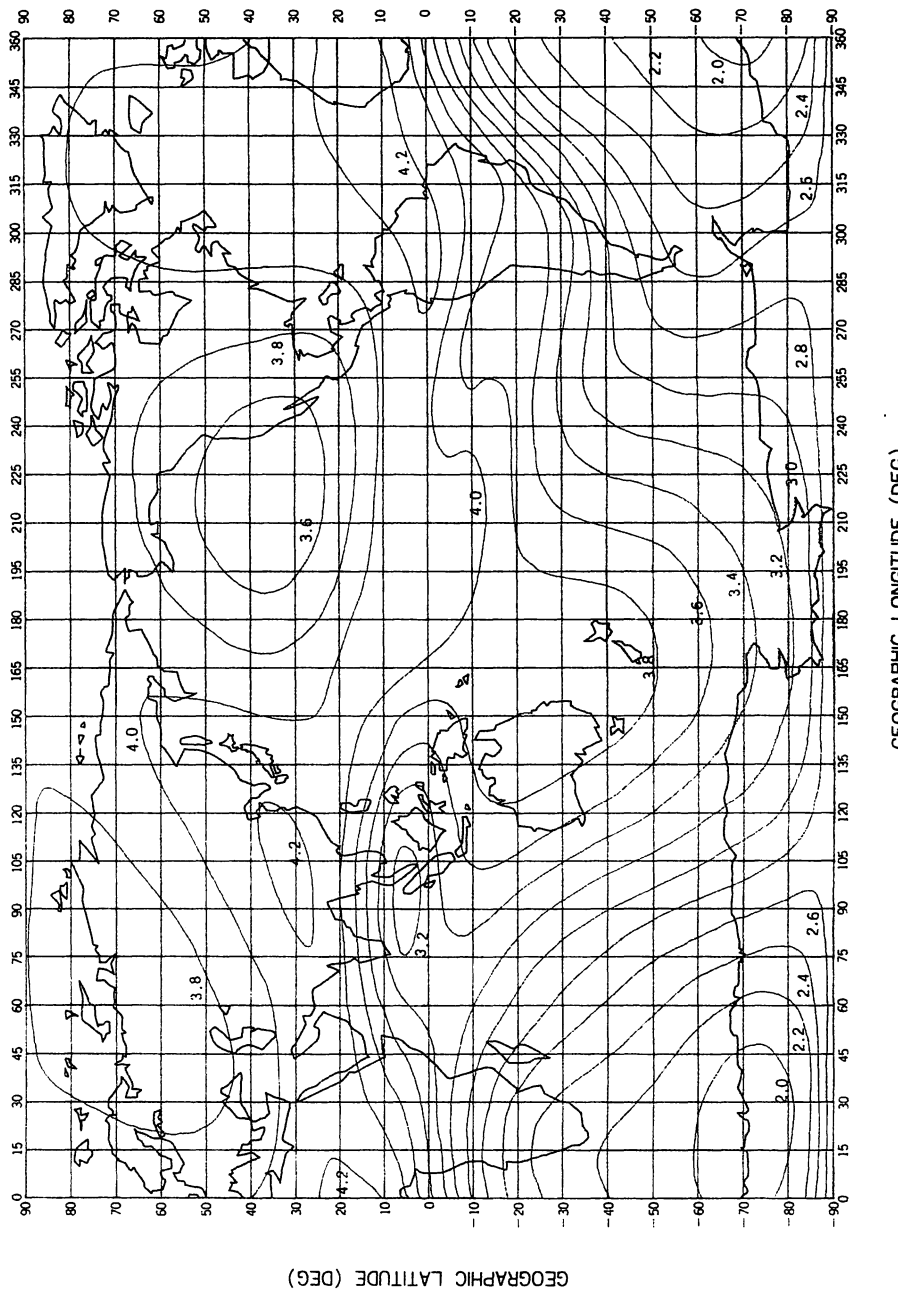

Fig. 96 LT map of O^+ density for LT = 00 hr. during northern summer.

5.2.4 Discussion of LT-MAPs

We have seen above that the LT-MAPs derived from the ISS-b observations at 1100 km altitude exhibit pronounced longitudinal variations for all three ion species, H^+, He^+ and O^+.

One of the most probable cause of the longitudinal dependence is effects of neutral winds. Of course the plasma drift due to the electric field has been known to significantly modify ionospheric distribution, its longitudinal dependence has been poorly known so that its effect is not discussed here.

It is well known that there are global neutral winds blowing from the dayside to the nightside in the thermosphere due to the absorption of solar EUV radiation. The direction of the neutral wind is mainly horizontal. This wind drags the ionospheric plasma to exert movement of the plasma constituents. Because movement of the plasma across the magnetic field is forbidden usually, the plasma obtains a velocity component parallel to the magnetic field, and because the magnetic field has a vertical component, the plasma eventually obtains a vertical velocity from the horizontal neutral wind. When one observes the plasma in the topside ionosphere upward movement results in a density increase and downward movement results in a density decrease. Because O^+ is the major constituent in the region where the effect of neutral wind predominates, the effect of neutral wind will manifest itself primarily in O^+ distribution. The distribution of light ions (H^+, or He^+)are controlled by buoyancy force of O^+, so that influence of the neutral wind to the light ions will appear through O^+.

If we let v_n and v_z be the velocity of horizontal neutral wind and the vertical velocity of plasma exerted by the former, respectively, then v_z is given by

$$v_z \propto v_n \cos I \sin I \cos \phi \quad \text{..... (115)}$$

where ϕ is the angle between the neutral wind vector and the horizontal component of the geomagnetic field. If v_n is in the meridional plane, ϕ is equal to the declination angle. The declination angle causes the longitudinal dependence. Because the term $\cos I \sin I$ maximizes at $I = 45$, v_z takes large values at middle latitudes. Because the direction of the neutral wind is predominantly zonal at most local times other than 03 or 14 hours, it is expected that the regions where the declination angle is greater are generally more affected by the neutral winds. Figure 97 shows the distribution of declination angle at 300 km altitude as calculated by IGRF-1975[115]. Miyazaki et al.[115] revealed that region of high or low O^+ density are closely connected with the regions of westward or eastward declination of the geomagnetic field in the northern hemisphere, respectively, and vice versa in the southern hemisphere.

Figure 98 shows the calculated vertical plasma velocity induced by the neutral wind at 300 km altitude and at LT = 20 hours during the December solstice (a) and June solstice (b), respectively[116]. To obtain these distributions, the neutral wind vectors calculated by Blum and Harris[117] are used. The neutral wind at LT = 20 is chosen as a typical nighttime condition when the wind velocity becomes maximum[117].

Comparing Fig. 98(a) with Fig. 95 for the December solstice conditions, it is found[116] that region of the O^+ density depressions roughly coincide with the regions of maxima in the downward flow. Likewise for June solstice condition, comparison of Fig. 98(b) with Fig. 96 gave similar conclusion[116].

Thus it is very probable that the remarkable longitudinal dependence shown in the LT-MAPs of O^+ (and hence of H^+ or He^+ through O^+), derived from the ISS-b observations at 1100 km altitude is a result of the declination angle effect of the neutral wind.

Ionospheric plasmas have been extensively observed from the ground and space, but the neutral atmosphere has been observed less and hence its effects have been less well understood so far.

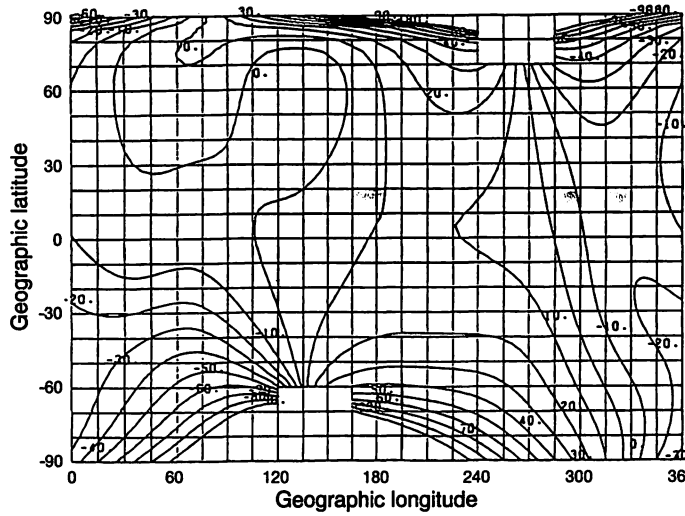

Fig. 97 Contour plots of declination angle of the geomagnetic field at 1100 km altitude [after Miyazaki et al., 1983[115]].

Because neutral species are still predominant at the altitude of the ISS-b observations, it is natural that the plasma there is affected by the neutral atmosphere. However, because ISS-b did not carry any instruments that could measure the neutral atmosphere, it is difficult to study further the effects of the neutral atmosphere only from ISS-b observations. Investigation of the interactions between the thermosphere and the ionosphere is an important area of research to be tackled in the future, by the STEP program, for example.

Now let us take a look at similar studies so far reported. Papagiannis and Mullaney[118] pointed out that the evening anomaly, in which the values of foF2 in the evening hours are higher than those around noon, is well correlated with the neutral winds deduced by Kohl and King[119]. The maps of "evening anomaly index" in their paper, which is quoted in Fig. 99, are very analogous to the LT-MAPs from ISS-b. The evening anomaly index represents the deviation of foF2 from its value at noon. It is also noted that the seasonal variations in this figure are very similar to those of the ISS-b results. The above authors attributed these seasonal variations to the declination angle affect of the neutral wind. Eyfrig[120] first found this declination angle effect in foF2 using data from ionosonde stations. On the other hand, Evans[118] reported that no such effect could be seen when comparing the data of two stations of contrasting declination angles. To this point, Papagiannis and Mullaney[118] argue that among other things the difference of the solar activity might be an important factor. Incidentally, the observation by Papagiannis and Mullaney[118] was made during a solar maximum period, as in the case of ISS-b.

As for the satellite observations, we should mention two studies. Firstly, Brinton et al.[121] reported that the longitudinal characteristics in the transition height between O^+ and H^+ observed by the Explore 32 satellite could be interpreted by the interaction between the neutral winds and the geomagnetic field. They also pointed out that there was not much longitudinal variation in H^+ while O^+ and N^+ had great longitudinal variations. This feature is contrary to the ISS-b results, but since their observations were limited to the American-European zones, the smaller longitudinal variations in H^+ may be partly attributable to this limited observation region. A difference of solar activity levels may also be important. The observations by the Explorer 32 were made during a period of low

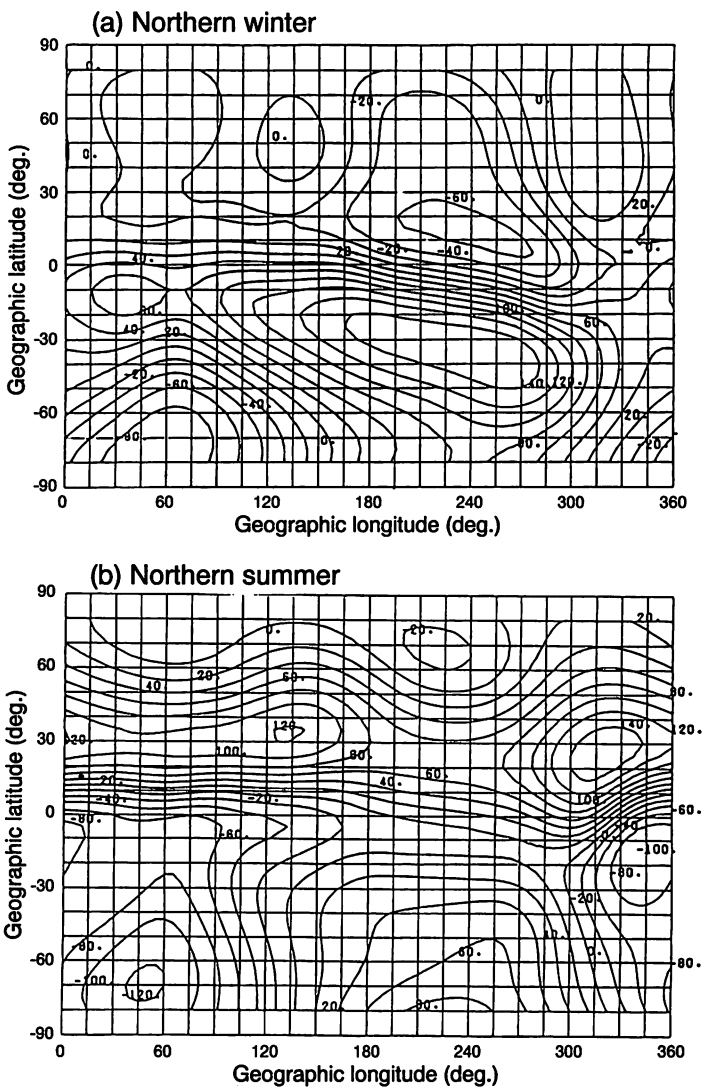

Fig. 98 Calculated upward drift velocity exerted by the neutral wind at 300 km altitude [after Miyazaki et al., 1983[115]]. (a) northern winter (b) northern summer

solar activity while those of ISS-b were made during a solar maximum. As discussed later, the dominant ion species at about 1000 km altitude is O^+ during a solar maximum, while it is H^+ during a solar minimum. Kutiev et al.[122] supported this idea from observations made by the RPA on OGO-6.

Secondly, Taylor et al.[123] produced LT-MAPs of H^+ for LT = 14:00–18:00 at 400–550 km altitude using OGO-6 data and they discussed the longitudinal dependence of the equatorial anomaly (EA) in H^+ distribution. They pointed out that EA structure is persistent in eastern Asia zone while in eastern American zone evidence of EA signature is absent. They also identified influence of meridional neutral wind to longitudinal variations of EA.

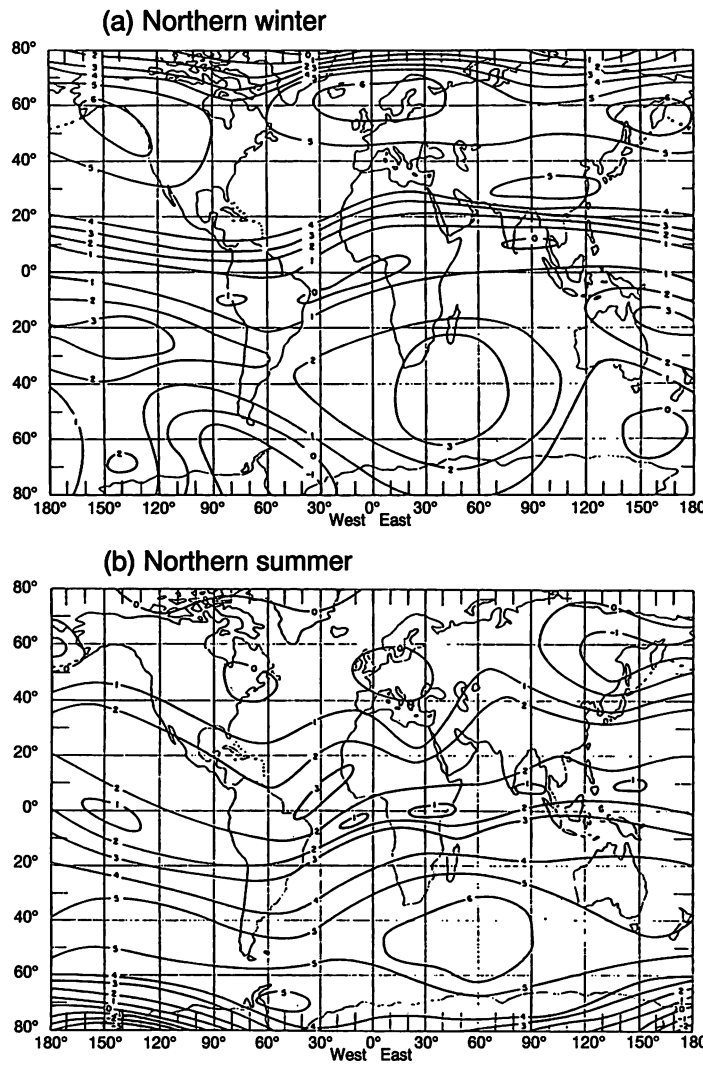

Fig. 99 Global distribution of "Anomaly Index" [after Papagiannis and Mullaney, 1971[118]]. (a) Northern winter (b) Northern summer.

Although it is difficult to compare their results directly with those of the present study because the altitudes and seasons of observation are very different, their results show generally very complex structures compared to present study. Since the orbital inclination of OGO-6 is 82 degrees, it was possible for their observations to produce the LT-MAPs by accumulation of data over relatively short periods. This difference in accumulation periods would result in very different LT-MAPs. We have seen in the previous section that the medium scale longitude dependent structures seemed to continue for a period of a few days. Because LT-MAPs from OGO-6 were produced from a data sets spanning about 20 days, the short-lived medium scale structures could be retained in the maps. On the other hand, the maps from ISS-b presented above are produced by five months' accumulation. The medium

scale structures may be smeared out by this accumulation and only the long-lived global structures remain in the ISS-b case.

6. Statistical analyses of ISS-b data

We have seen in the previous section that the distributions of ion densities show pronounced longitudinal dependence even for fixed latitudes and local time. For very detailed descriptions of the ionosphere it is apparent that these longitudinal characteristics must be taken into account. However, in order to understand the basic physical processes at work in the ionosphere, a simpler and clearer treatment may be appropriate. In this section we select one particular variable (latitude, local time, solar activity) as a reference coordinate and average the ion densities with respect to the other variables to elucidate the dependence upon that variable.

6.1 Characteristics of latitude-local time plane distributions

Figures 100, 101, 102, 103, 104 and 105 show the averaged distributions of H^+, He^+ and O^+, respectively, with respect to (a) latitude and (b) local time. The upper and lower panels of each figure shows the one-year average of ISS-b data obtained from August 1978 to July 1979 and from August 1979 to July 1980, respectively. In (a), the data are accumulated in bins of 5 degrees in geomagnetic latitude and 3 hours in local time, and in (b) the bins cover 1 hour in local time and 20 degrees in geomagnetic latitude. Each bin includes about 300 observational points of data. Since both sets of data were accumulated over a one-year period, these distributions represent the fictitious season-independent structure of the ion density distributions. Although the upper and lower panels are produced from completely independent data sets, very similar structures are reproduced for the two periods.

The latitudinal profiles of light ions, H^+ and He^+, decrease gradually around 45 degrees geomagnetic latitude and they relax around 60 degrees latitude. It is interesting to note that the latitudinal gradients are stronger at night than at day time, and sharper for He^+ than for H^+. This structure is not seen in the O^+ profiles so that O^+ becomes the major ion at higher latitudes.

6.1.1 Light Ion Distributions

The sharp density drop around 50–60 degrees latitude mainly seen at night was named as the "light ion trough" (LIT) by Taylor et al.[102] based on the OGO-2 observations. This LIT effect significantly contributes to the averaged distributions of light ions at higher latitudes shown above. Taylor[124] and Taylor and Walsh[125] suggested that LIT is the signature of the plasmapause at the ionospheric height which is located at a high altitude above the equator.

However, LIT does not have an evening bulge structure unlike the plasmapause[126] and a detailed comparison by Foster et al.[127] showed that there were systematic latitude deviations between the two. The view that LIT is the signature of the equatorial plasmapause has been questioned.

Nishida[128] showed that the equatorial plasmapause corresponds to the equipotential surface determined by the superposition of corotation- and convection-electric fields, inside which the plasma corotates with the earth. The plasmapause contracts when the convection becomes stronger due to the enhancement and/or inversion of the interplanetary magnetic field direction from north to south. The plasma in the plasmasphere is carried away by the enhancement of convection and the distribution of plasma deviates strongly from that of the diffusive equilibrium state. The plasmas in the plas-

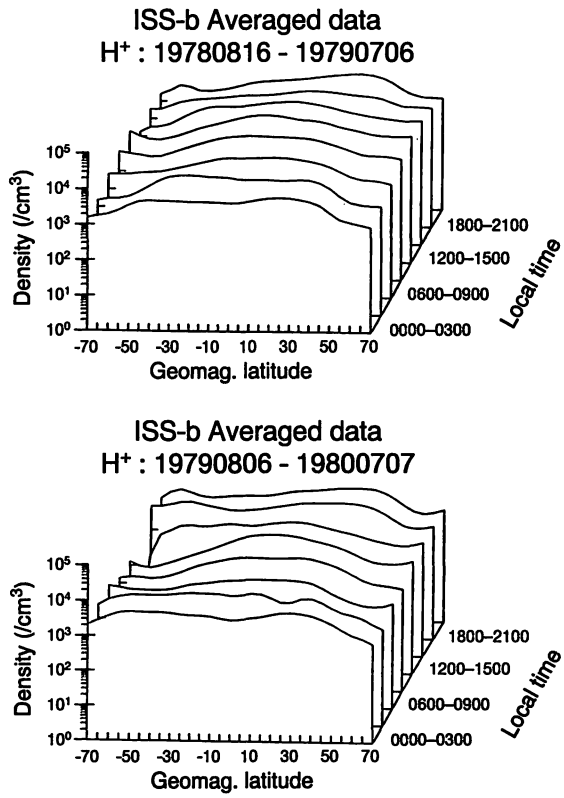

Fig. 100 Latitudinal distribution of H^+ obtained from ISS-b data.

masphere are provided from the ionosphere and it takes several days to refill the depleted plasmasphere[50]. More days are necessary for refilling higher latitudes because the volumes of the magnetic flux tubes are larger there.

Since significant magnetospheric disturbance takes place about once per week during solar maximum periods, the flux tubes at higher latitude are generally being refilled and the lighter ions are streaming upwards, so that equilibrium is seldom reached at higher latitudes. The lighter ions are carried to higher altitudes, resulting in the formation of light ion structures.

The most probable mechanism for carrying the light ions upwards is the polar wind, which was discussed in Section 3. According to the polar wind theory[51], the velocity and flux of the ions are greater for H^+ than He^+. However, as shown in the figures, the structure is sharper for He^+ than for H^+. This tendency was also pointed out by Taylor and Walsh[125]. The reason for this apparent discrepancy has not been yet established. The author's opinion is that it may be due to the chemical nature of H^+ and He^+ in the topside ionosphere:

H^+ is produced by the resonance charge transfer reaction,

$$H + O^+ \rightleftarrows H^+ + O \quad \text{(116)}$$

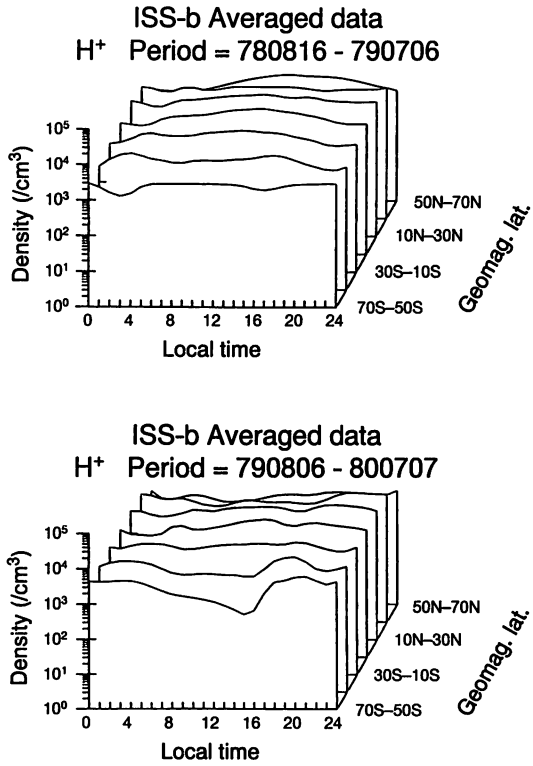

Fig. 101 Local time distribution of H^+ obtained from ISS-b data.

while He^+ is produced by the direct photoionization of neutral helium. The direct photoionization of H is negligible compared to (116). Production of H^+ continues even at night if the density of O^+ is high enough. This production compensates the loss of H^+ due to the polar wind, and can well explain the different latitudinal structures between H^+ and He^+.

6.1.2 Low latitude structures

Next, let us consider the structures at low latitudes. For He^+, the density decrease at the equatorial region, or the equatorial trough (ET), is a prominent feature, and the combination of ET and high latitude structure produces "crest" structure with broad maxima at middle latitudes in both hemispheres. The crest structure begins to develop in the evening hours, maximizes at midnight and is hardly recognizable in the daytime (06–18 LT). As for the H^+ distribution, no ET or crest structures are evident in the averaged profiles, while they are occasionally observed in individual pass plots. As for the O^+ distribution in Fig. 104, the daytime density in the low latitude is lower than that in the higher latitude. This feature is opposite to the case of H^+ or He^+. As for the LT dependence shown in Fig. 105, the density is higher in the daytime than in the nighttime for all the latitudes, showing the direct consequence of solar radiation. This feature of O^+ is also very contrasting to those of the light ions.

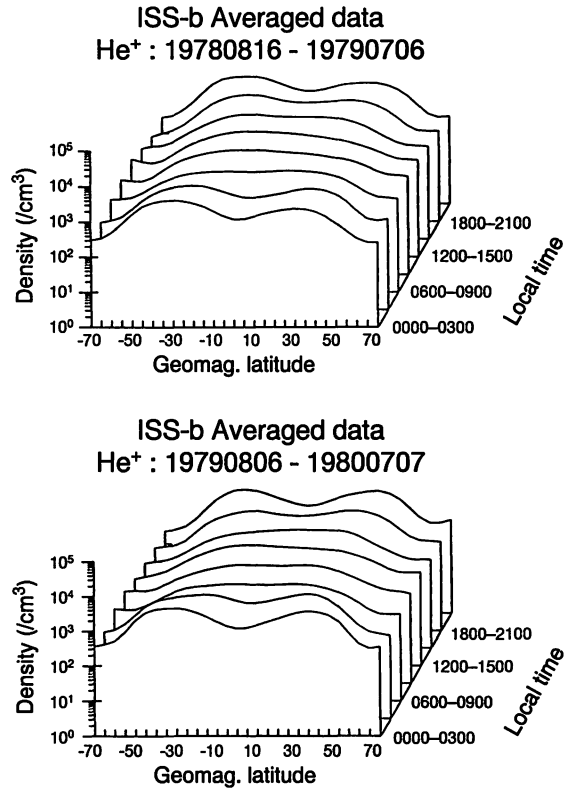

Fig. 102 Latitudinal distribution of He^+ obtained from ISS-b data.

Figure 106 shows the distributions of NmF2 derived from the first period (August 1978–July 1979). The profiles of the second period are essentially very similar and are not shown here. Comparing the profiles of O^+ and NmF2, it can be seen that their features of LT dependence are very similar. However, their latitudinal dependence is not very similar. That is, the depression in NmF2 at the equator (the so-called equatorial anomaly) is clearly identified, while no such structure is seen in the O^+ profiles, which instead rise to peaks at the equator and in particular, the density enhancements at the equator for LT = 18–21 are outstanding.

The equatorial anomaly in NmF2 is well explained by the "fountain effect" due to E × B drift followed by diffusion along the magnetic field[110][129]. The observed feature of O^+ by ISS-b can be well explained by this fountain effect.

Figure 107[130] shows the vertical velocities measured by the drift meter on AE-E during similar periods to those observed by ISS-b. These results were obtained from data within a dip latitude of ±5°near the equinox condition. The drift velocities measured by the IS radar at Jicamarca for solar maximum and for minimum are also plotted in the same figure. The results from the satellite and the IS radar generally agree very well. The evening enhancement of drift at solar maximum is very prominent. This enhancement is due to the F region dynamo[59]. A strong electric field can be exerted by the neutral wind due to the F region dynamo but it cannot become large in the daytime because it is shorted by the high density plasma in the E region connected through the magnetic field line. In the evening when the plasma density in the E region decreases suddenly because of the sunset, the electric field can become large.

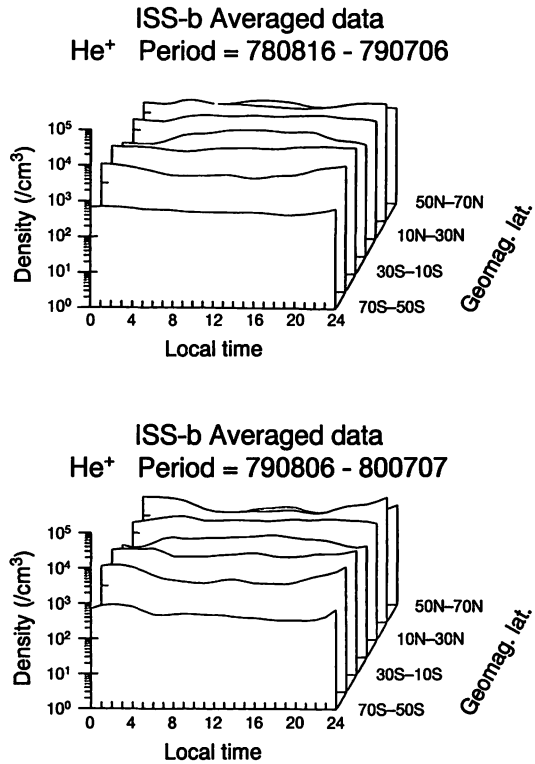

Fig. 103 Local time distribution of He^+ obtained from ISS-b data.

It is clear that the enhancement of O^+ density in the evening shown in Figs. 104 and 105 are related to this enhancement of upward drift motions. This evening enhancement of O^+ in the topside ionosphere has not been reported elsewhere. However, for the electron density in the topside ionosphere, a lot of detailed data have been produced by the Alouette-1, -2 and so on. For example, Chan and Colin[131] presented electron density distributions, similar to those of Figs. 106 and 105, obtained from the topside sounder at altitudes of 400 and 1000 km. Examination of their results shows that the evening enhancement can be identified, although these authors did not mention it explicitly. It is also interesting to note that the evening enhancement of NmF2 is not large though it is perceptible to some extent. This indicates that the drift motions mainly cause lift-up of the F region without much density increase.

6.1.3 Equatorial trough of He^+ and equatorial anomaly of NmF2

The previous section pointed out the close resemblance between the equatorial trough of He^+ (ET) and the equatorial anomaly in NmF2 (EA) that can be seen in the individual pass plots. This is also confirmed in the statistical results shown in Figs. 102, 103, 106. These three figures differ in that the latitudinal extent of ET in He^+ is much broader than that of EA in NmF2 and that the local time of maximization is at LT = 00–03 for He^+ while it is at LT = 20–21 for NmF2 [see also Matuura et

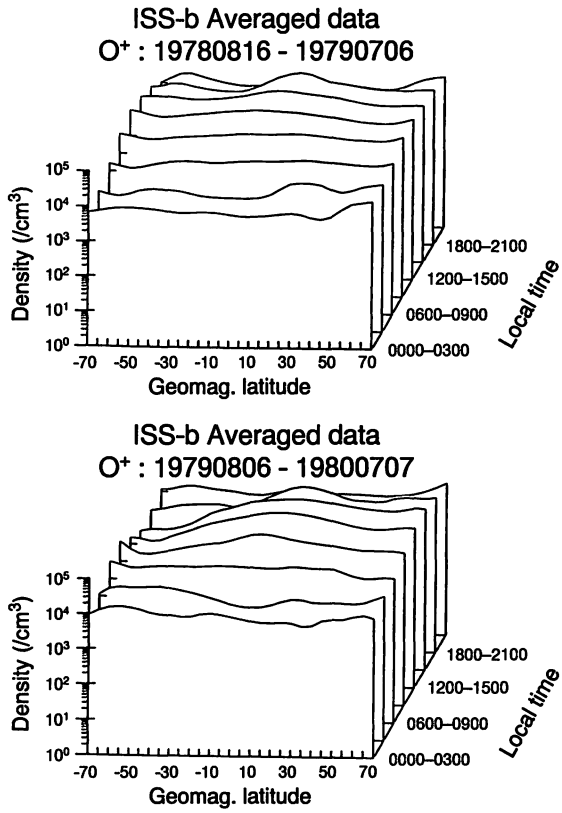

Fig. 104 Latitudinal distribution of O^+ obtained from ISS-b data.

al., 1982[11]]. As stated above, the viewpoint that the fountain effect is responsible for the formation of EA has been established rather firmly. On the other hand, no such firm theory seems to have been established for the He^+ ET. The He^+ ET was first discovered by RPA measurements on OGO-4[132] and in order to explain this phenomenon, Chandra et al.[132] discussed that besides the principal loss mechanism of He^+,

$$He^+ + N_2 \rightarrow He + N_2^+ \quad (117)$$

$$He^+ + O_2 \rightarrow He + O_2^+ \quad (118)$$

the reaction

$$He^+ + O \rightarrow He + O^+ \quad (119)$$

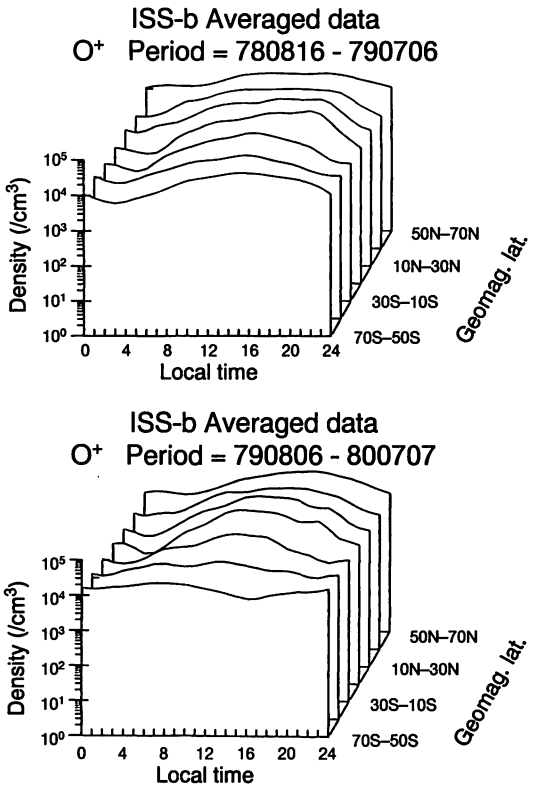

Fig. 105 Local time distribution of O^+ obtained from ISS-b data.

might play important role. However, it was concluded that this possibility is small by a simulation assuming an appropriate reaction rate for (119)[133].

Chandra[134] pointed out the resemblance between ET and EA, and by assuming the fountain effect also applies to the ET of He^+, he deduced the approximate latitude of the He^+ crest, θ_m, as

$$\theta_m \sim \cos^{-1}[(R+Z)/(R+Z_m+H_i)]^{1/2} \quad \text{(120)}$$

where

Z altitude of crest

Z_m equatorial altitude where [He^+] becomes maximum

R radius of the earth

H_i scale height of He^+.

This formula is deduced by requiring that the magnetic field line which passes the crest θ_m at altitude Z must cross the equator at altitude Z_m. When this formula is applied to NmF2, the result is of course consistent with the observations. But as for He^+, because $\theta_m \sim 40°$ and assuming T = 2000

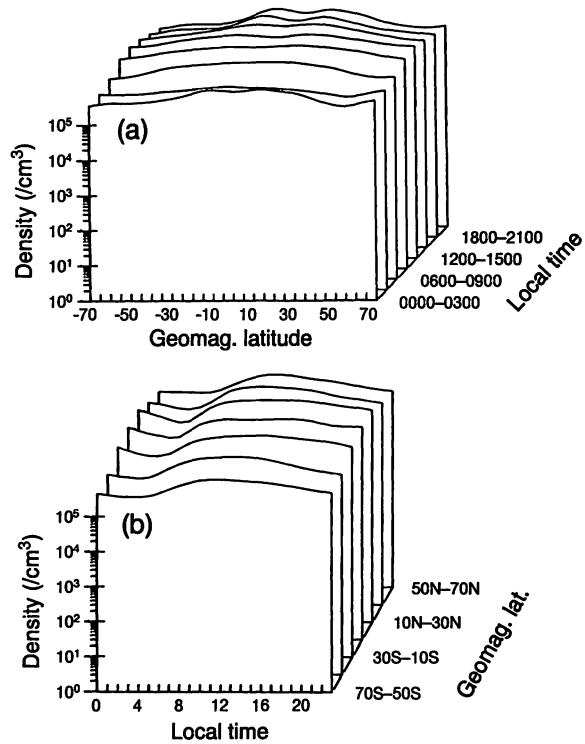

Fig. 106 Latitudinal distribution of NmF2 obtained from ISS-b data. (b) Local time distribution of NmF2 obtained from ISS-b data.

k and H_i = 400 km, then Z_m is equal to about 3500 km. This result is inconsistent with observations and existent theory. For example, Hanson[135] reported by rocket observation that the altitude of maximum [He^+] was 600 km above Natal where the geomagnetic latitude is about 1 degree, or about 500 km from our experiment made at middle latitude[18]. Many model calculations also indicate that the maximum of [He^+] should be within 500–2000 km altitude range. Thus if we try to explain the crest of He^+ in terms of the fountain effect, the peak of [He^+] should exist at an unrealistically high altitude contrary to observations and theory. It must also be noted that the ET structure is only seen in He^+ distributions while E × B drifts transport the total plasma. The explanation must incorporate the fact that only He^+ exhibits ET. This reasoning was not clearly described in the argument of Chandra[134].

As stated before, the development of crests and ET in the He^+ distribution is emphasized by the fact that [He^+] decreases at the equator and increases at the crest latitude in the evening to nighttime.

In Fig. 108 the LT dependencies of He^+, NmF2 and electron density (Ne) at 1100 km are replotted on linear scales[136]. The curves for He^+ clearly demonstrates highly contrasting variations between the distributions at the equator and the crest latitude.

Corresponding variations of NmF2 at the equator and crest do not differ much, contrary to the He^+ case. The EA can be seen during most of the local time, except during the early morning hours. This feature observed by ISS-b is consistent with previous studies [Goldberg[110] and references therein].

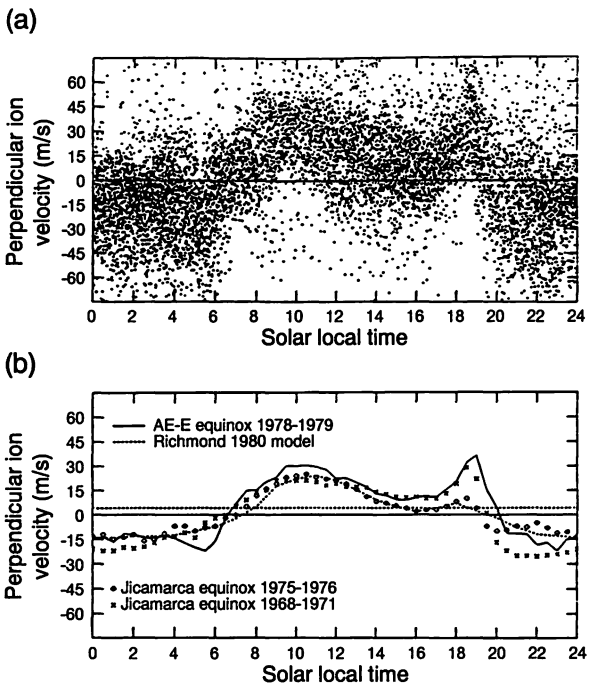

Fig. 107 drift velocity observed by AE-E satellite during the similar period as ISS-b [after Coley et al., 1990[130]]. (a) Scatter plot of the data for the dip latitude within ±5 degrees. (b) Comparison with the data from the IS radar at Jicamarca and model calculation.

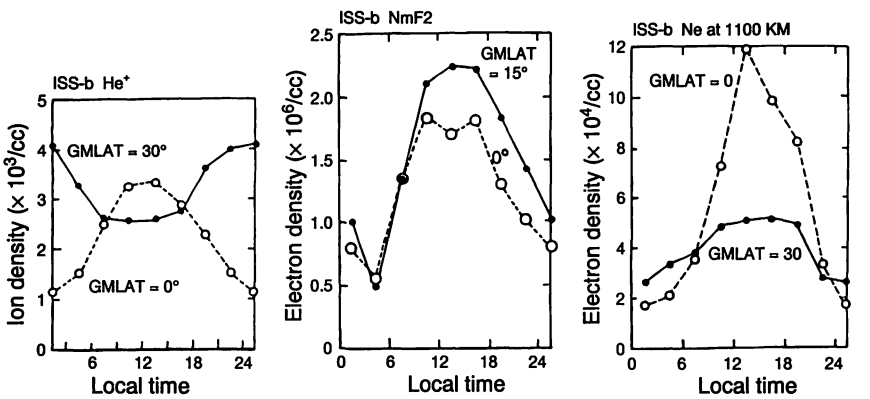

Fig. 108 Diurnal variations of He^+ density, NmF2 and Ne at the geomagnetic equator and middle latitude average in one-year period (August 1978–July 1979) [after Iwamoto, 1993[136]].

EA in NmF2 develops to a maximum extent in the afternoon to evening hours as consistent with Matuura et al.[11].

The "noon byte out" in the NmF2 profile at the equator also intensifies the anomaly structure. It is clearly seen from these figures that the LT ranges during which trough is produced in He^+ and NmF2 are different although the latitudinal structures look very alike. From the above observations, the mechanism to produce ET in He^+ is considered to be as follows[136]:

Firstly, the LT dependence above the equator can be interpreted as a natural consequence of solar zenith angle variation. Since the length of the magnetic field line which passes the equator at the 1100 km altitude of ISS-b is short, the diffusive equilibrium state can be established in a short time for the plasma in that flux tube. Because heavy O^+ is the major constituent at this altitude in the daytime, He^+ is lifted up by the buoyancy electric field. At night, a decrease of $[O^+]$ results in a decrease of buoyancy so that He^+ is transported to lower altitudes. Because the equator is located at the apex of the field line, excessive He^+ cannot be carried from higher altitudes. The consequence of these processes is a reduction of $[He^+]$ above the equator at night.

Secondly, the increase of $[He^+]$ at middle latitudes from the evening hours can be obviously interpreted in terms of the "reservoir effect" of the plasmasphere[23]. That is, the flux of He^+ is provided from the plasmasphere along the magnetic field at night. At middle latitudes, reduction of $[O^+]$ at night causes a decrease of buoyancy and He^+ is transported from the reservoir at higher altitudes.

More precisely, Fig. 108 shows that at middle latitude the increase of $[He^+]$ continues up to LT = 00 hour and then $[He^+]$ begins to decrease. That is, He^+ at this height range seems to accumulate up to that local time. This behavior can be attributed to the frictional force of O^+ against the He^+ flow. Moffett and Hanson[133] showed that the flow velocity of He^+ becomes equal to that of O^+ below a certain altitude where the O^+ density is high enough. Since the O^+ density at 1100 km was observed to remain high at night as shown Figs. 104 and 105, the downward flow of He^+ should be decelerated by this high O^+ density. This effect causes the down flowing He^+ to accumulate at this altitude so that $[He^+]$ becomes larger at night than in the daytime.

The reservoir effect is also responsible for formation of the structure at higher latitudes beyond the crest. The volume of the magnetic field tube becomes larger at higher latitudes. Enhancement of magnetospheric disturbance dissipates the tube contents at higher latitudes and the plasma density there generally remains low.

Thus it can be concluded that ET in $[He^+]$ is mainly formed by the reservoir effect of the plasmasphere rather than the fountain effect which is responsible for EA in NmF2. These two mechanisms differ in one important respect. The driving force lifting up He^+ is the buoyancy of heavy ions in the former, while it is drift motion due to the electric field in the latter. However, diffusion along the magnetic field plays important roles in both cases.

In the above discussion of the reservoir effect, the essential point is that He^+ is lighter than O^+. Therefore, the same argument must also apply to the lightest ion, H^+. As in the case of LIT formation, the primary difference between He^+ and H^+ is considered to be due to the chemical natures of these two species. H^+ is kept in chemical equilibrium with O^+ below about 600 km altitude by reaction (116). This reaction continues to supply H^+ even at night into the altitude of ISS-b observations so that $[H^+]$ does not decrease much at the equator at night.

On the other hand because He^+ is heavier than H^+, He^+ at the equator is carried to lower altitude where it is eliminated by reactions (117) and (118). The situation is different at solar minimums. Because the production of H^+ from (116) is drastically reduced at an altitude of around 1000 km during solar minimum, H^+ is expected to behave like He^+ at solar maximum. In fact, the latitudinal distributions of electron density at 1000 km observed by the Explorer 22 during the 1964-1965 solar minimum [137] show a marked equatorial trough structure at night, similar to the He^+ distributions shown in Figs. 102 and 103. During solar minimum the plasma at about 1000 km is composed

mainly of H^+[22] so that the electron density there is almost equal to that of H^+. Thus H^+ behaves like He^+ during solar minimum, indicating the relevance of the above discussion.

Recently, Heelis et al.[17] reported an ET structure in He^+ observed by an RPA on the DE-2. They have shown by a simple simulation that downward drift due to $E \times B$ can reproduce the ET structure in He^+. The possibility of an important role being played by this downward drift at night cannot be ruled out for the case of ISS-b observation. It is particularly true for the decrease of $[He^+]$ at the equator during night. The downward drift would carry He^+ to lower altitudes where the losses by (117) and (118) are greater.

However, it seems that the $[He^+]$ increase at the crest at night observed clearly by ISS-b is difficult to explain by this drift mechanism alone. The above mentioned DE-2 observations were limited to a sector where LT is about 22 hours, and do not provide LT dependence. The LT dependence revealed by the ISS-b favors the reservoir effect for the main cause of the ET in He^+.

6.2 Seasonal variations

Figures 109, 110, 111, 112, 113 and 114 show the seasonal variations of H^+, He^+, and O^+, respectively, at 1100 km altitude derived from ISS-b observations. Each figure represents (a) a contour plot and (b) a cross sectional plot of the same data set. These two plots are complementary for viewing two dimensional structures. The upper panel of each figure shows the daytime data (06–18) and the lower shows the nighttime data (18–06). The abscissa represents the month, its origin corresponds to August 1978 and end point to 24 months after that. A four-month running average was used to produce these figures. For example, for the points corresponding to abscissa value of 0, the data from August 1978 to November 1978 are averaged. The ordinate represents the geomagnetic latitude. The data are averaged in 5-degree bins in geomagnetic latitude.

First of all, it is noticed that O^+ exhibits the most regular sinusoidal variations of the three species. Its density is higher in summer and lower in winter, suggesting direct control by the solar declination angle. The periodicity is particularly regular at night, and the amplitudes of the periodic variations are greater at higher latitudes, amounting to about one order of magnitude at the highest latitude. The daytime periodicity is clearer in the northern hemisphere, though the amplitudes are smaller. However, in the southern hemisphere the amplitudes of variation are very small at higher latitudes. This variations come from the fact that both the peak in summer and the valley in winter do not develop to the extent that might be expected from the nighttime variations. This feature can be seen for the two years presented in the figure, and so we may take it as a characteristic at least during solar maximum.

Next, let us examine the H^+ distributions. Periodic variations also exist in the H^+ distributions, but their profiles are very deformed from the sinusoidal ones seen in the O^+ distributions. As for the daytime distributions, the variations in the northern and southern hemispheres are in-phase so that the variation of H^+ in the northern hemisphere is opposite to that of O^+. As evident from the contour plots in (a), the distributions are very symmetric between the northern and southern hemispheres although the seasons are different. This feature contrasts peculiarly with the O^+ case and suggests that H^+ is not simply controlled by the solar declination angle. The solar activity may be one candidate for such a control. However, sinusoidal variation with a one-year period can been seen in the plots, and thus the situation is not simple. As for the nighttime distributions of H^+, seasonal variations are generally in-phase with those of O^+, but variations in the northern middle latitudes are very small.

It is also noted that there are sharp drops of $[H^+]$ in the northern high latitudes, but in the southern hemisphere seasonal changes are rather broad. Contrary to the daytime, the asymmetry between the southern and northern hemispheres is remarkable.

Finally let us take a look at the He^+ distributions. The magnitudes of seasonal variations in $[He^+]$ are very small compared to $[H^+]$ or $[O^+]$ and their patterns are far from sinusoidal. An especially

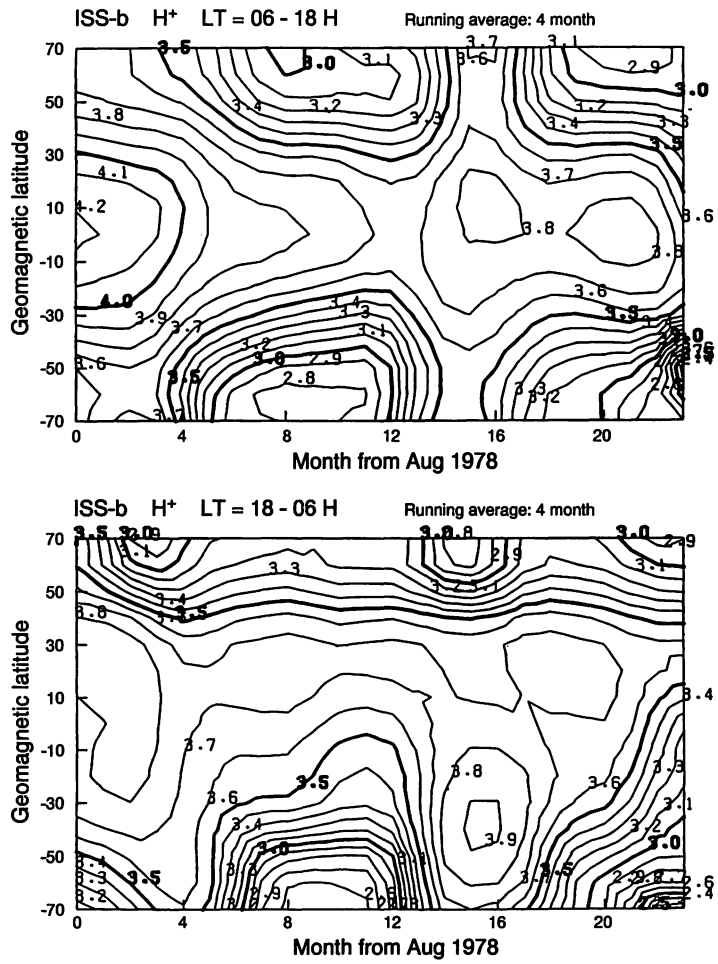

Fig. 109 Contour plots of seasonal variation of H^+ density obtained from ISS-b data. The upper panel show daytime data, and the lower nighttime.

peculiar feature is that both in the northern and southern hemispheres the day and night variations are in opposite phase. Namely, the nighttime He^+ density is higher in summer than in winter as in the case of O^+, whereas the daytime He^+ density is higher in winter than in summer. The "winter bulge" for neutral helium has been well known[138]. The daytime distributions of He^+ seem to reflect those of neutral helium. The reversal of the situation in the nighttime has been discovered for the first time by the ISS-b observations[136][139]

6.2.1 Discussion

1) Seasonal variation of O^+ distribution

The quite regular sinusoidal variations in nighttime O^+ distributions can be attributed to the solar declination angle. If we take these regular structures as "normal", anomalous structures also exist

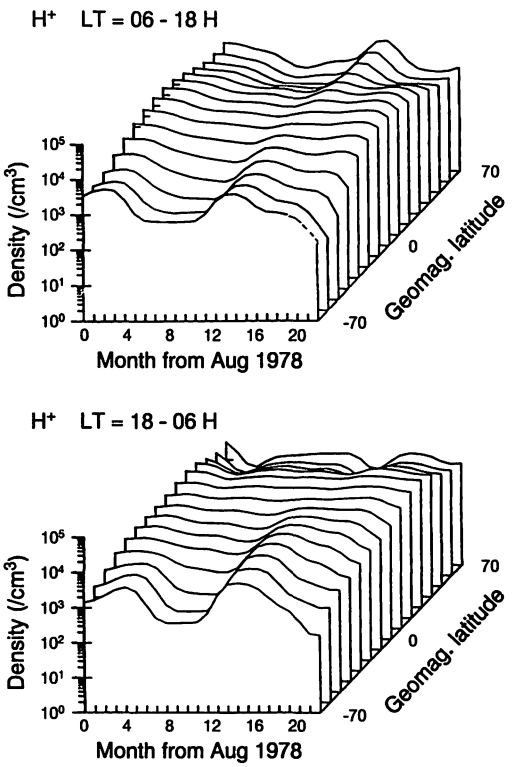

Fig. 110 Cross sectional view of Fig. 109.

in the O^+ distributions, as seen before. In particular, it is very strange that the amplitudes of daytime variations are smaller in the southern hemisphere than those in the northern hemisphere. Let us consider this point further.

Using the ISIS-2 data, Kohnlein[140] analyzed the distributions of H^+, He^+, N^+, and O^+ at 1400 km altitude. The period of the data extends from April 1971 to December 1972. Although the form of presentation is somewhat different from those described above and a strict comparison is rather difficult, it seems that the seasonal variations of O^+ in his figure do not show a large symmetry between north and south. The ISIS-2 observations were made during a period of low solar activity. This is a possible cause of the difference. The difference in the altitude of observations should not cause a serious difference because it is not so large (~300 km).

After analyzing the electron density distributions between 400 and 1000 km altitude obtained from the topside sounder on the Alouette-1 satellite, Chan and Colin[131] reported that there are asymmetrical seasonal anomalies between the northern and southern hemispheres above the F2 maximum and below about 600 km. They pointed out two seasonal anomalies, namely, a "winter anomaly" and a "December anomaly". Although their observations were made during low solar activity, they reported that the two anomalies should extend to higher altitude for higher solar activity. On the basis of their suggestion, it is possible that these two anomalies really influenced the ionosphere at 1100 km altitude as observed by ISS-b during solar maximum. In view of these facts, let us examine the consequences of these anomalies for the ISS-b results more in detail. The winter anomaly in this case means that the values of NmF2 (foF2) in winter days are greater

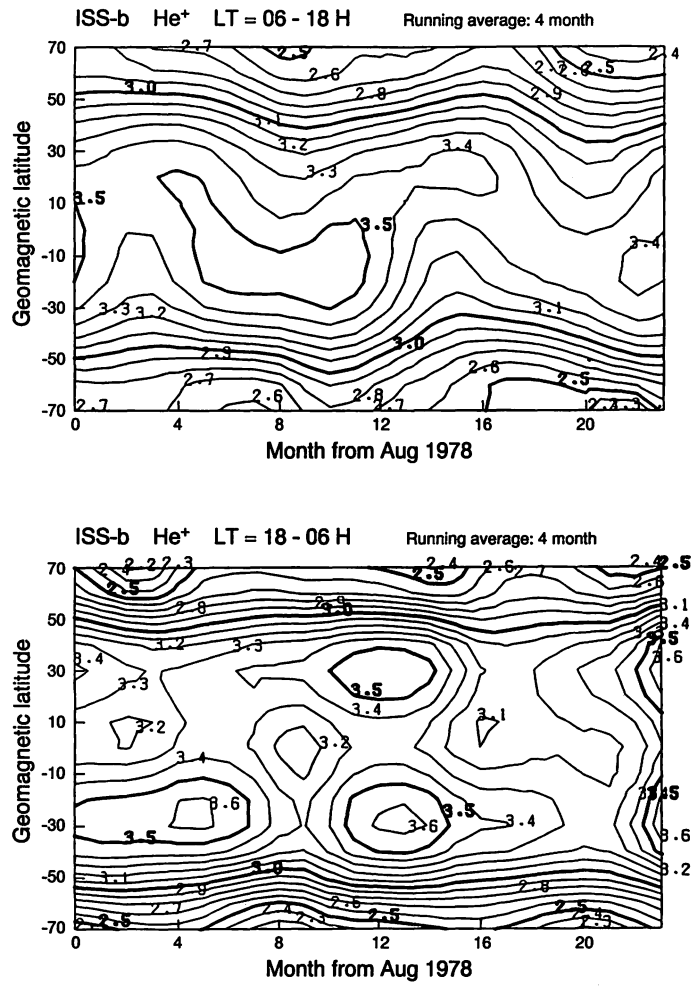

Fig. 111 Contour plots of seasonal variation of He^+ density obtained from ISS-b data. The upper panel shows daytime data, and the lower nighttime.

than those in the summer days at some location[141][142]. On the other hand, the December anomaly means that the values of NmF2 are greater than those in other seasons in both hemispheres irrespective of the season. Both phenomena are seen in the daytime. They have been known for a long time, but theoretical understanding seems to have been poor. The most representative interpretation is as follows;

From the discussion in Section 2, the production of O^+, $Q(O^+)$, is proportional to [O]

$$Q(O^+) \propto [O] \quad \text{..... (121)}$$

The losses of O^+ are

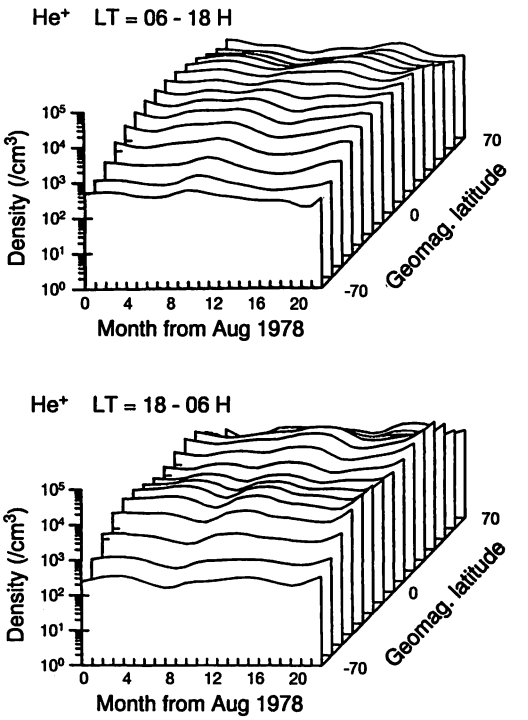

Fig. 112 cross sectional view of Fig. 111.

$$O^+ + N_2 \rightarrow NO^+ + N \quad \text{(122)}$$

$$NO^+ + e \rightarrow N + O \quad \text{(123)}$$

At chemical equilibrium,

$$[O^+] \propto [O]/[N_2] \quad \text{(124)}$$

Hence, if the ratio $[O]/[N_2]$ is greater in winter, $[O^+]$ would be greater in winter. In fact the winter ratio is greater by a factor of about 3 than that in summer according to MSIS model[3]. So far, the only one available interpretation of the December anomaly is that the distance between the sun and earth is minimum in December. However, this interpretation is not convincing because the difference in solar radiation is 10% at most. Yonezawa[141] presumed that there would be some contribution from solar wind ionization. So far, such a causality has not been identified between the solar wind and NmF2.

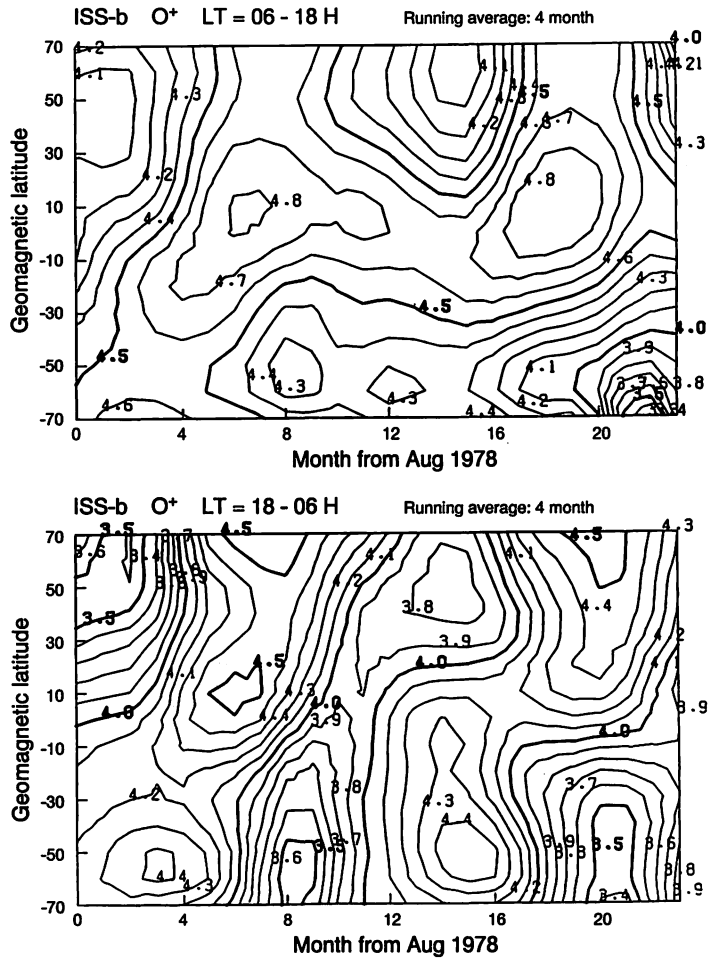

Fig. 113 Contour plots of seasonal variation of O^+ density obtained from ISS-b data. The upper panel shows daytime data, and the lower nighttime.

The two anomalies occur in phase in the northern hemisphere and out of phase in the southern hemisphere. The seasonal anomaly in the southern hemisphere could be qualitatively understood if the winter anomaly occurred strongly in this hemisphere during the observations. This interpretations is attractive, but we have no further evidence to support this view point. In any way, because O^+ is the heaviest major species and not easily affected by other ions, the anomaly in O^+ is likely to be explained by some effect in the neutral atmosphere. Here again the importance of understanding the neutral atmosphere is emphasized.

2) Seasonal variation of H^+ distribution

The distributions of H^+ in the topside ionosphere can be more affected by the transport processes than in the case of O^+. The production of H^+ from resonance charge transfer would also complicate the distributions of H^+. According to the ISS-b observations, the transition height

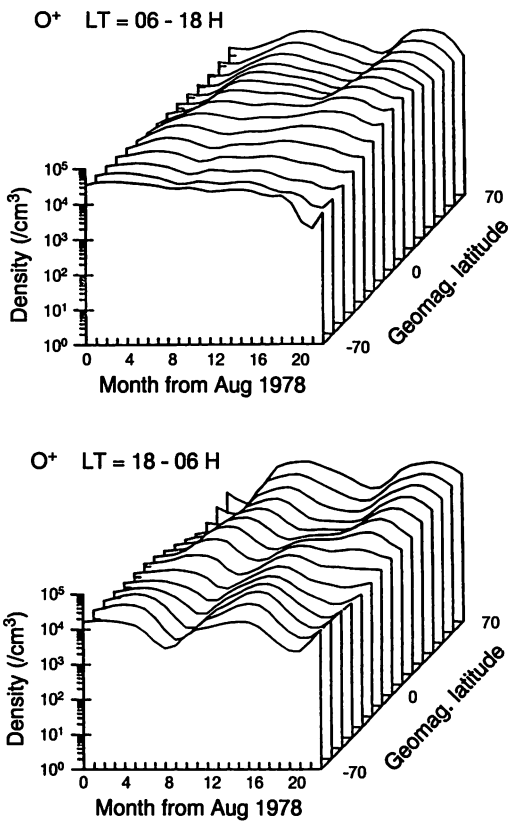

Fig. 114 Cross sectional view of Fig. 113.

between H^+ and O^+ goes above and below the 1100 km altitude. In light of these effects, it is surprising that the H^+ distributions are fairly symmetric between the northern and southern hemispheres in the daytime. It is also interesting that the H^+ distributions are very regular in the daytime whereas the O^+ distributions are regular at night. The remarkable season-independent symmetry between the two hemispheres indicates intimate interaction between them, that is, interhemispheric flow. There have been many theoretical studies on the interhemispheric flows[23][143][144].

These authors pointed out that flows of order of 10^8 ions cm^2 sec^{-1}should exist at about 1000 km altitude. Recent satellite observations have shown that such flows really do exist. For example, Chandler and Chappell[47] observed interhemispheric flows of H^+ and He^+ at L = 2.0–5.5 by the RIMS instrument of the DE-1 satellite. They reported that these ions were flowing with a velocity of several hundred meters per second to one km per second, and that H^+ and He^+ were counter streaming in some instances. Interhemispheric flows have also been detected by ground based observations[145]. Using the same data, Bailey et al.[146] pointed out that the observed abundance of H^+ can be reproduced only if the interhemispheric flow of H^+ is permitted. In view of these observations and theories, it is very probable that this interhemispheric flow had a substantial influence on the H^+ distributions during the ISS-b observations at 1100 km altitude, although we have no further evidence to support this hypothesis. Solar activity, for example,

might have controlled both hemispheres simultaneously. However, the distributions in Fig. 109 (a) clearly have a periodicity of one year, whereas the solar activity shown in Fig. 67 does not have such a structure, and the possibility of relying on the solar activity can be safely denied. Nevertheless, it should be noted that the influence of solar activity can be identified in the figure. The gradual decrease of $[H^+]$ at low latitudes from 1978 to 1979 is due to rising solar activity. This effect will be discussed in a later section.

3) Seasonal variations of He^+ distributions

A remarkable feature of the seasonal variations of He^+ is that the winter bulge phenomenon is seen only in the daytime and it disappears at night. Let us discuss this feature more in detail. The winter helium bulge in the neutral constituent was first discovered by analysis of the drag on satellites[138]. According to this analysis, the density ratio between the winter and summer hemispheres was about 4. Later experiments by a mass spectrometer on OGO-6 revealed that this ratio amounts to a factor of 10[146]. The reason why the helium density is higher in winter is attributed to a seasonal change of diffusion coefficient near the turbopause. Kockarts[147] shows that the eddy diffusion coefficient there should differ by a factor of about 50 in summer with respect to winter in order to explain the observed density ratio. Although it has not been confirmed that such a difference really exists, the above view seems to be the most probable. A similar winter-time dominance of other constituents such as O and H has also been identified[3].

Figure 115 shows the latitudinal distributions of He^+ density averaged in three-hour segments of local time for northern winter (October 1978–February 1979), equinox (January 1979–May 1979), and southern winter (April 1979–August 1979) conditions from the ISS-b observations. Here again it is clearly confirmed that the bulge structures are seen only in the daytime for both the northern and southern winters.

Further, Fig. 116 shows the monthly variation of the ratio of the He^+ density at 30°N to that at 30°S. The upper panel (a) shows daytime curves, and the lower panel (b) nighttime curves. The reversals of phase are clearly seen in this figure, but it is noted that the curve for LT = 06–09 does not show a clear seasonal change and the curve for LT = 18–21 is more like the daytime ones. These local times are somewhat transient from day to night. The maximum value of the logarithmic ratio is about 0.6, namely, the ratio is about a factor of 4. This value is consistent with that obtained for the neutral helium density[148].

Similarly, Fig. 117 shows the ratio of H^+ density at 30°N to that at 30°S. The winter bulge structure is not seen for H^+ contrary to the He^+ case.

Figure 118 shows the ratio between the densities of He^+ in the daytime at the same latitudes in northern and southern hemispheres for four solstice conditions. For all the solstices it is confirmed that the density of He^+ is higher in winter. The magnitudes of the ratio increase up to about 30° then they tend to decrease up to 60°. Beyond about 60°, the ratio becomes less than one.

As for the neutral helium density, Keating et al.[148] gave the following expression:

$$\log[He] = C - 0.4\delta p \delta s \quad \text{..... (125)}$$

where

δp Solar declination angle (in radians),

δs latitude (in radians).

Within $\delta s < 30°$, the above results from the ISS-b are compatible with equation (125). Therefore it is suggested that the distributions of He^+ at low latitudes reflect those of the neutral helium density rather faithfully. For higher latitudes than about 40°, the deviation between the

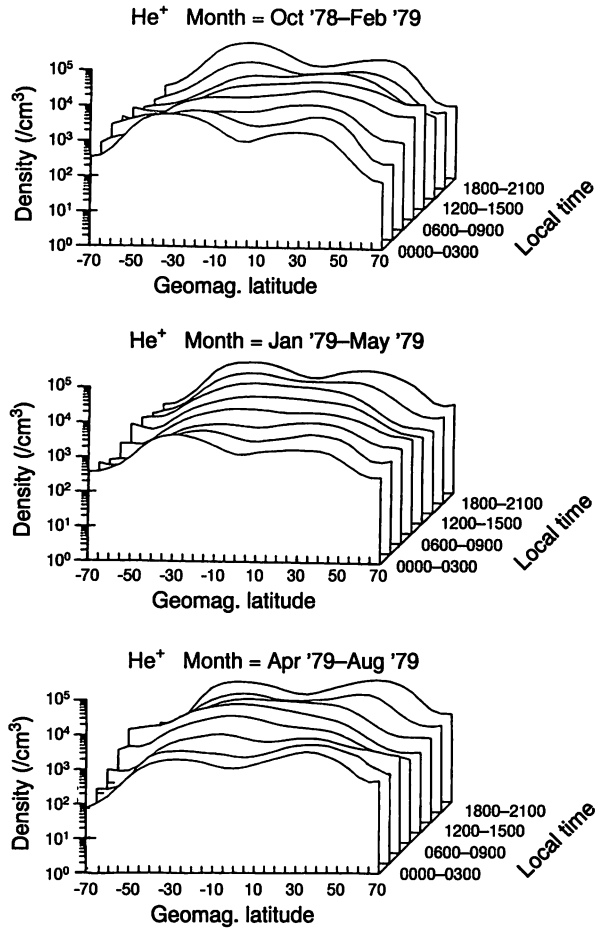

Fig. 115 Seasonal variation of the latitudinal profiles of He^+.

two becomes considerable. From these facts it can be concluded that the He^+ density at about 1100 km is controlled mainly by production at lower latitudes up to 40°, and it is controlled by other factors at higher latitudes.

6.3 Dependence on solar activity

It is well known that UV radiation, which is the primary source of the plasma in the ionosphere, changes according to the solar cycle so that the plasma below the F region is controlled by the solar cycle. Because the plasma in the topside ionosphere around 1000 km altitude is strongly dependent on the F region, it naturally follows that the plasma density and ion composition there should also depend on the solar cycle. However, observational evidence of such variations in the topside ionosphere is very scarce, mainly due to orbital limitations. Because ISS-b almost continuously observed the topside ionosphere at a fixed altitude of 1100 km for about three years during the solar

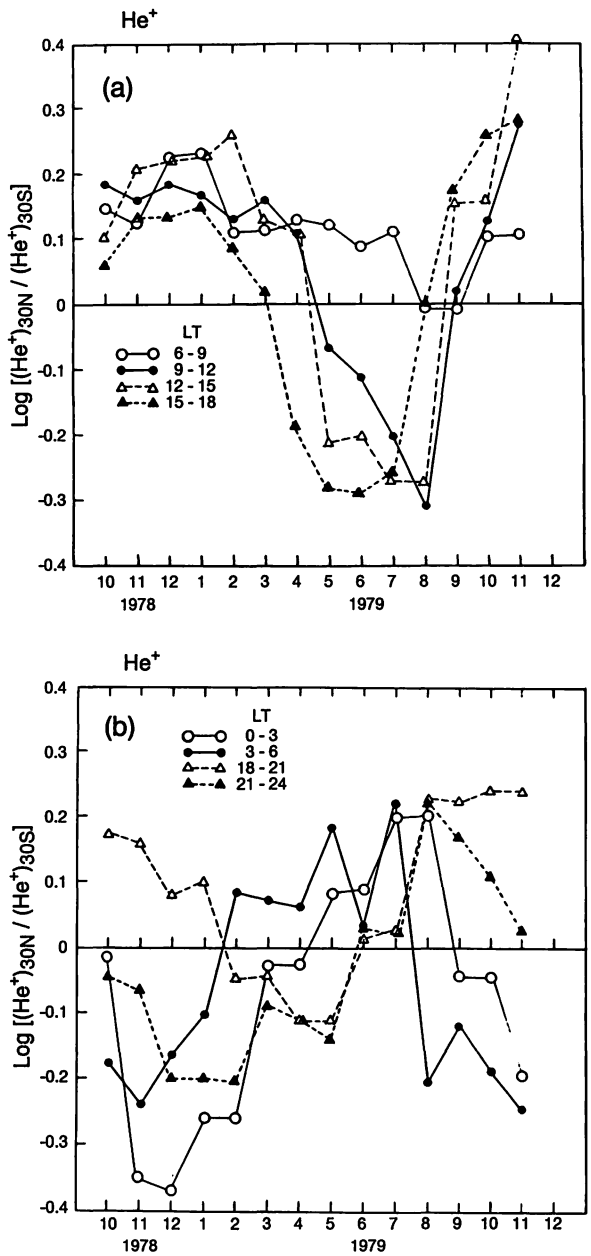

Fig. 116 Seasonal variation of He^+ density ratio at 30°N and 30°S. (a) daytime (b) Nighttime

maximum period of cycle No. 21, it is possible to analyze the solar activity dependence of the electron and ion densities.

Figure 119 shows the regression lines of the "global average" ion densities with respect to the solar flux, F10.7 obtained from the ISS-b data. The global average in this case means that the data

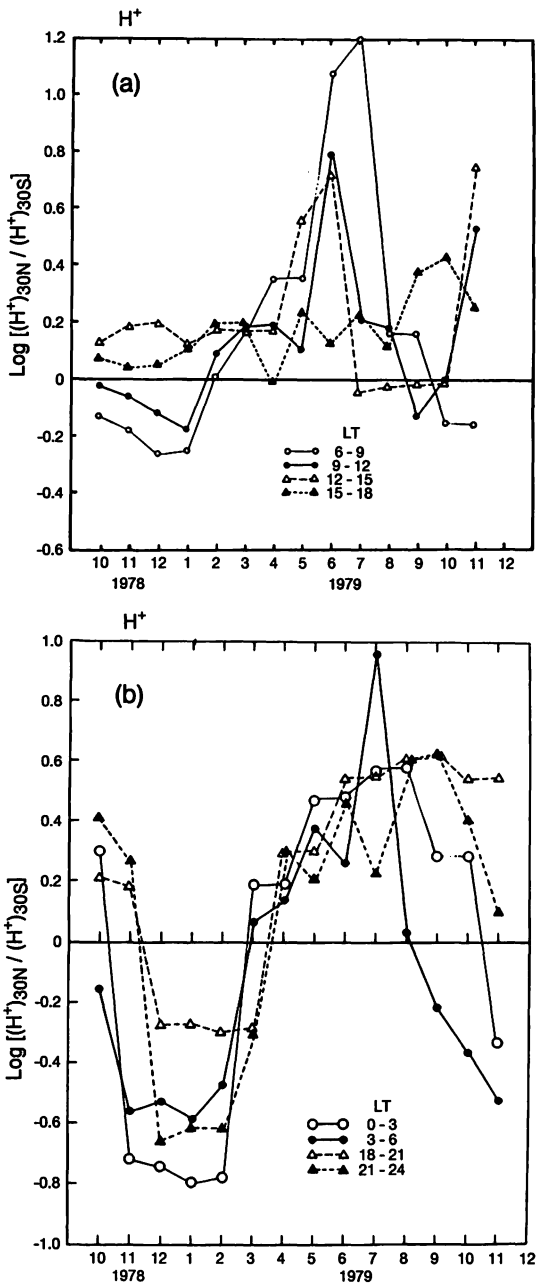

Fig. 117 Seasonal variation of H^+ density ratio at 30°N and 30°S. (a) daytime (b) Nighttime

observed in one day are simply averaged irrespective of local time, latitude or longitude. Hence, the data point number shown in the figure, N, corresponds to the number of effective days of

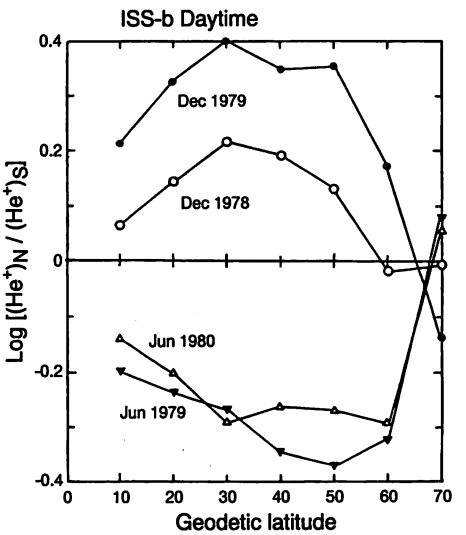

Fig. 118 Ratio of He^+ densities at the same latitudes in the northern and southern hemisphere.

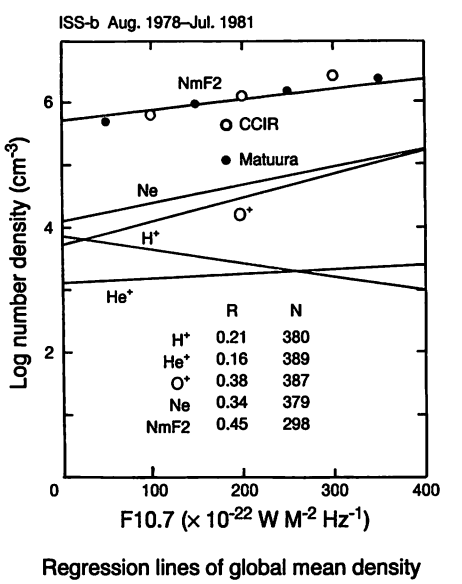

Fig. 119 Dependence of the global mean electron and ion densities at 1100 km altitude and NmF2.

observations. Although this method might be seen rather crude, it gives a good prospect as shown in the following.

As for NmF2, the solid line in the figure represents the present result. The open circle shows the result computed by the CCIR model, and the filled circle shows the result obtained by Matuura et al.[139] from an analysis of the ISS-b data during the earlier stages of the mission. The latter two are converted from foF2 values, so that these data are not aligned on straight lines. Although the CCIR model was based mainly on lower solar activity, it agrees well with the ISS-b results.

The electron density, Ne, at the satellite altitude of 1100 km, were derived from the AGC voltage of the topside sounder[99]. Ne has a positive correlation with F10.7. Its correlation coefficient, R, is 0.34 and is a little smaller than that for NmF2. The sum of densities of O^+, H^+ and He^+ is not necessary equal to Ne because they were measured independently. O^+ was the major ion species at this altitude during the observations and correlates positively with F10.7 with a correlation coefficient of 0.33. In contrast to O^+, H^+ has a negative correlation with F10.7. This is a remarkable feature which was found by the ISS-b observations for the first time[149]. This negative correlation can be interpreted as follows:

During high solar activity, lighter neutral constituents are lifted up to higher altitude due to enhanced thermospheric temperature, thereby reducing the ratio [H]/[O][150]. $[H^+]$ is proportional to this ratio at its main production layer where the chemical equilibrium by resonance charge transfer holds.

Higher solar activity also increases the O^+ density and temperature around the F2 region so that O^+ extends to higher altitudes. The buoyancy provided by the extended O^+ also causes H^+ to be lifted up to higher altitudes. The combination of these effects results in a reduced H^+ density at a fixed altitude around 1100 km during high solar activity.

As for He^+, the correlation coefficient is positive, but its magnitude is the smallest among the three species. When the observed He^+ densities are sorted into bins divided by the latitude and local time, the correlation becomes either negative or positive in each bin. Figure 120 shows some examples. In the upper panel the correlation is positive whereas in the lower panel it is negative. The correlation coefficients are rather large and significance of the correlation is high in both cases. These analyses infer that the situation is complex for the case of He^+. Because He^+ is lighter than O^+ and its density is generally smaller than those of O^+ or H^+ at 1100 km altitude, the distribution of He^+ is greatly affected by those of O^+ and H^+.

The height of the transition between O^+ and H^+ goes above and below 1100 km in the daytime and nighttime as described before. Competition between the two controls the distribution of He^+ in a way that cannot be simply predicted. The currently held view about He^+ in the topside ionosphere has been that the He^+ density becomes higher in higher solar activity[16]. The ISS-b results presented above partly confirm and partly deny this view point.

As shown in the figure, the F10.7 dependence of $[He^+]$ is very small when expressed as a global average. If we extend this result to lower solar activity, $[He^+]$ would be not much different from that in the higher solar activity.

At first glance the magnitudes of the correlation coefficients listed in Fig. 119 might seem to be small. However, it can be confirmed by t-tests that the correlations are statistically significant with 99% confidence level because a large number of data points is involved.

In the above treatment, we have simply seen the solar activity dependence of ion densities in a very synoptic way, neglecting dependence on latitude or local time. Next let us examine the solar dependence in a somewhat more detailed manner. In the following treatment, the observed data are sorted into bins of 30° in dip latitude and 6 hours in local time during a four-month period. We then obtain average ion densities, N_i, for each bin and for each four-month term starting from August 1978 with a one-month step. That is, running means are obtained in one-month steps. Of course, this treatment is necessitated because the full diurnal cycle is four months for the ISS-b observations. We assume the following functional functional dependence for N_i:

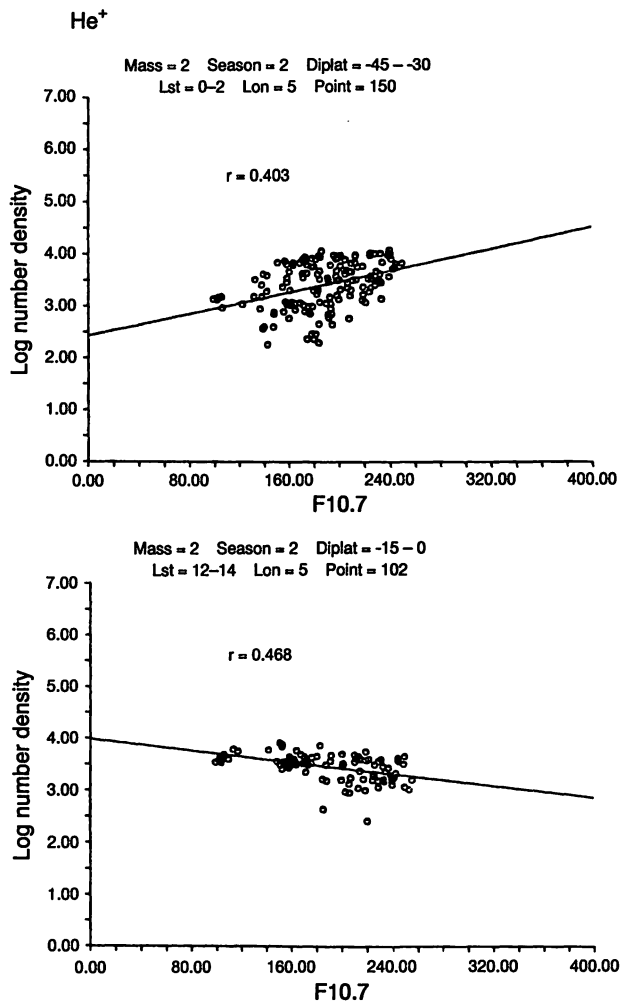

Fig. 120 Correlation between He^+ density and F10.7. a) Positive correlation (b) Negative correlation

$$Log(N_i) = A(1 + B \cdot F10.7)[1 + C\sin(k \cdot M - D)] \quad (126)$$

where M represents the number of months elapsed since August 1978, and k is a constant. The coefficients A, B, C, and D are determined by a non-linear least squares method, "SALS", which was developed by the Computer Center of the University of Tokyo[151].

Figures 121 and 122 show the levels of statistical confidence in the correlations with the solar flux for H^+ and He^+, respectively, in each latitude-LT bin. Lines with positive gradients indicate positive correlations and those with negative gradients, negative correlations. Dense hatching shows a significance of greater than 99%, thinner hatching indicates over 95%, and a single line symbol shows a level of below 95%. As for H^+, there is a highly significant negative correlation in all

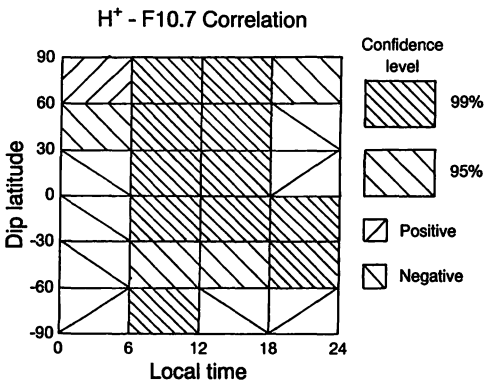

Fig. 121 Distribution of correlation coefficients between H^+ and F10.7 in the dip latitude-local time plane. The line with positive slope shows positive correlation and vise versa. The heavier hatch shows that the level of significance is larger.

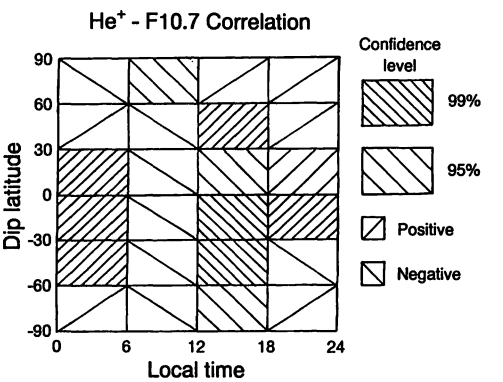

Fig. 122 Distribution of correlation coefficients between He^+ and F10.7 in the dip latitude-local time plane. The line with positive slope shows positive correlation and vise versa. The heavier hatch shows that the level of significance is larger.

latitude bins in the daytime, but this becomes lower at night. A positive correlation appears in a few limited domains. The negative correlation between $[H^+]$ and the solar flux in the global average sense discussed above is well justified by this result. As for He^+, in the daytime most of the regions show negative correlation, but at night more domains of positive correlation appear.

However, the occurrence of positive or negative correlation does not seem to be systematic. Therefore, one should bear in mind that the weak positive correlation found in the global average is based on such distributions. That is, the global average of He^+ density mainly reflect the nighttime condition, because the nighttime density is generally larger than that in the daytime except at the equator, as discussed in the previous section.

Figures 123, 124 and 125 show the amplitude (C) and phase (D) terms for H^+, He^+ and O^+, respectively. Variations due to F10.7 are primarily subtracted from the seasonal terms because of

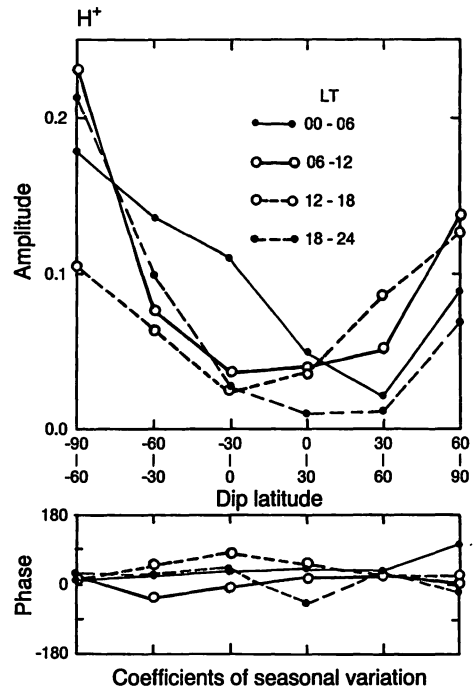

Fig. 123 Latitudinal dependence of the amplitude and phase terms of the seasonal variation of H^+ density.

equation (126), whereas it was not possible in the treatment of the seasonal variations presented in the previous section. For all the three species, the amplitudes tend to be greater at greater latitudes. It is noted that the amplitudes are systematically larger in the southern hemisphere. As for the phase terms, inversion of the phase due to change of season is observed for O^+. In contrast, the phase terms for H^+ do not exhibit seasonal inversion. The He^+ phase terms differ by about 180° compared to O^+ in the daytime reflecting the winter helium bulge, but these take similar values as O^+ at night. These characteristics are consistent with those described in the previous section, where the variations due to F10.7 were not excluded.

In the above description, the influence of geomagnetic activity is not considered. It might be expected that geomagnetic activity would make an important contribution. A multiple regression analysis of the averaged ion densities against F10.7 and Kp has also been tried in a similar way as above, but no significant dependence on Kp has been found from this analysis except at high latitudes. This statistical result is consistent with the statement in the previous section that the distributions of individual passes do not show much Kp-dependent variation.

6.4 Light ion trough (LIT) dependence on geomagnetic activity

As described in the previous section, no clear correlation can be seen between the ion densities and the geomagnetic index, Kp, in the global statistical analyses. Generally the effects of geomagnetic disturbance are different at different latitudes, altitudes, or phases of the disturbance[4].

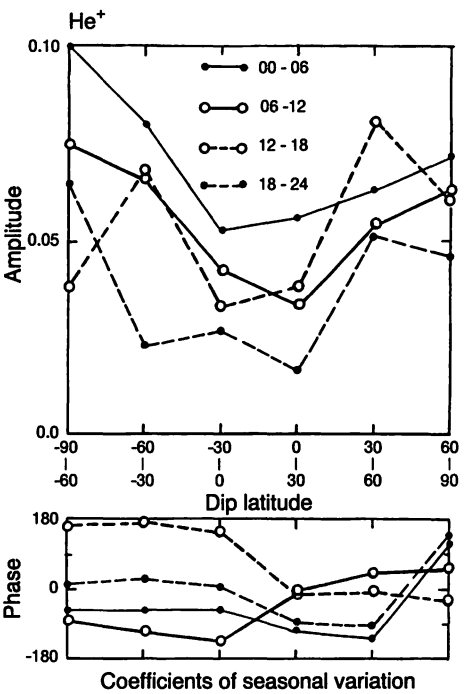

Fig. 124 Latitudinal dependence of the amplitude and phase terms of the seasonal variation of He^+ density.

Therefore the effects of the disturbance, if any, would be canceled out from statistics taken over a long time.

An interesting phenomenon which should be affected by geomagnetic activity is the light ion trough (LIT). The "middle latitude trough" was first discovered in the distributions of electron density observed by the Alouette satellites[152] and was confirmed by an ion trap experiment[153]. Because it was recognized that the trough in the topside ionosphere would be connected through the magnetic field line to the plasmapause observed above the equator, many studies have been devoted to investigating the relationship between them. Observations made by studying whistlers[154] and by the OGO-5[66] revealed that the L-value of the plasmapause position decreased for increasing Kp value, and that it had a distinct bulge in the evening local time. From the observations of the mid-latitude troughs by the Alouette-1 it was pointed out that there were systematic deviations between the positions of the plasmapause and the trough[155][156]. In particular, the trough did not have an evening bulge structure in contrast to the plasmapause. Using ISIS-1, Ariel-3 and -4, similar characteristics have been reported[126][157][158].

On the other hand LIT was found by OGO-2 observations[102]. From the observations of the OGO-4 and -6, it was discussed that LIT, rather than the trough, would have better correlation with the plasmapause[124][125]. Indeed LIT seems to have a more sharply defined wall and to correlate better with the plasmapause than the troughs in the electron density profiles[159]. However, the relation between them has proved to be not so simple[160] and LIT has been shown to have no evening bulge, which was also confirmed by the ISS observations[97].

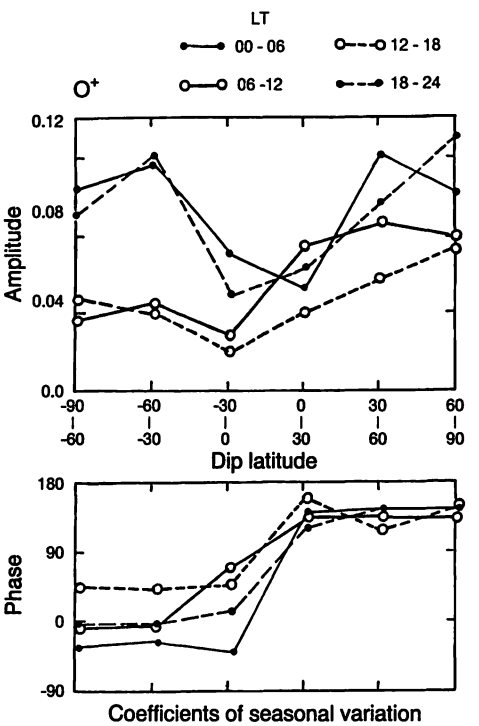

Fig. 125 Latitudinal dependence of the amplitude and phase terms of the seasonal variation of O^+ density.

Consequently, it has been recognized that LIT, the mid-latitude trough and the plasmapause are not necessarily collocated on the same magnetic field line although these occur at positions of similar L-value. More complex ionosphere-plasmasphere-magnetosphere coupling processes seem to exist among these phenomena[127]. Because there have been very few observations at intermediate altitude regions, studies of these phenomena have not been conclusive. The EXOS-D satellite, which will be described in Section 7, is expected to make an important contribution in this respect because its orbit is very suitable.

Previous investigations, such as those made by the OGO series satellites, did not shed light on the relation between LIT and geomagnetic activity. Therefore, let us examine the dependence of LIT on the geomagnetic index, Kp. Because LIT is more sharply defined for He^+ than H^+ in the ISS-b observations as pointed out before, we will examine the LIT in He^+ distributions here. The position of the plasmapause can be defined easily because the plasma density changes by an order of magnitude over a distance of about 0.1 R_E[161]. As for the ionospheric trough, definition of its position is somewhat arbitrary and ambiguous [162]. In previous studies, the position were defined as the maximum gradient of latitudinal profile, the minimum of the plasma density, or the latitude where the plasma density becomes lower than a prescribed value. In all cases, the position of the trough was determined from individual pass plots and then statistical analyses were done in these studies. In the present ISS-b case, because the distance between the consecutive measurements is not small enough (about three degrees in latitude), determination of the trough position by individual pass plot is not accurate so that statistical processing is done first as follows;

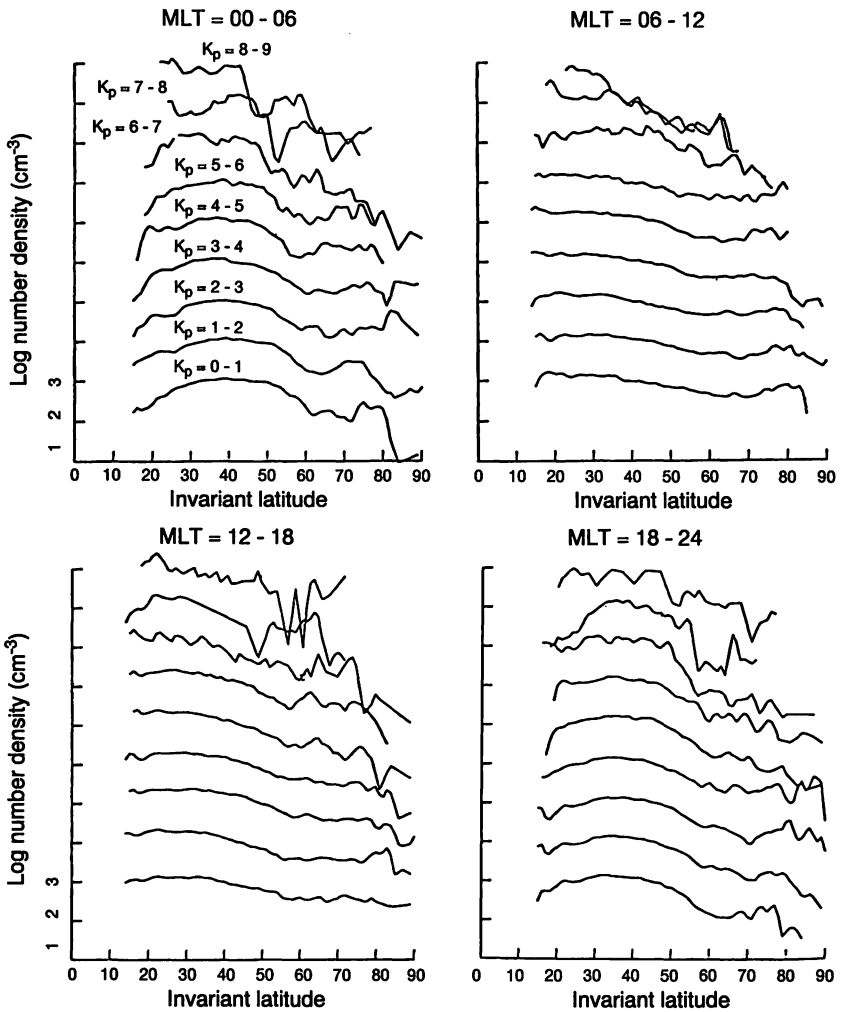

Fig. 126 Dependence of He^+ density averaged for fixed range of Kp values on the invariant latitude. Each curve is shifted by one order for each Kp range.

As shown in Fig. 126, He^+ densities from August 1978 to March 1979 are averaged in the bins of the magnetic local time (MLT) and Kp, these parameters being divided into 4 and 9, respectively. Because there are few data for extremely large value of Kp, the corresponding distribution for large Kp is rather irregular. Regardless of the definition of the trough position, the characteristics of [He^+] dependence on Kp are well displayed in the figure. It is seen that LIT is sharp in the nighttime and its position moves toward lower latitude at larger Kp values. Comparing the curves for 00–06 MLT and 18–24 MLT, we can hardly recognize any bulge structure in the evening side which has been shown to exist in the case of the equatorial plasmapause. In the daytime LIT is generally not pronounced and it is difficult to define its position. From inspection of the nighttime curves, approximate position of LIT, LT, can be defined by

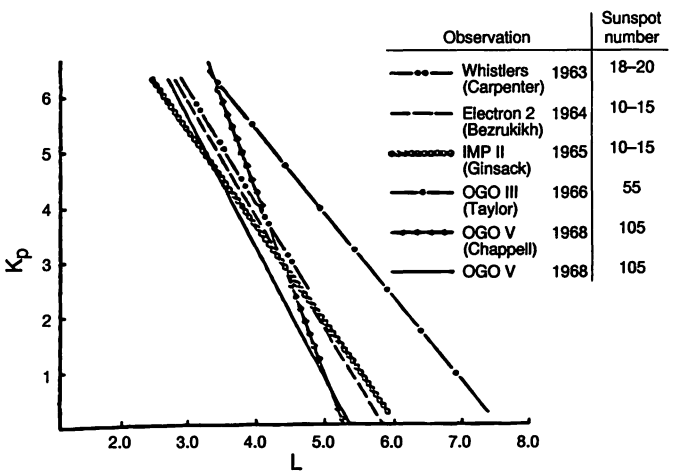

Fig. 127 Correlation between the position of plasmapause and Kp-index [after Serbu and Maier, 1970[161]].

ISS-b He^+ (1100 km)[98]

$$LT = 4.52 - 0.3Kp \quad (127)$$

The previous results by other authors are as follows: Ariel-4 Ne (550 km)[158]

$$LT = 4.85 - 0.37Kp \quad (128)$$

ISIS-1 Ne (3500 km)[126]

$$LT = 4.65 - 0.23Kp \quad (129)$$

Alouette-1 Ne (1000 km)[156]

$$LT = 5.64 - (1.09 \pm 0.02)\sqrt{K_p} \quad (130)$$

On the other hand, the results for the plasmapause position are quoted in Fig. 127 from Serbu and Maier[161], and these are summarized as

$$LP = (5 \sim 6) - 0.5Kp \quad (131)$$

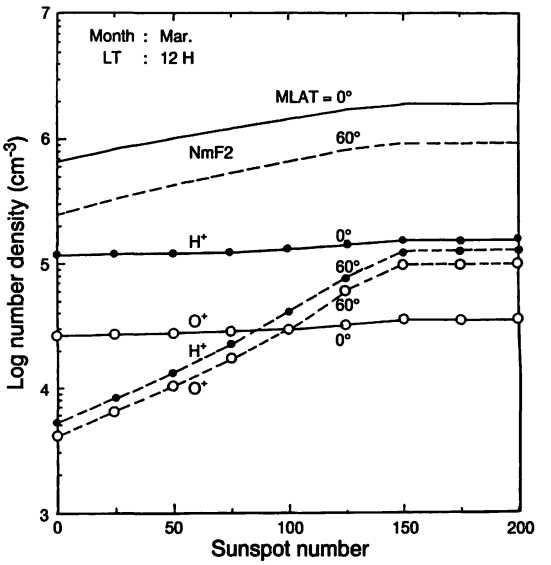

Fig. 128 Calculated dependence of H^+ and O^+ densities by IRI model at 0 and 60 degrees latitude and 1100 km altitude.

From these results it is concluded that the L-value of the trough position is generally smaller than that of the plasmapause, and that the dependence on Kp is also smaller for the trough than for the plasmapause. The result from ISS-b using He^+ distributions is also consistent with these previous results obtained by different methods. What is new in the present treatment is that LIT in the He^+ distribution is shown to have a clear Kp dependence, and that statistical averaging is done without defining the position of the trough in the individual profiles. This approach is convenient for gaining statistical insight regardless of the strict definition of the trough.

6.5 Comparison with IRI model

The International Reference Ionosphere (IRI) is most frequently used to model various aspects of the ionosphere, including ion composition. It is a purely empirical model derived from the data of worldwide ionosonde, rocket and satellite experiments and IS radars. In this section we will compare the ISS-b results presented above with the IRI model.

Figure 128 shows the relationship between NmF2 and ion densities of H^+ and O^+ at 1100 km altitude, and the sunspot number calculated by the IRI-86 model. Here the input parameters are selected as month = March, LT = 12 hours, geomagnetic latitudes = 0, and 60. For NmF2, the gradients of the curves for latitudes of 0 and 60 are not very different and their general tendency is consistent with the results obtained from the ISS-b shown in Fig. 119, although this comparison is not very strict.

In the IRI-86 model, values of NmF2 for Rz greater than 150 are clipped to for Rz = 150. This measure was introduced because the electron density had a tendency to saturate for higher sunspot numbers from observations by the INTERCOSMOS-19 satellite[163].

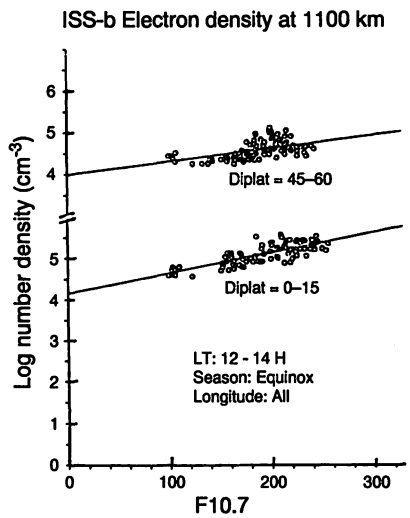

Fig. 129 Correlation between F10.7 and the electron density at 1100 km altitude observed by ISS-b.

During the ISS-b observation period, the maximum value of Rz reached 200. However, as shown in Fig. 119, the tendency of such saturation for NmF2 is not noticed. As for the electron density at 1100 km, an example of no such saturation is shown in Fig. 129. In these figures, F10.7 is used instead of Rz. (An almost linear relationship between F10.7 and Rz holds, and Rz = 200 corresponds to F10.7 = 240).

Therefore according to the ISS-b observations, the clipping of NmF2 for Rz greater than 150 introduced in the IRI-86 model seems to be unnecessary. Close examination of the data by Benkova et al.[163] showed that the spread of data is quite large and that the area and period of observations are restricted. It seems premature to introduce conclusive measures to the IRI model from their observations alone. The ISS-b observations indicate that extension of the original CCIR model up to at least Rz = 200 seems to be appropriate.

The IRI model in Fig. 128 shows that the dependence on the sunspot number becomes stronger at higher latitudes. Figure 130 shows the latitudinal distribution of the regression coefficients between Ne at 1100 km and Rz derived from daytime observation data obtained by ISS-b. This figure indicates that the regression coefficient tends to be larger at lower latitudes. The extremely large coefficient for higher latitude seen in the IRI-86 model is not observable in the ISS-b observations. Another problem with the IRI-86 model is that the major ion species at 1100 km altitude is taken to be H^+, whereas ISS-b observations showed that it was O^+ during periods of high solar activity as shown in Fig. 119. H^+ has negative correlation with the solar activity, and predominance of H^+ at 1100 km altitude is only expected during very low solar activity. This feature should be taken into consideration in the next improvement of the IRI model.

As for the seasonal variation of the electron density at 1100 km altitude, Fig. 131 compares the results from ISS-b with those from IRI-86. Although the conditions under which these results were derived are not strictly the same, this figure also suggests a problem in the IRI-86 model. According to the ISS-b results, the electron density at high latitude varies by about one order of magnitude with changes of season, while the IRI-86 model shows very little variation.

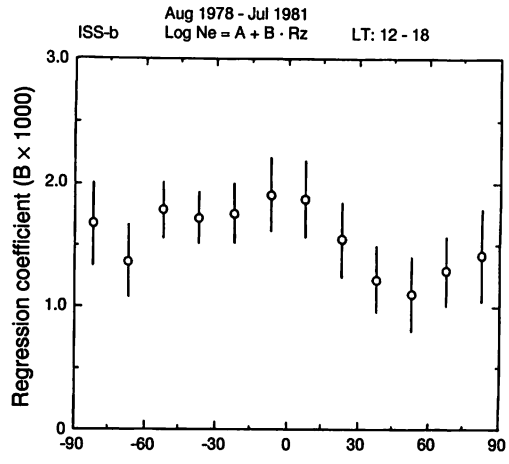

Fig. 130 Latitudinal variation of the regression coefficient between the sun spot number (Rz) and the electron density at 1100 km altitude observed by ISS-b.

Figures 132 and 133 compare the dependencies on latitude and LT, respectively, of the ISS-b and IRI-86 results. For these characteristics, agreement between the two is generally good. As for the ion composition, the IRI model assumes the ratio between H^+ and He^+ to be constant, that is 10:1. This is of course a crude approximation as admitted by the model's developer[10]. This approximation was obliged to be incorporated because there were very few observations on the ion composition of the topside ionosphere. ISS-b has provided a good data base to improve this situation because it observed global regions for an extended period.

From the global average shown in Fig. 119, the period when the ratio $[H^+]/[He^+]$ is equal to about 10 at 1100 km altitude is expected during very low solar activity. Because H^+ and He^+ have opposite sign correlations with solar activity, this ratio decreases with increasing solar activity and the densities of the two constituents become comparable when F10.7 is about 250 (or Rz ~ 200).

Figure 134 shows the distributions of the ratio $[H^+]/[He^+]$ in the geomagnetic latitude versus the LT plane derived from the ISS-b data. Distribution (a) is produced by the data obtained from January 1979 to May 1979, and (b) corresponds to the period from January 1980 to May 1980. The patterns in (a) and (b) are very similar but very complex. The ratio is large at low and high latitudes due to the marked equatorial trough and light ion trough in the He^+ distributions.

While the ISS-b observations have provided the horizontal distributions of the ion composition at 1100 km altitude, the IRI model puts a stress on altitude distributions. It seems a little difficult to incorporate the ISS-b results into the IRI model because of the way in which the IRI program is structured. Further studies are needed in these respects.

7. Measurement of magnetospheric ions

7.1 Review of magnetospheric ion composition

Ionospheric plasmas in the low and middle latitudes have "cold" temperatures of below a few thousand degrees, and they can be measured by mass spectrometers which are not capable of energy

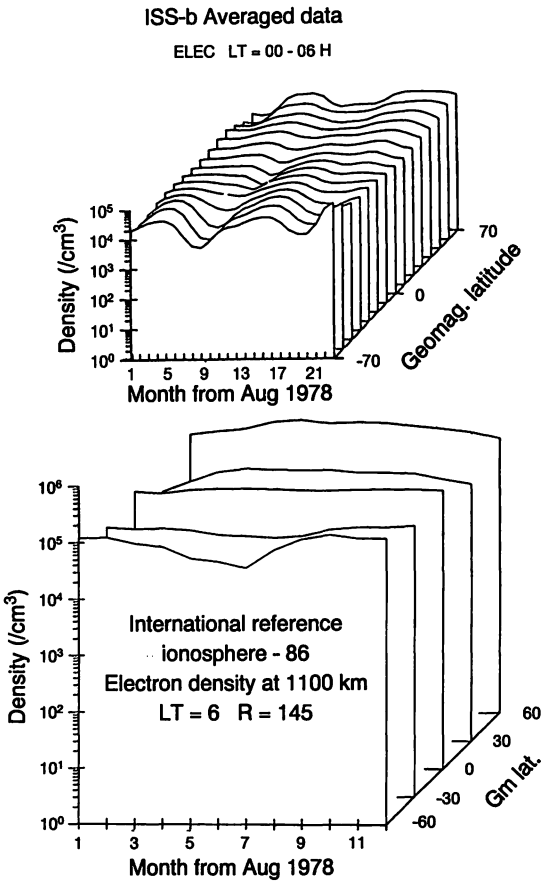

Fig. 131 Comparison of the seasonal variations between modeled (IRI-86) and observed (ISS-b) electron densities at 1100 km altitude.

analysis. On the other hand, the magnetospheric plasmas have higher temperatures, and the ions have frequently been observed to be accelerated to high energies. In particular, the ions in the auroral region have been found to be in a supra-thermal or energetic state. When the ions have appreciable initial energy, conventional mass analyzers, such as the Bennett type or magnetic sector type, cannot function well. An energy analysis function must be added to measure these ions properly. The first mass spectrometer which had an energy analysis function for detecting magnetospheric ions was developed in the early seventies. The Lockheed group at Palo Alto[67] discovered highly accelerated O^+ at 800 km altitude in the polar region flowing along magnetic field lines using an RPA combined with a Wien-filter which was flown on the 1971-089A satellite. They also found a large field-aligned flux of O^+ at a high altitude of 8000 km by an improved detector on the S3-3 satellite[164]. These unexpected discoveries focused a great deal of attention on the acceleration mechanism in the magnetosphere. Similar mass and energy analyzers were developed for GEOS-1[165], GEOS-2[166], ISEE-1[167], DE-1[168], and AMPTE/CCE[169]. A group in the Marshall Space Flight Center, NASA, developed "Retarding Ion Mass Spectrometer (RIMS)", in which an RPA and a magnetic sector mass spectrometer are combined, for the Scatha satellite[164], and for the DE-1[71]. The DE-1 RIMS has

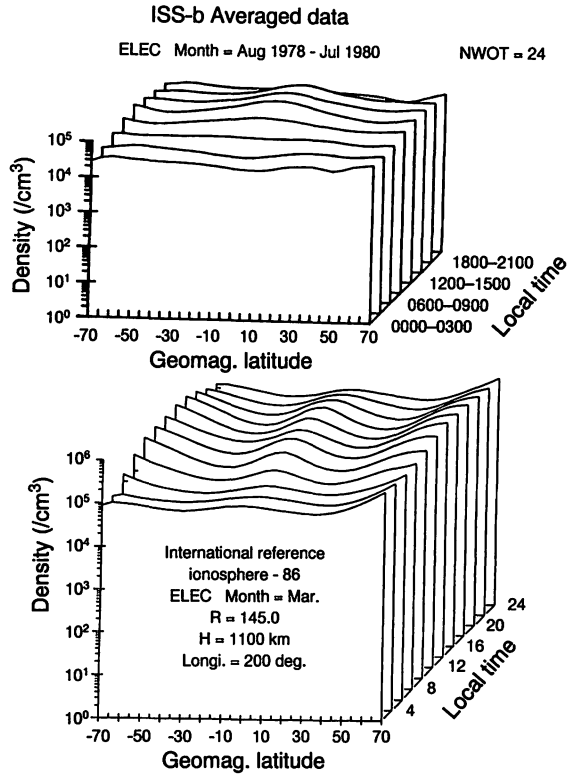

Fig. 132 Comparison of the latitudinal variations between modeled (IRI-86) and observed (ISS-b) electron densities at 1100 km altitude.

three sensors and is suitable for detecting pitch angle distributions of low-energy ions. A group from Sweden and USSR flew an instrument in which a Wien-filter and a semispherical electro-static analyzer were combined on the PROGNOZ-7 satellite (PROMICS-1 experiment) to observe the deep magnetospheric mantle region and they found O^+ ions transported from the ionosphere[170].

We proposed a mass and energy analyzer, incorporating an RPA and a Bennett mass spectrometer, for the 12th Japanese scientific satellite[171], and launched "SMS" (Supra thermal and energetic Mass Spectrometer on the EXOS-D satellite (or Akebono) cooperating with a group in HIA/NRCC (Herzberg Institute of Astrophysics, National Research Council Canada)[86][172]. The SMS has been successfully observing the supra-thermal and energetic ions in the magnetosphere. We also proposed a similar spectrometer for the Japanese planetary mission[173]. The following describes the characteristics of the instruments which have been developed by our group to measure the supra-thermal and energetic ions in the magnetosphere and ionosphere.

7.2 Energy and mass analyzer with energy deceleration

Figure 135 shows a cross sectional view of a spectrometer developed for simultaneous mass and energy analyses of low energy ions in the ionosphere and magnetosphere[171][174]. The analyzer consists of an RPA, a Bennett mass spectrometer, two parallel plate electro-static analyzers and a

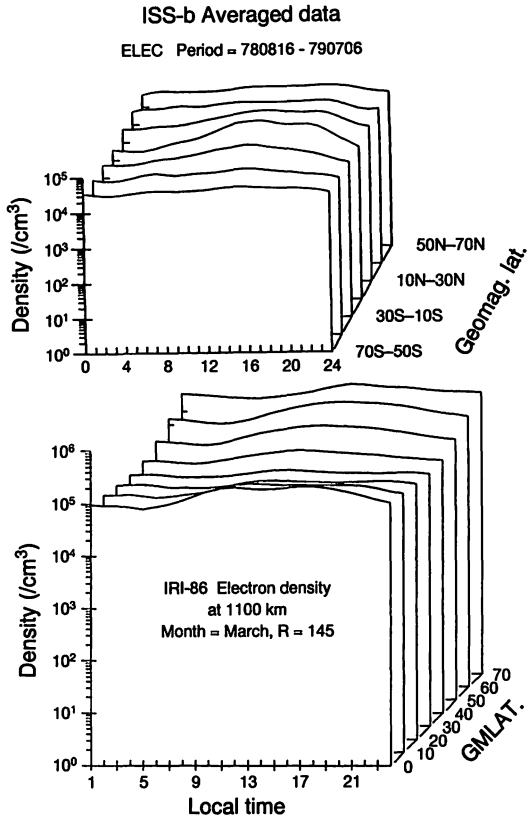

Fig. 133 Comparison of the local time variations between modeled (IRI-86) and observed (ISS-b) electron densities at 1100 km altitude.

channel electron multiplier. The voltage applied to the entrance grid draws the ambient ions into the instrument in such a case when the spacecraft has positive potential relative to the space plasma. In the high altitude magnetosphere, the spacecraft is frequently charged to a positive potential because the plasma density is so low that the emission of photoelectrons from the surface cannot be compensated for by the ambient plasma. Such negative draw-in voltage has been reported to be partly successful in the case of the DE-1 satellite[54][71].

The voltage V_R gives a retarding potential to the entering ions and acts as a high pass filter for the ion energy. The Bennett section operates similarly as described in Section 4, but decelerated ions are selected in this case. The acceleration and deceleration in the Bennett tube are completely equivalent. A difference arises from the entrance phase angle relative to that of the applied RF field. Therefore the transmission and resolution are given by the same formula as deduced in Section 4.

The parallel-plate electro-static analyzer with an inclination of 45 degrees to the instrument axis acts as a low pass filter for the ion energy. This filter deflects only those ions which have lost maximum energy in the RF field in the direction of the detector. Because parallel-plate analyzers have a focusing property at 45 degrees[175], they collect resonant ions. The combination of two parallel plates also define the field of view. We define the z-axis along the axis of analyzer, with the x-axis normal to the paper, and the y-axis perpendicular to both axes. If we let the ion deflecting

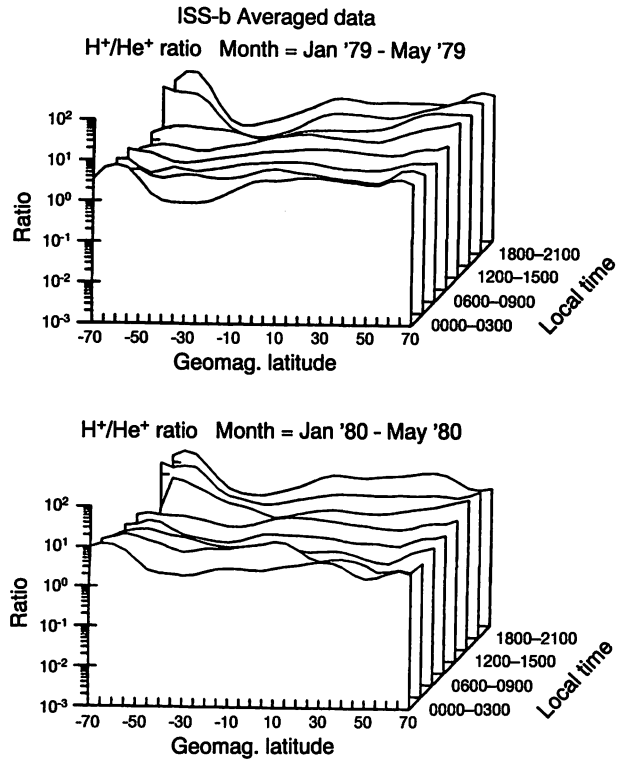

Fig. 134 Latitudinal distribution of [H⁺]/[He⁺] ratio. (a) Average during January–May, 1979 (b) Average during January–May, 1980

voltage be V_R - (V_A + ΔV), where V_A is the accelerating voltage as described in Section 4, and if we let β be the incidence angle of ions in the y-z plane against z-axis, then it can be deduced[171] that the pass band of ions in the β-Ez plane is given by the shaded area in Fig. 136, where Ez is the energy in the direction of the z-axis. From this figure, the energy pass band is equal to $2\Delta V$ regardless of the initial ion energy. This feature is very different from the case of a conventional spherical or semi-spherical electro-static analyzer, where the pass band and resolution are proportional to the initial energy. It can be also seen from Fig. 136 that the field of view in the y-z plane, $\Delta\beta$, is given by

$$\Delta\beta = \Delta V / \sqrt{(V_A \cdot V_R)} \quad \text{..... (132)}$$

Similarly the field of view in the x-y plane, $\Delta\alpha$, can be readily derived from geometrical consideration[171] as

$$\Delta\alpha = (R_i / l)\sqrt{V_A / V_R} \quad \text{..... (133)}$$

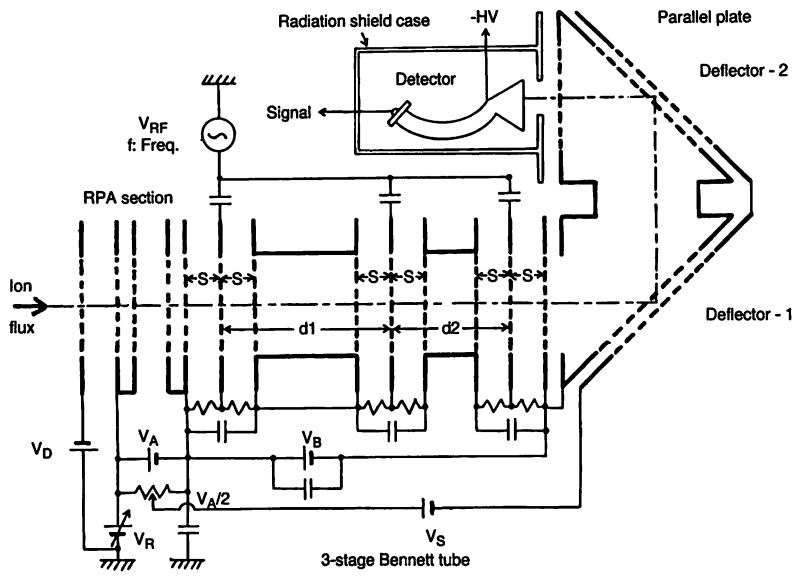

Fig. 135 Improved Bennett mass spectrometer which can analyze energetic ions in the magnetosphere.

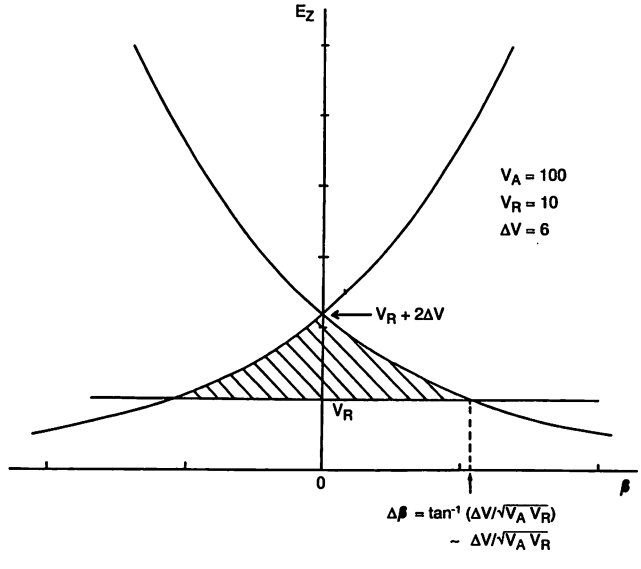

Fig. 136 Energy pass band of the improved mass spectrometer.

where

R_i radius of the entrance aperture

l pass length of the ions.

The geometrical factor or transmission coefficient, G, of this instrument is defined as

$$G = \eta \cdot S \cdot \Delta\alpha\Delta\beta \quad \text{..... (134)}$$

where

η transmission coefficient due to grids

S area of the aperture.

Substituting (132) and (133) into (134) we get

$$G = \eta \cdot S(R_i / \cdot)(\Delta V / V_R) \quad \text{..... (135)}$$

From this expression we can see that this instrument has high sensitivity in the low energy range. A prominent feature is that the sensitivity and resolution can be regulated by changing ΔV. In contrast to these properties, the G-factor of conventional electro-static analyzers becomes small in the low energy range, and the resolution is fixed mechanically. These unique features of the present analyzer complement those of conventional analyzers for observation of the magnetosphere and ionosphere.

7.2.1 Results of laboratory testing

In order to demonstrate the operation principle described above, a bread-board model was manufactured and tested in the laboratory. For simplicity the Bennett section was of two-stage design (see Section 4). The results are shown in Figs. 137, 138 and 139. Figure 137 shows the energy spectra obtained when the energy resolution, ΔV, was stepped. Incident ions in this case were He^+ with a nearly monochromatic energy of 40 eV and an RPA voltage which was swept from 0 to 72 volts. The figure confirms that energy pass band is proportional to ΔV, as expected from the theory above.

Figure 138 shows the energy spectra obtained when ΔV was fixed to 2 volts and the incident energy was stepped from 5 to 40 eV. This figure shows that the energy resolution is essentially constant regardless of the incident energy, as expected from the theory. Figure 139 shows mass spectra obtained when ΔV was stepped with the incident energy fixed. When the resolution is low, spurious peaks appear due to harmonic effects as in the case of an ordinary Bennett mass spectrometer. The mass resolution measured in this case is confirmed to be near the value expected from the theory for a 2-stage 2-cycle analyzer (see Section 4).

7.3 Ion mass spectrometer on EXOS-D satellite

Japan's 12th scientific satellite, EXOS-D, was planned to investigate the acceleration region of auroral particles and was launched on February 22, 1989 into an orbit of 270 km in perigee, 10,500

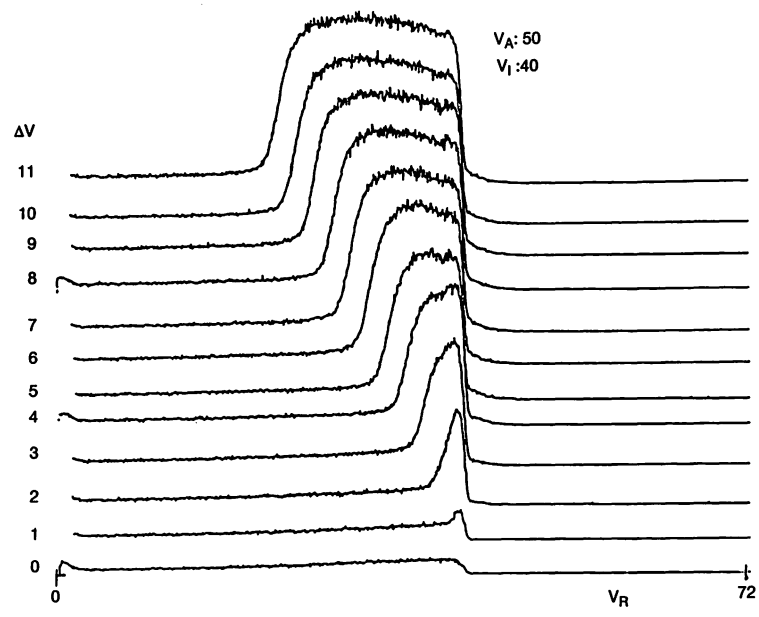

Fig. 137 Results of Energy resolution test of the improved mass spectrometer. ΔV is stepped with the energy of the incident ions kept to 40 eV.

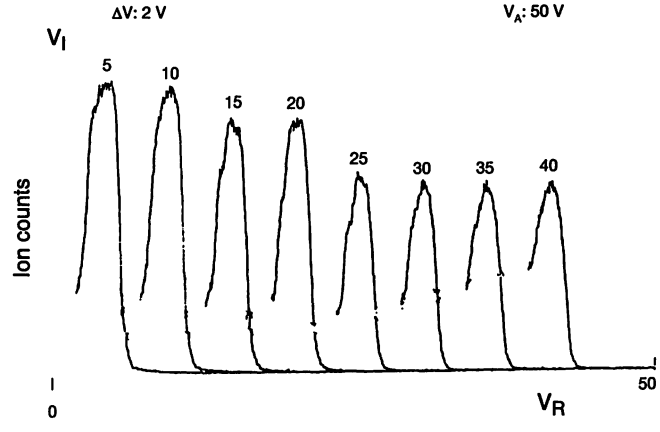

Fig. 138 Energy resolution of the improved mass spectrometer. The energy of incident ions is steeped with ΔV kept constant.

km in apogee and 75 degrees in inclination angle[176]. We proposed using the decelerating mass spectrometer described in the previous section, but an improved version was developed in conjunction with Canadian scientists. A cross sectional diagram of this instrument is shown in Fig. 140. This instrument was named the SMS (Supra thermal and energetic Mass Spectrometer) and has been successfully observing magnetospheric and ionospheric ions[172]. Table 8 shows the principal charac-

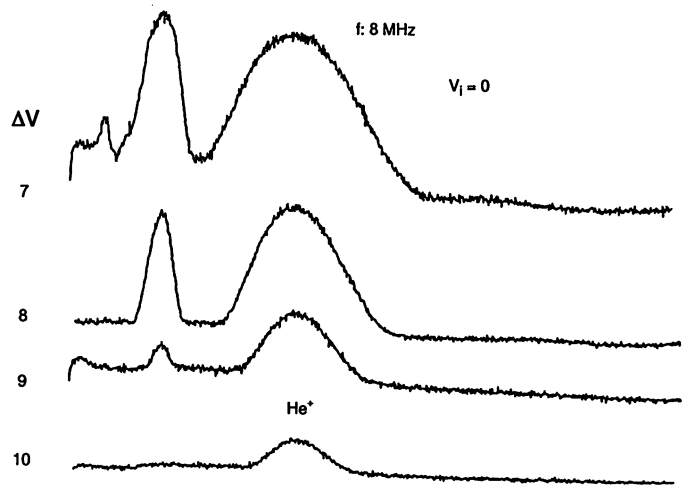

Fig. 139 Mass spectra when ΔV is stepped.

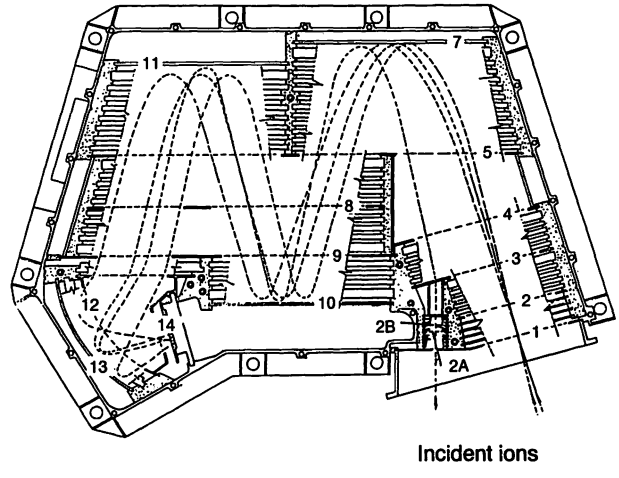

Fig. 140 Cross sectional view of the mass spectrometer on EXOS-D (SMS) [after Whalen et al., 1990[172]].

teristics of this instrument. It operates in much the same way as those described in the previous section, but many new ideas are incorporated. These are presented below.

7.3.1 Principle of operation

DC and/or AC voltages are applied to the grids or electrodes numbered in Fig. 140. A voltage of 0 to -10 volts is applied to grid 1 to draw in the ambient ions. This voltage also serves to prevent a large flux of low energy electrons from entering the analyzer in the energetic modes described below. Otherwise these electrons would cause a considerable amount of noise.

Table 8 Characteristics of SMS.

Mass Range	$0.8 < M < 60AMU$
Energy Resolution	$0.05 < \Delta E < 0.2keV$ variable
Mass Resolution	$0.05 < \Delta M/M < 0.2$ variable
Energy Range	$0 < E/Q < 4keV$
G-Factor	$4 \times 10^{-8} < G < 2 \times 10^{-2}$ variable
Angular Resolution	
In the Spin-plane	$3 < \Delta\theta < 90$ deg
In the Plane perpendicular to Spin	$3 < \Delta\theta < 90$ deg

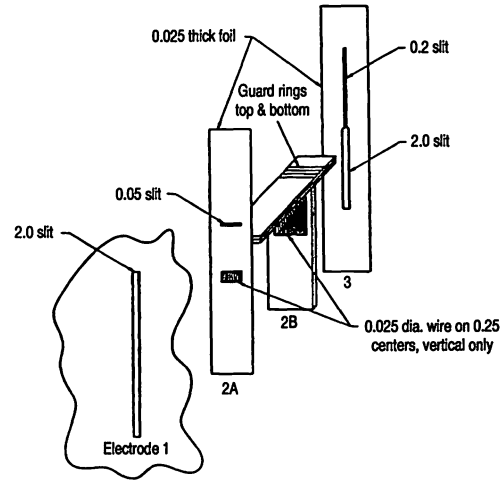

Fig. 141 Aperture of SMS [after Whalen et al., 1990[172]].

One of the outstanding properties of this instrument is that it has three kinds of apertures to control its sensitivity. As shown in the figure, the ions enter the analyzer either through grid 1 of the large aperture or through electrodes 2A-2B. When the large aperture is selected, V_{2A} is set to +50 V and thermal ions are prevented from entering through this electrode into the analyzer. Passing through grid 1, the ions are analyzed by an RPA voltage applied to grid 2.

When the satellite is in the lower ionosphere, where there is a large density of ions, grid 2 is biased to +50 V to stop these thermal ions from entering through the large aperture and ions are admitted through the 2A-2B section. The detailed configuration of this part is shown in Fig. 141. In the thermal mode, electrode 2A is biased to the same voltage as that applied to grid 1, V_1. In the energetic mode when the ion flux is small, electrode 2A is biased to +50 V. As shown in the figure, two slits of 5 mm (medium aperture) and 0.05 mm (small aperture) are made in electrode 2A. When the small aperture is selected, V_{2B} is set to +50 V to prevent entrance through the medium aperture. When the medium aperture is selected, V_{2B} is set to the average value of V_{2A} and V_3. The ratios of the three apertures are 1:100:10000. By selecting an appropriate aperture from the three, a very wide dynamic range of the sensitivity can be achieved.

After passing through the RPA stage, the ions are pre-accelerated by V_3 (-20 V) and further accelerated by V_4 to an energy of 1 kV regardless of the incident energy. That is, $V_4 = V_{RPA}$ - 1 kV. Grid 5 has the same potential as grid 4, and no acceleration occurs in this space. Reflecting electrode 7 is inclined 15 degrees away from grid 1 and it is biased to $V_7 = V_5 + 1$ kV (= VRPA).

In the thermal mode $V_7 = 0$ V and if an incident ion has energy $E < [\cos^{-2}(15°) - 1]$ keV, that is, if $E < 72$ eV, the ion will be transferred to the next stage. Thus in the thermal mode, the ions which have an energy of less than 72 eV are analyzed. On the other hand in the energetic mode, since $V_2 = V_{2A} = V_{2B} = +50$ V and $V_7 = 0.1$–4 kV, the ions which an energy of 50 eV to 4 keV can be analyzed. Thus an essential energy analysis is done by V_7 in the energetic mode.

An RF voltage, $V_{RF} = 100$ Vpeak is applied to grid 8. Electrodes 10 and 11 are biased so as to reflect all the incident ions. In this way, this portion constitutes a folded Bennett mass spectrometer. The ions are accelerated (or decelerated) by the RF voltage in the same way as described in Section 4 so that the mass number, M, of resonant ions is given by

$$M(AMU) = 0.2636\,V(volts)/[s^2(cm)f^2(MHz)] \quad (136)$$

where s is the spacing between grids 8 and 9, f is the frequency of RF voltage, and V is the accelerating voltage. The following parameters were selected for the SMS on EXOS-D:

$$s = 3.06\ cm \quad (137)$$

$$\mathrm{f} = 0.7 - 6\ \mathrm{MHz} \quad (138)$$

$$\mathrm{V} = 1\ \mathrm{kV} \quad (139)$$

Therefore

$$M = 0.8 - 60\ \mathrm{AMU} \quad (140)$$

M is stepped by changing the frequency f of the RF voltage. As a special case, the RF voltage can be switched off, in which case energy analysis can be done without mass analysis (RPA mode). The reflector plates 10 and 11 are so arranged that the resonant ions pass grid 8 with delays of 2 cycles and 3 cycles, respectively, from the last acceleration by the RF field. That is, this portion constitutes a three-stage 2-3 cycle Bennett analyzer as described in Section 4. The maximum energy increment, ΔE, given to the resonant ions is

$$\Delta E = 3 \times 1.45\,V_{RF} = 435\ volts \quad (141)$$

Grid 12 and electrode 13 constitute a concentric cylindrical electro-static energy analyzer. The ions

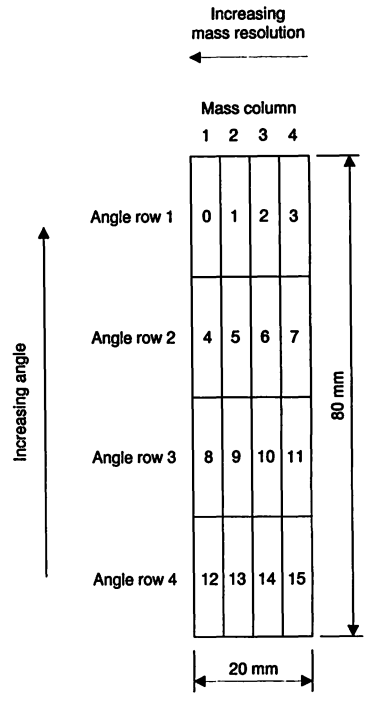

Fig. 142 Configuration of the anode of MCP [after Whalen et al., 1990[172]].

are dispersed according to their energy in the surface of the micro channel plate (MCP). As shown in Fig. 142, the anode of the MCP is divided into 4 x 4 pixels; the columns of pixel 1 to 4 correspond to high to low ion energies.That is, high energy corresponds to high mass resolution and low energy to low resolution. The pixel rows represent the entrance angle with respect to the plane shown in Fig. 140 in the small or medium aperture mode. The principle is similar to a pin hole camera. Since the entrance aperture is aimed perpendicular to the spin axis of the satellite, the smaller the pixel row number, the larger the angle from the spin axis. Four independent counters are prepared for the 16 MCP pixels, and Fig. 143 shows 8 kinds of binning modes. An appropriate binning mode is selected for real observation and the ion counts from these four counters are sent to telemetry.

7.3.2 Ground tests

A typical example of a mass spectrum taken by SMS during the ground tests is shown in Fig. 144. The ion counts are displayed by gray scales in the frequency-energy plane. He^+ ions accelerated to about 1 kV were injected into the SMS, which was set to the energetic mode with V_7 fixed to 1 kV, and counter 3 of binning mode 3 was used. It is seen that good mass resolution is achieved at 2.95 MHz, which corresponds to He^+, and the energy pass band is about 100 eV.

Figure 145 shows the mass spectra obtained from column 2 (high resolution) and column 4 (low resolution) under the same conditions as above.

Simulated results are also shown in the figure, which show a reasonable agreement with the experiment. The slightly higher background count in the spectrum from column 4 is considered to be

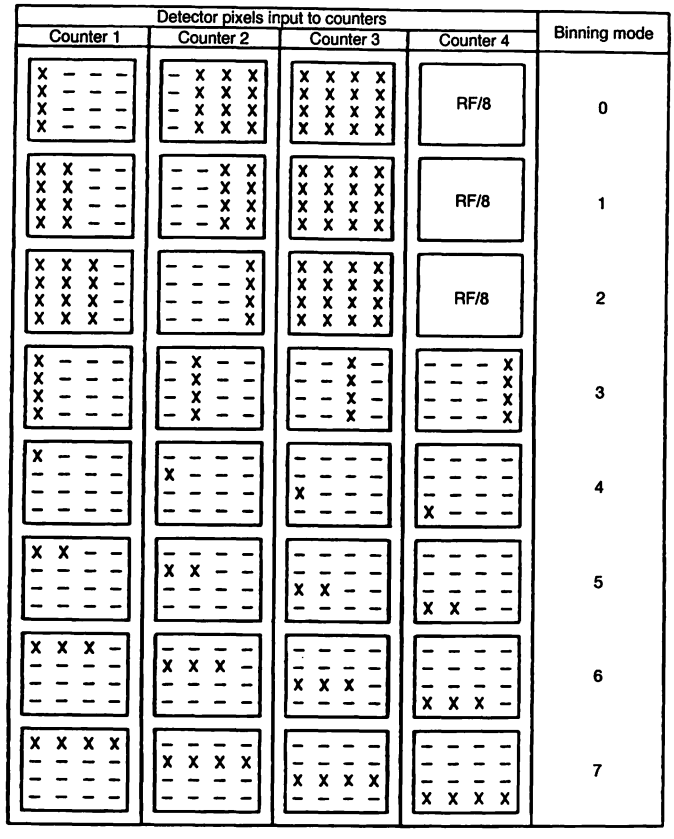

Fig. 143 Binning mode of the ion counters [after Whalen et al., 1990[172]].

due to some specific feature of the MCP used for this instrument. Figure 146 shows an example taken in the thermal mode, using an ion source similar to that shown in Fig. 51. This ion source did not have a mass separation capability, and hence ion species of the residual gas in the vacuum chamber were also detected, although the principal input gas was Ar. The energy of the ions was about 8 eV, V_{RPA} = 0 V, and V_2 = 50 V (medium aperture). It is noted that O_2^+ and N_2^+ are well discriminated by this instrument. This means that SMS has the highest class of mass resolution among similar instruments so far launched to measure the magnetospheric ion composition. (Although of course such a capability is still primitive when it comes to measuring the thermal plasma in the ionosphere.) Figure 147 shows the RPA characteristics taken under the same conditions as the previous figure. It shows sharp cut-off at VRPA = 8 V for 8-eV Ar^+ ions.

7.3.3 Observational modes

As shown in Table 9, SMS has many parameters which must be set to appropriate values according to the specific observational purposes, orbital conditions and so on. In order to organize the parameter setting, "mode components" are defined as in Table 10. The first character of each mode component name represents the following energy range of the observation

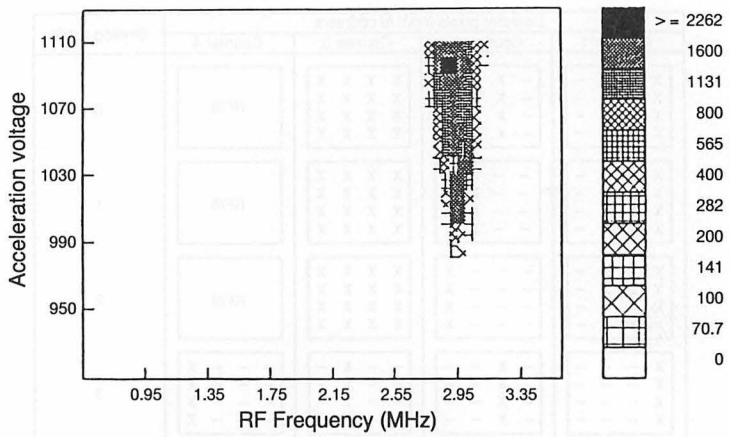

Fig. 144 Performance of SMS in the ground test. SMS is in the energetic mode with V_7 kept to 1 kV. The energy of the incident ion, He^+, and the frequency of RF field are changed [after Whalen et al., 1990[172]].

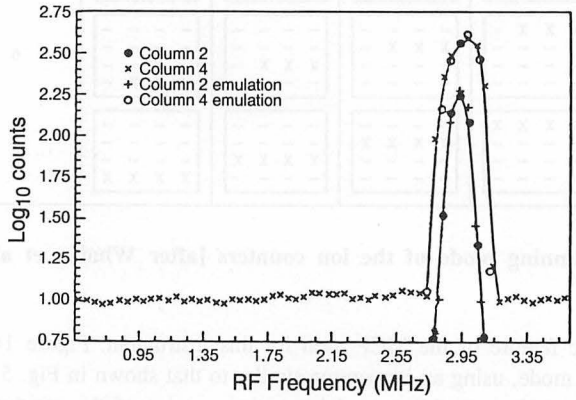

Fig. 145 Mass spectra obtained in the same condition as the previous figure [after Whalen et al., 1990[172]].

E Energetic (50 eV < E < 4 keV)

S Supra thermal (10 eV < E < 50 eV)

T Thermal (0 eV < E < 50 eV)

The second and third characters represent the following:

MS Mass Survey

HS Heavy ion Survey

EM Energy Mass scan

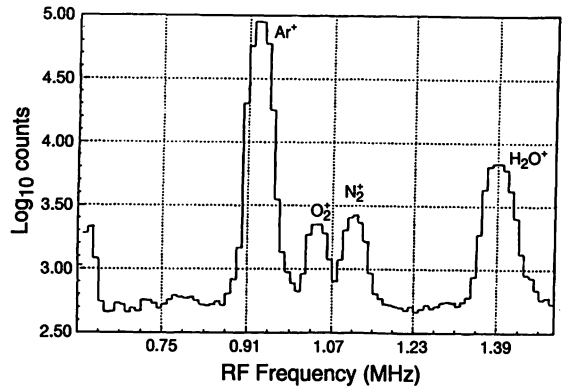

Fig. 146 Performance of SMS in the ground test when the thermal mode is selected.

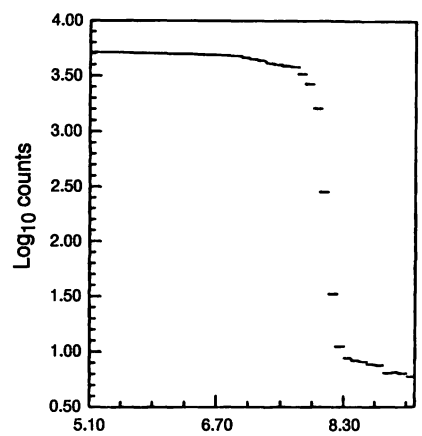

Fig. 147 RPA characteristics with the same condition as the previous figure [after Whalen et al., 1990[172]].

ME Mass Energy scan

DV Drift Velocity

EQ E/Q scan

The numbers and characters after the name in the table show the number of scan steps in mass (M) and in energy (E). For example, the scan sequence "64M T 8S 16E" means that the mass is scanned in 64 steps (64M), then these data are transmitted (T), this measurement is repeated 8 times in one spin period (8S), and finally the entire sequence is repeated for 16 steps in energy value (16E). The symbols in Iter. Type represent the following meaning:

E Sawtooth scan

ET Triangular scan

L Stepping in arbitrary values

Table 9 Variable parameters for SMS and their ranges.

Parameter	Symbol	Step	Variable Range
Draw-in Voltage	V_1	4	0 ~ 10 V
Aperture	AP	4	3 kinds
Energy	E	273	0 ~ 4kV
Mass	M	256	0 ~ 72AMU
Binning Mode	B	8	
Counter	C	4	
MCP Voltage	V_{MCP}	256	1250 ~ 3325 V
RF Voltage	TL	16	186 ~ 217 V

Table 10 Mode components of SMS.

MC Name	MC Msg ID	Scan Sequence Inner loop → outer loop	Mass Iter Type	Mass Scan Range	Energy Iter Type	Energy Scan Range	BM	IE
EMS01	01	64M T 8S 16E	ET	4–256	ET	257–272	Y	
TMS01	0A	64M T 8S 16E	ET	4–256	L	1–255		
EHS01	11	32M 2S T 8S 4E	ET	191–222	E	257–263		
THS01	1A	32M 2S T 8S	ET	191–222	-	0		
TEM01	2A	8E 4M 4S T 8S	L	4–168	L	1 -128		
TEM02	2B	4E 8M 4S T 8S	L	45–256	L	4–225		
TEM03	2C	16E 8S T 8S 4M	L	4–168	L	1–255	Y	
TEM04	2D	16E 2M 4S T 8S	E	4–168	L	8–248		
EME01	31	8M 16E T 8S	L	4–205	ET	257–272		
EME02	32	4M 4E 8S T 4S	L	4–268	E	269–257		
EME03	33	16E 2M 4S T 2S	E	4–168	ET	257–272		
EME04	34	4E 4M 8S T 8S	L	4–168	E	257–260		Y
EDV01	41	16E 8S T 2S 4M	L	4–168	ET	257–272		
TDV01	4A	16E 8S T 8S 4M	L	4–168	L	1–255		
TDV02	4B	32E 4S T 8S 2M	L	4–168	L	1–255		
TDV03	4C	32E 4S T 8S 2M	E	4–168	L	1–102		
TDV04	4D	8E 16S T 8S	-	168	L	20–76		
EEQ01	51	16E 8S T 2S	-	0	E	257–272		
TEQ01	5A	8E 16S T 8S	-	0	L	20–76		
CALMCP	A0	16MCP 4S T	-	168	-	0		
CALRF	A3+	256M T	-	1–256	-	266		
CALTL	A1	128M T 4S 8TL	E	118–245	-	266		
CALV1	A2	4V1 8E 2S T 8S 2M	E	4–168	E	0–210		
IHmode	B3+							
MCPITO	BA							

Table 10 Mode components of SMS.—continued

MC Name	MC Msg ID	Scan Sequence Inner loop → outer loop	Mass Iter Type	Mass Scan Range	Energy Iter Type	Energy Scan Range	BM	IE
SNAP-SHOT	B0+							
TEST_PAT	B2							

Table 11 Length of time interval and amount of data needed for mode components.

	Duration		RF Check Period	Number of MC Data Message		Data Bytes		Data Bytes Accumulated at the Lowest Level
	In Spins	In sec	(sec)	Total	Per Spin	Per Message	Per Spin	
EMS01	16	128	128	128	8	256	2048	256
TMS01	16	128	128	128	8	256	2048	256
EHS01	4	32	32	32	8	384	3072	256
THS01	1	8	8	8	8	384	3072	256
TEM01	1	8	8	8	8	384	3072	128
TEM02	1	8	8	8	8	384	3072	128
TEM03	4	32	32	32	8	256	2048	256
TEM04	1	8	8	8	8	256	2048	256
EME01	1	8	8	8	8	256	2048	256
EME02	1	8	8	4	4	384	1024	64
EME03	1	8	8	2	2	256	512	256
EME04	1	8	8	8	8	256	2048	256
EDV01	4	32	32	8	2	256	512	256
TDV01	4	32	32	32	8	1024 MAX	--	128
TDV02	4	32	32	32	8	512 MAX	--	128
TDV03	2	16	16	16	8	1024 MAX	--	256
TDV04	1	8	8	8	8	1024 MAX	--	64
EEQ01	1	8	-	2	2	256	512	256
TEQ01	1	8	-	8	8	1024 MAX	--	64
CALMCP	1/8	1	-	1	8	128	1024	128
CALRF	-	6+	-	1+	-	-	-	-
CALTL	8	64	-	32	4	512	512	256
CALV1	2	16	16	16	8	384	384	256

Because the SMS must measure ions with a low velocity compared to that of the satellite, the angle between the field of view and the velocity vector of the satellite has a very important effect on the SMS measurements. The SMS observation sequence is synchronized to the spin phase which is determined by the star sensors of the satellite. Table 11 shows the details of measurements in each mode component in relation to the spin. This method of observation is very effective for the measurement of thermal ions. The mode components described above form the units of observation. In real observation, a number of components are combined to form an "operation mode", which is to be executed by commands from the ground. The program to define the mode components resides in the RAM of the SMS micro-processor, and it can be changed from the ground command, if needed. Thus, the architecture of the SMS observational mode is very flexible.

7.4 Magnetospheric ion composition observed by EXOS-D

The SMS observation began on April 2, 1989, one month after the launch of the EXOS-D satellite. Figure 148 shows the mass spectra of thermal ions observed by the finest mass scan mode which was specially prepared in addition to those shown in Table 10. As shown in Table 9, the maximum possible numbers of mass scan steps is 256, but the number of steps per observation is restricted to 64 due to RAM limitations. That is, a full mass scan at the finest mass step is not possible in one scan. Therefore, the mass range in this figure is between 0.9–2.85 AMU. Although the left hand side of mass peak 1, H^+, is shown only up to its shoulder, its right hand side shows a clear cut off characteristic, similar to those obtained in the laboratory tests. It is noted that the upward-flowing ion flux is about 25 times greater than the downward-flowing flux in this observation. This feature is true for most of the observations.

Figure 149 shows a mass spectrum for the full mass range of 1–64 AMU, observed on May 27, 1990. The mass peaks, A, B, C, D, E correspond to H^+, He^+, N^{++}/O^{++}, N^+/O^+, and N_2^+/O_2^+, respectively. The detection of molecular ions at high altitudes (above 6000 km in this case) is a very rare event.

It has been found by EXOS-D observations[21][177] that the appearance of molecular ions at high altitude is limited to periods of very high geomagnetic activity, which is consistent with previous studies[77][78].

It is noted that N^{++} and O^{++} are well resolved at position C in Fig. 149. Although N^+ and O^+ are not well resolved at position D, they can be resolved by a fine step scan, which is displayed in Fig. 150. From this observation it is noted that the ratio $[N^+]/[O^+]$ amounts to about 1/3. This value is large compared to the value of 0.1 determined from the DE-1 observations[71]. A case study of the peaks at position D [Yau et al., 1991] revealed that this ratio reaches up to 1.0. However, the ratio of doubly charged species, $[N^{++}]/[O^{++}]$, whose peaks lie at position C has been found to be only ~0.2. Further it is noted that the ratio $[O^{++}]/[O^+]$ exceeds 0.1. By examining many observations, Yau et al.[21] found that this value becomes about 0.3, which is much larger than the value of 0.1–0.01 found by GEOS observations[72]. The major difference between the two observations is their energy ranges. That is, the GEOS energy range is of the order of keV while in the present case it is several tens of eV. Thus it is possible that observations at different energy ranges will reveal quite different ion compositions. The consequences of such observations are still under consideration and are not conclusive at the present time.

Figure 150 and many other cases show that the ionospheric ions are flowing upward (UFI) most of the time. Downward-flowing ions (DFI) are very rare, consistent with the DE-1 observations[84]. If the upward-flowing ions exist in both hemispheres, it might be expected that the downward-flowing ions should be observed with equal frequency. The rarity of DFIs observed in practice suggests that there should be some process which obstructs the flow around the apex of the magnetic field lines.

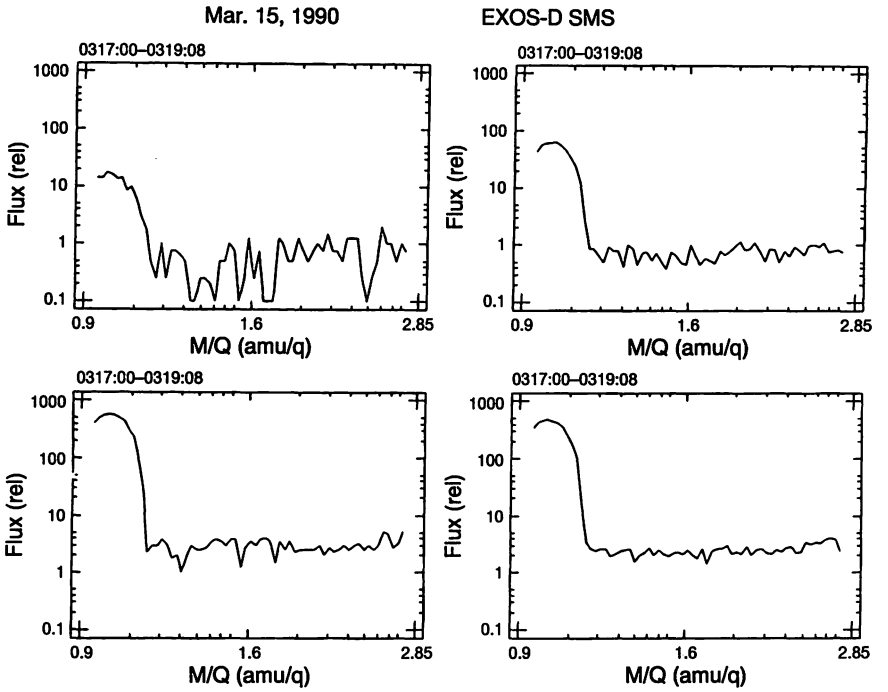

Fig. 148 Examples of the mass spectra in the low mass range from EXOS-D/SMS on orbit. The lower panels show downward (left) and upward (right) flowing flux along the magnetic field and the upper two panels show perpendicular flux.

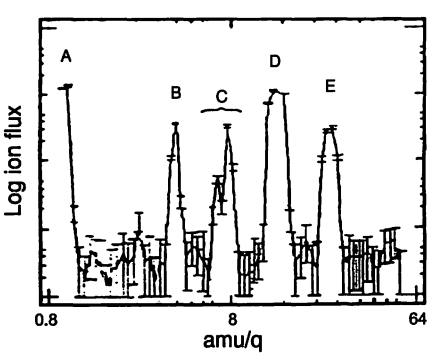

Fig. 149 The same as the previous figure but in the full mass range mode. Mass peaks A, B, C, D, and E correspond to H^+, He^+, N^{++}/O^{++}, N^+/O^+, NO^+/O^+, respectively [after Yau et al., 1991[21]].

The presence of such a process has been indicated by the plasma wave experiments on EXOS-D[178][179]. Generally speaking, resonant condition between particles and waves is held for extended distance above the equator, because the intensity of the magnetic field there changes slowly.

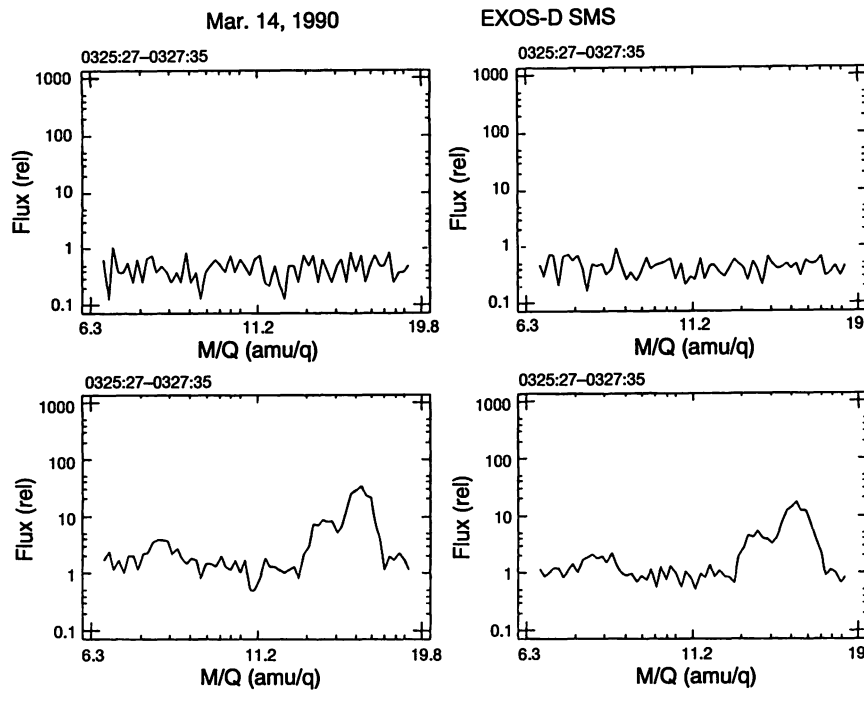

Fig. 150 The same as Fig. 148 but in the medium mass range.

That is the main reason why the pitch angle scattering takes place frequently at the equatorial region. The interrelation between the observations of particles and waves should be explored further.

Figure 151 shows the successive mass spectra of thermal ions (0–25 eV) observed in the polar region on March 16, 1990[180]. The range of the mass scan is the same as that in Fig. 149 (1–64 AMU).

Since this observation was made in the northern hemisphere, parallel components correspond to downward flow and anti-parallel to upward flow. The black painted peaks show 2^+ (He^{++} or D^+)ions. It is noted that the ionospheric ions, O^+ and He^+, exist only in the upward flows while H^+ and 2^+ ions flow in both directions. This feature is clearly demonstrated in the pitch angle distribution shown in Fig. 152. An appreciable flux of 2^+ ions was very seldom. By examining a large number of plots, Watanabe et al.[180] showed that the flux of 2^+ ions is limited to the polar cusp region. This feature suggests that the 2^+ ions can be identified as He^{++} from the solar wind origin. It is well known that the major constituents of the solar wind plasma are H^+ and He^{++} with a ratio of about 20:1. The ratio of $[2^+]/[1^+]$ in the downward flow in Fig. 151 is consistent with this ratio.

The upward flows in the same figure contain about the same He^{++} flux as the downward flux. This can be interpreted as mirror ions from the geomagnetic field. Another important aspect of the above observation is that He^{++} ions are detected at very low energies.

Figure 153 shows the RPA characteristics for four ion species in the upward flow during 1225–1227 UT. It is seen that the ionospheric ions (O^+ and He^+) and the solar wind ions (He^{++} and H^+) have very different energy distributions. The former have a clear-cut off at about 6 V for He^+ and 16 V for O^+, while the latter have an extended energy spread. The bulk energy of He^{++} in the solar wind is usually greater than about 1.5 keV. If we presume 2^+ ions to be injected from the solar wind,

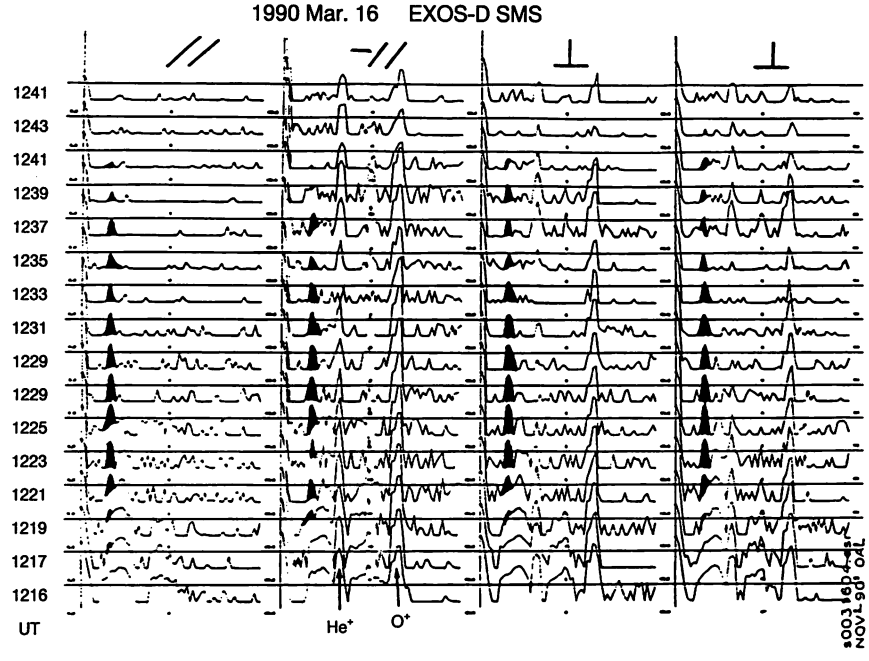

Fig. 151 Mass spectra successively observed by EXOS-D/SMS above polar region on March 16, 1990 [after Watanabe et al., 1992[180]].

these ions should lose their energy in the process of injection. This poses another interesting problem in magnetospheric physics which has not been studied much so far.

The four panels in Fig. 154 show, in descending order, the RPA characteristics of H^+, He^+, O^{++} and O^+ in the thermal plasma observed on August 2, 1990. The flux of each ion is identified by color coding. The abscissa shows the UT, and the ordinate shows the spin phase angle. The zero-point of vertical scales represents the projection of the magnetic field onto the spin-plane. That is to say, the values of the scales roughly indicate the pitch angles. Each block of data shows one RPA sweep sequence of 0–25 volts, which is displayed in the fifth panel from the top. Thus, the abscissa in this unit block corresponds to the RPA voltage or ion energy. The data observed in 8 spins (72 seconds) are averaged in each block. The dotted lines displayed in the upper four panels show the projection of the ram vector on the spin plane. This observation started at 125533 UT and the altitude was 3933 km. The satellite crossed the region over the auroral zone. At the beginning of the observation all the ions, except H^+, have flux peaks at the ram direction, indicating that these ions have very low velocity. The H^+ flux peak deviates from this direction, indicating that H^+ had extra flow velocity. The flux of H^+ from all directions, not just that of ram, increases with time as the sub-satellite latitude decreases.

In the last two blocks, two flux peaks appear with respect to the spin phase. These structures are known as ion "conics". Because the pitch angle of this flux is about 90 degrees, we can presume that transverse acceleration of H^+ (TAI) occurred at this altitude (~2000 km). Weak conics can also be identified in the He^+ distribution, but no such structure is seen for other ions. The fact that the acceleration of ions is mass-dependent indicates that a process such as ion cyclotron resonance might be responsible for the acceleration in this particular event.

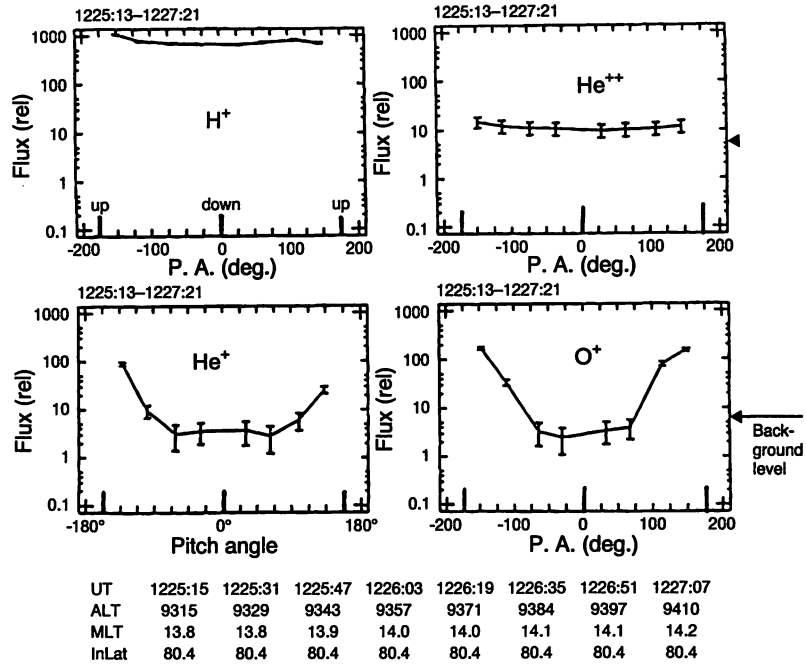

Fig. 152 Pitch angle distributions for H^+, He^{++}, He^+ and O^+ for the observation on March 16, 1990 [after Watanabe et al., 1992[180]].

The lowest three panels in Fig. 154 show the suprathermal mode data. The lowest panel shows the scan voltage and the dotted line in the same panel indicates the angle between the magnetic field and the spin plane, whose scales are shown on the right side. Only O^+ and H^+ were measured in this suprathermal mode. It should be recalled that the energy analysis in this mode was done in the band-pass mode. It is interesting to note that the energetic ions were not detected before but they suddenly appeared at about 1305 UT (~69 invariant latitude). The conics are clearly visible in the H^+ distributions and we can also identify a "beam" structure directed downward along the magnetic field (pitch angle ≈0) overlapping the conics. On the other hand for O^+ ions, only the beam structure can be seen with no conics. In the last observation block (~62 invariant latitude), both conics and beams disappeared from the H^+ and O^+ distributions and the flux patterns became broader in energy and isotropic in pitch angle distribution. It is also interesting that the thermal and energetic ions show extremely different and contrasting structures in the last block.

Figure 155 shows another example of RPA characteristics observed on March 22, 1990, at high altitude (8000–9000 km) over the polar cap region. The flux of the lightest ion, H^+, maximizes at 180° pitch angle, that is, H^+ is flowing upward along the magnetic field. On the other hand the flux of the heaviest ion, O^+, maximizes in the ram direction as in the previous example. The flux of intermediate mass, He^+, maximizes at an intermediate angle between the ram and field line directions. The RPA characteristics show that O^+ has negligible velocity relative to the satellite velocity (~5 km/sec) while H^+ has far greater velocity (~20–30 km/sec) along the magnetic field. Consequently we can visualize the situation as being that H^+ ions are flowing upwards against a stationary O^+ background. This situation can be interpreted as the polar wind. Flows due to the polar wind have been identified by ISIS-2[52], and DE-1[54][181] observations. The present observation is

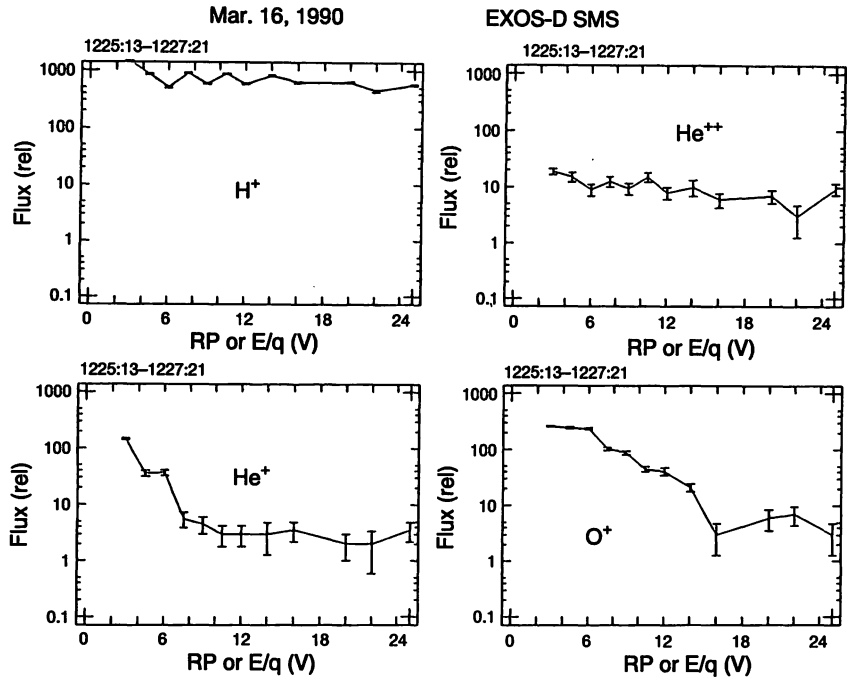

Fig. 153 RPA characteristics for four ion species observed on March 16, 1990 [after Watanabe et al., 1992[180]].

very similar to these observations and is also consistent with the predictions of classical polar wind theory[51].

One more example is shown in Fig. 156 observed on December 2, 1989, over the auroral region. In this case one block of the data shows the average of 6 spins (48 seconds) and He^{++} is shown instead of O^{++}. The flux of ions against the spin phase changed dramatically in this example. Let us examine the distribution of H^+ first. In the first block of the measurement which started at 0300 UT, the H^+ flux shows a typical conics structure. In the second block the flux decreases and reaches maximum magnitude at 180° pitch angle, that is, the flux changes into an upward flow along the magnetic field. In the third block, the flux intensifies a little compared to the second block and a downward beam appears along the magnetic field (0° pitch angle). Complex flux variations continue up to 0308 UT. It is noted that asymmetric phase angle distributions appear in the 5th, 7th and 10th blocks. At about 0309 UT, the color code of the flux becomes isotropically yellow and it does not change much as the RPA voltage changes. Because no appreciable flux change can be detected in the energetic mode shown in the lower panel, the energy of isotropic H^+ ions is considered to be below 100 eV. In the block beginning at 0311 UT, upward and downward streams are added to the isotropic background. That is, H^+ ions are counter-steaming in this region. It is also noted that the energy of the down flowing ions is greater than that of up flowing ions. The pitch angle distribution of the down flowing ions becomes narrower in the block before last. In the last block (the lowest latitude in this observation), the down flowing ion disappears altogether and the distribution of H^+ flux looks more like a loss cone type. That is, the flux along the field line is very small for both upward and downward directions.

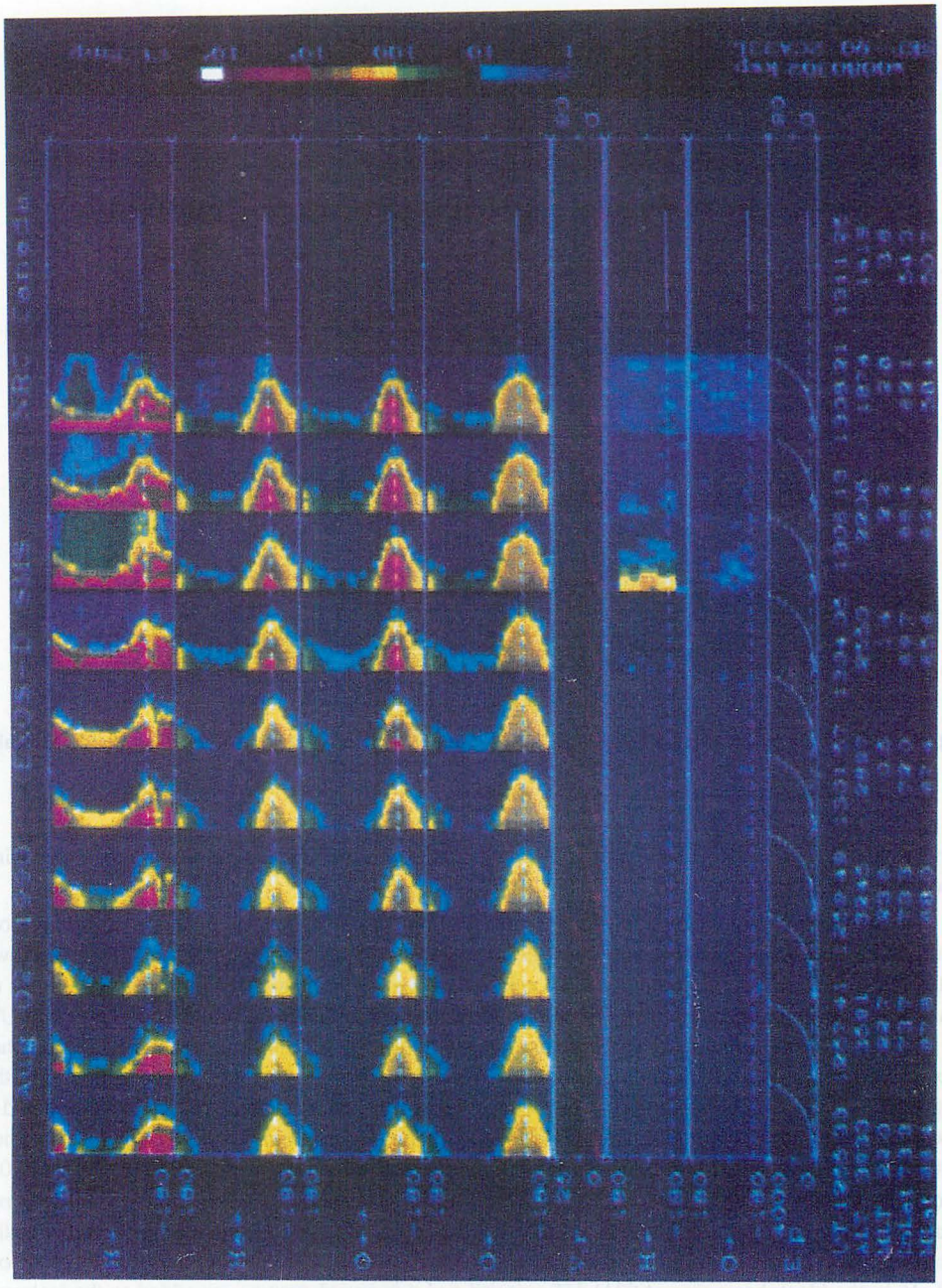

Fig. 154 RPA characteristics observed on August 2, 1990 by EXOS-D.

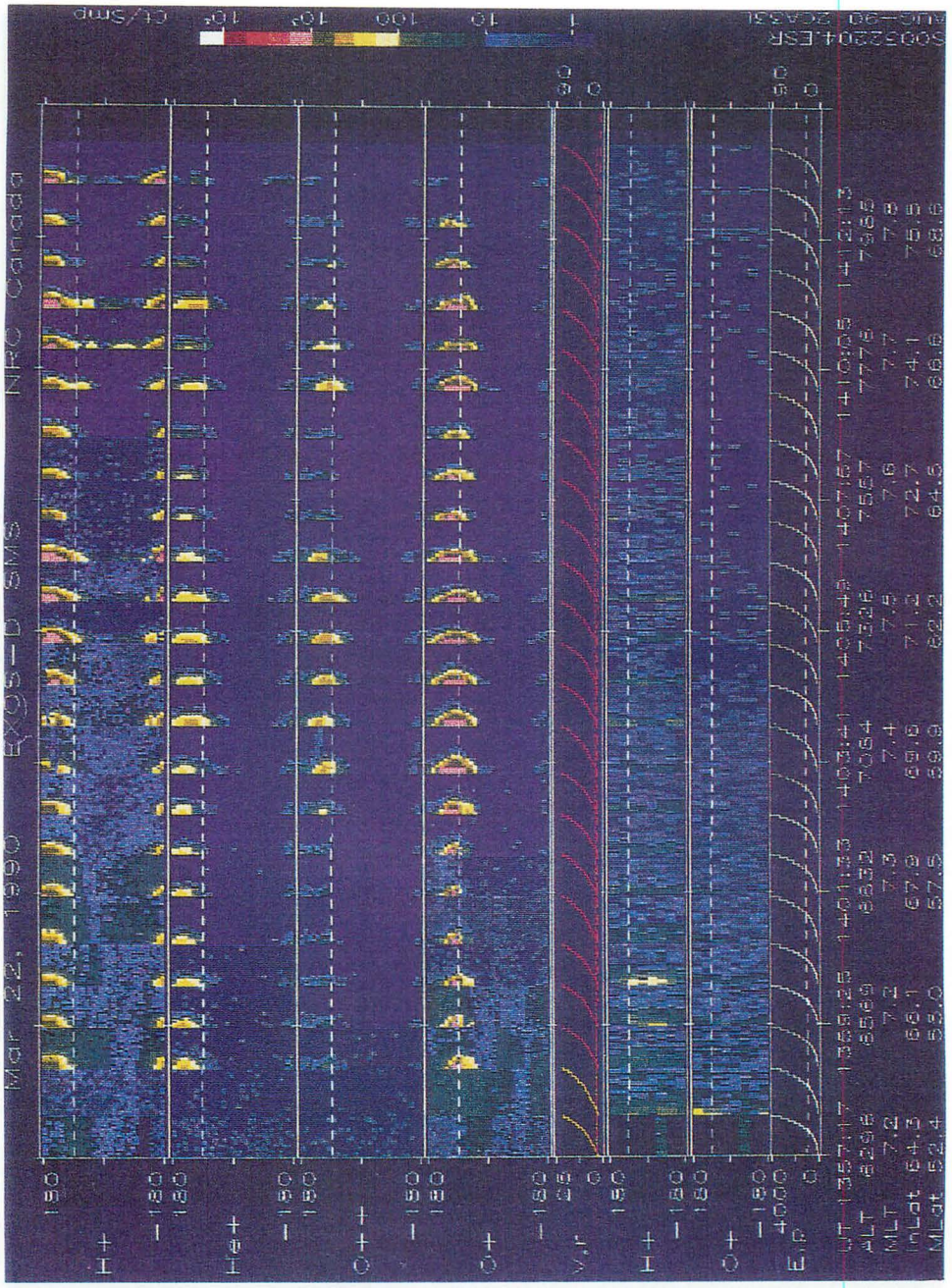

Fig. 155 RPA characteristics observed on March 22, 1990 by EXOS-D.

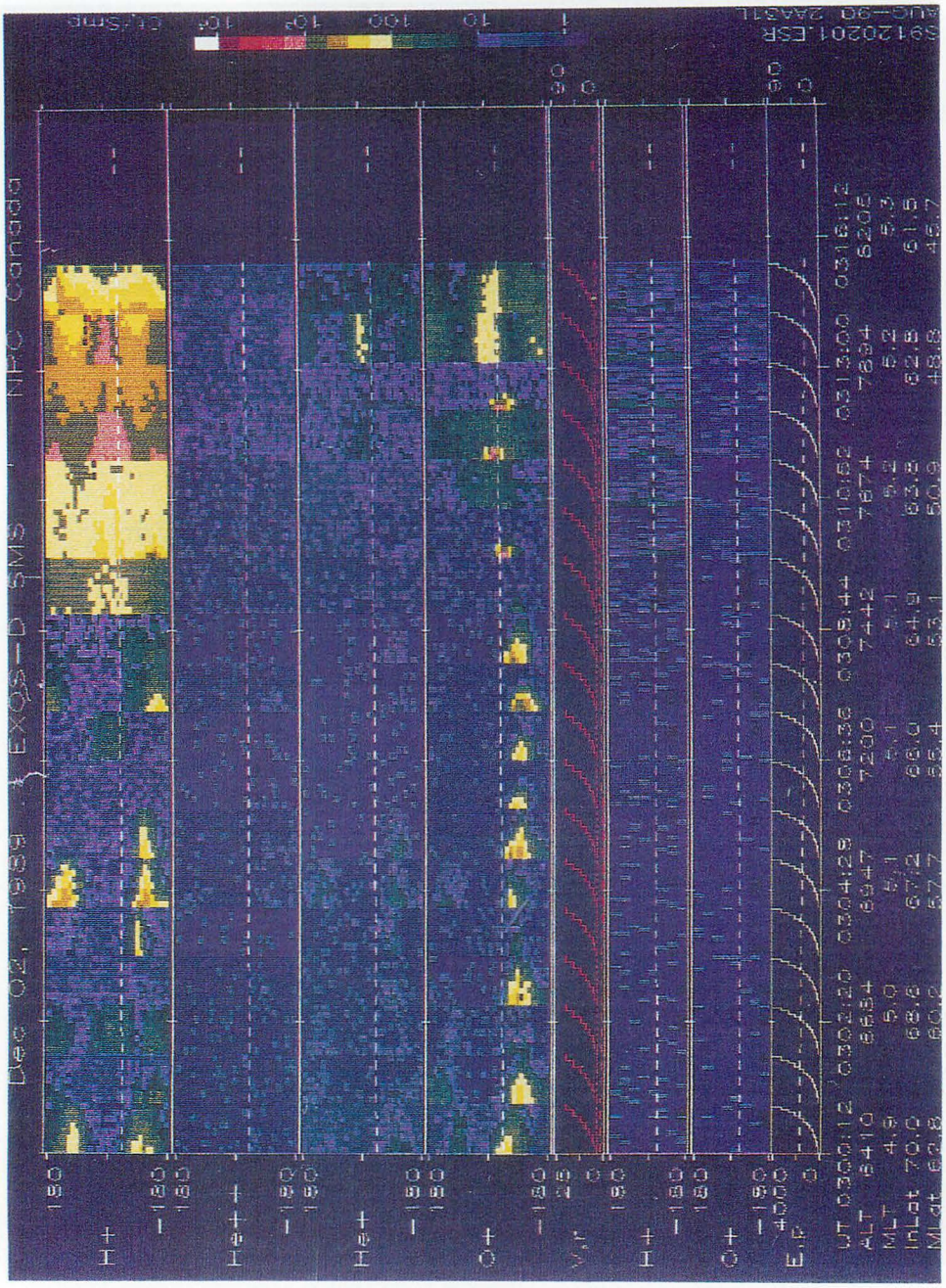

Fig. 156 RPA characteristics observed on December 2, 1989 by EXOS-D.

As for He^{++}, we cannot see any appreciable flux in this particular observation. Many observations have suggested that He^{++} abundance is restricted to the polar cusp region[180]. As for He^{+}, it has a similar time history to H^{+}, although the magnitude of the flux is considerably lower than that of H^{+}.

Next let us examine the distribution of O^{+} flux in Fig. 156. We can recognize a conics structure similar to the H^{+} case, but it is noted that the two peaks in the spectrogram are very asymmetric compared to the case of H^{+}. For low energy O^{+}, the ram effect would be expected, but the position of the O^{+} flux peak apparently deviates from the ram direction. This fact suggests that O^{+} has an extra velocity component other than the satellite motion in one direction not conic to the magnetic field. This velocity could be interpreted as due to drift motion. At the present time, we do not have further evidence to support this interpretation, but it should be confirmed in a future study by consulting the data of other companion instruments on EXOS-D, such as the electric field detector (EFD). Here we have only pointed out the variety of the ion distributions which have been found by SMS observations.

8. Summary and concluding remarks

This paper is based on our work in developing ion-mass spectrometers for rocket and satellite to observation of the ionosphere and magnetosphere. It describes the mass spectrometers on the ISS-b and EXOS-D satellites and the results they have produced.

The ion composition of the earth and other planets is reviewed in Section 2. Based primarily on our group's observations, the basic characteristics of the composition and relevant chemical reactions in the Earth's ionosphere are summarized. The ion composition of the other planetary ionospheres, obtained primarily from NASA deep-space explorers, is also reviewed.

The ion transport processes in the Earth's ionosphere are reviewed in Section 3. We focus on the diffusive equilibrium because it is very important in the topside ionosphere, which is the main subject of this study. Since the distributions of plasma in the real ionosphere deviate considerably from this diffusive equilibrium state, the basic processes which cause these deviations are also discussed.

The theory of operation and basic characteristics of the Bennett mass spectrometer, which is on the ISS-b and EXOS-D satellites, are described in detail in Section 4. The electrical and mechanical specifications of the mass spectrometer on the ISS-b are also presented.

The global ion distributions at an altitude of 1100 km, as observed by the ISS-b satellite, are presented in Section 5. A prominent feature in these distributions is that dependence on the longitude is much larger compared to previous studies. This longitudinal dependence means that the distributions are specific to the world location. This means that ion distribution is strongly controlled by the geomagnetic field.

By inspecting individual pass, medium-scale structures, which seem to persist at particular longitudes for a few days, have been found. The medium-scale structures for H^{+} distributions are frequently periodic in their latitudinal extent. This periodicity is rarely seen in other ion species, such as He^{+} or O^{+}. These structures may be due to the neutral waves in the thermosphere or from the lower atmosphere, although we do not have further evidence to support such a view.

From our analysis of LT maps, global structures that persist for a few months were also found. Some features of these structures can also be attributed to the effect of the neutral atmosphere. The longitudinal anomaly in the LT maps of O^{+} can be explained by the effect of the neutral wind, which is different for different declination angles and specific to the particular location.

In Section 6, the variations in ion densities are statistically analyzed with respect to a selected parameter, such as latitude, local time, season, solar activity, or geomagnetic activity. Since the ion observations by ISS-b were global and were for an extended duration compared to those of other previous satellites, such as the OGO and ISIS series, several new ion composition characteristics were found in the topside ionosphere. They are presented in Section 6.

The quality of the observations was especially good for He^+, disclosing several interesting He^+ phenomena. One is that the winter bulge structure in the ionic helium can be seen only in the day and it disappears at night. Another is that the equatorial trough in the He^+ distribution becomes dominant at night. Apparently it is very similar to those for NmF2, or the so-called equatorial anomaly. However, since these phenomena have different local time dependence as found from ISS-b observations, it has been revealed that the plasmaspheric dynamics plays an essential role for the He^+ trough, rather than the fountain effect due to E × B drift, which has been known as the main cause of the NmF2 equatorial anomaly.

Our analysis of the dependence on solar activity showed that the density of H^+ at 1100 km shows negative correlation with F10.7. Although He^+ density has weak positive correlation with F10.7 in the global average sense, either positive or negative correlation is statistically significant in the sub-divided latitude and local time domains, which is contrary to the previous view that He^+ has strong positive correlation with solar activity. The ISS-b observations have revealed that the situation is not simple for He^+, at least at an altitude of 1100 km.

Regarding seasonal variation, O^+ has very regular periodic behavior, whereas H^+ and He^+ have very complex behaviors. In particular, the seasonal variation in H^+ in the daytime shows marked symmetry between the northern and southern hemisphere, in spite of the seasonal differences. It is suggested that the interhemispheric flow plays an important role in this distribution.

The latitudinal distributions of the light ions, H^+ and He^+, show prominent light ion trough structures at higher latitudes. The trough is sharper for He^+ than for H^+. The dependence of the trough in the He^+ distributions on geomagnetic activity Kp is compared with other reported observations.

A new energy and mass analyzer, in which the retarding potential analyzer and the Bennett mass spectrometer are combined, is described in Section 7. This SMS analyzer is flown on the 12th scientific satellite, EXOS-D, in coordination with a Canadian scientist group. It has been observing the magnetospheric and the ionospheric ion composition since its launch in 1989. A detailed description of the instrument and initial results are presented. The observations and analyses are still under way and considerable contributions to ionospheric and magnetospheric studies are expected. These have appeared and will appear in relevant publications.

In conclusion, the author have engaged in the development of ion mass spectrometers and other instruments for rocket and satellite experiments. When this work started about 25 years ago, the space technology in Japan was in infant stage. The development of ISS-b was initiated just at such time. Compared to present-day satellite systems, ISS-b had limited capabilities. Nevertheless, the results produced by ISS-b are still important to the fields such as the ionosphere modeling, because the duration of ISS-b observation at a constant altitude has not been surpassed by others.

The development of a new mass spectrometer for EXOS-D in collaboration with a Canadian scientist group was very valuable and exciting experience to Japanese space science community. This cooperation has produced and is producing very fruitful results in the ionospheric and magnetospheric research. This cooperation is now being extended to the Planet-B program, in which the ionosphere and atmosphere of Mars will be explored. Besides the Canadian group, participation of some other foreign groups is planned for the Planet-B mission. Japanese space program is now becoming truly international. It is expected that such cooperation will produce great progress in the space science field.

Acknowledgements

The author wishes to express his deep gratitude to Prof. I. Kimura, of the Kyoto University, for his continued encouragement throughout the preparation of this paper and careful reading of the

manuscript. His leaderships in the researches in the radio- and space-science field as a guest scientist in the laboratory and also in the investigations by EXOS-D satellite are also appreciated. The author thanks constructive comments and suggestions from Prof. H. Matsumoto and Prof. S. Fukao.

The Ionosphere Sounding Satellite program was planned as the first applications satellite series by N-rocket, by the National Space Activity Council, the Science and Technology Agency, the National Space Development Agency of Japan (NASDA) and the Ministry of Posts and Telecommunications including the Radio Research Laboratory (now the Communications Research Laboratory). The data acquisition of ISS-b was partly done by the Communication Research Centre of Canada. The author would like to acknowledge all of these agencies.

The author participated in the joint observation programs, including the sounding rockets, TAIYO, KYOKKO, and AKEBONO (EXOS-D) satellites, sponsored by the Institute of Space and Astronomical Science (ISAS). The author is very grateful to Prof. K. Hirao, Prof. T. Itoh, Prof. K. Tsuruda, Prof. Nishida, Prof. H. Oya, and late Prof. T. Obayashi, who leaded the joint programs and admitted him to the programs. The author also thanks to all the staffs who supported these experiments.

The ion mass spectrometer on the EXOS-D, or SMS, was jointly developed with a Canadian scientist group, leaded by Dr. B. A. Whalen of the Herzberg Institute of Astrophysics, National Research Council, Canada. The author would like to appreciate great contributions to the EXOS-D program by his group.

In the Radio Research Laboratory, the Ionosphere Sounding Satellite program was leaded by Dr. Y. Ogata, Dr. Y. Hakura, Dr. N. Wakai, and Dr. N. Matuura. Data acquisition and processing were done by staffs in the Kashima Space Center, the Satellite Data Analysis Section and the Computer Center. Without their efforts the present research was not possible.

The author is indebted to Dr. N. Fugono, former director general of the laboratory, who initiated the ion mass spectrometer experiment on Japanese rockets and satellites and encouraged him to accomplish this paper. Thanks are also due to colleagues in the laboratory, Dr. S. Miyazaki, Dr. E. Sagawa, Dr. S. Watanabe, Dr. K. Marubashi, Mr. T. Mori, Mr. K. Aikyo, Mr. T. Suitz, and Dr. T. Ogawa, for their discussion, stimulation, and assistance.

References

(1) Alfven, H. O. G., "Cosmology in the plasma universe : An introductory exposition", Trans. IEEE Plasma Sci., **PS-18**, pp. 5–10, 1990.

(2) Kessler, D. J., B. J. Cour-Palais, "Collision frequency of artificial satellite: Creation of debris belt, in Space Systems and Their Interactions with earth's Space Environment", pp. 707–736, ed. H.B. Garrett, AIAA, 1980.

(3) Hedin, A. P., "MSIS-86 thermospheric model", J. Geophys. Res., **92**, pp. 4649–4662, 1987.

(4) Tohmatsu, T., Compendium of Aeronomy, Tera Sci. Pub. Co., Tokyo, 1990.

(5) Torr, M. R., D. G. Torr, and R. A. Ong, "Ionization frequencies for major thermospheric constituents as a function of solar cycle 21", Geophys. Res. Lett., **6**, pp. 771–774, 1979.

(6) Torr, D. G., and M. R. Torr, "Ionization frequencies for solar cycle 21: revised", J. Geophys. Res., **90**, pp. 6675–6679, 1985.

(7) Roble, R. G., "Global dynamic models of the earth's thermosphere and ionosphere", ESA J., **7**, pp. 405–415, 1983.

(8) Sojka, J. J., R. W. Schunk, J. F. E. Johnson, J. H. Waite and C. R. Chappell, "Characteristics of thermal and suprathermal ions associated with the dayside plasma trough as measured by the Dynamics Explorer retarding ion mass spectrometer", J. Geophys. Res., **88**, pp. 7895–7911, 1983.

(9) Bailey, G. J., and R. Sellek, "A mathematical model of the earth's plasmasphere and its application in a study of He^+ at L = 3", Ann. Geophys., **8**, pp. 171–190, 1990.
(10) Rawer, "Introduction to IRI 1979", Report UAG–82, WDC-A, NOAA, 1981.
(11) Matuura, N., K. Aikyo, R. Nishizaki, T. Ogata, M. Nagayama, S. Igi, T. Maruyama, H. Yabuuma, M. Yamanishi and T. Ide, "Global distributions of the ionospheric F-layer critical frequency (foF2)", Rev. Radio Res. Lab., **28**, pp. 315–331, 1982 (in Japanese).
(12) Raitt, W. J., and W. W. Dorling, "The global morphology of light ions measured by the ESRO-4 satellite", J. Atmos. Terr. Phys., **38**, pp. 1077–1083, 1975.
(13) Taylor, H. A. jr., "Evidence of solar and geomagnetic seasonal control of the topside ionosphere", Planet. Space Sci., **19**, pp. 77–93, 1971.
(14) Roble, R. G., A. I. Stewart, M. R. Torr, D. W. Rush, and R. H. Wand, "The calculated and observed ionospheric properties during Atmospheric Explorer-C satellite crossings over Millstone Hill", J. Atoms. Terr. Phys., **40**, pp. 21–30, 1978.
(15) Yonezawa, T., "Theory of formation of the ionosphere", Space Sci. Rev., **5**, pp. 3–56, 1966.
(16) Bauer, S. J., "Hydrogen and helium ions", Annal. Geophys., **22**, pp. 247–254, 1966.
(17) Heelis, R. A., W. B. Hanson, and G. J. Bailey, "Distributions of He^+ at middle and Equatorial latitudes during solar maximum", J. Geophys. Res., **95**, pp. 10313–10320, 1990.
(18) Sagawa, E., I. Iwamoto, and T. Suitz, "Ion composition distribution above the ionospheric F–layer obtained by a rocket-borne ion mass spectrometer", J. Geomag. Geoelectr., **32**, pp. 551–559, 1980.
(19) Brinton, H. C., M. W. Pharo, H. G. Mayr and H. A. Taylor, jr., "Implications for ionospheric chemistry and dynamics of a direct measurement of ion composition in the F2 region", J. Geophys. Res., **74**, pp. 2941–2951, 1969.
(20) Hoffman, J. H., "Ion mass spectrometer on Explorer 31 satellite", Proc. IEEE, **57**, pp. 1063–1067, 1969.
(21) Yau, A. W., B. A. Whalen, and E. Sagawa, "Minor ion composition in the polar ionosphere", Geophys. Res. Lett., **18**, pp. 345–348, 1991.
(22) Brinton, H. C., R. A. Pickett, and H. A. Taylor jr., "Diurnal and seasonal variation of atmospheric ion composition; Correlation with solar zenith angle", J. Geophys. Res., **74**, pp. 4064–4073, 1969
(23) Marubashi, K., and J. M. Grebowsky, "A model study of diurnal behavior of the ionosphere and protonosphere coupling", J. Geophys. Res., **81**, pp. 1700–1706, 1976.
(24) Suitz, T., I. Iwamoto, N. Fugono, and H. Yamada, "Observation of the ion composition in the lower ionosphere at Syowa station", Rev. Radio Res. Lab., **20**, pp. 475–481, 1974
(25) Fugono, N., T. Suitz, and I. Iwamoto, "Ion composition measurement with a rocket-borne mass spectrometer at Syowa station", Antarctica Record, **52**, pp. 147–150, 1975.
(26) Ferguson, E. E., F. C. Fehsenfeld, and Albritton, Gas phase ion chemistry, ed. Bower, Academic Press, New York, 1979.
(27) Iwamoto, "Negative ions in the D region", Rev. Radio Res. Lab., **15**, pp. 340–346, 1968 (in Japanese).
(28) Arnold, F., and A. A. Biggiano, "Combined mass spectrometric composition measurements of positive and negative ions in the lower ionosphere 2. Negative ions", Planet. Space Sci., **30**, pp. 1307–1314, 1982.
(29) Wong, A. Y., P. Y. Cheung, M. J. McCarrick, J. Stanley, R. F. Wuerker, R. Close, B. S. Bauer, E. Fremouw, W. kruer, and B. Langdon, "Large-scale resonant modification of the polar ionosphere by electromagnetic waves", Phys. Rev. Lett., **63**, pp. 271–274, 1989.
(30) Ogawa, T., "Generation and propagation of earth's electric field", J. I. Static Electr. **13**, pp. 790–801, 1989.
(31) Pfeilsticker, K., and F. Arnold, "First ion composition measurement in the stratopause region, using a rocket-borne parachute drop sonde", Planet. Space Sci., **37**, pp. 315–328, 1989.

(32) Perkins, D., and F. L. Eisele, "First mass spectrometric measurements of atmospheric ions at a ground level", J. Geophys. Res., **89**, pp. 9649–9657, 1984.

(33) Heitman, H., and F. Arnold, "Composition measurements of tropospheric ions", Nature **306**, pp. 747–748, 1983.

(34) Eisele, F. L., "Mass spectrometric study of tropospheric ions in the northeastern and southwestern United States", J. Geophys. Res., **91**, pp. 5183–5188, 1986.

(35) Iwamoto, I., T. Suitz and N. Fugono, "Study on the development of portable mass spectrometer", in Results of Environment Preservation Studies published by Environment Agency, 72–1, 1974 (in Japanese).

(36) Taylor, H. A. jr., H. C. Brinton, S. J. Bauer, R. E. Hartle, T. M. Donahue, R. D. Daniel jr., and B. H. Blackwell, Ionosphere of Venus: "First observations of the dayside ion composition near dawn and dusk", Science **203**, pp. 752–754, 1979.

(37) Hanson, W. B., S. Santani, and D. R. Zuccara, "The Martian ionosphere as observed by the Viking retarding potential analyzer", J. Geophys. Res., **30**, pp. 4351–4358, 1977.

(38) Taylor, H. A.,jr., H. C. Brinton, S. J. Bauer, R. E. Hartle, P. A. Cloutier, F. C. Michel, R. D. Daniel jr., T. M. Donahue, and R. C. Michel, "Ionosphere of Venus: First observations of the effect of dynamics on the dayside ion composition", Science **203**, pp. 755–757, 1979a.

(39) Taylor, H. A. jr., H. C. Brinton, J. C. J. Wagner, B. H. Blackwell, and G. R. Cordier, "Bennett ion mass spectrometers on the Pioneer Venus bus and orbiter", IEEE Trans., **GE-18**, pp. 44–49, 1980.

(40) Iwamoto, I., K. Marubashi, M. Shimizu and T. Ashihara, "Ion mass spectrometer for PLANET-B", Proc. Sci. Sat. Symp. 1987 (in Japanese).

(41) Sagdeev, R. Z., and A. V. Zakharov, "Brief history of the Phobos mission", Nature, **341**, pp. 581–585, 1989.

(42) Balsiger, H., K. Altwegg, F. Buhler, J. Geiss A. G. Ghielmetti, B. E. Goldstein, W. T. Huntress, W-H, Ip, A. J. Lazarus, A. Muer, M. Neugebauer, U. Retlenmund, H. Rosenbauer, R. Schwenn, R. D. Sharp, E. G. Shelley, E. Ungstrup, and D. T. Young, "Ion composition and dynamics at comet Halley", Nature, **321**, pp. 330–334, 1986.

(43) Waite, J. H. jr., and T. E. Cravens, "Current review of the Jupiter, Saturn, and Uranus ionosphere", Adv. Space Res., **7**, pp. 119–134, 1987.

(44) McCornnel, J. C., and T. Majeed, "$H3^+$ in the Jovian Ionosphere", J. Geophys. Res., **92**, pp. 8570–8578, 1987.

(45) Mahajan, K. K., and J. Kan, "Planetary ionospheres", Space Sci. Rev., **40**, pp. 303–340, 1988

(46) Tyler, G. L., D. N. Sweetnam, J. D. Anderson J. K. Cambell, V. R. Eshleman, D. P Hinson, G. S. Levy, G. F. Lindal E. A. Marouf, and R. A. Simpson, Radio science observations of the Uranian system with Voyager 2: Properties of the atmosphere, rings, and satellite, Science, **215**, pp. 553–555, 1986.

(47) Chandler M. O., and C. R. Chappell, "Observations of the flow of H^+ and He^+ along magnetic field lines in the plasmasphere", J. Geophys. Res., **91**, pp. 8847–8860, 1986.

(48) Naghmoosh, A. A., and J. A. Murphy, "A comparative study of H^+ and He^+ at sunspot minimum and sunspot maximum", J. Atmos. Terr. Phys., **45**, pp. 673–680, 1983.

(49) Song, X-T, R. Gendrin and G. Caudal, "Refilling process in the plasmasphere and its relation to magnetic activity", J. Atmos. Terr. Phys., **50**, pp. 185–194, 1988.

(50) Banks, P.M., and G. Kockarts, Aeronomy, Academic Press, Yew York, 1973.

(51) Banks, P. M., and T. E. Holzer, "High-latitude plasma transport: The polar wind", J. Geophys. Res., **74**, pp. 6317–6332, 1969.

(52) Hoffman, J. H., W. H. Dodson, C. R. Lippincott, and H. D. Hammack, "Initial ion composition results from the Isis 2 satellite", J. Geophys. Res., **79**, pp. 4246–4251, 1974.

(53) Hoffman, J. H., and W. H. Dodson, "Light ion concentrations and fluxes in the polar regions during magnetically quiet times", J. Geophys. Res., **85**, pp. 626–632, 1980.
(54) Nagai, T., J. H. Waite, jr., J. R. Green, C. R. Chappell, R. C. Oslen, and R. H. Comfort, "First measurements of supersonic polar wind in the polar magnetosphere", Geophys. Res. Lett., **11**, pp. 669–672, 1984.
(55) Dickinson, R. E., E. C. Ridley, and R. G. Roble, "A three-dimensional general circulation model of the thermosphere", J. Geophys. Res., **86**, pp. 1499–1512, 1981.
(56) Yonezawa, T., "On the seasonal, nonseasonal and semi-annual variations in the peak electron density of the F2 layer at noon in the equatorial zone", J. Radio Res. Labs., **14**, pp. 1–25, 1967.
(57) Hargreaves, J. K., The upper atmosphere and solar-terrestrial relations, Van Nostrand Reinhold Co. Ltd., New York, 1979.
(58) Makino, M., and T. Ogawa, "Quantitative estimation of global circuit", J. Geophys. Res., **90**, pp. 5961–5966, 1985.
(59) Matuura, N., "Dynamics of the F region", J. Atmos. Terr. Phys., **36**, pp. 1963–1974, 1974.
(60) Kelley, M. C., The Earth's Ionosphere, Academic Press, New York, 1989.
(61) Fejer, B. G., D. T. Farley, R. F. Woodman, and C. Calderon, "Dependence of equatorial F-region vertical drifts on season and solar cycle", J. Geophys. Res., **84**, pp. 5792–5799, 1979.
(62) Stern, D. P., "Large-scale electric fields in the earth's magnetosphere", Rev. Geophys. Space Phys., **15**, pp. 156–214, 1977.
(63) Babcock R. B., and J. V. Evans, "Effects of geomagnetic disturbances on neutral winds and temperatures in the thermosphere observed over Millstone Hill", J. Geophys. Res., **84**, pp. 5349–5356, 1979.
(64) Heelis, R. A., "Studies of ionospheric plasma and electrodynamics and their applications to ionosphere–magnetosphere coupling", Rev. Geophys., **26**, pp. 317–328, 1988.
(65) Kileen, T. L., and R. G. Roble, "Thermosphere dynamics: Contributions from the first 5 years of the Dynamics Explorer program", Rev. Geophys., **26**, pp. 329–367, 1988.
(66) Chappell, C. R., K. K. Haris, and G. W. Sharp, "A study of the influence of magnetic activity on the location of the plasmapause as measured by OGO-5", J. Geophys. Res., **75**, pp. 50–56, 1970.
(67) Shelley, E. G., R. G. Johnson, and R. D. Sharp, "Satellite observations of energetic heavy ions during a magnetic storm", J. Geophys. Res., **77**, pp. 6104–6110, 1972.
(68) Reasoner, D.L., C. R. Chappell, S. A. Fields, and W. J. Lewter, "Light ion mass spectrometer for space-plasma investigations", Rev. Sci. Instrum., **53**, pp. 441–446, 1982.
(69) Coplan, M. A., K. W. Ogilvie, P.A. Buchsler, and J. Geiss, "Ion composition experiment", IEEE Tras. GE-16, pp. 186–192, 1978.
(70) Balsiger, H., P. Eberhardt, J. Geiss, A. Ghielmetti, H. P. Walker, and D. T. Young, "A satellite-borne ion mass spectrometer for the energy range 0 to 16 kev", Space Sci. Instrum., **2**, pp. 499–521, 1976.
(71) Chappell, C. R., S. A. Fields, C. R. Baughter, J. H. Hoffman, W. B. Hanson, W. W. Wright, H D, Hammuck, G. R. Carrignum, and A. F. Nagy, "The retarding ion mass spectrometer on Dynamics Explorer-A", Space Sci. Instrum., **5**, pp. 477–485, 1981.
(72) Young, D. T., H. Balsiger and J. Geiss, "Correlation of magnetospheric ion composition with geomagnetic and solar activity", J. Geophys. Res., **87**, pp. 9077–9096, 1982.
(73) Young, D. T., and C. J. Farrugia, "Quantitative analysis of thermal(-1ev) ion data from magnetospheric spacecraft", J. Geophys. Res., **92**, pp. 12307–12318, 1987.
(74) Farrugia, C. J., D. T. Young, J. Geiss, and H. Balsiger, "The composition, temperature, and density structure of cold ions in the quiet terrestrial plasmasphere: GEOS 1 results", J. Geophys. Res., **94**, pp. 11865–11891, 1989.

(75) Taylor, H. A. jr., "Parametric description of thermospheric ion composition results", J. Geophys. Res., **78**, pp. 315–319, 1973.
(76) Geiss, J., H., and D. T. Young, "Production and transport of O^{++} in the ionosphere and plasmasphere", J. Geophys. Res., **86**, pp. 4739–4750, 1981.
(77) Craven, P. D., R. C. Oslen, C. R. Chappell and L. Kakani, "Observations of molecular ions in the earth's magnetosphere", J. Geophys. Res., **90**, pp. 7599–7605, 1985.
(78) Klecker, B., E. Mobius, D. Hovestadt, M. Scholer, G. Gloeckler, and F. M. Ipavich, "Discovery of energetic molecular ions (NO^+ and O_2^+) in the storm time ring current", Geophys. Res. Lett., **13**, pp. 632–635, 1986.
(79) Horwitz, J. L., "Core plasma in the magnetosphere", Rev. Geophys. **25**, pp. 574–587, 1987.
(80) Yau, A. W., E. G. Shelley, W. K. Peterson and L. Lenchyskyn, "Energetic auroral and polar ion outflow at DE 1 altitude: Magnitude, composition, magnetic activity dependence and long-term variations", J. Geophys. Res., **90**, pp. 8417–8432, 1985.
(81) Chappell, C. R., T. E. Moore, and J. H. Waite, Jr, "The ionosphere as a fully adequate source of plasma for the earth's magnetosphere", J. Geophys. Res., **92**, pp. 5896–5910, 1987.
(82) Singh, N., and R. W. Schunk, "Numerical calculations relevant to the initial expansion of the polar wind", J. Geophys. Res., **87**, pp. 9154–9170, 1982.
(83) Barakat, A. P., and R. W. Schunk, "O^+ ion in the polar wind", J. Geophys. Res., **88**, pp. 7887–7894, 1983.
(84) Sagawa, E., A. W. Yau, B. A. Whalen, and W. K. Peterson, "Pitch angle distributions of low energy ions in the near-earth magnetosphere", J. Geophys. Res., **92**, pp. 12254–12263, 1987.
(85) Hultquist, H. and T. Hagfors, High-latitude space plasma physics, Plenum Press, 1983
(86) Sagawa, E., K. Marubashi, I. Iwamoto, S. Watanabe, H. Mori, B. A. Whalen, and A. W. Yau, "A model for long-term response of the plasmaspheric activity and related measurement plans by EXOS-D", Adv. Space Res., **8**, pp. 35–44, 1988.
(87) Wakai, N., and N. Matuura, "Operation and experimental results of the Ionosphere Sounding Satellite–b", Acta Astronaut., **7**, pp. 999–1020, 1980.
(88) Bennett, W. H., "Radiofrequency mass spectrometer", J. Appl. Phys., **21**, pp. 143–149, 1950.
(89) Blauth, E. B., Dynamic mass spectrometers, Elsevier Pub. Co., Amsterdam, 1966.
(90) Isotomin, V. G., and A. A. Pokhunkov, "Mass spectrometer measurements of atmospheric composition in the USSR", Space Res. **3**, pp. 117–121, 1963.
(91) Isotomin, V. G., "Observational result on atmospheric ions in the region of the outer ionosphere", Ann. Geophys., **22**, pp. 255–261, 1966.
(92) Taylor, H. A. jr., L. H. Brace, H. C. Brinton, and C. R. Smith, "Direct measurements of helium and hydrogen ion concentration and total ion density to an altitude of 940 kilometers", J. Geophys. Res., **68**, pp. 5339–5347, 1963.
(93) Taylor, H. A. jr., H. C. Brinton, and R. Smith, "Positive ion composition in the magnetosphere obtained from Ogo-A satellite", J. Geophys. Res., **70**, pp. 5769–5781, 1965.
(94) Brinton, H. C., L. R. Scott, M. W. Pharo, and J. T. C. Coulson, "The Bennett ion-mass spectrometer on Atmosphere Explorer-C and -E", Radio Sci., **8**, pp. 323–332, 1973.
(95) Fugono, N., "Study of the mass spectrometer for direct measurement of the upper atmosphere composition", J. Radio Res. Labs., **17**, pp. 235–335, 1971.
(96) Iwamoto, I., T. Suitz and N. Fugono, "The Bennett ion mass spectrometer aboard TAIYO (CPI)", J. Geomag. Geoelectr., **27**, pp. 303–310, 1975.
(97) Iwamoto, I., N. Fugono, and T. Suitz, "Observations of the positive ion composition by ISS", Proc. 12th Int. Symp. on Space Tech. and Sci., Tokyo, pp. 843–845, 1977.
(98) Iwamoto, I., N. Fugono, and T. Suitz, "Ion mass spectrometer on Ionosphere sounding Satellite (ISS-b)", Rev. Radio Res. Lab., **28**, pp. 183–195, 1982 (in Japanese).
(99) Iwamoto, I., (Ed.), Summary plots of Ionospheric parameters obtained from Ionosphere Sounding Satellite-b, Vol. 1, 1983, Vol. 2, 1984, Vol. 3, 1985, Vol. 4, 1985, Published by Radio Res. Labs.

(100) Solar-Geophysical Data, No. 508 Part 1, p. 10, 1986.
(101) Bilitza, D., The world ionospheric data base, NSSDC/WDC-A-R&S 89–03, 1989.
(102) Taylor, H. A. jr., H. C. Brinton, M. W. Pharo, and N. K. Rahman, "Thermal ions in the exosphere; Evidence of solar and geomagnetic control", J. Geophys. Res., **73**, pp. 5521–5533, 1968.
(103) Taylor, H. A. jr., H. G. Mayr, and H. C. Brinton, "Observations of hydrogen and helium ions during a period of rising solar activity", Space Res., **X**, pp. 663–678, 1970.
(104) Taylor, H. A. jr, H. C. Brinton, D. L. Carpenter, F. M. Borner, and R. L. Heyborne, "Ion depletion in the high-latitude exosphere: Simultaneous OGO 2 observations of the light ion trough and VLF cut off", J. Geophys. Res., **74**, pp. 3517–3528, 1969.
(105) Reber, C. A., A. E. Hedin, A. D. Pelz, W. E. Potter, and L. H. Brace, "Phase and amplitude relationships of wave structure observed in the lower thermosphere", J. Geophys. Res., **80**, pp. 4576–4580, 1975.
(106) Potter, W. E., D. C. Kayser, and K. Mauersberger, "Direct measurement of neutral wave characteristics in the thermosphere", J. Geophys. Res., **81**, pp. 5002–5012, 1976.
(107) Hedin, A. E., and H. G. Mayr, "Characteristics of wavelike fluctuations in Dynamics Explorer neutral composition data", J. Geophys. Res., **92**, pp. 11159–11172, 1987.
(108) Crowley, G., "Dynamics of the earth's thermosphere: Review", Rev. Geophys. Suppl., pp. 1143–1165, 1991.
(109) Miyazaki, S., "Ion transition height distribution obtained with the satellite Taiyo", J. Geomag. Geoelectr., **31**, pp. 113–118, 1979.
(110) Goldberg, R. A., "A review of the theories concerning the equatorial F2 region ionosphere", Proc. IEEE, **57**, pp. 1119–1126, 1969.
(111) Fukao, S., T. Sato, I. Kimura, and R. M. Harper, "Seasonal mean structure of the night-time F2 region over Arecibo", J. Atmos. Terr. Phys. **41**, pp. 1205–1221, 1979.
(112) Taylor, H. A. jr., "Observed solar geomagnetic control of the ionosphere: Implications for reference ionospheres", Space Res. **12**, pp. 1275–1290, 1972.
(113) Hakura, Y. (Ed.), Atlas of Proton, Helium Ion and Oxygen Ion Densities obtained from Ionosphere Sounding Satellite-b in situ Observations October 1978 to August 1979, Published by Radio Res. Labs., 1982.
(114) Jones, W. B., R. P. Graham, and M. Leftin, Advances in ionospheric mapping by numerical methods, ESSA Technical Report, ERL107–ITS 75, 1969.
(115) Miyazaki, S., I. Iwamoto, E. Sagawa, H. Mori, T. Suitz, and T. Ogawa, "Characteristics O^+ depressions in the topside nighttime ionosphere revealed by ISS-b satellite", J. Geomag. Geoelectr., **35**, pp. 201–214, 1983.
(116) Miyazaki, S., and I. Iwamoto, "Characteristics of the O^+ ion density troughs in the topside nighttime ionosphere", Solar Terr. Env. Res. Jap., **5**, pp. 51–52, 1981.
(117) Blum. P. W., and I. Harris, "Full non-linear treatment of global thermospheric wind system-1. Mathematical method and analysis of force", J. Atoms. Terr. Phys., **37**, pp. 193–212, 1975.
(118) Papagiannis, M. D., and H. Mullaney, "The geographic distribution of the ionospheric evening anomaly and its relation to the global pattern of neutral winds", J. Atmos. Terr. Phys., **33**, pp. 451–459, 1971.
(119) Kohl, H., and J. W. King, "Atmospheric winds between 100 and 700 km and their effects on the ionosphere", J. Atmos. Terr. Phys., **29**, pp. 1045–1062, 1967.
(120) Eyfrig, R. W., "The effect of the magnetic declination of the F2 layer", J. Geophys. Res., **68**, pp. 2529–2530, 1963.
(121) Brinton H. C., H. G. Mayr, R. A. Pickett and H. A. Taylor jr., "The effects of atmospheric winds on the O^+-H^+ transition level", Space Res. **X**, pp. 652–662, 1970.
(122) Kutiev, I., R. A. Heelis, and S. Sanatani, "The behavior of the O^+ - H^+ transition level at solar maximum", J. Geophys. Res., **85**, pp. 2366–2372, 1980.

(123) Taylor, H. A. jr., and H. G. Mayr, "The signature of H^+ in the equatorial anomaly: An empirical model", Rev. Geophys., **16**, pp. 267–277, 1978.
(124) Taylor, H. A. jr., "The light ion trough", Planet. Space Sci., **20**, pp. 1593–1605, 1972.
(125) Taylor, H. A. jr., and W. J. Walsh, "The light ion trough, the main trough, and plasmapause", J. Geophys. Res., **77**, pp. 6716–6723, 1972.
(126) Brace, L. H., and R. F. Theis, "The behavior of the plasmapause at midlatitudes; ISIS 1 Langmuir probe measurements",J. Geophys. Res., **79**, pp. 1871–1884, 1974.
(127) Foster, J. C., C. G. Park, L. H. Brace, L. H. Burrows, J. H. Hoffman, E. J. Maier, and J. H. Whitteker, "Plasmapause signature in the ionosphere and magnetosphere", J. Geophys. Res., **83**, pp. 1175–1182, 1978.
(128) Nishida, A., "Formation of plasmapause, or magnetospheric plasma knee, by the combined action of magnetospheric convection and plasma escape from tail", J. Geophys. Res., **71**, pp. 5669–5679, 1966.
(129) Walker, G. O., "Longitudinal structure of the F-region equatorial anomaly—a review", J. Atmos. Terr. Phys., **43**, pp. 763–774, 1981.
(130) Coley, W. R., J. P. McClure, and W. B. Hanson, "Equatorial fountain effect and dynamo drift signature from AE-E observations", J. Geophys. Res., **95**, pp. 26285–26291, 1990.
(131) Chan, K. L., and L. Colin, "Global electron density distributions from topside soundings", Proc. IEEE, **57**, pp. 990–1004, 1969.
(132) Chandra, S., B. E. Troy Jr., J. L. Donley, and R. E. Bourdeau, "OGO 4 observations of ion composition and temperatures in the topside ionosphere", J. Geophys. Res., **75**, pp. 3867–3878, 1970.
(133) Moffett, R. J., and W. B. Hanson, "Calculated distributions of hydrogen and helium ions in the low-latitude ionosphere", J. Atmos. Terr. Phys., **35**, pp. 207–222, 1973.
(134) Chandra, S., "The equatorial helium ion trough and the geomagnetic anomaly", J. Atmos. Terr. Phys., **37**, pp. 359–367, 1975.
(135) Hanson, W. B., "Upper-atmosphere helium ions", J. Geophys. Res., **67**, pp. 183–188, 1962.
(136) Iwamoto, I., "Diurnal behavior of the equatorial He^+ trough at an altitude of 1100 km", J. Geomag. Geoelectr., **45**, pp. 29–40, 1993.
(137) Brace, L. H., B. M. Reddy, and H. G. Mayr, "Global behavior of the ionosphere at 1000-kilometer altitude", J. Geophys. Res., **72**, pp. 265–283, 1967.
(138) Keating, G. M., and E. J. Prior, "The winter helium bulge", Space Res., **7**, pp. 982–992, 1968.
(139) Matuura, N., M. Kotaki, S. Miyazaki, E. Sagawa, and I. Iwamoto, "ISS-b experimental results on global distributions of ionospheric parameters and thunder storm activity", Acta Astronaut., **8**, pp. 527–548, 1981.
(140) Kohnlein, W., "On the diurnal and season variations of H^+, He^+, N^+, O^+ and Ne at 1400 km altitude", Planet. Space Sci., **29**, pp. 775–782, 1981.
(141) Yonezawa, T., and Y. Arima, "On the seasonal and nonseasonal annual variations and the semiannual variations in the noon and midnight electron densities of the F2 layer in middle latitude", J. Radio Res. Labs., **6**, pp. 293–309, 1959.
(142) Yonezawa, T., "F region anomalies and related phenomena", Rev. Radio Res. Lab., **14**, pp. 153–166, 1968 (in Japanese).
(143) Banks, P. M., A. F. Nagy, and W. I. Axford, "Dynamical behavior of thermal protons in the mid-latitude ionosphere and magnetosphere", Planet. Space Sci., **19**, pp. 1053–1067, 1971.
(144) Moffett, R J., and J. A. Murphy, "Coupling between the F region and protonosphere: Numerical solution of the time dependent equations", Planet. Space Sci., **21**, pp. 43–49, 1973.
(145) Vickrey, J. F., W. E. Swartz, and D. F. Farley, "Ion transport in the topside ionosphere at Arecibo", J. Geophys. Res., **84**, pp. 7307–7314, 1979.

(146) Bailey G. J., J. F. Vickrey and W. E Swartz, "The topside ionosphere above Arecibo during summer at sunspot minimum and the influence of an interhemispheric flow of thermal protons", J. Geophys. Res., **87**, pp. 7557–7565, 1982.
(147) Kockarts, G., "Distribution of hydrogen and helium in the upper atmosphere", J. Atmos. Terr. Phys., **34**, pp. 1729–1743, 1972.
(148) Keating, G. M., J. A. Mullins, and E J. Prior, "The polar exosphere near solar maximum", Space Res., **X**, pp. 439–449, 1970.
(149) Iwamoto, I., E. Sagawa, and T. Suitz, "Observations of the ion composition by Ionosphere Sounding Satellite", Rev. Radio Res. Lab., **28**, pp. 457–470, 1982 (in Japanese).
(150) Brinton, H. C., H. G. Mayr, and W. E. Potter, "Winter bulge and diurnal variations in hydrogen inferred from AE-C composition measurements", Geophys. Res. Lett., **2**, pp. 389–392, 1975.
(151) Koyanagi, Y., Manual for the standard least squares program SALS, Computer Center of University of Tokyo, 1983 (in Japanese).
(152) Muldrew, D. B., "F layer ionization troughs deduced from Alouette data", J. Geophys. Res., **70**, pp. 2635–2650, 1965.
(153) Sharp, G. W., "Midlatitude trough in the night ionosphere", J. Geophys. Res., **71**, pp. 1345–1356, 1966.
(154) Carpenter, D. L., "Whistler studies of the plasmapause in the magnetosphere, 1 Temporal variations in the position of the knee and some evidence on plasma motions near the knee", J. Geophys. Res., **71**, pp. 693–709, 1966.
(155) Thomas, J. O., and M. K. Andrew, "Transpolar exospheric plasma: 1 Plasmasphere termination", J. Geophys. Res., **73**, pp. 7407–7417, 1968.
(156) Rycroft, M. J., and J. O. Tohmas, "The magnetospheric plasmapause and the electron density trough at the Alouette 1 orbit", Planet. Space Sci., **18**, pp. 65–80, 1970.
(157) Rycroft, M. J., and S. J. Burnell, "Statistical analysis of movement of the ionospheric trough and plasmapause", J. Geophys. Res., **75**, pp. 5600–5604, 1970.
(158) Tulnay, Y. K., and J. M. Grebowsky, "The noon and midnight midlatitude trough as seen by Ariel 4", J. Atmos. Terr. Phys., **40**, pp. 845–855, 1978.
(159) Grebowsky, J. M., N. C. Maynard, Y. K. Tulnay, L. J. Lanzerotti, "Coincident observations of ionospheric troughs and equatorial plasmapause", Planet. Space Sci., **24**, pp. 1177–1185, 1975.
(160) Wrenn, G. L., and W. J. Raitt, "In situ observation of mid-latitude ionospheric phenomena associated with the plasmapause", Ann. Geophys., **31**, pp. 17–28, 1975
(161) Serbu, G. P., and E. J. R. Maier, "Observation from Ogo 5 of the thermal ion density and temperature within the magnetosphere", J. Geophys. Res., **75**, pp. 6102–6113, 1970.
(162) Ahmed, M., R. C. Sagalyn, and P. J. L. Wildman, "Topside ionospheric trough morphology: Occurrence frequency and diurnal, seasonal, and altitude variations", J. Geophys. Res., **84**, pp. 489–498, 1979.
(163) Benkova, N. P., N. A. Kochenova, A. D. Legenka, M. N. Fatkukllin, and M. D. Fligel, "Model representation of mid-latitudinal electron density by means of Interkosmos-19 data", Adv. Space Res., **4(1)**, pp. 51–58, 1984.
(164) Shelley, E. G., R. D. Sharp, and R. G. Johnson, "Satellite observations of an ionospheric acceleration mechanism", Geophys. Res. Lett., **3**, pp. 654–656, 1976.
(165) Balsiger, H., J. Geiss, and D. T. Young, "The composition of thermal and hot ions observed by the GEOS-1 and -2 spacecraft", in Energetic ion composition in the earth's magnetosphere, ed. R. G. Jonson, Tera Sci. Pub. Co., Tokyo, pp. 195–230, 1983.
(166) Geiss, J., H., Balsiger, P. Eberhardt, H. P. Walker, L. Weber, and D. T. Young, "Dynamics of magnetospheric ion composition as obtained by the GEOS mass spectrometer", Space Sci. Rev., **22**, pp. 537–566, 1978.

(167) Shelley, E. G., R. D. Sharp, R. G. Tohmson, J. Geiss, P. Eberhardt, H. Balsiger, G. Haerendel, and R. Bauer, "Plasma composition experiment on ISEE-A", IEEE Trans. **GE-16**, pp. 266–270, 1978.

(168) Shelley, E. G., D. A. Simpson, T. C. Sanders, E. Herzberg, H. Balsiger, and A. Ghielmetti, "The energetic ion composition spectrometer (EICS) for the Dynamics Explorer-A", Space Sci. Instrum., **5**, pp. 443–450, 1981.

(169) Shelley, E. G., A. Ghielmetti, E. Herzberg, S. J. Bathel, K. Altwegg-von Burg, and H. Balsiger, "The AMPTE/CCE hot-plasma composition experiment (HPCE)", IEEE Trans. **GE-23**, pp. 241–245, 1985.

(170) Lundin, R., B. Hultqvist, N. Pissarenko, and A. Zackarov, "The plasma Mantle: Composition and other characteristics observed by means of the PROGNOZ-7 satellite", Space Sci. Rev., **31**, pp. 247–345, 1982.

(171) Iwamoto, I., "Low energy particle monitor", in Satellite Environment Monitor, pp. 24–38, Institute of Phys. and Chem. Res., 1982b (in Japanese).

(172) Whalen, B. A., J. R. Burrows, A. W. Yau, E. E. Budzinski, A. M. Pilon, I. Iwamoto, K. Marubashi, S. Watanabe, H. Mori, and E. Sagawa, "The suprathermal ion mass spectrometer (SMS) on board the Akebono (EXOS-D) satellite", J. Geomag. Geoelectr., **42**, pp. 511–536, 1990.

(173) Iwamoto, I., and E. Sagawa, "Examination of the International Reference Ionosphere by ISS-b data", 22nd URSI Assembly, 1987.

(174) Iwamoto, I., E. Sagawa, B. A. Whalen, J. R. Burrows, A. Y. Yau, E. E. Budzinski and A. M. Pilon, "Low energy ion mass spectrometer for the EXOS-D satellite", Rev. Comm. Res. Lab., **38**, pp. 89–102, 1992 (in Japanese).

(175) Schwitz, W., and W. Hehihorn, "Parallel plate analyzer with second order focusing property", J. Phys. E, **5**, pp. 64–73, 1972.

(176) Oya, H., and K. Tsuruda, "Introduction to the Akebono (EXOS-D) satellite observations", J. Geomag. Geoelectr., **42**, pp. 367–370, 1990.

(177) Sagawa, E., I. Iwamoto, S. Watanabe, B. A. Whalen, A. W. Yau, and H. Fukunishi, "Low energy upflowing ion events observed by EXOS-D: Initial results", Geophys. Res. Lett., **18**, pp. 337–340, 1991.

(178) Oya, H., A. Morioka, K. Kobayashi, M. Iizima, T. Ono, H. Miyaoka, T. Okada, and T. Obara, "Plasma wave observation and sounder experiments (PWS) using the Akebono (EXOS-D) satellite—Instrumentation and initial results including discovery of the high altitude equatorial plasma turbulence", J. Geomag. Geoelectr., **42**, pp. 411–442, 1990.

(179) Kimura, I., K. Hashimoto, I. Nagano, T. Okada, M. Yamamoto, T. Yoshino, H. Matsumoto, M. Ejiri, and K. Hayashi, "VLF observations by the Akebono (EXOS-D) satellite", J. Geomag. Geoelectr., **42**, pp. 459–478, 1990.

(180) Watanabe, S., E. Sagawa, I. Iwamoto, B. A. Whalen, and A. W. Yau, "Relation between IMF and thermal He^{++}: A tracer of thermal ions from the solar wind", Rev. Comm. Res. Lab., **38**, pp. 125–135, 1992.

(181) Chappell, C. R., "The terrestrial plasma source: A new perspective in solar-terrestrial processes from Dynamics Explorer", Rev. Geophys., **26**, pp. 229–248, 1988.

IWAO IWAMOTO
Space Instrumentation Section,
Space Division
Ionospheric and Magnetospheric Physics
E-Mail: iwamoto@crl.go.jp